Quantum-Spectroscopy Studies on Semiconductor Nanostructures

Dissertation
zur
Erlangung des Doktorgrades
der Naturwissenschaften
(Dr. rer. nat.)

dem Fachbereich Physik
der Philipps-Universität Marburg
vorgelegt

von
Martin Mootz

aus Schwalmstadt-Ziegenhain

Marburg (Lahn), 2014

Vom Fachbereich Physik der Philipps-Universität Marburg (Hochschulkennziffer: 1180)
als Dissertation angenommen am 10.06.2014

Erstgutachter: Prof. Dr. Mackillo Kira
Zweitgutachter: Priv. Doz. Sangam Chatterjee, PhD

Tag der mündlichen Prüfung: 27.06.2014

Zusammenfassung

Nach den Gesetzen der Quantenmechanik können die physikalischen Eigenschaften eines Systems nur durch die Messung ihrer Wellenfunktion vollständig charakterisiert werden. Solch eine *Quantenzustands-Tomographie* ('quantum-state tomography') [1,2] ist beispielsweise von besonderer Bedeutung für Quantencomputer und die Quanteninformations-Theorie, um die tatsächlichen Zustände von Quanten Bits verlässlich zu ermitteln [3–5]. Insbesondere die systematische Entwicklung von Nanotechnologien, basierend auf Atomen, Molekülen und Halbleitern, hängt entscheidend von der genauen Bestimmung des Quantenzustandes ab. Die vollständige Messung des Quantenzustandes wurde bisher bereits für einfache Systeme, wie ein einmodiges Lichtfeld [6–11], ein eingefangenes Atom [12, 13] oder einem Ensemble sich bewegender Atome [14], realisiert. Dabei wurden entweder direkt die Wellenfunktionen oder äquivalent die Phasenraumverteilungen gemessen. Im Vergleich dazu scheint die genaue Bestimmung der vollständigen Vielteilchenwellenfunktion in Festkörpern aufgrund der großen Dimensionalität der Dichtematrix im Moment noch unerreichbar zu sein.

Jedoch wurde in Ref. [15] ein neuer Theorierahmen entwickelt, bei dem die nichtklassischen Quantenfluktuationen [16–18] des Laserlichtes verwendet werden, um die Materie, zusätzlich zu den klassischen Aspekten des Laserlichtes, d. h. Amplitude, Phase, Dauer und Spektrum [19, 20], zu charakterisieren und zu kontrollieren. Diese zusätzlichen spektroskopischen Möglichkeiten erweitern die klassische Spektroskopie zur Quantenspektroskopie. Zur Illustration der Quantenfluktuationen einer Lichtquelle zeigt Abbildung 0.1 eine schematische Darstellung der zeitlichen Entwicklung eines wohldefinierten Laserpulses. Jede einzelne Messung des elektrischen Feldes ergibt eines von vielen möglichen Ergebnissen (Kreise). Die Messungen sind um den klassischen Wert (durchgezogene Linie) angeordnet, der dem Erwartungswert des elektrischen Feldes entspricht. Quantenmechanisch werden die intrinsischen Schwankungen (schattierte Fläche) um den klassischen Wert durch eine quantenmechanische Verteilung beschrieben, die als Quantenstatistik des Lichtfeldes bezeichnet wird.

Als ein Ergebnis der quantisierten Eigenschaften der Licht–Materie-Wechselwirkung zeigt die Quantenspektroskopie neue Phänomene auf, die der traditionellen Laserspektroskopie verborgen bleiben. Insbesondere in theoretischen Studien an Halbleiter-Quantendrähten ('semiconductor quantum wires') und Halbleiter-Quantenfilmen ('semiconductor

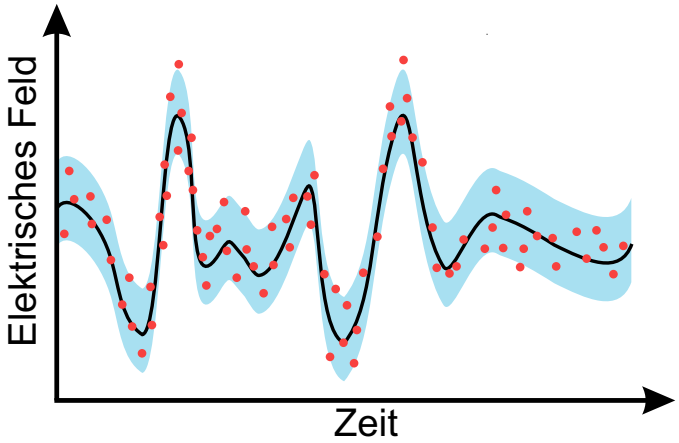

Abbildung 0.1: Schematische Darstellung der Quantenfluktuationen einer Lichtquelle. Die zeitliche Entwicklung des elektrischen Feldes eines wohldefinierten Laserpulses wird dargestellt. Kreise kennzeichnen das Ergebnis eines Ensembles von Messungen. Der Mittelwert des elektrischen Feldes (durchgezogene Linie) wird zusammen mit der mittleren Größe der Fluktuationen (schattierte Fläche), definiert durch die Quantenstatistik, gezeigt. (Nach Referenz [18]).

quantum wells') wurde gezeigt, dass bestimmte Vielteilchenzustände gezielt durch Anpassung der Quantenfluktuationen der Lichtquelle angeregt werden können [15, 21]. Dies ist der erste Schritt in Richtung einer Quantenzustands-Tomographie für wechselwirkende Vielteilchensysteme.

Zur Realisierung von Quantenspektroskopie-Experimenten an Halbleitern werden Quantenlichtquellen benötigt, die stark in ihrer Intensität sind, um ausgeprägte Nichtlinearitäten zu generieren. Darüber hinaus sollten sie ultrakurze Pulse erzeugen können, um die Quantenkinetik von Vielteilchenzuständen darzulegen. Zusätzlich sollten die Quantenlichtquellen über eine flexibel einstellbare Quantenstatistik verfügen, um direkt gezielte Vielteilchenzustände anregen zu können. Bisher wurden bereits mehrere Quantenlichtfelder, wie gequetschte Zustände ('squeezed states') [22–26], Fock-Zustände ('Fock states') [27, 28] und Schrödinger-Katzen-Zustände ('Schrödinger-cat states') [29, 30], experimentell realisiert. In heutigen Experimenten existieren jedoch noch keine Quantenlichtquellen, die über frei einstellbare Quantenfluktuationen verfügen. Daher ist ein alternativer Ansatz in Ref. [31] entwickelt worden, um die Quantenspektroskopie zu realisieren. In diesem Artikel wurde gezeigt, dass klassische Messungen mathematisch auf die quantenoptische Antwort, resultierend von einer beliebigen Quantenlichtquelle, projiziert werden können.

Gegenstand dieser Dissertation ist es, Quantenspektroskopie-Studien an Halbleiternanostrukturen durchzuführen. Neben einer grundlegenden Studie über die allgemeine Anwendbarkeit der Quantenspektroskopie in dissipativen Systemen, werden die optischen Eigenschaften von Halbleiter-Quantenfilmen und -Quantenpunkten ('semiconductor quantum dots') mit Quantenspektroskopie analysiert. Dazu wird eine große Zahl hochpräziser klassischer Messungen auf die Antwort eines mathematisch präzise definierten Quantenlasers projiziert. Die inhärenten Quantenfluktuationen der Lichtquelle werden insbesondere dazu verwendet, um stark korrelierte Vielteilchenzustände in Halbleiter-Quanten-

filmen direkt zu adressieren und quantenoptische Effekte in Quantenpunktsystemen zu kontrollieren. Die Ergebnisse zeigen, dass die Quantenspektroskopie bestimmte Vielteilchenzustände und quantenoptische Effekte mit einer hohen Genauigkeit charakterisieren und kontrollieren kann. Die Untersuchungen verdeutlichen zudem, dass die Quantenspektroskopie neue Kategorien von Vielteilchenzuständen offenbart, die der traditionellen Laserspektroskopie verborgen bleiben.

Im Hauptteil dieser Dissertation wird die Quantenspektroskopie angewendet, um gezielt stark korrelierte Vielteilchenzustände in Halbleiter-Quantenfilmen mit direkter Bandlücke anzuregen. Die systematische Beschreibung solcher Vielteilchensysteme basiert im Allgemeinen auf das Finden von stabilen Konfigurationen, die als Quasiteilchen bezeichnet werden. Diese vereinfachen das Verständnis des Systems signifikant. Beispielsweise wechselwirken die Leitungsbandelektronen im Halbleiter mit dem Gitter und anderen Elektronen. Diese Wechselwirkungen können durch den Austausch der Leitungsbandelektronen mit Quasiteilchen-Elektronen beschrieben werden, die in der Regel eine effektive Masse haben, die sich stark von der eigentlichen Elektronenmasse unterscheidet [18]. Analog können Wechselwirkungen zu größeren Komplexen führen, die selbst Quasiteilchen darstellen. Zum Beispiel können jeweils ein Elektron und ein Loch (fehlendes Elektron im gefüllten Valenzband) ein gebundenes Paar bilden, welches als Exziton bezeichnet wird [32,33] und eine wasserstoffartige Wellenfunktion besitzt [31,34]. Zwei Exzitonen mit entgegengesetztem Spin wiederum können einen molekülartigen Zustand formen, bekannt als Biexziton [35, 36], oder es können sogar Polyexzitonen, bestehend aus mehr als zwei Exzitonen, entstehen [37–39]. Bei Halbleitern mit indirekter Bandlücke ist die Lebenszeit der Elektron–Loch-Anregungen so lang, dass ein thermodynamischer Übergang zu makroskopischen Elektron–Loch-Tropfen ('electron–hole droplets') möglich wird [40–42]. In dieser Dissertation demonstrieren wir nicht nur, dass die Quantenspektroskopie die Eigenschaften von bestimmten Quasiteilchen-Zuständen wie Biexzitonen wesentlich genauer charakterisieren kann als die traditionelle Laserspektroskopie, sondern wir zeigen auch Belege für eine neue stabile Konfiguration geladener Teilchen in GaAs-Quantenfilmen, dem Dropleton, das ein Quantentröpfchen ('quantum droplet'), bestehend aus mehreren Elektronen und Löchern, ist. Die Dropletonen bestehen aus vier bis sieben Elektron–Loch-Paaren, die in einer kleinen Blase eingeschlossen sind. Sie haben Eigenschaften einer Flüssigkeit und weisen Quantisierungseffekte aufgrund ihrer mikroskopischen Größe auf.

Um die detektierbare Energetik von solchen stark korrelierten Vielteilchenzuständen zu bestimmen, kann man im Prinzip Dichtefunktionaltheorie [43–45] anwenden, bei der die Eigenschaften des Systems auf der Basis der funktionalen Abhängigkeit der Gesamtenergie von der Elektronendichte berechnet werden. Wir haben einen neuen Theorierahmen entwickelt, um die Anregungsenergetik von stark korrelierten Quasiteilchen in optisch angeregten Halbleiter-Quantenfilmen zu bestimmen. Bei dieser Methode wird die Anregungsenergetik der Quasiteilchen direkt mit Hilfe ihrer Paarkorrelationsfunktion berechnet.

Die Elektron–Loch-Paarkorrelationsfunktion $g(\mathbf{r})$ definiert die bedingte Wahrscheinlichkeit dafür, ein Elektron an Position $\mathbf{r}$ zu finden, wenn ein Loch im Ursprung positioniert ist. Abbildung 0.2 zeigt ein Beispiel für $g(\mathbf{r})$ von Exzitonen (links) und Dropletonen (rechts). Im Allgemeinen hat $g(\mathbf{r})$ einen konstanten Elektron–Loch-Plasmabeitrag (grau schattierte Fläche), der das gleichmäßig verteilte Plasma in einem homogenen System beschreibt. Quasiteilchen werden durch den korrelierten Beitrag $\Delta g(\mathbf{r})$ (blau schattierte

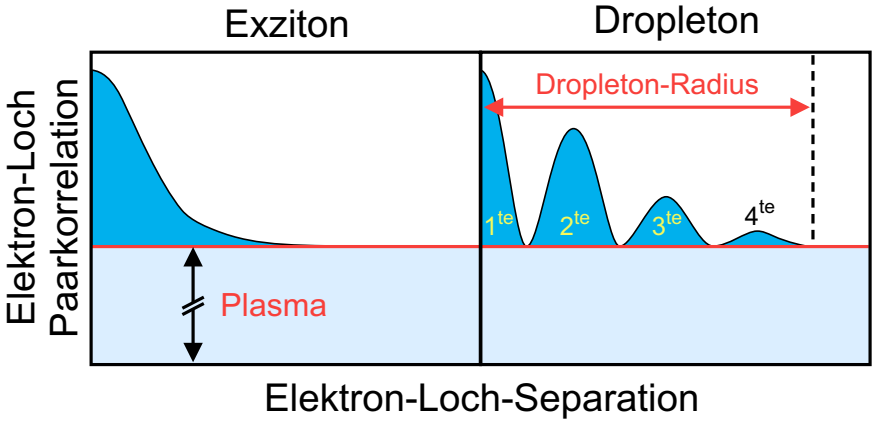

Abbildung 0.2: Beispiel für die Elektron–Loch-Paarkorrelationsfunktion $g(\mathbf{r})$ von Exzitonen (links) und Dropletonen (rechts). Der Plasma-Beitrag wird als grau schattierte Fläche dargestellt, während der blaue schattierte Bereich den korrelierten Beitrag $\Delta g(\mathbf{r})$ zeigt. Der Dropleton-Radius R wird durch eine vertikale gestrichelte Linie gekennzeichnet. (Nach Veröffentlichung (II)).

Fläche) beschrieben, der für große Elektron–Loch-Abstände auf Null abfällt. Die Form des korrelierten Anteils der Paarkorrelationsfunktion von 1s-Exzitonen, $\Delta g(\mathbf{r}) \propto |\phi_{1s}(\mathbf{r})|^2$, ist durch die 1$s$-Exziton-Wellenfunktion $\phi_{1s}(\mathbf{r})$ bestimmt [46], so dass $\Delta g(\mathbf{r})$ monoton abfällt. Im Vergleich dazu befinden sich die Elektronen und Löcher in einem Quantentröpfchen in einer Flüssigkeitsphase, in der die Teilchen ein ringartiges Muster bilden, wobei der Ringabstand ungefähr durch den mittleren Teilchenabstand definiert ist [47–51]. Im Gegensatz zu Einkomponenten-Flüssigkeiten [52–55] hat $\Delta g(\mathbf{r})$ einen zentralen Peak aufgrund der Coulomb-Anziehung zwischen den Elektronen und Löchern. Da die Dropletonen innerhalb einer mikroskopischen Blase mit Radius R eingeschlossen sind, verschwindet $\Delta g(\mathbf{r})$ außerhalb von R.

In einer weiteren Untersuchung im Rahmen dieser Dissertation werden die Emissionseigenschaften von optisch gepumpten Quantenpunkt-Mikroresonatoren ('quantum-dot microcavities') analysiert. Viele Studien an Quantenpunkt-Mikroresonatoren haben bereits bemerkenswerte Quanten-Phänomene, wie den Purcell-Effekt [56], die Vakuum-Rabi-Aufspaltung [57,58], oder die starke Licht–Materie-Kopplung [59–64], demonstriert. Somit stellen diese Systeme eine geeignete Plattform für systematische quantenoptische Untersuchungen [65,66], Resonator-Quanten-Elektrodynamik-Studien [31,67] und die Entwicklung von Komponenten, wie Einzelphotonenemitter [68–70] oder Lichtquellen für verschränkte Photonenpaare [71–73], die erforderlich sind um Quanteninformations-Technologien [74–79] zu realisieren, dar. Außerdem werden diese Quantenpunkt-Mikroresonatoren als hochwertige Laser verwendet, die extrem niedrige Laserschwellen aufweisen [61, 80]. Allerdings ist der Betrieb dieser Systeme unter Laserbedingungen weniger für Resonator-Quanten-Elektrodynamik-Studien geeignet, da das emittierte Licht eines Lasers durch einen kohärenten Zustand [16, 17, 81] beschrieben werden kann, der einer perfekten klassischen Emission entspricht. In dieser Dissertation analysieren wir die Emissionseigenschaften optisch gepumpter Quantenpunkt-Mikroresonatoren in dem Anregungsleistungs-Bereich unterhalb der Laserschwelle. Unsere Untersuchungen zeigen experimentelle und theoretische Beweise für die Entdeckung eines neuen faszinierenden Quantengedächtnis-

effekts ('quantum-memory effect'), der durch das Anpassen der Quantenfluktuationen der Pumplichtquelle kontrolliert werden kann.

Die Dissertation ist wie folgt aufgebaut: In Kapitel 2 wird ein kurzer Überblick über die verwendeten theoretischen Konzepte gegeben. Das 3. Kapitel zeigt experimentelle und theoretische Belege für Quantentröpfchen als neue stark korrelierte Quasiteilchen in GaAs-Quantenfilmen. Zur Detektion der Dropletonen verwenden wir Quantenspektroskopie, um direkt stärker korrelierte Vielteilchenzustände im System anzuregen. Zur Bestimmung der Anregungsenergetik der Dropletonen haben wir ein neues theoretisches Verfahren entwickelt. Diese Methode ermöglicht es das Anregungsspektrum von stark korrelierten Quasiteilchen in optisch angeregten Halbleitern, basierend auf der Paarkorrelationsfunktion des Quasiteilchen-Zustands, zu berechnen. Das präsentierte Verfahren kann im Allgemeinen zur Bestimmung und Vorhersage des Anregungsspektrums einer Vielzahl von stark korrelierten Vielteilchenzuständen verwendet werden.

Kapitel 4 zeigt, dass die Quantenspektroskopie die Eigenschaften von stark korrelierten Quasiteilchenzuständen mit einer sehr hohen Genauigkeit charakterisieren kann. Zur Illustration werden die Eigenschaften der Biexziton-Resonanz in den Absorptionsspektren von GaAs-Quantenfilmen mit Quantenspektroskopie analysiert. Unsere Studie verdeutlicht, dass die Quantenspektroskopie eine Vielzahl von biexzitonischen Details aufzeigt, die der klassischen Spektroskopie verborgen bleiben.

In Kapitel 5 werden die Ergebnisse der Quantenspektroskopie-Studien an Quantenpunktsystemen vorgestellt. Der erste Teil des Kapitels beschäftigt sich mit der Untersuchung der Emissionseigenschaften von optischen gepumpten Quantenpunkt-Mikroresonatoren in dem Anregungsbereich unterhalb der Laserschwelle. Die Eingangs–Ausgangs-Charakteristik weist unerwartete Nichtlinearitäten auf, die unter Anwendung einer systematischen mikroskopischen Analyse als Quantengedächtniseffekt identifiziert werden. Quantenspektroskopie verifiziert nicht nur den Ursprung des Quantengedächtniseffekts, sondern zeigt auch, dass die Nichtlinearitäten durch Anpassung der Quantenfluktuationen der Lichtquelle kontrolliert werden können.

Der zweite Teil des 5. Kapitels beschäftigt sich mit einer Grundlagenstudie über die allgemeine Anwendbarkeit der Quantenspektroskopie in dissipativen Systemen. Die vorgestellten Ergebnisse zeigen, dass Quantenspektroskopie-Studien an einer Vielzahl von Systemen durchgeführt werden können. Schließlich werden die Ergebnisse dieser Dissertation in Kapitel 6 zusammengefasst. Die Veröffentlichungen werden im 7. Kapitel vorgestellt.

Acknowledgement

First, I would like to thank my supervisor Professor Mackillo Kira who guided me through the world of research, provided me with constructive criticism, and gave me permanent support.

I also thank Professor Stephan Koch for his friendly reception in the group and his ever competent feedback on my work.

This Thesis in its present form would not be possible without the experiments which I had the opportunity to analyze. Therefore, I thank Professor Steven Cundiff, Andrew Almand-Hunter, and Dr. Hebin Li for providing the nice data and for many fruitful discussions. I would also like to thank Professor Manfred Bayer, Dr. Jean-Sebastian Tempel, and Dr. Marc Aßmann for the collaboration in the quantum-dot microcavity project.

Thanks also to Privat-Dozent Sangam Chatterjee for providing the second opinion on this Thesis and to Professor Reinhard Noack for chairing the Thesis defense.

I would also like to thank Professor Peter Thomas for the organization of the hiking holidays. Just as much, I would like to thank Renate Schmid who always helped me with all the bureaucracy.

Many thanks to all my colleagues of the Semiconductor Theory Group, especially my roommates Phillip Springer and Dominik Breddermann for the pleasant atmosphere, Dr. Andrea Klettke, Jakob Geipel and Dr. Benjamin Breddermann for the coffee breaks, Dr. Lukas Schneebeli for many interesting physical discussions, Dr. Christoph Böttge and Dr. Tineke Warncke for many helpful hints, Ulrich Huttner for the interesting discussions about quantum spectroscopy, and Christian Berger for the running workouts and for discovering the Marburger Hinterland via bicycle.

I would also like to thank all my friends, especially Michael Opper for the nice bike rides.

Last but not least, I would like to thank my family for their permanent support during my studies in Marburg.

Author's contributions

This Thesis consists of an introductory review part discussing the main ideas and results of my doctoral studies followed by five research publications.

Publications

(I) **M. Mootz**, M. Kira, and S. W. Koch, "Sequential build-up of quantum-optical correlations", *J. Opt. Soc. Am. B* **29**, A17–A24 (2012).

(II) **M. Mootz**, M. Kira, and S. W. Koch, "Pair-excitation energetics of highly correlated many-body states", *New J. Phys.* **15**, 093040 (2013).

(III) A. E. Almand-Hunter, H. Li, S. T. Cundiff, **M. Mootz**, M. Kira, and S. W. Koch, "Quantum droplets of electrons and holes", *Nature* **506**, 471–475 (2014).

(IV) **M. Mootz**, M. Kira, S. W. Koch, A. E. Almand-Hunter, and S. T. Cundiff, "Characterizing biexciton coherences with quantum spectroscopy", *Phys. Rev. B* **89**, 155301 (2014).

(V) C. Berger, U. Huttner, **M. Mootz**, M. Kira, S. W. Koch, J.-S. Tempel, M. Aßmann, M. Bayer, A. M. Mintairov, and J. L. Merz, "Quantum-memory effects in the emission of quantum-dot microcavities", *Phys. Rev. Lett.* **113**, 093902 (2014).

Posters and Talks

- **M. Mootz**, M. Kira, and S. W. Koch, "Quantum-optical correlations in dissipative quantum-dot systems", Contributed Talk, DPG (German Physical Society) spring conference in Dresden (Germany) (2011).

- **M. Mootz**, M. Kira, S. W. Koch, A. E. Almand-Hunter, and S. T. Cundiff, "Identifying many-body states with quantum light", Poster presented at the 11^{th} international workshop on Nonlinear Optics and Excitation Kinetics in Semiconductors (NOEKS 11) in Stuttgart (Germany) (2012).

- **M. Mootz**, M. Kira, S. W. Koch, A. E. Almand-Hunter, H. Li, and S. T. Cundiff, "Accessing many-body complexes with quantum light", Poster presented at the 13$^{\text{th}}$ international conference on Optics of Excitons in Confined Systems (OECS 13) in Rome (Italy) (2013).

- **M. Mootz**, M. Kira, S. W. Koch, A. E. Almand-Hunter, H. Li, and S. T. Cundiff, "Quantum-spectroscopy studies on semiconductor quantum wells", Contributed Talk, DPG (German Physical Society) spring conference in Dresden (Germany) (2014).

Original contributions

All studies presented in this Thesis are the result of frequent group meetings where intermediate results have been discussed and new calculations have been planned. Most of the actual programming and calculations have been performed by myself.

In my first research project, I analyzed the build-up dynamics of quantum-optical correlations in a Jaynes–Cummings system modeling quantum-dot systems. The aim was to investigate the possibilities of quantum-spectroscopy studies in dissipative systems. I started this project as diploma student and continued it during my PhD time. Therefore, preliminary results of the study are already presented in my diploma thesis [130]. To investigate the dynamics of quantum-optical correlations, I had to write a new program which numerically solves the dynamics of the Jaynes–Cummings system. In order to study the effect of dissipation, I also included dephasing via the Lindbladian to my code. Furthermore, I solved the full dynamics analytically and verified that the system evolves towards a steady state when the system contains dissipation. The results of the project have been published in Paper (I). I did all numerical and analytical calculations presented therein and was mainly responsible for the writing. I presented the results as a contributed talk at the DPG spring meeting in 2011 in Dresden (Germany). The project is discussed in Chapter 5 of this Thesis.

The second project was a collaboration with the group of Steven T. Cundiff (JILA, University of Colorado & NIST, Boulder, USA). The experiments were performed by Steven T. Cundiff *et al.* while the theoretical studies were done in Marburg. We investigated the biexciton resonance in the absorption spectra of semiconductor quantum wells using quantum spectroscopy. Therefore, I wrote a program which allows for the computation of the quantum-optical response to several quantum-light fields from a set of classical measurements. Using this program, I studied the excitation-induced dephasing and the dynamical properties of the biexciton resonance in the quantum-well absorption by comparing the results of classical and quantum spectroscopy. The outcome of this project is presented in Paper (IV). In this paper, I was responsible for the computations and contributed significantly to the paper writing. I presented these results as a Poster at the NOEKS 11 conference in 2012 in Stuttgart (Germany). In this Thesis, the results are discussed in Chapter 4.

In the same study, we observed an unexpected red shift of the biexciton resonance in the quantum-well absorption as the excitation intensity is increased. We studied this effect in more detail using quantum spectroscopy. In particular, I theoretically deduced a new quantum-light field, slanted Schrödinger's cat state, that allows for a direct excitation of higher correlated electron–hole clusters in the quantum well system. Consequently,

I had to extend my code to project the quantum-optical response to slanted-cat states from classical measurements. As a result, we found that three new discrete energy levels emerged below the biexciton resonance in slanted-cat state's differential absorption spectra. We could also observe quantum beats between the new energy levels such that we had evidence for a new quasiparticle. We had several meetings in our group and with the group of Steven T. Cundiff where intermediate results have been discussed and new measurements and calculations have been planned to find out the origin of the new energy levels. The analysis of control measurements excluded the polyexcitonic character of the quasiparticle. As a result, we hypothesized that the new quasiparticle is a quantum droplet of electrons and holes.

To verify the quantum-droplet hypothesis, I had to develop a new theoretical scheme to compute the excitation spectrum of highly correlated many-body states. As a new aspect, I expressed the system energy as a functional of the electron–hole pair-correlation function. As a result, I obtained a generalized Wannier equation which allows for the computation of the pair-excitation energetics based on the electron–hole pair-correlation function of the many-body state. To apply the scheme, I had to write a new program to compute the pair-excitation energetics based on a pair-correlation input. By using this systematic approach, I tried different ansatzes for the quasiparticle pair-correlation function to find the many-body state which explains the detected new spectral features. As a result, I found that a pair-correlation function characteristic for liquids explains the measured energetics. The study also revealed detailed properties of the quantum droplets. Our joint findings have been published in Paper (III) while Paper (II) presents an exclusively theoretical study about the computation scheme of the pair-excitation spectrum. To these publications, I contributed all analytical and numerical calculations and was mainly responsible for the writing of Paper (II) and the theory part of the Supplementary Information to Paper (III). I presented these results as a Poster at the OECS 13 conference in 2013 in Rome (Italy). The results of this project are presented in Chapter 3 of this Thesis.

Another project was a collaboration with Manfred Bayer *et al.* (Technische Universität Dortmund, Germany) who performed the measurements. The theory part was done together with Ulrich Huttner and Christian Berger of our group. The aim was to study the quantum-optical aspects in the input/output characteristics of optically pumped quantum-dot microcavities in the excitation regime below lasing. We found that the input/output characteristics shows unexpected oscillations. A systematic microscopic analysis performed by Christian Berger identifies the oscillations in the input/output characteristics as a genuine quantum-memory effect. Together with Ulrich Huttner, I studied the quantum-memory effect with quantum spectroscopy. We had several meetings about how to process the data to efficiently analyze the quantum-memory effect with quantum spectroscopy. The quantum-spectroscopy calculations have been performed by Ulrich Huttner. The findings of the project are presented in Paper (V). To this paper, I contributed to the writing of the manuscript. The project is reviewed in Chapter 5 of this Thesis.

Contents

1 Introduction

According to the laws of quantum mechanics, only a measurement of system's wavefunction provides the ultimate characterization of all its physical properties. For example, such a *quantum-state tomography* [1,2] is essential for quantum computing and quantum-information theory to precisely determine the actual states of quantum bits [3–5]. In particular, the systematic development of nanotechnology, based on atoms, molecules, and semiconductors, depends critically on the precise extraction of quantum state's wavefunction. Until now, the measurement of the quantum state has already been realized for simple systems like a single-mode light field [6–11], a trapped ion [12,13], or an ensemble of moving atoms [14] where either the wavefunction directly or equivalently the phase-space distributions have been determined. At the same time, the extraction of the full many-body wavefunction in solids seems to be impossible due to the large dimensionality of the density matrix involved.

However, a new theoretical framework has been developed in Ref. [15] where laser's nonclassical quantum fluctuations [16–18] are used to characterize and control matter in addition to laser's classical aspects, i. e. amplitude, phase, duration, and spectrum [19,20]. This enhancement of the spectroscopic capabilities extends classical spectroscopy to quantum spectroscopy. To illustrate light source's quantum fluctuations, Fig. 1.1 shows a schematic representation of the temporal evolution of a designed laser pulse. Each individual measurement of the electric field yields one of many possible outcomes (circles). The measurement ensemble is arranged around the classical value (solid line) which corresponds to the expectation value of the electric field. Quantum mechanically, the intrinsic fluctuations (shaded area) around the classical value are described by a quantum mechanical distribution which is called quantum statistics of the light field.

As a new aspect, quantum spectroscopy reveals new classes of phenomena that are hidden to classical spectroscopy, resulting directly from the quantized nature of the light–matter interaction. In particular, in theoretical studies on semiconductor quantum wires and quantum wells (QWs) it has been shown that specific many-body states can be directly excited by adjusting the quantum fluctuations of the applied light field [15, 21]. This is the first step towards a quantum-state tomography for interacting many-body states.

In general, quantum-spectroscopy experiments on semiconductors require quantum-light sources that are strong, in order to generate distinct nonlinearities in many-body systems, and ultrafast, to monitor the quantum dynamics of many-body states. Addition-

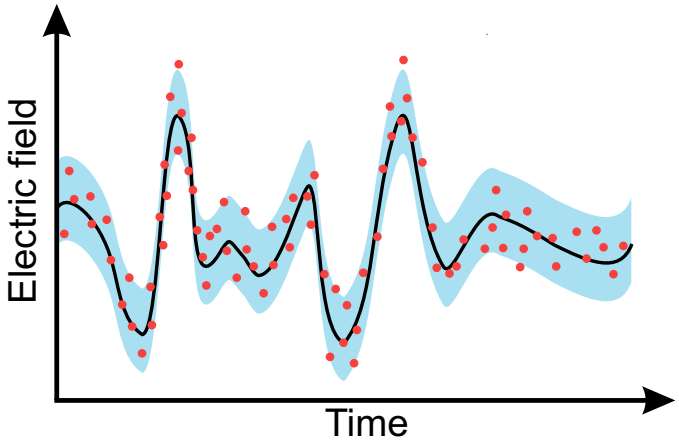

Figure 1.1: Schematic representation of light source's quantum fluctuations. The temporal evolution of a designed laser pulse is shown. Circles indicate the outcome of a measurement ensemble. The mean of the electric field (solid line) is presented together with the average size of fluctuations (shaded area) defined by the quantum statistics. (According to Ref. [18]).

ally, the quantum sources should have flexibly adjustable quantum statistics to directly excite targeted many-body states. Until now, several quantum-light states have already been synthesized in experiments including squeezed states [22, 23, 26] even with strong squeezing of light's quantum noise [24, 25], Fock states [27, 28], and Schrödinger's cat states [29, 30]. However, so far, no quantum sources exist in present-day experiments that are free adjustable in their quantum fluctuations. Nevertheless, an alternative approach has been developed in Ref. [31] to realize quantum spectroscopy. In that article, it has been shown that an extensive set of classical measurements can be mathematically projected into a quantum-optical response resulting from any possible quantum sources.

The subject of this Thesis is to perform quantum-spectroscopy studies on semiconductor nanostructures. Besides a fundamental study about the general applicability of quantum spectroscopy in dissipative systems, the optical properties of semiconductor QW and quantum-dot (QD) systems are analyzed with quantum spectroscopy by projecting high-precision optical measurements into quantum-optical responses. More specifically, light source's inherent quantum fluctuations are adjusted to directly excite highly correlated many-body states in semiconductor QWs and to control quantum-optical effects in QD systems. The results demonstrate that quantum spectroscopy can characterize and control specific many-body states and quantum-optical effects with a high accuracy. In particular, the studies show that quantum spectroscopy reveals new classes of many-body states that remain hidden to traditional laser spectroscopy.

In the major part of this Thesis, quantum spectroscopy is applied to directly excite highly correlated many-body states in direct-gap semiconductor QWs. In general, the systematic description of such many-body systems is based on finding stable configurations that are known as quasiparticles. Their discovery and identification is critical to develop a physical understanding of the system. For example, in semiconductors the conduction-band electrons interact with the lattice and other electrons. These interactions can be handled by replacing the bare electrons with quasiparticle electrons that typically have an effective mass that is very different from the bare electron mass [18].

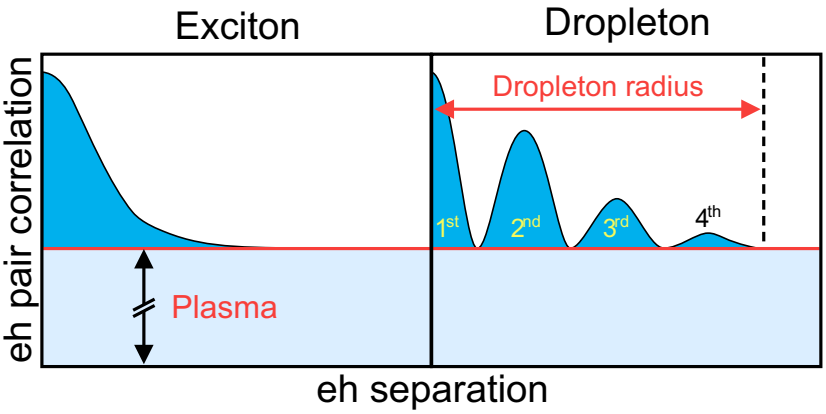

Figure 1.2: Example for exciton's (left) and dropleton's (right) electron–hole (eh) pair-correlation function $g(\mathbf{r})$. The plasma contribution is shown as gray shaded area while the blue shaded area indicates the correlated part $\Delta g(\mathbf{r})$. The dropleton radius is denoted by a vertical dashed line and each of the rings is labeled. (According to Paper (II)).

Analogously, interactions can result in larger complexes that are themselves quasiparticles. For instance, an electron can bind with a hole, which is the absence of an electron in the filled valence band, to create a bound pair referred to as exciton [32, 33] that has a hydrogenic wavefunction for the relative coordinate [31, 34]. Two excitons with opposite spin can bind to a molecular-like state known as biexciton [35, 36] or even polyexcitons consisting of more than two excitons can form [37–39]. In indirect-gap semiconductors, the life time of the electron–hole excitations becomes so long that a thermodynamic transition into macroscopic electron–hole droplets becomes possible [40–42]. In this Thesis, we not only demonstrate that quantum spectroscopy can characterize the properties of specific quasiparticle states like biexcitons much more sensitively than traditional laser spectroscopy, but we also show evidence for a new stable configuration of charged particles in direct-gap GaAs QWs, the dropleton, that is a quantum droplet of electrons and holes. The dropletons contain four-to-seven electron–hole pairs in the form of a liquid confined inside a small correlation bubble. They form via Coulomb interactions long before the system has reached the thermal equilibrium and show quantization effects due to their microscopic size.

To determine the detectable energetics of such highly correlated many-body complexes, one can in principle apply density-functional theory which uses the functional dependence of the total energy on the electron density to compute the properties of the system [43–45]. We have developed an alternative approach to compute the excitation energetics of highly correlated quasiparticles in optically excited semiconductor QWs. Since it is very natural to identify highly-correlated quasiparticles through their pair-correlation function, we have formulated a theoretical framework to determine the excitation spectrum directly from the pair-correlation function.

The electron–hole pair-correlation function $g(\mathbf{r})$ determines the conditional probability of finding an electron at position $\mathbf{r}$ when a hole is positioned at the origin. Figure 1.2 presents an example for exciton's (left) and dropleton's (right) $g(\mathbf{r})$. In general, $g(\mathbf{r})$ always has a large constant electron–hole plasma part (gray shaded area) resulting from

the mean-field properties of the many-body state. Quasiparticle cluster are determined by the correlated part $\Delta g(\mathbf{r})$ (blue shaded area) which decays at elevated electron–hole separation. The $1s$-exciton wave function $\phi_{1s}(\mathbf{r})$ determines the correlated part of $1s$ exciton's $g(\mathbf{r})$ via $\Delta g(\mathbf{r}) \propto |\phi_{1s}(\mathbf{r})|^2$ [46], yielding a monotonically decreasing $\Delta g(\mathbf{r})$. Compared to that, the electrons and holes in the quantum droplet are in a liquid state such that $\Delta g(\mathbf{r})$ has the typical liquid structure where particles form a ring-like pattern with ring separation roughly defined by the mean particle distance [47–51]. In contrast to single-component liquids [52–55], dropleton's $\Delta g(\mathbf{r})$ has a central peak because of the Coulomb attraction between electrons and holes. Since dropletons are confined inside a microscopic bubble of radius R, $\Delta g(\mathbf{r})$ vanishes outside R.

Another study in this Thesis deals with the emission properties of optically pumped QD microcavities. Pioneering work on QD microcavities has already produced demonstrations of striking quantum-optical phenomena including the Purcell effect [56], vacuum Rabi splitting [57, 58], and strong-coupling investigations [59–64]. Thus, these systems have become a suitable platform for systematic quantum-optical studies [65, 66], semiconductor-based quantum electrodynamics investigations [31, 67], and the development of components like single-photon emitters [68–70] or sources for entangled photon pairs [71–73] that are needed to realize quantum-information protocols [74–79]. Additionally, such QD microcavities are used as high-quality lasers which exhibit extremely low laser thresholds [61, 80]. However, the operation of the system under lasing conditions is less important for cavity quantum electrodynamics investigations because the output of a laser is a coherent state [16, 17, 81] that corresponds to a perfect classical emission. In this Thesis, the emission properties of optically pumped QD microcavities are analyzed in the excitation power regime below the laser threshold. The study reveals experimental and theoretical evidence for a new intriguing quantum-memory effect that is controllable by adjusting pump source's quantum fluctuations.

The Thesis is organized as follows: In Chapter 2, a brief overview is given about the theoretical concepts used. Chapter 3 shows experimental and theoretical evidence for the dropleton as a new highly correlated quasiparticle in GaAs QWs while the characterization of the biexciton resonance with quantum spectroscopy is discussed in Chapter 4. In Chapter 5, the results of the quantum-spectroscopy studies on QD systems are presented. In particular, the first part deals with the identification of a new quantum-memory effect in the emission of optically pumped QD microcavities while the second part provides a fundamental study about the general applicability of quantum spectroscopy in dissipative systems. Finally, the findings of this Thesis are summarized in Chapter 6. A short introduction to the papers is given in Chapter 7.

2 Theoretical approach

This Chapter provides an overview about the theoretical background that forms the basis for the results presented in Chapters 2–5 and related Papers. In the major part of this Thesis, direct-gap semiconductor QWs are studied such that the corresponding full many-body theory is briefly introduced, which is mainly based on Refs. [18, 46]. In addition, the limitation of highly correlated quasiparticle characterization with traditional laser spectroscopy is described and it is shown how quantum spectroscopy can be used to directly excite specific many-body states in semiconductor QWs. The general concept of quantum spectroscopy is thoroughly discussed in Refs. [15, 18, 31, 46].

The system Hamiltonian describing the many-body Coulomb interaction among electrons and the fully quantized light–matter interaction in direct-gap semiconductor QWs is introduced in Sec. 2.1. The limitation of quasiparticle identification with classical spectroscopy and the state-injection aspects of quantum spectroscopy in semiconductor QWs are discussed in Secs. 2.2 and 2.3, respectively. In Sec. 2.4, it is shown how the quantum-optical response to arbitrary quantum-light sources can be projected from a set of classical measurements. The presented framework introduced in Ref. [31] is completely general and can be applied to realize quantum spectroscopy in generic condensed-matter systems and beyond. Examples for quantum-light sources studied within this Thesis are shown in Sec. 2.5.

2.1 System Hamiltonian

To formulate the system Hamiltonian describing semiconductor QWs, it is convenient to use the second quantization formalism. The microscopic description of elementary charge carrier excitations is obtained by introducing the Fermionic operators $a^\dagger_{\lambda,\mathbf{k}}$ and $a_{\lambda,\mathbf{k}}$ that create and annihilate an electron with crystal momentum $\hbar\mathbf{k}$, respectively, to the conduction ($\lambda = \mathrm{c}$) or valence band ($\lambda = \mathrm{v}$). The quantum statistics of the applied light field is defined by Bosonic creation and annihilation operators $B_\mathbf{q}$ and $B^\dagger_\mathbf{q}$ with photon-wave vector $\mathbf{q}$. A quantization of laser's light field yields the mode expansion of the electric field [15, 18]

$$\mathbf{E}(\mathbf{r}) = \sum_\mathbf{q} \mathcal{E}_\mathbf{q} \left[\mathbf{u}_\mathbf{q}(\mathbf{r}) B_\mathbf{q} + \mathbf{u}^\star_\mathbf{q}(\mathbf{r}) B^\dagger_\mathbf{q}\right] , \tag{2.1}$$

where $\mathbf{u_q}$ is the mode function with frequency $\omega_\mathbf{q} = c|\mathbf{q}|$ while $\mathcal{E}_\mathbf{q}$ corresponds to the vacuum-field amplitude.

For resonant excitation conditions, direct-gap semiconductor QWs can be modeled by a two-band Hamiltonian [15, 18]

$$\hat{H} = \hat{H}_\mathrm{eh} + \hat{H}_\mathrm{lm}\,, \qquad \hat{H}_\mathrm{eh} = \sum_{\mathbf{k},\lambda} \epsilon^\lambda_\mathbf{k} a^\dagger_{\lambda,\mathbf{k}} a_{\lambda,\mathbf{k}} + \frac{1}{2} \sum_{\mathbf{k},\mathbf{k}',\mathbf{q},\lambda,\lambda'} V_\mathbf{q}\, a^\dagger_{\lambda,\mathbf{k}+\mathbf{q}} a^\dagger_{\lambda',\mathbf{k}'-\mathbf{q}} a_{\lambda',\mathbf{k}'} a_{\lambda,\mathbf{k}}\,,$$
$$\hat{H}_\mathrm{lm} = \sum_\mathbf{q} \hbar\omega_\mathbf{q} \left(B^\dagger_\mathbf{q} B_\mathbf{q} + \tfrac{1}{2}\right) - \mathrm{i}\hbar \sum_{\mathbf{k},\mathbf{q}} \mathcal{F}_\mathbf{q} \left(a^\dagger_{\mathrm{c},\mathbf{k}} a_{\mathrm{v},\mathbf{k}} + a^\dagger_{\mathrm{v},\mathbf{k}} a_{\mathrm{c},\mathbf{k}}\right) B_\mathbf{q} + \mathrm{h.c.}\,, \tag{2.2}$$

that describes the many-body Coulomb interaction among electrons and the fully quantized light–matter interaction. The valence and conduction band can be treated as parabolic for excitations close to the Γ-point such that the kinetic energies can be written as

$$\epsilon^\mathrm{c}_\mathbf{k} = \frac{\hbar^2\mathbf{k}^2}{2m_\mathrm{e}} + \mathrm{E_g}\,, \qquad \epsilon^\mathrm{v}_\mathbf{k} = -\frac{\hbar^2\mathbf{k}^2}{2m_\mathrm{h}}\,, \tag{2.3}$$

where E_g is the bandgap energy and $m_\mathrm{e(h)}$ defines the effective electron (hole) mass. The Coulomb interaction is described by the second term of $\hat{H}_\mathrm{eh}$, containing the Coulomb matrix element $V_\mathbf{q}$ of the confined system [82].

The light–matter interaction follows from $\hat{H}_\mathrm{lm}$ where $\hbar\omega_\mathbf{q}$ corresponds to the free-photon energy. The strength of the light–matter interaction is determined by $\mathcal{F}_\mathbf{q} = \mathbf{d}\,\mathcal{E}_\mathbf{q} \cdot \mathbf{u_q}(0)$ including the dipole-matrix element $\mathbf{d}$ for interband transitions.

2.2 Limitation of quasiparticle identification with classical spectroscopy

A central goal of this Thesis is to characterize and control highly correlated quasiparticles in semiconductor QWs. In general, the direct characterization of such quasiparticles with classical spectroscopy is very limited which is demonstrated in this section. Therefore, the dynamics of quasiparticles after the excitation with a classical laser pulse is illustrated.

Experimentally, the quantum kinetics of quasiparticles can be analyzed using a pump–probe measurement setup as it is done in the quantum-spectroscopy studies on semiconductor QWs in this Thesis. More specifically, a strong ultrafast laser excites the matter system from its ground state before the excitation configuration is probed by a weak laser pulse to monitor the quantum kinetics of the light-generated quasiparticles. In the analyzed experiments within this Thesis, the matter system is excited by a single-mode pump laser whose quantum statistics can be presented using the photon-correlation representation [83]

$$\left[\Delta I^J_K\right]_\mathrm{B} = \Delta\langle \left[B^\dagger\right]^J B^K \rangle\,, \tag{2.4}$$

that correspond to $(J{+}K)$-particle clusters according to the cluster-expansion approach [18, 46,83–87]. In particular, by applying the cluster-expansion approach, the quantum-optical

correlations (2.4) can be uniquely expressed in terms of the normally ordered expectation values

$$I_K^J = \langle \left[B^\dagger\right]^J B^K \rangle = \mathrm{Tr}\left[\left(B^\dagger\right)^J B^K \hat{\rho}\right] , \tag{2.5}$$

where $\hat{\rho}$ is system's density matrix. The expectation values (2.5) also define laser's quantum statistics.

Analogously to Eq. (2.4), many-body correlations in electron–hole excitations can be introduced by

$$\left[\Delta I_K^J\right]_X = \Delta\langle \left[\hat{X}^\dagger\right]^J \hat{X}^K \rangle . \tag{2.6}$$

Here, electron–hole excitations are described by the exciton operator

$$\hat{X}^\dagger = \sum_{\mathbf{k}} \phi_{1s}(\mathbf{k})\, a^\dagger_{\mathrm{c},\mathbf{k}} a_{\mathrm{v},\mathbf{k}} , \tag{2.7}$$

when the single-mode laser is resonant to the $1s$-exciton state defined by the wavefunction $\phi_{1s}(\mathbf{k})$. In general, $\hat{X}^\dagger$ exhibits nonbosonic corrections resulting from its Fermionic substructure [88].

The electron–hole correlations (2.6) correspond to quasiparticle cluster like true bound excitons ($\Delta\langle \hat{X}^\dagger \hat{X}\rangle$) or biexcitonic transition amplitude ($\Delta\langle \hat{X}\hat{X}\rangle$). The computation of the corresponding cluster dynamics using the Heisenberg-equation-of-motion technique produces the well-known hierarchy problem of many-body physics [18, 46]

$$\mathrm{i}\hbar\frac{\partial}{\partial t}\Delta\langle \hat{N}\rangle = \mathrm{T}\left[\Delta\langle \hat{N}\rangle\right] + \mathrm{NL}\left[\langle \hat{1}\rangle, \cdots, \Delta\langle \hat{N}\rangle\right] + \mathrm{Hi}\left[\Delta\langle \hat{N}+1\rangle\right] , \tag{2.8}$$

where N-particle correlations couple to $(N+1)$-particle correlations. Contributions without hierarchy coupling are symbolized by 'T' while the hierarchy contribution is indicated by 'Hi'. The nonlinear coupling among clusters is described by 'NL'. The hierarchy problem (2.8) is a direct consequence of the many-body Coulomb and light–matter interactions, yielding an infinite hierarchy of coupled equations.

In Paper (I), the dynamics of the quantum-optical correlations (2.4) and the hierarchy problem (2.8) are investigated in a Jaynes–Cummings system [89] modeling QD systems. Compared to complicated many-body systems, this simple model allows for an exact computation of the correlation dynamics to all orders. In that study, the system is excited by a coherent state $|\beta\rangle$ [16, 17, 81] where β is its complex-valued displacement amplitude. In general, the coherent state corresponds to a classical light field because its quantum statistics, $I_K^J = [\beta^\star]^J \beta^K$, yields the classical factorization [18] where the photon operators in Eq. (2.5) are substituted by the complex-valued amplitude $\beta = \langle B\rangle$. In particular, the output of a perfect single-mode laser is described by a coherent state [31, 81].

The results in Paper (I) show that the quantum-optical correlations build up *sequentially* for a coherent-state excitation. In other words, higher order correlations only build up after the lower ones are already present. Thus, in a physically relevant time window, the system is essentially described by C-particle correlations while correlated clusters beyond C are weak or build up at later times. As a result, the 'Hi' contribution in Eq. (2.8) can be

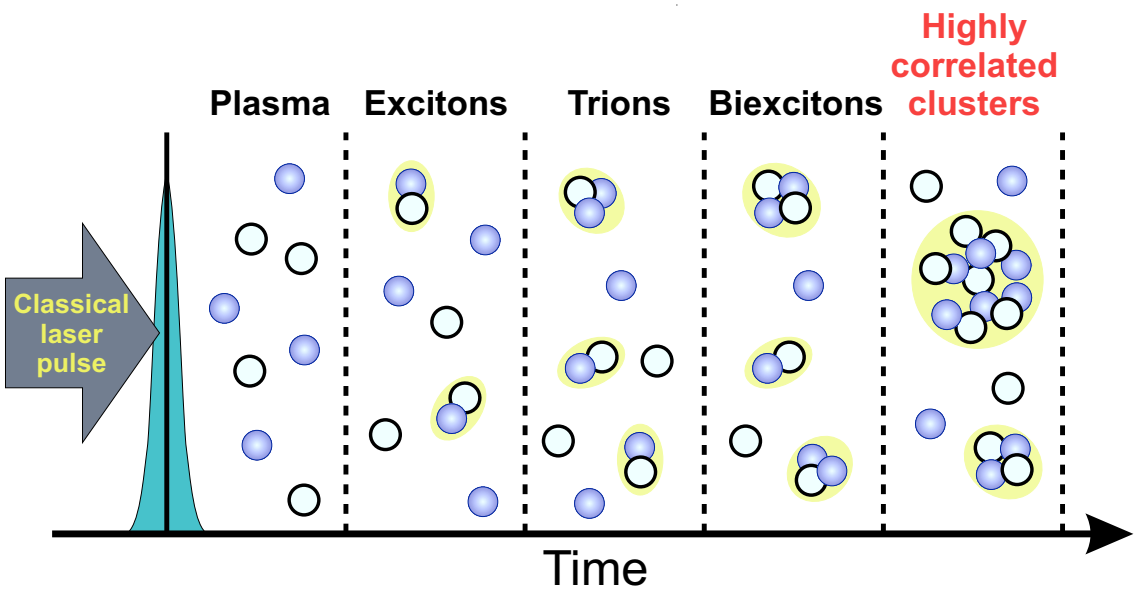

Figure 2.1: Quantum dynamics of quasiparticle clusters after a coherent-state laser excitation. The classical laser pulse is indicated as a shaded area. Electrons (holes) are denoted by open (dark) circles. Correlations among electrons and holes are indicated by a yellow oval enclosing the particles. (According to Ref. [90]).

neglected, according to the cluster-expansion truncation scheme, such that the equations of motion are closed. The results of this study are discussed in more detail in Sec. 5.3.

Also in many-body systems the clusters build up sequentially after the excitation with a classical light field [18,91]. Figure 2.1 illustrates the quantum dynamics of quasiparticle clusters in a semiconductor QW system after a coherent-state laser excitation. When the laser pulse (shaded area) is resonant to the 1s-exciton state, excitonic polarization and plasma consisting of electrons (open circles) and holes (dark circles) are generated before the onset of Coulomb and phonon scattering. Many-body and quantum-optical interactions yield a sequential build up of clusters via nonlinear scattering processes such that incoherent excitons and later trions, consisting of two electrons and one hole or two holes and one electron, can form. Further equilibration binds two excitons with opposite spins to one biexciton while highly correlated electron–hole complexes only build up at later times. As a result, the cluster-expansion truncation scheme can also be applied to describe the dynamics of many-body systems because up to a certain time only correlations up to C particles are important. However, the control and characterization of the interesting highly correlated many-body states is very limited with traditional laser spectroscopy because individual quasiparticles cannot be directly detected but only after the sequential build up of correlations. Consequently, a mixture of several quasiparticle states is generated via scattering resulting in broad spectral features, which complicates the identification and characterization of specific highly correlated quasiparticle states.

2.3 State-injection aspects of quantum spectroscopy

To directly excite targeted quasiparticle states, the quantum aspects of the applied light field can be used because the quantized light–matter interaction (2.2) has the inherent capability to transfer quantum-optical correlations (2.4) injected by the light field to corresponding electron–hole correlations (2.6). More specifically, when the single-mode laser is resonant with the $1s$-exciton state, one finds the mapping [15, 18]

$$\Delta\langle\left[\hat{X}^\dagger\right]^J \hat{X}^K\rangle = \eta^{\frac{J+K}{2}} \Delta\langle\left[B^\dagger\right]^J B^K\rangle \tag{2.9}$$

between pump laser's quantum-optical correlations (2.4) and the electron–hole correlations (2.6) where η defines the fraction of photons absorbed as electron–hole pairs.

In general, the quantum-statistical state injection (2.9) is satisfied before the emergence of significant Coulomb and phonon scattering. Thus, ultra-short laser pulses are needed that are faster than system's dominant scattering processes. However, state-of-the-art experiments use laser pulses in the femto- or even in the atto-second range [92–95] whose spectral, temporal, or phase properties are well controllable. As a result, a large set of many-body states can be *directly* excited by shaping light source's quantum fluctuations. This additional spectroscopic capability extends classical ultrafast laser spectroscopy to quantum spectroscopy. This principle is used to search for new highly correlated quasiparticles in semiconductor QWs in Chapter 3 and to characterize specific quasiparticle states in Chapter 4.

2.4 Realization of quantum spectroscopy

An experimental realization of quantum spectroscopy requires quantum-light sources with free shapeable quantum fluctuations which are currently not available. Nevertheless, in present-day experiments the *classical* response $R_{|\beta\rangle}$ to a classical light field defined by a coherent state $|\beta\rangle$ can be routinely measured with a high precision as a function of pump laser's amplitude β. For example, $R_{|\beta\rangle}$ can be the QW absorption measured using a pump–probe absorption setup as in Chapters 3 and 4 or the output power of optically pumped QD microcavities as in Chapter 5. The *quantum-optical* response R_{QM} to arbitrary quantum-light sources can then be mathematically projected from classical measurements using the convolution integral [96]

$$R_{\mathrm{QM}} = \int \mathrm{d}^2\beta P(\beta) R_{|\beta\rangle}\,, \tag{2.10}$$

where $P(\beta)$ is the Glauber–Sudarshan function [96, 97] defining the quantum statistics of the quantum-light source. As a result, the convolution integral (2.10) enables the computation of the quantum-optical response resulting from many possible quantum-light sources. However, the direct numerical integration has complications because the measured response is not known continuously throughout the entire phase space and exhibits noise as any measurement does. Additionally, $P(\beta)$ is often nonanalytic for

quantum-optical light fields.

Nevertheless, an alternative approach has been developed in Ref. [31] to project the quantum-optical response to nonclassical light sources from a set of classical measurements. The presented projection scheme is not restricted to semiconductor QWs but can be applied to realize quantum spectroscopy in generic condensed-matter systems and beyond. As shown in that paper, the measured response $R_{|\beta\rangle}$ can be viewed as an unnormalized phase-space distribution. One can then apply the cluster-expansion transformation (CET) [83] which converts $R_{|\beta\rangle}$ to an analytical phase-space distribution $R_{\mathrm{CET}}(\beta)$ known throughout the entire phase space; the explicit CET algorithm is provided in Appendix B of Paper (IV) for a situation where $R_{|\beta\rangle} = R(|\beta|)$ depends only on $|\beta|$, i. e. the measured system response is phase-independent as it is in the measurements presented in this Thesis. The CET form $R_{\mathrm{CET}}(\beta)$ defined in Eq. (B6) of Paper (IV) is a Gaussian times polynomials such that the projection integral (2.10) can be computed even for nonanalytic $P(\beta)$ when $R_{|\beta\rangle}$ is replaced by $R_{\mathrm{CET}}(\beta)$, see Appendix C of Paper (IV) for an efficient calculation of the projection integral (2.10) using the CET. In addition, the CET is robust against experimental noise, which is demonstrated in Sec. III of Paper (IV).

As a result, the quantum-optical response R_{QM} can be efficiently projected from a large set of classical measurement using the CET. To directly access specific many-body states in semiconductor QWs, differential responses

$$R_{1,2} = R^{(1)}_{\mathrm{QM}} - R^{(2)}_{\mathrm{QM}} = \int \mathrm{d}^2\beta \, P_{1,2}(\beta) R_{|\beta\rangle} \,, \qquad P_{1,2}(\beta) \equiv P_1(\beta) - P_2(\beta) \tag{2.11}$$

are computed where $R^{(\lambda)}_{\mathrm{QM}}$ is the projected quantum-optical response to quantum source $P_\lambda(\beta)$ labeled by λ. As shown in the Supplementary Information to Paper (III), $P_{1,2}(\beta)$ uniquely defines differences in quantum-optical correlations

$$\left[\Delta I^J_K\right]_{1,2} \equiv \left[\Delta I^J_K\right]_1 - \left[\Delta I^J_K\right]_2 \,. \tag{2.12}$$

In general, the quantum-light sources defined by $P_1(\beta)$ and $P_2(\beta)$ excite two many-body states according to the state-injection relation (2.9). If the quantum sources have identical quantum-optical correlations (2.4) for $J + K \leq (C-1)$, the difference in their quantum-optical correlations (2.12) can deviate only from C-particle correlations on. Consequently, also the injected many-body states of $P_1(\beta)$ and $P_2(\beta)$ can differ only from C-particle electron–hole correlations on according to the state-injection relation (2.9). Thus, the differential (2.11) monitors then the dynamics of $\geq C$ electron–hole clusters. This fact is used in Chapters 3 and 4 to directly excite specific quasiparticle clusters in semiconductor QWs.

2.5 Quantum-light sources

To directly excite and control quasiparticles with quantum spectroscopy, quantum-light sources are needed within the differential (2.11) whose differences in photon correlations (2.12) match the corresponding correlations in electron–hole excitations (2.6) of the desired many-body state. In this Thesis, quantum-light sources are used that correspond

to a small perturbation of the classical pump laser. In this situation, those quasiparticles can be studied which are present under conditions generated by the pump laser.

The classical pump laser is defined by a coherent state $|\beta_0\rangle$ such that $N_{\mathrm{pump}} = |\beta_0|^2$ is the photon number within the pump pulse. As quantum-light sources, Schrödinger's cat states are used which are the quantum superposition of two different coherent states. In particular, two different classes of Schrödinger's cat states are theoretically formulated in this Thesis. The ordinary displaced Schrödinger's cat states are defined by [31]

$$\begin{aligned} |\beta,\,\gamma\rangle &= \mathcal{N}\left(\mathrm{e}^{-\mathrm{iIm}[\beta\gamma^\star]}|\Gamma_-\rangle + \mathrm{e}^{\mathrm{iIm}[\beta\gamma^\star]}|\Gamma_+\rangle\right), \quad \text{with} \\ \mathcal{N} &\equiv \frac{1}{\sqrt{2+2\,\mathrm{e}^{-2|\gamma|^2}}}, \qquad \Gamma_\pm \equiv \beta \pm \gamma\,. \end{aligned} \tag{2.13}$$

For $\gamma = \mathrm{i}|\gamma|$ ($\gamma = |\gamma|$), the $\pm\gamma$ displacements of the cat state are perpendicular (parallel) to the real-valued displacement β referred to as squeezing- (stretching-) cat state [31]. The projected quantum-optical response to Schrödinger's cat state, $R_{|\beta,\,\gamma\rangle}$, is explicitly given in Eq. (S16) of the Supplementary Material to Paper (V).

To directly access the response stemming from many-body correlations of two and more electron–hole pairs, the differential

$$\Delta R_{\mathrm{sqz}} \equiv R_{|\beta,\,\mathrm{i}|\gamma|\rangle} - R_{\mathrm{CET}}(\beta_0) \tag{2.14}$$

is computed between the responses resulting from the excitation with a classical laser $|\beta_0\rangle$ and a squeezing-cat state $|\beta, \mathrm{i}\,|\gamma|\rangle$. The cat state $|\beta, \mathrm{i}\,|\gamma|\rangle$ has exactly one more photon in quantum fluctuations than $|\beta_0\rangle$ while its coherences are reduced such that both states within the differential (2.14) have the same average photon number $N_{\mathrm{pump}} = |\beta_0|^2$. A more detailed discussion of the state construction is given in Ref. [31]. There it is also shown that the differential yields direct access to the biexcitonic amplitude $\Delta\langle\hat{X}\hat{X}\rangle$. This aspect is used in Chapter 4 to characterize the properties of the biexciton resonance in the absorption spectra of semiconductor QWs.

Analogously, the stretching-cat differential is defined by

$$\Delta R_{\mathrm{str}} \equiv R_{|\beta,\,|\gamma|\rangle} - R_{\mathrm{CET}}(\beta_0)\,, \tag{2.15}$$

which is used in Chapter 5 to control nontrivial oscillations in the input/output characteristics of optically pumped QD microcavities.

To directly excite highly correlated quasiparticle clusters in semiconductor QWs, slanted Schrödinger's cat states

$$\begin{aligned} |\beta,\gamma,\theta\rangle &= \mathcal{N}_{\gamma,\theta}\left[\cos\left(\theta+\tfrac{\pi}{4}\right)\mathrm{e}^{\mathrm{iIm}[\beta\gamma^\star]}|\Gamma_+\rangle + \sin\left(\theta+\tfrac{\pi}{4}\right)\mathrm{e}^{-\mathrm{iIm}[\beta\gamma^\star]}|\Gamma_-\rangle\right], \text{ with} \\ \mathcal{N}_{\gamma,\theta} &\equiv \left(1+\cos\,2\theta\;\mathrm{e}^{-2|\gamma|^2}\right)^{-\frac{1}{2}}, \qquad \Gamma_\pm \equiv \beta \pm \gamma \end{aligned} \tag{2.16}$$

are introduced that are a generalization of Schrödinger's cat state (2.13). The amplitude ratio of both coherent-state components can be adjusted by the specific choice of θ. In particular, the slanted-cat state (2.16) reduces to the cat state (2.13) for $\theta = 0$. The projected response to slanted-cat states, $R_{|\beta,\gamma,\theta\rangle}$, is explicitly given in Eq. (29) of the Supplementary Information to Paper (III).

To monitor the effect of higher order electron–hole correlations, the two slanted-cat states

$$\begin{aligned} &|\beta_1,\gamma_1,\theta_1\rangle \quad \text{with} \quad \beta_1 = \beta_0 - |\gamma|\,\mathcal{N}^2_{\gamma,\theta} \sin 2\theta\,, \quad \gamma_1 = |\gamma|\,, \quad \theta_1 = -\theta\,, \\ &|\beta_2,\gamma_2,\theta_2\rangle \quad \text{with} \quad \beta_2 = \beta_0 + |\gamma|\,\mathcal{N}^2_{\gamma,\theta} \sin 2\theta\,, \quad \gamma_2 = |\gamma|\,, \quad \theta_2 = \theta \end{aligned} \tag{2.17}$$

are used to compute the quantum-optical differential

$$\Delta R_{\text{slt}} \equiv R_{|\beta_1,\gamma_1,\theta_1\rangle} - R_{|\beta_2,\gamma_2,\theta_2\rangle}\,. \tag{2.18}$$

Here, both slanted-cat states within the differential have the same photon number. Additionally, they contain one more photon in quantum fluctuations than the coherent state $|\beta_0\rangle$ while the displacement β_0 is unchanged, see Supplementary Information to Paper (III) for more details. There it is also shown that the differences in quantum-optical correlations (2.12) of the states (2.17) vanish up to $C = J + K = 2$. According to the state-injection relation (2.9), the differential (2.18) monitors then the effects starting from three-particle electron–hole correlations on in semiconductor QWs. In Chapter 3, this property is applied to identify a new highly correlated many-body state that is hidden to classical spectroscopy.

In this Thesis, the quantum-optical differential responses (2.14)–(2.15) and (2.18) are compared with the classical differential response [31]

$$\Delta R_{\text{class}} \equiv R_{\text{CET}}(\beta_0 + \Delta\beta) - R_{\text{CET}}(\beta_0)\,, \tag{2.19}$$

where $|\beta_0 + \Delta\beta\rangle$ contains one additional photon than $|\beta_0\rangle$, i. e. $\Delta\beta = \sqrt{N_{\text{pump}}+1} - \sqrt{N_{\text{pump}}}$. The differential (2.19) directly accesses excitonic polarization in semiconductor QWs [31] and thus monitors the effects down to the single-particle level.

3

Dropletons: Quantum electron–hole droplets

A situation is considered where an ultrafast laser pulse is applied to excite a semiconductor QW from its ground state. As the pulse is partially absorbed by the QW, the electron–hole excitations increase monotonically as a function of the laser intensity. Consequently, the laser intensity controls how far from the nonequilibrium the system is excited. In direct-gap semiconductor QW systems, the lifetime of the carrier excitations is relatively short, roughly one nanosecond in GaAs-type systems [18], such that only simplest quasiparticles like excitons [98–101] or biexcitons [35,36] have been detected. Thus, the quasiparticles follow a nonequilibrium quantum kinetics because they have a too short lifetime for thermalization. However, this regime contains several intriguing many-body states, and yet it remains an open question whether stable configurations consisting of three or more Coulomb correlated electron–hole pairs exist. The study in Ref. [102] on GaAs QWs has already shown indications for polyexcitons with three electron–hole pairs. In this Chapter, high-precision optical measurements on GaAs QWs are analyzed. Experimental and theoretical evidence is presented for dropletons as new highly correlated quasiparticles that are quantum droplets consisting of four-to-seven electron–hole pairs. The analyzed measurements were performed by the group of Steven T. Cundiff (JILA, University of Colorado & NIST, Boulder, USA).

In general, classical spectroscopy cannot resolve the detailed properties of the dropletons because they are generated via scattering according to the discussion in Sec. 2.2. To directly detect dropletons, the GaAs QW absorption is analyzed with quantum spectroscopy by projecting the measured QW absorption into a quantum-optical differential absorption which directly monitors the effect of higher order electron–hole correlations. For the computation of dropleton's pair-excitation spectrum, a new theoretical framework has been developed to determine the pair-excitation energetics of highly correlated quasiparticles in optically excited semiconductors. Since such quasiparticles can be identified through their electron–hole pair-correlation function, the excitation spectrum is computed based on the pair-correlation function of the quasiparticle state.

The measured QW absorption is analyzed in Sec. 3.1 while quantum-optical differential absorption spectra are projected from the QW absorption measurements in Sec. 3.2. The theoretical scheme to determine the excitation spectrum of highly correlated many-body complexes is discussed in Sec. 3.3, before it is applied in Secs. 3.4 and 3.5 to compute the pair-excitation energetics of excitons and dropletons, respectively. The presented results are published in Papers (II) and (III).

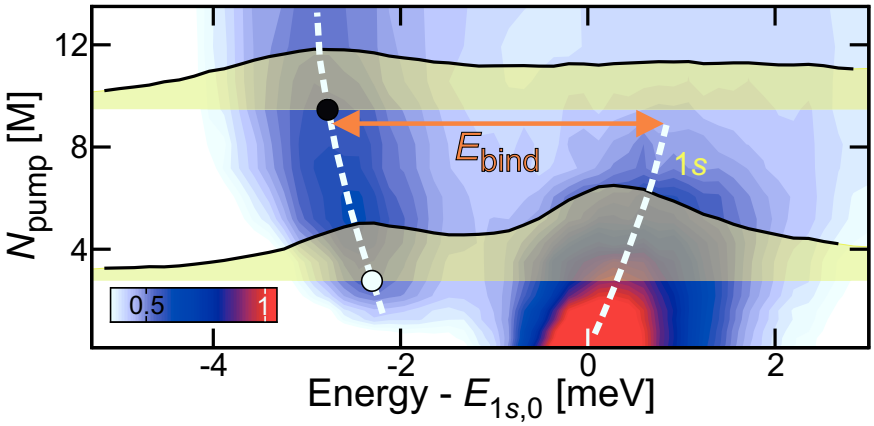

Figure 3.1: Characterization of quasiparticle resonances with classical spectroscopy. Measured probe-absorption spectra as a function of the pump-photon number N_{pump} for a pump–probe delay of $\Delta t = 2$ ps; the peak absorption is normalized to one; $E_{1s,0}$ is the low-density exciton energy and the transparent shaded areas show actual spectra at $N_{\mathrm{pump}} = 2.8\,\mathrm{M}$ (lower) and $N_{\mathrm{pump}} = 9.5\,\mathrm{M}$ (upper). The dashed lines indicate the resonance shifts. (According to Paper (III)).

3.1 Characterization of quasiparticle resonances with classical spectroscopy

Transient pump–probe absorption measurements have been performed on 10 uncoupled GaAs QWs at a sample temperature of 10 K. A circularly polarized 320 fs pump pulse excites the QW resonantly with respect to the $1s$ heavy-hole exciton state. The output of the pump laser is defined by a coherent state $|\beta_0\rangle$ such that $N_{\mathrm{pump}} = |\beta_0|^2$ is the number of photons in the pump pulse. After a delay of Δt, a weak probe pulse reaches the sample which is cross-circularly polarized with respect to the pump pulse. Thus, the measured response is phase independent because the opposite circular polarizations of pump and probe avoids that pump-generated coherences produce phase-sensitive contributions to the probe response. As a result, the probe absorption $\alpha_{\mathrm{QW}}(E, \Delta t, |\beta_0\rangle)$ is recorded as a function of the probe-photon energy E, the pump–probe delay Δt, and the pump-photon number N_{pump}. More experimental details are given in the Supplementary Information to Paper (III).

The quasiparticle resonances in the QW absorption spectra are first characterized with classical spectroscopy. Figure 3.1 shows a contour plot of the measured probe-absorption spectra as a function of pump-photon number N_{pump} for a pump–probe delay of $\Delta t = 2\,\mathrm{ps}$. The peak absorption is normalized to one and N_{pump} is quoted in units of million ($10^6 = \mathrm{M}$) photons. The transparent shaded areas show actual spectra at $N_{\mathrm{pump}} = 2.8\,\mathrm{M}$ (lower) and $N_{\mathrm{pump}} = 9.5\,\mathrm{M}$ (upper). At $N_{\mathrm{pump}} = 0$, a resonance is only observable at the $1s$ heavy-hole exciton energy $E_{1s,0} = 1.547$ eV. The heavy-hole resonance is 9 meV below the band edge (not shown), defining the excitonic binding energy with respect to the electron–hole plasma. In agreement with many similar experiments [31,103–105], the heavy-hole exciton resonance blue shifts and shows the typical excitation-induced dephasing as the pump intensity is increased. In general, the energetic position of the resonance is influenced by several effects: The Coulomb renormalization shifts the band gap to lower energies [31,46].

Therefore, the heavy-hole exciton resonance must red shift in order to maintain its binding energy. However, screening of the Coulomb interaction and Pauli blocking of low energy states reduce exciton's binding energy, yielding a blue shift of the resonance [104, 105].

At $N_{\mathrm{pump}} = 1.5\,\mathrm{M}$, a second resonance emerges 2.2 meV below $E_{1s,0}$ due to molecular binding which corresponds to the biexciton resonance. It is visible due to the opposite circular polarizations of pump and probe, which yield excitonic polarizations with opposite spin states. The biexciton resonance broadens and red shifts while the heavy-hole exciton resonance blue shifts. Consequently, the biexciton binding energy E_{bind}, defined with respect to the exciton resonance (double arrow), appears to *increase* from $E_{\mathrm{bind}} = 2.2\,\mathrm{meV}$ at low N_{pump} to roughly $E_{\mathrm{bind}} = 3\,\mathrm{meV}$ at elevated pump intensities. Additionally, the amplitude of the biexciton resonance exceeds the one of the heavy-hole exciton resonance at enhanced N_{pump}. The red shift of the biexciton resonance has also been confirmed using a another GaAs sample and a different measurement technique, two dimensional Fourier transform spectroscopy [106–108], that accesses the many-body resonances more accurately than classical pump–probe spectroscopy. The experimental details and results are presented in the Supplementary Information to Paper (III).

As a result, the *increased* E_{bind} is counterintuitive as long as one associates the low-energy resonance with biexcitons because one would expect that Pauli-blocking of Fermions and screening of the Coulomb interaction *reduce* E_{bind} of any molecular state as the excitation level is increased. Consequently, it is more plausible that the broad feature close to the biexciton actually hosts new quasiparticles. More precisely, only at low N_{pump} the resonance is biexcitonic while higher order correlated many-body complexes are present at elevated pump intensities, despite they cannot be individually resolved in classical spectroscopy due to appreciable broadening. The new quasiparticle is hypothesized to be a *dropleton* that is a quantum droplet of electrons and holes. In the following, further evidence for its quasiparticle nature is presented.

3.2 Detection of dropletons with quantum spectroscopy

To increase the sensitivity of the quasiparticle identification, differential absorption spectra are projected from the pump–probe absorption measurements. Therefore, the projection algorithm discussed in Sec. 2.4 is applied where it is shown that a N_{pump} ensemble as presented in Fig. 3.1 can be projected into a differential response with respect to any quantum fluctuations in the pump source. Here, the response is explicitly given by the probe absorption, i. e. $R_{|\beta\rangle} = \alpha_{\mathrm{QW}}$. The quantum-optical projection is chosen such that it isolates the effect of high-order electron–hole correlations from the N_{pump} ensemble by projecting the quantum-optical response to a slanted Schrödinger's cat state. The resulting projected differential $\Delta\alpha_{\mathrm{slt}}$ defined in Eq. (2.17) directly monitors the QW response resulting from three-particle electron–hole correlations on. As illustrated in Chapter 2, a classical differential follows the dynamics from the single-particle level on such that highly correlated electron–hole complexes are only generated via scattering which hinders their direct detection. Therefore, $\Delta\alpha_{\mathrm{slt}}$ monitors the effects of highly correlated quasiparticles much more sensitively than a classical differential $\Delta\alpha_{\mathrm{class}}$.

Figure 3.2(a) shows a contour plot of the projected slanted-cat differential $\Delta\alpha_{\mathrm{slt}}$ as a function of the binding energy E_{bind} and the pump-photon number N_{pump} for a pump–probe delay of $\Delta t = 16$ ps. The peak absorption of each spectrum is normalized to one

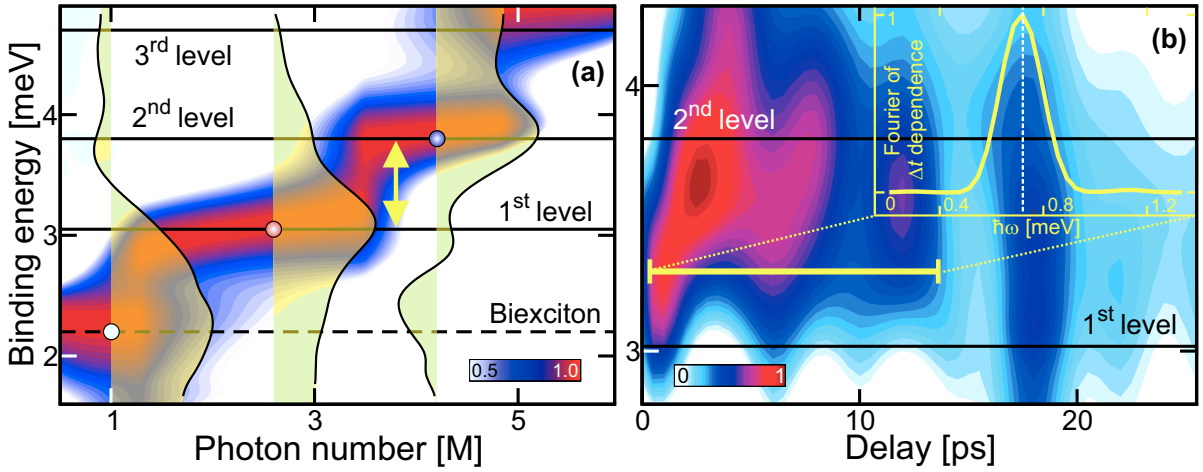

Figure 3.2: Detection of dropletons with quantum spectroscopy. (a) Projected $\Delta\alpha_{\mathrm{slt}}$ as a function of E_{bind} and N_{pump} for $\Delta t = 16\,\mathrm{ps}$. The peak absorption of each spectrum is normalized to one. The biexciton-binding energy (horizontal dashed line) matches the low-density E_{bind} in Fig. 3.1. Three new quantized energy levels are denoted with horizontal solid lines. The transparent shaded areas present actual spectra at $N_{\mathrm{pump}} = 1.0\,\mathrm{M}$ (left), $2.6\,\mathrm{M}$ (middle), and $4.2\,\mathrm{M}$ (right). (b) Temporal evolution of $\Delta\alpha_{\mathrm{slt}}$ for fixed $N_{\mathrm{pump}} = 3.8\,\mathrm{M}$ (double arrow in (a)); the peak absorption is normalized to one; horizontal lines denote the first and second energy level. Inset: Fourier transformed $\Delta\alpha_{\mathrm{slt}}$ time trace at $E_{\mathrm{bind}} = 3.3\,\mathrm{meV}$; the Δt trace is indicated by a yellow line. The vertical dashed line corresponds to the energetic spacing between the first and second quantized level, $\hbar\omega_{\mathrm{2nd,1st}} = 0.70\,\mathrm{meV}$. (According to Paper (III)).

and the binding energy E_{bind} is defined with respect to the N_{pump}-dependent $1s$ heavy-hole exciton energy, compare Fig. 3.1. Biexciton's low-density E_{bind} is indicated by a dashed horizontal line. The transparent shaded areas show actual spectra at $N_{\mathrm{pump}} = 1.0\,\mathrm{M}$ (left), $2.6\,\mathrm{M}$ (middle), and $4.2\,\mathrm{M}$ (right). For low N_{pump}, $\Delta\alpha_{\mathrm{slt}}$ shows a narrow resonance at the biexciton E_{bind} which is very stationary compared to the result of classical spectroscopy in Fig. 3.1. At $N_{\mathrm{pump}} = 1.3\,\mathrm{M}$, a sharp transition to a larger E_{bind} is observable which is followed by two further transitions at $N_{\mathrm{pump}} = 3.5\,\mathrm{M}$ and $N_{\mathrm{pump}} = 5.0\,\mathrm{M}$. This result verifies the state-injection aspects of quantum spectroscopy discussed in Sec. 2.3: Classical spectroscopy cannot resolve the new quasiparticle state due to appreciable scattering resulting in a gradual increasing E_{bind} in Fig. 3.1 while quantum spectroscopy yields sharp resonances due to the direct state injection of highly correlated electron–hole clusters. As a result, $\Delta\alpha_{\mathrm{slt}}$ spectroscopy resolves three new quantized energy levels within the spectral range studied here. The levels have a binding energy of roughly $E_{\mathrm{bind}} = 3.1\,\mathrm{meV}$, $3.8\,\mathrm{meV}$, and $4.6\,\mathrm{meV}$ marked by horizontal solid lines.

The detection of the quantized E_{bind} levels yields evidence for a new quasiparticle. As a further evidence, the discrete dropleton levels emerge only in $\Delta\alpha_{\mathrm{slt}}$ that monitors the effect of three-particle electron–hole correlations and beyond, indicating that dropletons are highly correlated quasiparticles. Additionally, the discrete dropleton levels appear at a N_{pump} range where the $1s$ heavy-hole exciton resonance in Fig. 3.1 becomes significantly broadened. Therefore, it is likely that excitons do not directly play a role for dropletons

due to their weakened binding. Thus, it is more plausible that dropletons are collectively bound electron–hole complexes. To rule out the polyexcitonic origin, the dropletons have also been studied in a co-circular pump–probe absorption measurement (pump and probe have the same circular polarization) where only electron–hole pairs with one spin species are generated. This case cannot produce molecular resonances because spin parallel electrons (holes) can only participate in antibonding states due to the underlying Fermionic symmetry. As a result, the co-circular excitation produces the same energetics for dropletons as identified in Fig. 3.2(a), which excludes the polyexcitonic character of dropletons. The co-circular measurement is discussed in detail in the Supplementary Information to Paper (III).

It is also interesting to study the dynamical properties of the new quasiparticle. Technically, each pump–probe delay Δt labels a closed N_{pump} ensemble of measurements that are independently projected into $\Delta\alpha_{\mathrm{slt}}$. In other words, Δt also labels completely independent projections that are not connected unless a true physical evolution is monitored. Therefore, both the consistency of the projection algorithm and the existence of the new quasiparticle can be confirmed by the detection of quantum beats with the correct oscillation frequency defined by the energy difference of the levels.

The resulting normalized $\Delta\alpha_{\mathrm{slt}}$ spectrum is presented in Fig. 3.2(b) as a function of delay time Δt and binding energy E_{bind} for a fixed $N_{\mathrm{pump}} = 3.8\,\mathrm{M}$. In this situation, the new quasiparticle can then be either at the first or at the second quantized level, as indicated by the double arrow in Fig. 3.2(a). The horizontal lines indicate the energetic positions of the first and second quantized level. At $\Delta t = 0\,\mathrm{ps}$, the $\Delta\alpha_{\mathrm{slt}}$ resonance is centered at the first quantized level followed by oscillations between the two quantized levels indicated. To verify the quantum-beat nature, the $\Delta\alpha_{\mathrm{slt}}$ spectrum is Fourier transformed at $E_{\mathrm{bind}} = 3.3\,\mathrm{meV}$ along a Δt trace indicated by the yellow line. The result is presented in the inset to Fig. 3.2(b) where the vertical dashed line indicates $\hbar\omega_{\mathrm{2nd,1st}} = 0.70\,\mathrm{meV}$ that corresponds to the energy difference between the second and the first energy level. The central frequency of the oscillation matches very well the energy difference of the two quantized levels which is the correct frequency for the corresponding quantum beats. As a result, the observed quantum beats provide a compelling further evidence for the existence of dropletons.

Figure 3.2(b) also shows that $\Delta\alpha_{\mathrm{slt}}$ spectroscopy directly injects the new quasiparticle state because the resonance emerges at the first quantized level at $\Delta t = 0\,\mathrm{ps}$. Additionally, the quantum beating is observable within the complete time window studied such the quasiparticle has roughly a lifetime of 25 ps. The quantum beats have also been directly detected in classical differential absorption measurements, which yields additional evidence for dropletons as a new quasiparticle. In more detail, classical spectroscopy detects a mixture of quantum beat frequencies due to beating between multiple dropleton levels, which is consistent with the fact that classical spectroscopy cannot resolve individual dropleton states. The results are shown in Fig. 4 of Paper (III) while the experimental details are discussed in the corresponding Supplementary Information.

To produce further confirmation for dropletons, transient pump–probe absorption measurements have been performed at a sample temperature of 70 K where weakly bound states like biexcitons and dropletons should dissociate due to phonon scattering. As expected, the 70 K measurement shows no dropleton features. The results of this control measurement are presented in the Supplementary Information to Paper (III).

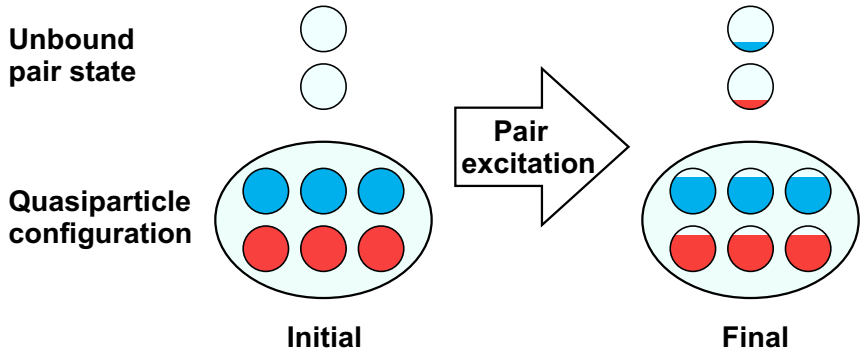

Figure 3.3: Example for pair excitation. A schematic representation of a quasiparticle configuration before (left panel) and after (right panel) the pair excitation is shown. Electrons (holes) are indicated by red (blue) circles while yellow ellipses enclose the correlated pairs. The level of filling symbolizes the portion of electrons and holes bound as correlated pairs. (According to Paper (II)).

As a result, the presented findings confirm the existence of dropletons through quantized energetics, correct quantum beats, direct visibility only in $\Delta\alpha_{\mathrm{slt}}$, and blue-shifting E_{bind} in classical spectroscopy. Obviously, the dropleton cannot be a macroscopic cluster which has a quasicontinuous pair-excitation spectrum. In addition, the co-circular pump–probe measurement excludes the polyexcitonic character of dropletons while the presence of quantum beats also rules out a thermodynamic transition. As a result, dropletons must be a plasma arrangement, not molecular. Based on this information, dropleton's energetics is computed in Sec. 3.5.

3.3 Pair-excitation energetics of quasiparticle states

To study if the observations in Secs. 3.1 and 3.2 are in agreement with a many-body state where electrons and holes constitute a quantum droplet, the pair-excitation spectrum of such a many-body configuration has to be computed. Therefore, a new theoretical approach has been developed in Paper (II) which allows for the computation of the pair-excitation energetics of a given quasiparticle configuration in optically excited direct-gap semiconductor QWs. As the main idea of this approach, the system energy is completely expressed as a functional of the electron–hole pair-correlation function, not density as in density-functional theory [45], because quasiparticles can be directly identified via their pair-correlation function. This section provides a brief review of the scheme while a more detailed discussion is given in Paper (II).

To illustrate the detectable energetics of a given quasiparticle state, Fig. 3.3 compares a quasiparticle configuration before (left panel) and after (right panel) the pair excitation. Electrons (holes) are indicated by red (blue) circles while yellow ellipses enclose the correlated pairs. The degree of filling denotes the fraction of electrons and holes bound as correlated pairs. As initial many-body state, a quasiparticle configuration is considered where all electron–hole pairs are bound to one quasiparticle type. Then, a weak optical probe pulse excites a small number of electron–hole pairs, δN, into an unbound pair state. When E_{ini} and E_{final} are the energies of the initial and excited many-body configuration,

respectively, the energy per excited electron–hole pair is $\bar{E}_{\mathrm{pro}} = \frac{E_{\mathrm{final}} - E_{\mathrm{ini}}}{\delta N}$ which represents the energetics detectable by the probe. Physically, $\bar{E}_{\mathrm{pro}}$ corresponds to the gained energy of an electron–hole pair when constituting a quasiparticle cluster from unbound pairs, as shown in Sec. 2 of Paper (II).

3.3.1 Average carrier energy

As initial many-body configuration, a generic many-body state is considered which is defined by the density matrix $\hat{\rho}_{\mathrm{MB}}$. In the first step of the scheme, the average carrier-excitation energy of $\hat{\rho}_{\mathrm{MB}}$ is determined based on the electron–hole pair-correlation function $g(\mathbf{r})$. In the dropleton investigations, only those $\hat{\rho}_{\mathrm{MB}}$ states are assumed that contain spatially homogeneous excitations and an equal amount of electrons and holes

$$N_{\mathrm{eh}} = \sum_{\mathbf{k}} f_{\mathbf{k}}^{\mathrm{e}} = \sum_{\mathbf{k}} f_{\mathbf{k}}^{\mathrm{h}}\,, \qquad \text{with} \qquad f_{\mathbf{k}}^{\mathrm{e}} \equiv \langle a_{\mathrm{c},\mathbf{k}}^{\dagger} a_{\mathrm{c},\mathbf{k}} \rangle\,, \qquad f_{\mathbf{k}}^{\mathrm{h}} \equiv 1 - \langle a_{\mathrm{v},\mathbf{k}}^{\dagger} a_{\mathrm{v},\mathbf{k}} \rangle\,, \tag{3.1}$$

where N_{eh} is the number of excited electron–hole pairs and $f_{\mathbf{k}}^{\mathrm{e}}$ ($f_{\mathbf{k}}^{\mathrm{h}}$) corresponds to the electron (hole) distribution given in the electron–hole picture [18].

Since the new quasiparticle resonances in Fig. 3.2 are observable in the incoherent regime, the polarization and all other coherent quantities of $\hat{\rho}_{\mathrm{MB}}$ are negligible. In this situation, the average carrier-excitation energy of $\hat{\rho}_{\mathrm{MB}}$ can be written as

$$\begin{aligned} E_{\mathrm{MB}} &= \langle \hat{H}_{\mathrm{eh}} \rangle - N_{\mathrm{eh}} E_{\mathrm{g}} = \mathrm{Tr}\left[\hat{H}_{\mathrm{eh}} \hat{\rho}_{\mathrm{MB}}\right] - N_{\mathrm{eh}} E_{\mathrm{g}} \\ &= \sum_{\mathbf{k}} \left(\frac{\hbar^2 \mathbf{k}^2}{2m_{\mathrm{e}}} f_{\mathbf{k}}^{\mathrm{e}} + \frac{\hbar^2 \mathbf{k}^2}{2m_{\mathrm{h}}} f_{\mathbf{k}}^{\mathrm{h}} \right) - \frac{1}{2} \sum_{\mathbf{k},\mathbf{k}'} V_{\mathbf{k}-\mathbf{k}'} \left(f_{\mathbf{k}}^{\mathrm{e}} f_{\mathbf{k}'}^{\mathrm{e}} + f_{\mathbf{k}}^{\mathrm{h}} f_{\mathbf{k}'}^{\mathrm{h}} \right) \\ &\quad + \frac{1}{2} \sum_{\mathbf{k},\mathbf{k}',\mathbf{q}} \left[V_{\mathbf{q}} \left(c_{\mathrm{v,v;v,v}}^{\mathbf{q},\mathbf{k}',\mathbf{k}} + c_{\mathrm{c,c;c,c}}^{\mathbf{q},\mathbf{k}',\mathbf{k}} \right) - 2\, V_{\mathbf{k}'+\mathbf{q}-\mathbf{k}}\, c_{\mathrm{eh}}^{\mathbf{q},\mathbf{k}',\mathbf{k}} \right]\,, \end{aligned} \tag{3.2}$$

according to Eq. (18) in Paper (V), that is an *exact* result in the incoherent regime and for spatially homogeneous excitations. Since each excitation increases the energy roughly by the band-gap energy E_{g}, the trivial contribution $N_{\mathrm{eh}} E_{\mathrm{g}}$ has been removed from $\langle \hat{H}_{\mathrm{eh}} \rangle$ to directly monitor the energetic changes. Additionally, the two-particle correlations

$$\begin{aligned} &c_{\mathrm{v,v;v,v}}^{\mathbf{q},\mathbf{k}',\mathbf{k}} \equiv \Delta \langle a_{\mathrm{v},\mathbf{k}}^{\dagger} a_{\mathrm{v},\mathbf{k}'}^{\dagger} a_{\mathrm{v},\mathbf{k}'+\mathbf{q}} a_{\mathrm{v},\mathbf{k}-\mathbf{q}} \rangle\,, \quad c_{\mathrm{c,c;c,c}}^{\mathbf{q},\mathbf{k}',\mathbf{k}} \equiv \Delta \langle a_{\mathrm{c},\mathbf{k}}^{\dagger} a_{\mathrm{c},\mathbf{k}'}^{\dagger} a_{\mathrm{c},\mathbf{k}'+\mathbf{q}} a_{\mathrm{c},\mathbf{k}-\mathbf{q}} \rangle\,, \\ &c_{\mathrm{eh}}^{\mathbf{q},\mathbf{k}',\mathbf{k}} \equiv \Delta \langle a_{\mathrm{c},\mathbf{k}}^{\dagger} a_{\mathrm{v},\mathbf{k}'}^{\dagger} a_{\mathrm{c},\mathbf{k}'+\mathbf{q}} a_{\mathrm{v},\mathbf{k}-\mathbf{q}} \rangle\,, \end{aligned} \tag{3.3}$$

have been introduced using the cluster expansion [18, 46]. Here, hole–hole and electron–electron correlations are determined by $c_{\mathrm{v,v;v,v}}^{\mathbf{q},\mathbf{k}',\mathbf{k}}$ and $c_{\mathrm{c,c;c,c}}^{\mathbf{q},\mathbf{k}',\mathbf{k}}$, respectively, while $c_{\mathrm{eh}}^{\mathbf{q},\mathbf{k}',\mathbf{k}}$ describes electron–hole correlations where $\hbar\mathbf{q}$ corresponds to the center-of-mass momentum of the correlated electron–hole pairs. The average carrier-excitation energy (3.2) is exclusively defined by correlations up to two-particle clusters. In the following, this aspect is used to express E_{MB} exactly as a functional of the pair-correlation function.

In general, the electron–hole correlation energy often dominates over the electron–electron and hole–hole correlation energy in dense interacting electron–hole systems. In particular, it has been shown in Sec. 5 of Paper (II) that the effect of electron–electron and hole–hole correlations on the dropleton energetics is negligible even for a significant

large correlation hole. Therefore, the problem is simplified by neglecting $c^{\mathbf{q},\mathbf{k}',\mathbf{k}}_{\mathrm{v},\mathrm{v};\mathrm{v},\mathrm{v}}$ and $c^{\mathbf{q},\mathbf{k}',\mathbf{k}}_{\mathrm{c},\mathrm{c};\mathrm{c},\mathrm{c}}$ contributions in Eq. (3.2). In addition, the analysis is simplified further by assuming that the quasiparticles are at rest, i. e. the center-of-mass momentum $\hbar\mathbf{q}$ vanishes, yielding

$$c^{\mathbf{q},\mathbf{k}',\mathbf{k}}_{\mathrm{eh}} = \delta_{\mathbf{q},0}\, c^{\mathbf{q},\mathbf{k}',\mathbf{k}}_{\mathrm{eh}} \equiv \delta_{\mathbf{q},0}\, g_{\mathbf{k},\mathbf{k}'} \tag{3.4}$$

for the electron–hole correlations.

To define the quasiparticle state $\hat{\rho}_{\mathrm{MB}}$ via a physically intuitive electron–hole pair-correlation function, the $g(\mathbf{r})$ ansatz is converted to the correct $f_{\mathbf{k}}$ and $g_{\mathbf{k},\mathbf{k}'}$. As shown in Paper (II), the electron–hole pair-correlation function becomes

$$g(\mathbf{r}) = \rho_{\mathrm{e}}\rho_{\mathrm{h}} + \Delta g(\mathbf{r})\,, \qquad \rho_{\mathrm{e(h)}} = \frac{1}{S}\sum_{\mathbf{k}} f^{\mathrm{e(h)}}_{\mathbf{k}}\,, \tag{3.5}$$

where $\rho_{\mathrm{e(h)}}$ is the electron (hole) density containing the normalization area S. Here, $\rho_{\mathrm{e}}\rho_{\mathrm{h}}$ correspond to an uncorrelated electron–hole plasma contribution while quasiparticle cluster are defined by $\Delta g(\mathbf{r})$. In particular, the ansatz

$$\Delta g(\mathbf{r}) = |g_0\,\phi(\mathbf{r})|^2 \tag{3.6}$$

is used for the correlated contribution where g_0 defines the strength of the electron–hole correlation while the detailed properties of the quasiparticle state are determined by the wave function $\phi(\mathbf{r})$. The ansatz (3.6) can be used to describe incoherent excitons and dropletons, as shown in Secs. 3.4 and 3.5.

The quasiparticle state $\hat{\rho}_{\mathrm{MB}}$ is then uniquely defined by the excitation configuration

$$g_{\mathbf{k},\mathbf{k}'} = g_0^2\,\phi^\star(\mathbf{k})\phi(\mathbf{k}')\,, \qquad f_{\mathbf{k}} = \tfrac{1}{2}\left(1 - \sqrt{1 - 4\,g_{\mathbf{k},\mathbf{k}}}\right)\,, \tag{3.7}$$

where $\phi(\mathbf{k})$ is the Fourier transformation of $\phi(\mathbf{r})$, see Paper (II) for more details. Here, the considered homogeneous and incoherent excitation conditions together with the vanishing electron–electron and hole–hole correlations yield identical $f_{\mathbf{k}} \equiv f^{\mathrm{e}}_{\mathbf{k}} = f^{\mathrm{h}}_{\mathbf{k}}$ electron and hole distributions. As a result, based on Eq. (3.7), the average carrier-excitation energy E_{MB} is completely expressible in terms of the pair correlation $g_{\mathbf{k},\mathbf{k}'}$ which is directly connected to the pair-correlation function $g(\mathbf{r})$ of $\hat{\rho}_{\mathrm{MB}}$.

3.3.2 Energetics of pair excitation

The pair-excitation energy is then computed for a situation where a weak optical probe pulse excites an infinitesimal amount of electron–hole pairs, starting from an incoherent and homogeneous initial state $\hat{\rho}_{\mathrm{MB}}$, compare Fig. 3.3. Theoretically, pair excitations can be created with the help of the coherent displacement-operator functional [18, 46]

$$\hat{D}[\psi] = \mathrm{e}^{\varepsilon\hat{S}[\psi]}\,, \quad \hat{S}[\psi] = \sum_{\mathbf{k}}\left(\psi_{\mathbf{k}}\, a^\dagger_{\mathrm{c},\mathbf{k}} a_{\mathrm{v},\mathbf{k}} - \psi^\star_{\mathbf{k}}\, a^\dagger_{\mathrm{v},\mathbf{k}} a_{\mathrm{c},\mathbf{k}}\right)\,, \tag{3.8}$$

where $\psi_{\mathbf{k}}$ is a function which will be computed via variational calculus while a weak pair excitation is realized by making ε infinitesimal. The displacement operator (3.8) defines then the pair-excitation state by

$$\hat{\rho}[\psi] = \hat{D}[\psi]\,\hat{\rho}_{\mathrm{MB}}\,\hat{D}^{\dagger}[\psi]\,. \tag{3.9}$$

In general, the operator functional $\hat{S}\,[\psi]$ depicts a situation where an electron is excited from the valence to the conduction band ($a^{\dagger}_{\mathrm{c},\mathbf{k}}a_{\mathrm{v},\mathbf{k}}$) and vice versa ($a^{\dagger}_{\mathrm{v},\mathbf{k}}a_{\mathrm{c},\mathbf{k}}$) such that $\hat{D}\,[\psi]$ indeed describes direct pair-excitation processes. Consequently, $\hat{\rho}[\psi]$ defines a general enough class of many-body states to determine the excitation energetics of the many-body state $\hat{\rho}_{\mathrm{MB}}$.

Pair excitations generate the average carrier energy $E_{\mathrm{pro}}[\psi] \equiv \mathrm{Tr}\left[\hat{H}_{\mathrm{eh}}(\hat{\rho}[\psi] - \hat{\rho}_{\mathrm{MB}})\right]$ to the system, which is also completely expressible in terms of the pair correlation $g_{\mathbf{k},\mathbf{k}'}$. The ground state pair-excitation energy is then determined using variational calculus by finding the $\psi_{\mathbf{k}}$ which minimizes the energy functional $E_{\mathrm{pro}}[\psi]$. As a result, the minimization produces the *generalized Wannier equation*

$$E_{\mathbf{k}}\,\psi_{\mathbf{k}} - \sum_{\mathbf{k}'} V^{\mathrm{eff}}_{\mathbf{k},\mathbf{k}'}\,\psi_{\mathbf{k}'} = E_{\lambda}\,\psi_{\mathbf{k}}\,, \tag{3.10}$$

where E_{λ} corresponds to an effective eigenvalue, see Paper (II) for a more detailed discussion of the variation procedure. Here, the renormalized kinetic electron–hole pair energy,

$$E_{\mathbf{k}} \equiv \left[\frac{\hbar^2\mathbf{k}^2}{2\mu} - 2\sum_{\mathbf{k}'} V_{\mathbf{k}-\mathbf{k}'} f_{\mathbf{k}'}\right](1 - 2f_{\mathbf{k}}) + 2\sum_{\mathbf{k}'} V_{\mathbf{k}-\mathbf{k}'}\,g_{\mathbf{k},\mathbf{k}'}\,, \quad \mu = \frac{m_{\mathrm{e}}m_{\mathrm{h}}}{m_{\mathrm{e}} + m_{\mathrm{h}}}\,, \tag{3.11}$$

has been identified which contains the reduced mass μ. The presence of electron–hole densities and correlations yields an effective Coulomb interaction

$$V^{\mathrm{eff}}_{\mathbf{k},\mathbf{k}'} \equiv (1 - 2f_{\mathbf{k}})\,V_{\mathbf{k}-\mathbf{k}'}\,(1 - 2f_{\mathbf{k}'}) + 2g_{\mathbf{k},\mathbf{k}'}V_{\mathbf{k}-\mathbf{k}'}\,. \tag{3.12}$$

In general, the minimization procedure only yields the variational ground state E_0 of the pair excitation that is applied on $\hat{\rho}_{\mathrm{MB}}$. However, it is also interesting to analyze the corresponding excited states to gain additional informations about the pair-excitation energetics of $\hat{\rho}_{\mathrm{MB}}$. At vanishing density and $g_{\mathbf{k},\mathbf{k}'}$, the many-body state $\hat{\rho}_{\mathrm{MB}}$ corresponds to the semiconductor ground state where all valence bands are completely filled while the conduction bands are empty. In this situation, Eq. (3.10) reduces to the usual exciton problem that is formally equivalent to the hydrogen problem for the relative coordinate [31], yielding the series of exciton resonances in the absorption spectrum [18]. Compared to that, the presence of electron–hole densities and correlations alters the Coulomb interaction (3.12), making the emergence of new quasiparticle resonances possible. The general form of the Wannier equation (3.10) including all coherent quantities and electron–electron and

hole–hole correlations is presented in Appendix C of Paper (II).

For the identification of the quasiparticle energetics, the energy per excited electron–hole pair $\bar{E}_{\mathrm{pro}}$ is computed which represents the energy resonances that can be detected by the probe when the system is initially at the many-body state $\hat{\rho}_{\mathrm{MB}}$. The energy per excited electron–hole pair follows from

$$\bar{E}_{\mathrm{pro}} = E_\lambda \frac{\sum_{\mathbf{k}} |\psi_{\mathbf{k}}|^2}{\sum_{\mathbf{k}} |\psi_{\mathbf{k}}|^2 (1 - 2f_{\mathbf{k}})} , \tag{3.13}$$

compare Eq. (37) in Paper (II), which corresponds to the energy per probe-generated electron–hole pair at the variational ground state.

In its most general form, the presented scheme can be applied to determine the excitation spectrum for a large range of quasiparticle configurations based on a pair-correlation formulation of the many-body state $\hat{\rho}_{\mathrm{MB}}$. In the actual calculations, the specific quasiparticle state is defined by the wave function $\phi(\mathbf{r})$. For a given electron–hole density $\rho_{\mathrm{eh}} \equiv \rho_{\mathrm{e}} = \rho_{\mathrm{h}}$, the self-consistent $(f_{\mathbf{k}}, g_{\mathbf{k},\mathbf{k}'})$ pair is computed using Eq. (3.7) which defines the input for the generalized Wannier equation (3.10). Once the energy E_λ and wavefunction $\psi_{\mathbf{k}}$ are determined, the energy per excited electron–hole pair results from Eq. (3.13). The steps from the wavefunction $\phi(\mathbf{r})$ to the energy per excited electron–hole pair $\bar{E}_{\mathrm{pro}}$ are discussed in detail in Paper (II).

3.4 Excitation spectrum of excitons

Since the dropleton E_{bind} is defined with respect to the $1s$ heavy-hole exciton $\bar{E}_{\mathrm{pro}}$ in Fig. 3.1, the excitation spectrum is first computed for a many-body state $\hat{\rho}_{\mathrm{MB}}$ consisting of incoherent excitons, which also allows to test the scheme for a well-known case. The shape of $1s$ exciton's $\Delta g(\mathbf{r})$ is determined by the $1s$-exciton wave function $\phi_{1s}(\mathbf{r})$, compare Fig. 1.2. Thus, $1s$-exciton state's electron–hole pair correlation is [18, 46]

$$g_{\mathbf{k},\mathbf{k}'} = \phi_{1s}(\mathbf{k})\phi_{1s}(\mathbf{k}') , \tag{3.14}$$

according to Eq. (3.7), where the strength of the electron–hole correlation g_0 has been included into the $1s$-exciton wavefunction $\phi_{1s}(\mathbf{k})$ for simplicity. The details of the pair-excitation spectrum computation are discussed in Appendix D of Paper (II).

The resulting pair-excitation energetics of incoherent excitons is presented in Fig. 3.4 as a function of the electron–hole density ρ_{eh}. The ground-state energy E_0 (solid black line) is shown together with the energy of the first excited state E_1 (red line), the continuum (shaded area), and the energy per excited electron–hole pair $\bar{E}_{\mathrm{pro}}$ (dashed line). The continuum, E_0, and E_1 blue shift as ρ_{eh} is increased. Since E_0 shows a stronger blue shift than the continuum, exciton's binding energy E_{bind} defined with respect to the continuum (double arrow) decreases from 9.5 to 8.9 meV at $\rho_{\mathrm{eh}} = 3.6 \times 10^{10}\,\mathrm{cm}^{-2}$. Also the detectable $\bar{E}_{\mathrm{pro}}$ blue shifts which is consistent with the observed blue shift of the $1s$ heavy-hole exciton resonance in the QW absorption in Fig. 3.1. The almost linear increase of $\bar{E}_{\mathrm{pro}}$ as a function of ρ_{eh} is in agreement with earlier theoretical studies [109–111]. As

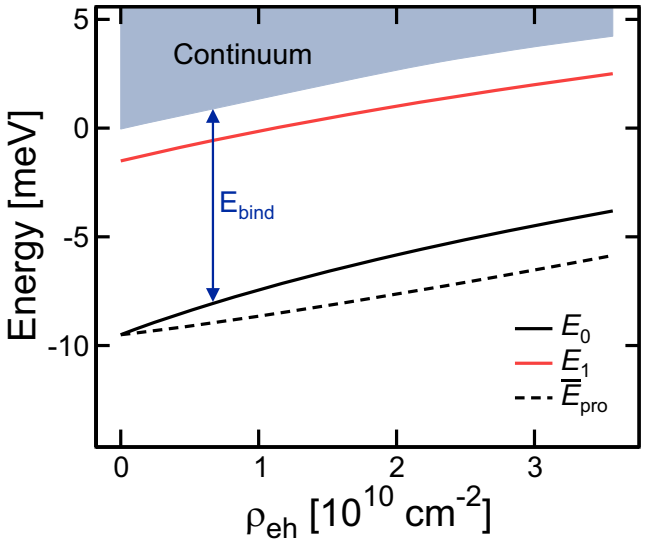

Figure 3.4: Pair-excitation energetics of incoherent excitons. The ground-state energy E_0 (solid black line), the energy of the first excited state E_1 (red line), the continuum (shaded area), and the energy per excited electron–hole pair $\bar{E}_{\mathrm{pro}}$ (dashed line) are plotted as a function of ρ_{eh}. (According to Paper (II)).

a result, the computed pair-excitation energetics of incoherent excitons is consistent with the expected physics.

3.5 Excitation spectrum of dropletons

The study in Sec. 3.2 has revealed a set of new discrete resonances clearly above the biexciton binding energy and none of them can be attributed to molecular excitons, i. e. polyexcitons. Additionally, the related quasiparticle exists in plasma and contains more than two electron–hole pairs because it is only accessible through three-photon correlation injection. Based on these informations, the new quasiparticle is assumed to be a quantum droplet where the electrons and holes are in a liquid phase confined within a droplet shell of microscopic size R. Since the QW is two-dimensional, the shell is a circular disk with radius R. As a result, $\Delta g(\mathbf{r})$ has the usual liquid structure where particles form a ring-like pattern with the ring separation roughly defined by the mean particle separation in the droplet [55, 112, 113]. Thus, each electron in the quantum droplet forms a standing wave around any given hole.

Intuitively, the dropleton is formed by the pressure of the surrounding plasma acting upon the liquid droplet. This force can be described as a potential wall around the droplet. Since the wall is created by particle–particle interactions, it should have a finite size. However, we have shown in the Supplementary Information to Paper (III) that a hard-wall approximation does not essentially change the dropleton energetics. Therefore, for simplicity, the hard-wall ansatz,

$$\phi(r) = J_0\left(x_n \tfrac{r}{R}\right) \mathrm{e}^{-\kappa r}\theta(R-r)\,, \tag{3.15}$$

is used, based on Eq. (3.6), to define the dropleton state where x_n is the n-th zero of the Bessel function $J_0(x)$. The Heaviside $\theta(x)$ function confines the dropleton inside a circular disk of radius R. For a given ring number n and dropleton radius R, the electron–hole density ρ_{eh} is adjusted by the specific choice of the decay constant κ and the correlation strength g_0, see Paper (II) for more details.

An example of dropleton's $g(r)$ is shown in Fig. 3.5(a) for $n = 4$ rings, $R = 90.8\,\mathrm{nm}$, and $\rho_{\mathrm{eh}} = 2.5 \times 10^{10}\,\mathrm{cm}^{-2}$. The cylinder indicates the droplet shell while the plasma contribution ($\rho_{\mathrm{e}}\rho_{\mathrm{h}}$) and the correlated part ($\Delta g(r)$) are presented as a gray shaded and a yellow transparent area, respectively. Unlike to single-component liquids [52–55], dropleton's $\Delta g(r)$ has a central part due to the Coulomb attraction of electrons and holes such that $\Delta g(r)$ exhibits four rings. In addition, $\Delta g(r)$ vanishes outside the hard shell according to the ansatz (3.15).

3.5.1 Dropleton-radius configuration

The dropleton radius R has been introduced via a physically intuitive ansatz (3.15) while the detailed density dependence of R remains an open question. In general, the dropleton energetics can be computed for any given dropleton-radius configuration. However, dropletons should have a larger binding than the other detectable quasiparticles in Fig. 3.2(a) like excitons and biexcitons to be energetically stable. Additionally, the energetics of the actual dropleton-radius configuration has to match the measured dropleton energetics in Fig. 3.2(a).

Typically, macroscopic electron–hole droplets form due to favorable energetics as the plasma density exceeds a critical density [40]. After their formation, they grow in size with increasing density. Therefore, it is reasonable to surmise that also quantum droplet's size increases as the electron–hole density becomes larger. More explicitly, the dropleton-radius configuration is assumed to be

$$R = R_0 \sqrt{\frac{\rho_{\mathrm{eh}}}{\rho_0}}\,, \tag{3.16}$$

such that the area of the dropleton, $S_{\mathrm{drop}} = \pi R^2$, is proportional to the electron–hole density. Here, the dropleton radius R_0 is defined at the reference density ρ_0. In the actual calculations, $R_0 = 90.8\,\mathrm{nm}$ and $\rho_0 = 2.5 \times 10^{10}\,\mathrm{cm}^{-2}$ are used because this choice produces dropleton energetics that matches the experiments best, as shown later in Fig. 3.6. Consequently, compared to exciton's Bohr radius of $a_{\mathrm{B}} = 12\,\mathrm{nm}$, dropletons have a roughly 8 times larger extension than excitons.

The resulting energetics of the density-dependent dropleton-radius configuration (3.16) is shown in Fig. 3.5(b) as a function of electron–hole density ρ_{eh}. The ground-state energy E_0 (solid black line) is plotted together with the first excited state E_1 (red solid line), the continuum (shaded area), and the energy per excited electron–hole pair $\bar{E}_{\mathrm{pro}}$ (dashed black line); the dropleton has $n = 4$ rings. The dashed blue and dotted red line present the density-dependent exciton and biexciton $\bar{E}_{\mathrm{pro}}$, respectively, according to the exciton energetics in Fig. 3.4 and the experimentally deduced low-density biexciton-binding energy in Fig. 3.1.

The 4-ring dropleton does not exist below $\rho_{\mathrm{eh}} = 2.5 \times 10^{10}\,\mathrm{cm}^{-2}$ (vertical line) which is comparable to macroscopic electron–hole droplets that also only form above a critical

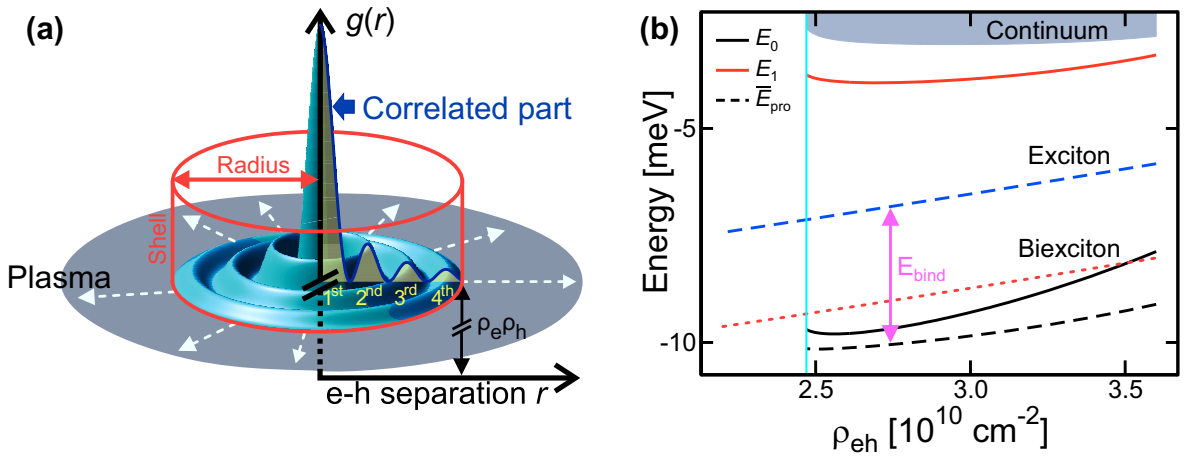

Figure 3.5: Dropleton's quantum state. (a) Dropleton's computed $g(r)$ for $R = 90.8\,\mathrm{nm}$, $n = 4$ rings, and $\rho_{\mathrm{eh}} = 2.5 \times 10^{10}\,\mathrm{cm}^{-2}$. The cylinder denotes the droplet shell. The correlated part ($\Delta g(r)$) is presented as a yellow transparent area while the plasma contribution ($\rho_{\mathrm{e}}\rho_{\mathrm{h}}$) is indicated as a gray shaded area. (b) The ground-state energy E_0 (black solid line), the first excited state E_1 (red solid line), the continuum (shaded area), and $\bar{E}_{\mathrm{pro}}$ (dashed black line) are shown as a function of ρ_{eh} for $n = 4$ rings. The density-dependent exciton (biexciton) $\bar{E}_{\mathrm{pro}}$ is plotted as dashed blue (dotted red) line. The vertical line indicates the threshold ρ_{eh} where the 4-ring dropleton emerges with the configuration shown in (a). (According to Papers (II) and (III)).

threshold density. For densities above $\rho_{\mathrm{eh}} = 2.5 \times 10^{10}\,\mathrm{cm}^{-2}$, $\bar{E}_{\mathrm{pro}}$ is lower than the exciton and biexciton $\bar{E}_{\mathrm{pro}}$. Consequently, the 4-ring dropleton is energetically stable for ρ_{eh} exceeding $2.5 \times 10^{10}\,\mathrm{cm}^{-2}$. In contrast to that, all excited states of the 4-ring dropleton have a binding energy smaller than the exciton which make them unstable at any density.

It is interesting to note that the 4-ring dropleton emerges at an electron–hole density where the exciton E_{bind} in Fig. 3.4 is already reduced, indicating that dense electron–hole plasma is needed to form dropletons. More specifically, the effect of Fermi pressure on the dropleton formation can be estimated by the phase-space filling (Pauli-blocking) factor $(1 - 2f_{\mathbf{k}})$ for zero-momentum electrons. In the actual calculations, the Pauli-blocking factor has already reduced to 0.41 at $\rho_{\mathrm{eh}} = 2.47 \times 10^{10}\,\mathrm{cm}^{-2}$ (vertical line), which is significant compared with the unblocked value of 1. Since Pauli blocking is directly related to Fermi pressure, the intuitive explanation indeed captures the basic cause for the formation of dropletons. A more detailed discussion of the effect of Fermi pressure on the dropleton formation is given in the Supplementary Information to Paper (III).

3.5.2 Ground-state energy of dropletons

To define the ground state of the dropleton, the energy difference

$$E_{\mathrm{bind}} = \bar{E}_{\mathrm{pro}}(1s) - \bar{E}_{\mathrm{pro}}(\mathrm{dropleton}) \tag{3.17}$$

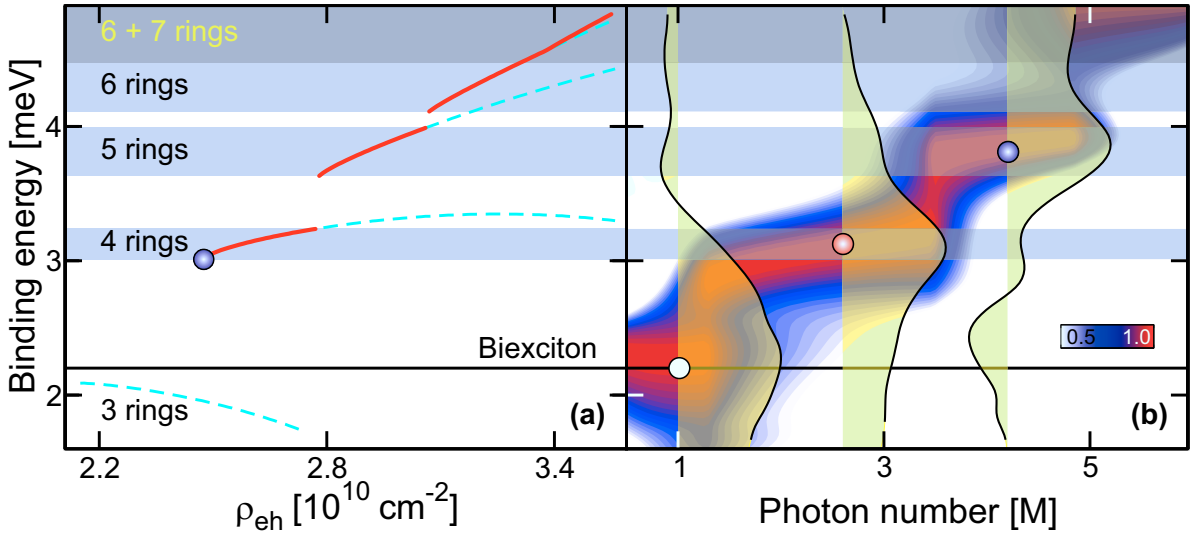

Figure 3.6: Pair-excitation energetics of dropletons. (a) Dropleton's ground state energy (red solid line) is shown as a function of electron–hole density ρ_{eh}. Shaded areas indicate the allowed energy ranges while the excited states are plotted as dashed lines; the horizontal line denotes the low-density biexciton-binding energy. The circle indicates the binding energy of the configuration shown in Fig. 3.5(a). (b) Projected $\Delta\alpha_{\mathrm{slt}}$ spectra as a function of N_{pump} for $\Delta t = 16\,\mathrm{ps}$. The peak absorption of each spectrum is normalized to one. Horizontal shaded areas indicate energy bands deduced in (a); the biexciton E_{bind} is plotted as horizontal line. Transparent shaded areas show actual spectra at $N_{\mathrm{pump}} = 1.0\,\mathrm{M}$ (left), $2.6\,\mathrm{M}$ (middle), and $4.2\,\mathrm{M}$ (right). (According to Paper (III)).

is computed for all ring numbers n as a function of the electron–hole density ρ_{eh} where $\bar{E}_{\mathrm{pro}}(1s)$ and $\bar{E}_{\mathrm{pro}}(\mathrm{dropleton})$ are the energies per excited electron–hole pair of the exciton and dropleton, respectively. Dropleton's ground state is then the lowest E_{bind} among all possible n-ring states. Figure 3.6(a) shows dropleton's ground state E_{bind} (red solid line) as a function of ρ_{eh}. The dashed lines denote the excited states while the measured biexciton binding energy is plotted as horizontal line. The dropleton ansatz (3.15) produces discrete energy bands; the allowed energy ranges are indicated by shaded areas. In particular, new energy levels emerge after sharp transitions where each transition increases the ring number by one. As a result, the quantum number of the discrete energy bands is defined by the ring number n. At elevated electron–hole densities, the 7-ring dropleton emerges (darker shaded area) but is not yet dropleton's ground state, yielding a continuous increase of dropleton's binding energy from 6-ring dropleton on. Dropletons with less than $n = 4$ rings have a binding smaller than the biexciton binding energy which make them undetectable in measurements where the biexciton resonance is present.

To study if the computed pair-excitation energetics of dropletons explains the measured energetics, Fig. 3.6(b) compares the experimental and theoretical results. In particular, the projected $\Delta\alpha_{\mathrm{slt}}$ spectra are shown as a function of the pump-photon number N_{pump} for a pump–probe delay of $\Delta t = 16\,\mathrm{ps}$ together with the energy bands deduced in Fig. 3.6(a) (shaded areas). The horizontal line indicates the low-density biexciton-binding energy while the transparent shaded areas show actual spectra at $N_{\mathrm{pump}} = 1.0\,\mathrm{M}$ (left), $2.6\,\mathrm{M}$

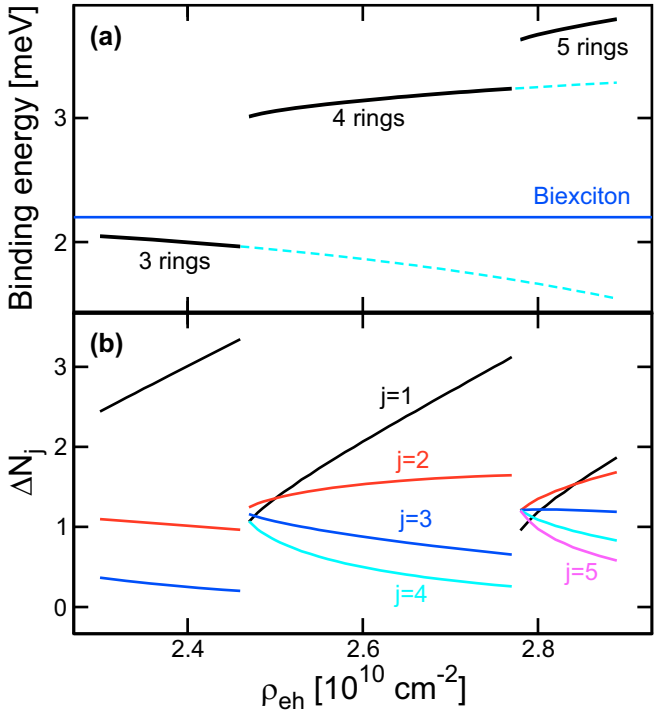

Figure 3.7: Ring structure of dropletons. (a) Dropleton's ground state energy (black solid line) is plotted as a function of ρ_{eh}. The excited states are presented as dashed lines while the horizontal line denotes biexciton's binding energy. (b) Number of correlated electron–hole pairs ΔN_j within the j-th ring is shown as a function of ρ_{eh} from the first ($j = 1$)- up to the fifth ($j = 5$) ring. (According to Paper (II)).

(middle), and 4.2 M (right).

The calculated energy bands for the 4- and 5-ring dropleton agree very well with the measured quantized energy levels. Also the merging of the 6- and 7-ring dropleton is observable in the projected $\Delta\alpha_{\mathrm{slt}}$. More specifically, above $N_{\mathrm{pump}} = 4.0\,\mathrm{M}$, $\Delta\alpha_{\mathrm{slt}}$ shows a broad 6-ring dropleton tail followed by the emergence of a hump corresponding to the 7-ring dropleton. As expected, the observed features are very broad in this pump-intensity range because they are generated via scattering after the three-particle electron–hole correlation injection. Also the signal becomes very weak at that range, which decreases the signal-to-noise ratio. Nevertheless, the dropleton energetics computed based on the density-dependent dropleton-radius configuration (3.16) matches well the measured energy bands. Therefore, it can be concluded that the dropleton size indeed increases with ρ_{eh}. The 3-ring dropleton is not detectable in the measurement with cross-circular pump–probe configuration due to the presence of the biexciton resonance. However, it is observable in the co-circular measurement presented in the Supplementary Information to Paper (III) because the biexciton is absent in the absorption spectra.

To verify the highly correlated character of dropletons, the number of electron–hole pairs within the j-th ring, ΔN_j, is studied next, which is defined in Eq. (44) of Paper (II). The result is presented in Fig. 3.7(b) where ΔN_j is plotted as a function of ρ_{eh} from the first (j=1) up to the fifth (j=5) ring. As a comparison, Fig. 3.7(a) shows again dropleton's

ground state energy as a function of ρ_{eh}. The number of electron–hole pairs within the innermost rings grows while it becomes smaller in the outermost rings as ρ_{eh} is increased. Remarkably, each ring contains roughly one electron–hole pair just after the ring-to-ring transition. Consequently, the number of rings matches approximately the number of electron–hole pairs within the quantum droplet such that already the first detectable 4-ring dropleton in Fig. 3.6(b) contains four correlated electron–hole pairs. Thus, the dropleton is indeed a highly correlated many-body state.

In conclusion, the study presented in this Chapter shows experimental and theoretical evidence for dropletons as a new stable highly correlated configuration of charged particles in GaAs QWs. The dropletons contain four-to-seven electron–hole pairs confined inside a microscopic correlation bubble, exhibit a quantized binding energy, and have a liquid-like electron–hole pair-correlation function. They exist in dense electron–hole plasma and form via attractive Coulomb interactions much before the system has reached the thermodynamic equilibrium.

4 Characterizing the biexciton resonance with quantum spectroscopy

As demonstrated in Chapter 3, quantum spectroscopy yields direct access to desired many-body states by adjusting light source's quantum fluctuations. This Chapter shows that quantum spectroscopy can characterize the properties of specific many-body states with a much higher accuracy than classical spectroscopy. To illustrate the accurate characterization capabilities of quantum spectroscopy, the biexciton resonance is investigated in the absorption spectra of GaAs QWs, which is well accessible in present-day experiments [31]. The analyzed measurements were performed by Steven T. Cundiff *et al.* (JILA, University of Colorado & NIST, Boulder, USA).

The discussion in Chapter 3 has already shown that classical spectroscopy generates a mixture of biexciton and dropleton states via scattering such that it is very difficult to characterize biexcitons that way. Thus, quantum spectroscopy is applied to directly excite biexcitons, yielding detailed access to the biexciton properties without blurring by scattering. Therefore, quantum-optical absorption spectra are projected from the measured QW absorption spectra using the projection scheme discussed in Sec. 2.4. With the help of this method, it is shown how the biexciton resonance in the absorption spectra changes as a function of pump source's intensity and quantum fluctuations.

The biexciton resonance in the measured QW absorption is investigated in Sec. 4.1 before quantum-optical differential absorption spectra are studied in Sec. 4.2. The excitation-induced dephasing [31, 46, 105] of the biexciton resonance as a function of pump intensity is discussed in Sec. 4.3. The results presented in this Chapter are based on Paper (IV).

4.1 Measured quantum well absorption

Analogously to Chapter 3, the ten QW absorption $\alpha_{\mathrm{QW}}(E, \Delta t, |\beta_0\rangle)$ is measured in absolute units as a function of probe-photon energy E, pump–probe delay Δt, and pump intensity $N_{\mathrm{pump}} = |\beta_0|^2$; pump and probe have again opposite circular polarizations. Figure 4.1(a) shows an example of the measured $\alpha_{\mathrm{QW}}(E, \Delta t, |\beta_0\rangle)$ for six representative pump intensities. Here, the pump intensity is again quoted in million (10^6 = M) photons. The pump–probe delay is $\Delta t = 12\,\mathrm{ps}$ and the spectra are shown with respect to the low-N_{pump} $1s$ heavy-hole exciton energy $E_{1s,0}$.

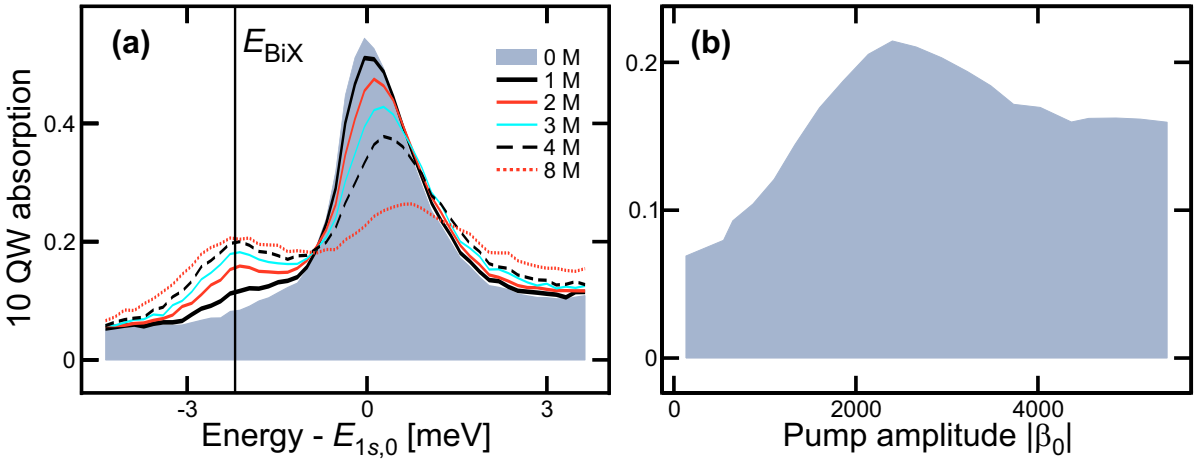

Figure 4.1: Characterizing the biexciton resonance with classical spectroscopy. (a) Measured ten QW absorption spectra $\Delta\alpha_{\mathrm{QW}}(E, \Delta t = 12\,\mathrm{ps}, |\beta_0\rangle)$ for six representative pump-photon numbers N_{pump}. The vertical line indicates the energetic position of the biexciton resonance for low N_{pump}; $E_{1s,0} = 1.547\,\mathrm{eV}$ denotes the $1s$ heavy-hole exciton energy at $N_{\mathrm{pump}} = 0$. (b) Measured QW absorption $\Delta\alpha_{\mathrm{QW}}(E_{\mathrm{BiX}}, \Delta t = 12\,\mathrm{ps}, |\beta_0\rangle)$ as a function of the pump amplitude $|\beta_0|$ at the biexciton energy $E_{\mathrm{BiX}} = -2.2\,\mathrm{meV} + E_{1s,0}$. (According to Paper (IV)).

In agreement with the observations in Fig. 3.1, the spectra have a pronounced $1s$ heavy-hole exciton resonance that broadens and blue shifts as the pump intensity is increased. At $N_{\mathrm{pump}} = 1\,\mathrm{M}$, the biexciton resonance (vertical line) emerges 2.2 meV below the heavy-hole exciton resonance. The biexciton resonance shows the typical excitation-induced dephasing as a function of the pump intensity while the energetic position is very stationary within the pump-intensity range studied.

To investigate the properties of the biexciton resonance in the measured QW absorption in more detail, Fig. 4.1(b) shows $\Delta\alpha_{\mathrm{QW}}(E_{\mathrm{BiX}}, \Delta t = 12\,\mathrm{ps}, |\beta_0\rangle)$ as a function of the pump amplitude $|\beta_0|$ at the biexciton energy $E_{\mathrm{BiX}} = -2.2\,\mathrm{meV} + E_{1s,0}$. The QW absorption at E_{BiX} increases up to $|\beta_0| = 2500$ before saturating above $|\beta_0| = 4000$. The response is clearly nonlinear such that the biexciton resonance is sensitive to the quantum fluctuations of the pump source according to the general quantum-response theory developed in Ref. [21] and briefly summarized in the Supplementary Material to Paper (V).

4.2 Projected differential quantum well absorption

Based on the observation in Fig. 4.1(b), the biexciton resonance is next analyzed with quantum spectroscopy. To characterize the biexciton resonance with a higher accuracy, spectral noise is removed from the measurement by applying a low-pass filter, see Paper (IV) for further details. The quantum-optical differential absorption $\Delta\alpha$ is then projected from the low-pass filtered $\alpha_{\mathrm{QW}}(E, \Delta t, |\beta_0\rangle)$.

As illustrated in Chapter 2, the biexciton resonance is particularly sensitive to squeezing-cat states. In more detail, the circular polarized pump pulse directly excites unbound biexciton coherences in squeezing-cat differential spectroscopy, according to the state-injection relation (2.9). The probe then detects a biexciton resonance due to the opposite

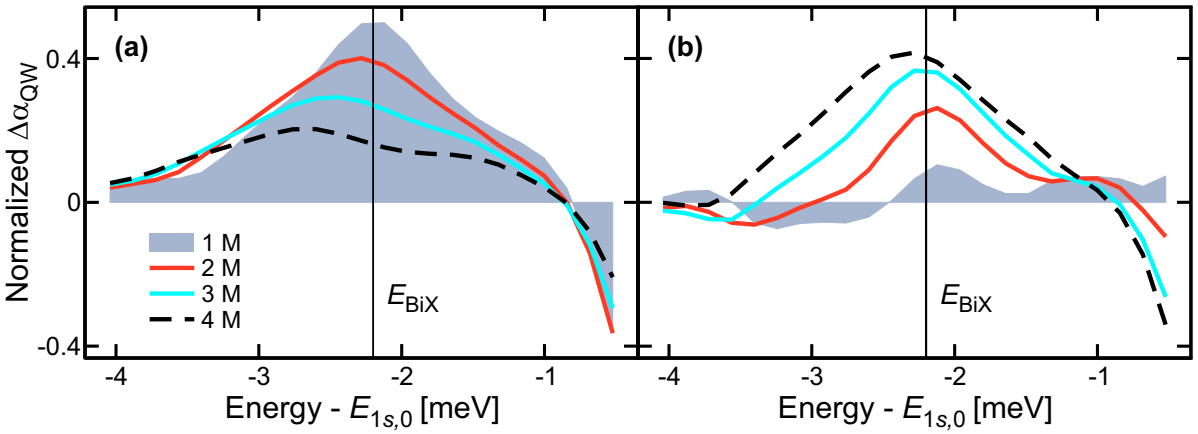

Figure 4.2: Constructed quantum-optical differential absorption. (a) Projected $\Delta\bar{\alpha}_{\text{class}}(E, \Delta t = 12\,\text{ps}, |\beta_0\rangle)$ is shown for 1 M (shaded area), 2 M (red line), 3 M (cyan line), and 4 M (dashed line) photon-number excitation. The vertical line denotes the low N_{pump} spectral position of the biexciton resonance. (b) The corresponding squeezing-cat differential $\Delta\bar{\alpha}_{\text{sqz}}(E, \Delta t = 12\,\text{ps}, |\beta_0\rangle)$. (According to Paper (IV)).

circular polarizations of pump and probe. In the following, the projected classical differential response (2.19) is compared with the squeezing-cat differential response (2.14) to demonstrate the accurate characterization capabilities of quantum spectroscopy. To directly compare both responses, the differential absorption of each excitation type is normalized via

$$\Delta\bar{\alpha}_{\text{type}}(E, \Delta t, |\beta_0\rangle) \equiv \frac{\Delta\alpha_{\text{type}}(E, \Delta t, |\beta_0\rangle)}{\alpha_{\text{type}}^{\text{peak}}}\,, \tag{4.1}$$

where $\alpha_{\text{type}}^{\text{peak}}$ is the peak differential absorption among all studied probe-photon energies E, pump intensities N_{pump}, and pump–probe delays Δt. Here, type is 'class' ('sqz') for classical (squeezing-cat) differential spectroscopy. The studied energy and pump-intensity ranges involve the energy and $N_{\text{pump}} = |\beta_0|^2$ regions shown in Fig. 4.1 while the delay-time range is $[1, 40]$ ps.

Figure 4.2(a) shows $\Delta\bar{\alpha}_{\text{class}}(E, \Delta t = 12\,\text{ps}, |\beta_0\rangle)$ for $N_{\text{pump}} = 1\,\text{M}$ (shaded area), 2 M (red line), 3 M (cyan line), and 4 M (dashed line). The vertical line indicates biexciton's low-N_{pump} energetic position. The analysis is focused to the probe-energy range around the biexciton resonance. As expected, classical differential spectroscopy resolves the biexciton resonance clearer compared to the measured QW absorption in Fig. 4.1(a). However, the biexciton resonance is very broad at $N_{\text{pump}} = 1\,\text{M}$ and also it broadens due to excitation-induced dephasing as N_{pump} is increased. In agreement with the observations in Chapter 3, the biexciton resonance red shifts at elevated pump intensities, indicating that a mixture of biexciton and dropleton states is present for N_{pump} exceeding 2 M. In addition, the high-energy part of the resonance is strongly influenced by the $1s$ heavy-hole exciton feature 2.2 meV above the biexciton resonance. As a result, the characterization of the biexciton resonance with classical spectroscopy is challenging.

The corresponding result of the squeezing-cat excitation is plotted in Fig. 4.2(b). At $N_{\text{pump}} = 1\,\text{M}$ (shaded area), squeezing-cat differential spectroscopy produces a *narrow*

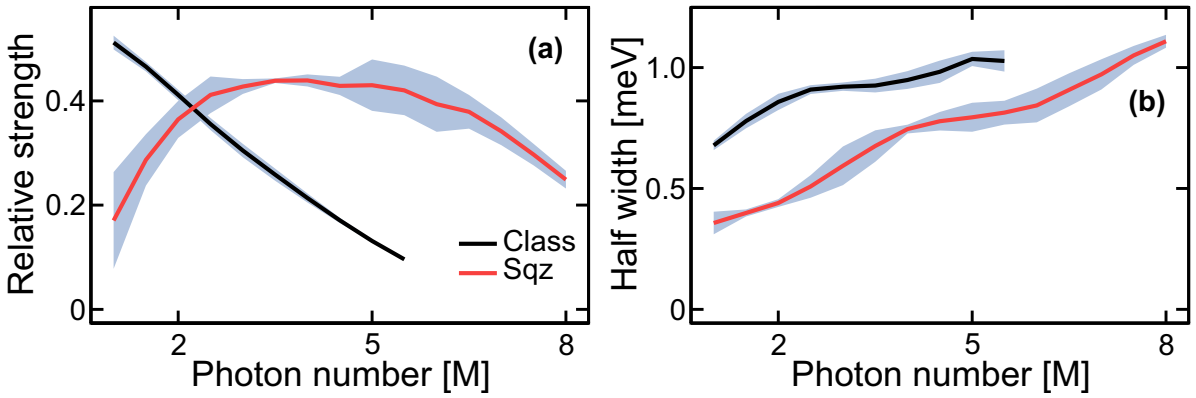

Figure 4.3: Excitation-induced broadening of the biexciton resonance. (a) The relative strength $\Delta\bar{\alpha}_{\text{strength}}$ is shown as a function of N_{pump} for classical (black line) and squeezing-cat (red line) differential spectroscopy. The pump–probe delay is $\Delta t = 12\,\text{ps}$. The shaded areas indicate the confidence interval of the $\Delta\bar{\alpha}_{\text{strength}}$ identification. (b) The corresponding half width γ_{half}. (According to Paper (IV)).

biexciton resonance that slightly broadens with growing N_{pump} while the relative strength of the resonance increases. In contrast to the result of classical differential spectroscopy in Fig. 4.2(a), the energetic position of the biexciton resonance is much more stationary and the high energy part of the resonance is less affected by the $1s$ heavy-hole exciton feature. Consequently, quantum spectroscopy can characterize the biexciton resonance much more accurately because it directly accesses the biexciton state while classical spectroscopy generates a mixture of biexciton and dropleton states.

4.3 Excitation-induced broadening

To emphasize the differences between classical and quantum spectroscopy in the biexciton characterization, the excitation-induced dephasing of the biexciton resonance is studied in more detail. Therefore, the change of biexciton resonance's strength and width as a function of the pump intensity is analyzed. The relative strength of the resonance is defined by

$$\Delta\bar{\alpha}_{\text{strength}} \equiv \Delta\bar{\alpha}_{\text{peak}} - \Delta\bar{\alpha}_{\text{floor}}\,, \tag{4.2}$$

where $\Delta\bar{\alpha}_{\text{floor}}$ is the floor value of the resonance. In classical differential spectroscopy, the biexciton resonance decays to a floor value of zero while $\Delta\bar{\alpha}_{\text{floor}}$ is slightly negative and N_{pump}-dependent for the squeezing-cat excitation according to Fig. 4.2. The width is computed based on the low-energy part of the biexciton resonance due to the distortion of the high-energy part by the $1s$ heavy-hole exciton feature in classical differential spectroscopy.

Figure 4.3(a) compares $\Delta\bar{\alpha}_{\text{strength}}$ in classical differential spectroscopy (black line) with the corresponding one of the squeezing-cat excitation (red line). Shaded areas indicate the confidence interval of the $\Delta\bar{\alpha}_{\text{strength}}$ identification, see Paper (IV) for more details. As in Figs. 4.1 and 4.2, the pump–probe delay is $\Delta t = 12\,\text{ps}$. The classical $\Delta\bar{\alpha}_{\text{strength}}$ decreases

monotonically, peaking at 0.49. Due to significant broadening, classical spectroscopy cannot resolve the biexciton resonance for pump-photon numbers above 5.5 M. In contrast to that, squeezing-cat differential spectroscopy generates a biexciton resonance whose relative strength grows up to roughly $N_{\mathrm{pump}} = 5\,\mathrm{M}$ followed only by a slow decrease up to 8 M photon-number excitation. As a result, quantum spectroscopy with squeezing-cat states can detect the biexciton resonance across a much broader pump-intensity range than classical spectroscopy.

The corresponding half width γ_{half} of the biexciton resonance is shown in Fig. 4.3(b). Both excitations produce a monotonically increasing γ_{half}. However, the half width of the classical excitation is roughly two times broader than the corresponding squeezing-cat γ_{half} for low N_{pump}. Consequently, classical differential spectroscopy cannot resolve the detailed excitation-induced dephasing of the biexciton resonance. Instead, it generates the biexciton resonance via scattering which masks the actual excitation-induced dephasing of the quasiparticle state. Compared to that, quantum spectroscopy with squeezing-cat states is capable to resolve the actual excitation-induced dephasing because it directly excites one biexciton state. More specifically, the line width of the biexciton resonance is 0.4 meV at $N_{\mathrm{pump}} = 0.5\,\mathrm{M}$ and increases up to 1.1 meV at 8 M photon-number excitation. Also the study of the dynamical properties of the biexciton resonance in Sec. III.D of Paper (IV) verifies the state-injection aspects of quantum spectroscopy and thus shows that quantum spectroscopy can monitor the properties of the biexciton resonance with a much higher accuracy than classical spectroscopy.

In conclusion, the study of the excitation-induced dephasing of the biexciton resonance shows that quantum spectroscopy directly excites one biexciton state while the classical excitation generates a distribution of biexciton and dropleton states via scattering. Consequently, quantum spectroscopy reveals a completely new level of biexciton details that remain hidden to classical spectroscopy.

5

Quantum-spectroscopy studies on quantum-dot systems

In Chapters 3 and 4, the optical properties of semiconductor QWs have been analyzed with quantum spectroscopy. In this Chapter, quantum-spectroscopy studies are performed on semiconductor QD systems. In particular, in the first part of this Chapter the input/output (I/O) characteristics of optically pumped QD micro-ring cavities is analyzed. The measurements have been performed by M. Bayer *et al.* (Technische Universität Dortmund, Germany).

In general, such QD micro-ring cavities are used to realize solid-state based cavity quantum electrodynamics experiments [114–116]. Additionally, these structures exhibit ultralow laser thresholds for a strongly non-resonant dot excitation [117,118]. In this situation, the electron–hole pairs in the wetting layer are excited, yielding carrier relaxation to the dots and eventually lasing. However, this setup is not suited for the discovery of new quantum-optical effects because lasing studies show a weaker quantum sensitivity due to coherent-state emission. In our study, the dots are pumped near-resonant, which cannot invert the system such that it operates in the excitation power regime below the laser threshold. As a new aspect, the I/O characteristics of the optically pumped QD microcavities shows unexpected oscillatory nonlinearities. These oscillations are identified as a genuine quantum-memory effect that can be controlled by shaping pump source's quantum fluctuations.

In general, quantum-optical response theory [31] states that the quantum-optical sensitivity originates exclusively from the response's nonlinearities even when some of them have classical explanations or are detected via classical measurements. In particular, one can then find individual quantum-optical correlations related to the quantum sensitivity. To identify the new intriguing quantum-optical effect in the I/O curve, a systematic three-step approach is applied. In the first step, the nonlinearities are extracted from the I/O characteristics before in step two a fully systematic microscopic analysis is used to find the quantum-optical correlation that produces the nonlinearities. More specifically, the QDs embedded within the microcavity are modeled by an extension of the Jaynes–Cummings model [89] to multiple dot states. There are already several extension of the Jaynes–Cummings model like the generalization to multiple atoms [119], light modes [120], or the coupling to one or more reservoirs [121–123] describing dephasing processes. These models have been successfully applied to demonstrate a multitude of quantum-optical

phenomena like reversible spontaneous emission [124, 125], quantum-Rabi flopping [126], or entanglement effects and their applications [71, 75, 76, 127–129]. In the last step of the three-step approach, quantum spectroscopy is used to verify the expected behavior of the in step two identified quantum-optical correlation.

The analysis in the second part of this Chapter represents a fundamental study to investigate the possibilities of quantum spectroscopy in dissipative systems. The results in Chapters 3 and 4 already suggest that quantum spectroscopy studies are possible in many-body systems even in the presence of dephasing. Therefore, the connection of quantum-optical correlation generation and dissipation is studied in more detail. Technically, QDs are modeled by a Jaynes–Cummings system including dissipation which allows for an exact computation of the correlation dynamics to all orders. In general, this simple model can be applied to understand the qualitative results for many-body systems because dissipation can be perceived as a general many-body effect. Additionally, the analysis gives also guidance when one can efficiently apply the cluster-expansion truncation scheme to describe the dynamics of the system.

Section 5.1 briefly introduces the theoretical description of QD systems embedded inside a microcavity using an extended Jaynes–Cummings model. The identification of a new quantum-memory effect in QD microcavities is discussed in Sec. 5.2 while the dynamics of the quantum-optical correlations in QD systems is analyzed in Sec. 5.3. A more detailed discussion of the results is given in Ref. [130] and in the Papers (I) and (V).

5.1 Theoretical description

To study the emission properties of a QD in a microcavity, the standard Jaynes–Cummings Hamiltonian is extended to N emitting states, which is formally equivalent to investigate N QDs in a microcavity. The dot system has then 2^N basic states because each state can either be excited or unexcited. When the QD is driven by classical pumping, the system Hamiltonian is [81]

$$\hat{H} = \hbar\omega(B^\dagger B + \frac{1}{2}) + \sum_{n=1}^{N} \hbar\omega_{21,n}\hat{P}_{z,n} - \hbar g \sum_{n=1}^{N}(B^\dagger \hat{P}_n + \text{h. c.}) - \hbar g \sum_{n=1}^{N}(\alpha^*(t)\hat{P}_n + \text{h. c.})\,, \tag{5.1}$$

where $\hat{P}_{z,n}$ and $\hat{P}_n$ are the population-inversion and polarization operators, respectively, of dot state n. The energy difference $\hbar\omega_{21,n}$ of dot state n is detuned with respect to the energy of the single-mode light field $\hbar\omega$. The strength of the light–matter interaction is defined by g. The last contribution of $\hat{H}$ describes classical pumping with pump pulse

$$\alpha(t) = \alpha_0 \mathrm{e}^{-\frac{t^2}{\tau^2}} \mathrm{e}^{-\mathrm{i}\omega_\mathrm{L} t}\,. \tag{5.2}$$

The excitation power is determined by α_0 while $\hbar\omega_\mathrm{L}$ is the central photon energy and τ corresponds to the duration of the pump pulse.

The system's density matrix is

$$\hat{\rho} = \sum_{n_1,n_2}^{\infty} \sum_{S_1,S_2} |S_1\rangle|n_1\rangle C_{n_2,S_2}^{n_1,S_1} \langle n_2|\langle S_2| \,, \tag{5.3}$$

where the single-mode light field is described by Fock states $|n_j\rangle$ while the basis states of the QD are defined by $|S_j\rangle$. The dynamics of $\hat{\rho}$ is computed by using the Liouville–von Neumann equation [131]

$$\mathrm{i}\hbar \frac{\partial}{\partial t}\hat{\rho}(t) = [\hat{H}, \hat{\rho}]_- + \mathrm{i}\hbar(\gamma_z \sum_{n=1}^{N} \mathrm{L}[\hat{P}_{z,n}] + \gamma_\mathrm{a} \sum_{n=1}^{N} \mathrm{L}[\hat{P}_n] + \kappa \mathrm{L}[\hat{B}]) \,, \tag{5.4}$$

where dissipation has been included via the Lindbladian [121]

$$\mathrm{L}[\hat{O}] = 2\hat{O}\hat{\rho}\,\hat{O}^\dagger - \hat{O}^\dagger\hat{O}\hat{\rho} - \hat{\rho}\,\hat{O}^\dagger\hat{O} \,. \tag{5.5}$$

In particular, $\gamma = \gamma_z + \gamma_\mathrm{a}$, $2\gamma_\mathrm{a}$, and κ determine the strength of polarization, population, and cavity-photon dephasing, respectively. A more detailed discussion of the theoretical approach is given in the Supplementary Material to Paper (V).

5.2 Quantum-memory effects in the quantum-dot microcavity emission

Measurements have been performed on GaInP micro-ring cavities with embedded InP QDs. A linear polarized 2 ps-long pump pulse excites the QDs with a photon energy that is below the GaInP bandgap and 30.7 meV above the main whispering-gallery cavity mode M1 which is one of three whispering-gallery modes denoted by M1–M3, compare Fig. 1 of Paper (V). Due to the near-resonant pumping conditions, the QD system is not inverted such that it operates in the excitation power regime below lasing. More experimental details are given in Paper (V) and Ref. [117].

To study the quantum-optical aspects of the I/O characteristics, Fig. 5.1(a) shows the measured output power I_out of cavity mode M1 as a function of the input power I_in. At first glance, the I/O curve shows the expected linear behavior. Nonetheless, the I/O characteristics exhibits small systematic oscillations. In particular, the output stays either above (superlinear output) or below (sublinear output) the perfect linear output for a large range of pump intensities.

To identify the origin of the nonlinearities in the I/O characteristics, a systematic three-step approach is applied. In the first step of this approach, the true nonlinearities of the I/O curve are isolated by computing the difference I_osc between the measured and perfect linear output. Figure 5.1(b) shows I_osc as a function of the input power. The relative strength of the oscillations can be determined directly from I_osc because the input and output in Fig. 5.1(a) are set to be one at the first sublinear dip. As a general trend, the actual I/O curve oscillates between super- and sublinear output as the input power is increased. The first sublinear minimum is roughly 10 % below the expected linear output while the noise floor is 6 %. Thus, the output indeed contains nontrivial oscillations which

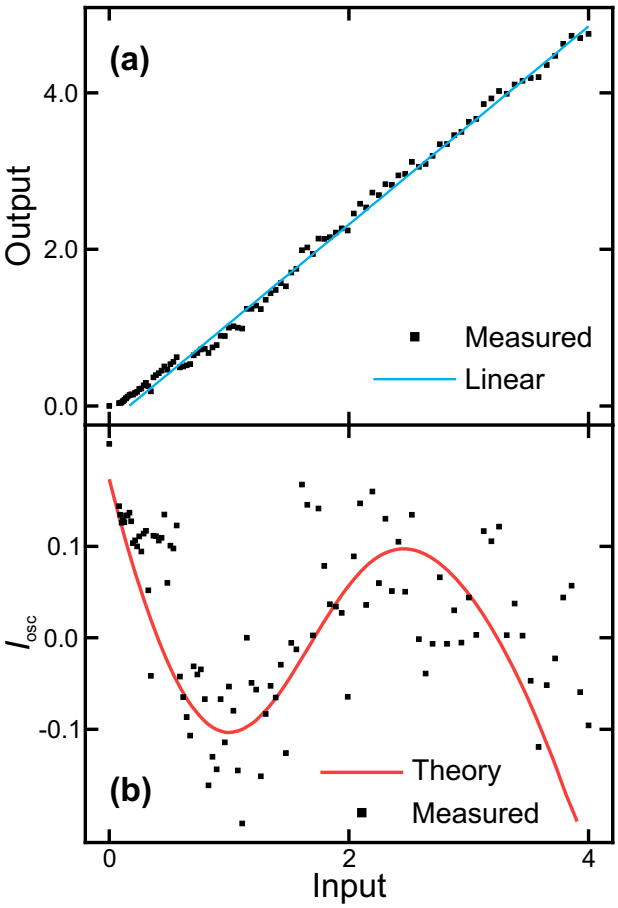

Figure 5.1: Quantum-optical aspects of I/O characteristics. (a) Measured output power (squares) as a function of input power. The solid line shows the result of a perfect linear output. Both powers are scaled to be one at the first sublinear dip. (b) Difference I_{osc} between the measured and perfect linear output (squares) is plotted as a function of the input power. The computed I_{osc} for a 2 ps-long pump pulse is presented as a solid line. (According to Paper (V)).

are confirmed by several measurements performed under multiple different experimental conditions, as shown in the Supplementary Material to Paper (V).

As a result, due to the nonlinearities the system must have a true quantum-optical aspect according to the quantum-optical response theory. Therefore, in the second step of the three-step approach, a fully systematic quantum theory is applied to determine which quantum-optical correlation produces the nonlinearities. In the study, the measured QD emission is assumed to originate mainly from one single QD because of the quasi-resonant excitation and the dot density. Additionally, due to the relative large size of the QDs in the experiment, it is estimated that roughly four states of the dot are near-resonant with the main cavity mode M1. Thus, the experimental results are analyzed with an extension of the standard Jaynes–Cummings model to four emitting states, as shown in Sec. 5.1. By computing the dynamics of system's density matrix $\hat{\rho}$ using the Liouville–von Neumann equation (5.4), the output intensity follows from $I_{\mathrm{out}} \propto \langle B^\dagger B \rangle = \mathrm{Tr}[B^\dagger B \hat{\rho}]$ while the input intensity is defined by $I_{\mathrm{in}} \propto \int \mathrm{d}t\, |\alpha(t)|^2$. The details of the calculations and the scaling of

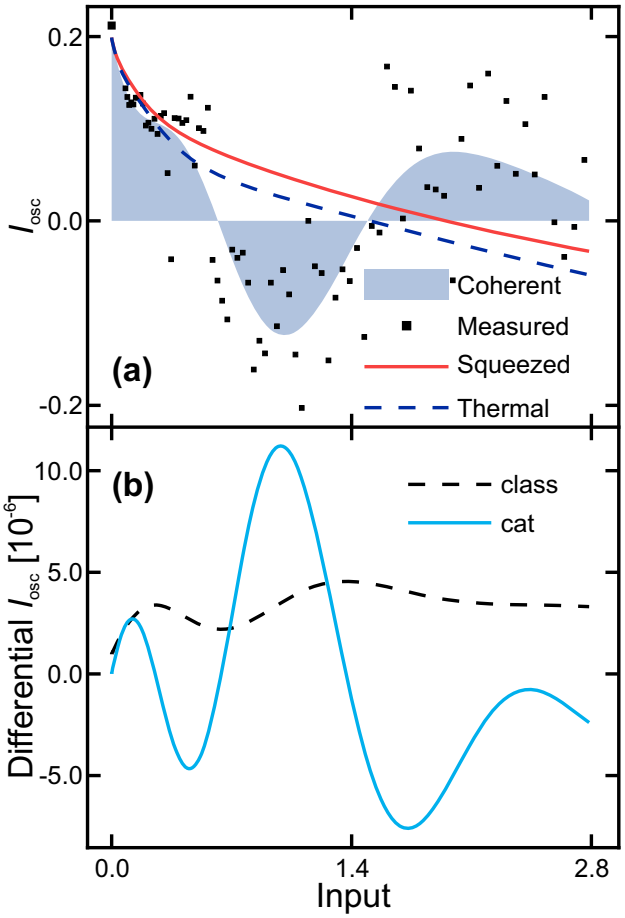

Figure 5.2: Characterization and control of I/O oscillations. (a) Measured I_{osc} (squares) is shown together with the projected coherent-state (shaded area), squeezed-vacuum (solid line), and thermal-state (dashed line) I_{osc}. (b) Differential I_{osc} is presented for classical (dashed line) and stretching-cat (solid line) differential spectroscopy. (According to Paper (V)).

the computed I_{in} and I_{out} are given in Paper (V) and the corresponding Supplementary Material.

Figure 5.1(b) also shows the computed I_{osc} for a 2 ps-long pump pulse as a function of the input power. The computed I_{osc} agrees well with the measured nonlinearities. Thus, the oscillations in the I/O characteristics are explained by the extension of the standard Jaynes–Cummings model (5.1). A systematic microscopic analysis presented in the Supplementary Material to Paper (V) reveals that the oscillations stem from the quantum-memory contribution $S^{\mathrm{QM}} = \Omega\Delta\langle B^\dagger \hat{P}_{z,n}\rangle$ that is a product of the classical Rabi frequency Ω and the photon-density correlation $\Delta\langle B^\dagger \hat{P}_{z,n}\rangle$. In particular, $\Delta\langle B^\dagger \hat{P}_{z,n}\rangle$ describes the correlation between emitted photons and state inversion. Since the dot inversion depends on the photon emission, $\Delta\langle B^\dagger \hat{P}_{z,n}\rangle$ can be understood as a quantum memory that stores informations about QD's previous photon-emission events.

As also elaborated in the Supplementary Material to Paper (V), the quantum-memory correlations are driven by the simultaneous presence of coherences and squeezing of the light emission. To verify the origin of the nontrivial I/O oscillations and thus complete

the systematic three-step approach, quantum spectroscopy is applied. Therefore, the classical measurements presented in Fig. 5.1(a) are projected into quantum-optical responses resulting from quantum-light sources that have either no coherences or do not produce squeezed emission. Here, the measured response is explicitly given by the output power, i. e. $R_{|\beta\rangle} = I_{\mathrm{out}}$. As quantum sources, squeezed-vacuum and thermal states are used [31]. As general properties, the squeezed-vacuum source has no first-order coherences while the thermal state has no coherences and additionally does not produce squeezed emission, see Supplementary Material to Paper (V) for more details. Thus, the excitation of the system with thermal or squeezed-vacuum light should not produce oscillations to the I/O curve because both quantum sources cannot induce quantum-memory correlations. In contrast to that, the output of the pump source in the experiment has quantum statistics of a coherent state which has coherences and generates squeezing to the emission [132] such that a coherent-state excitation should reproduce the oscillations in the I/O characteristics.

To test this, Fig. 5.2(a) shows the measured I_{osc} (squares) together with the projected coherent-state (shaded area), squeezed-vacuum (solid line), and thermal-state (dashed line) responses. As expected, the coherent-state output matches the measured I/O oscillations while the outputs of squeezed-vacuum and thermal state show no oscillations. As a result, the simultaneous presence of coherences and squeezing of the light emission yields the nontrivial oscillations in the I/O characteristics, which corresponds to a genuine quantum-memory effect.

The measured I/O oscillations can also be controlled by adjusting pump source's quantum fluctuations. As shown in the Supplementary Material to Paper (V), stretching-cat states simultaneously exhibit coherences and squeezing such that they should enhance the effect of quantum-memory correlations. To demonstrate this, the classical differential response (2.19) is compared with the stretching-cat differential response (2.15). Figure 5.2(b) presents the projected classical (dashed line) and stretching-cat (solid line) differential I_{osc}. Classical differential spectroscopy produces a positive valued response whose minima and maxima agree with the nodes of the measured I_{osc} oscillations in Fig. 5.2(a). Compared to that, stretching-cat state's differential I_{osc} is an order of magnitude larger. In addition, the oscillations have an opposite phase compared to the measured I_{osc} oscillations in Fig. 5.2(a). Consequently, the amplitude of the I_{osc} oscillations can be controlled by a suitably shaped pump source.

In conclusion, the I/O characteristics of optically pumped QD microcavities shows nontrivial oscillations in the excitation power regime below the laser threshold, originating from quantum-memory correlations that are simultaneously driven by coherences and squeezed emission. This quantum-memory effect can either be disabled or strongly enhanced by shaping pump source's quantum fluctuations.

5.3 Connection of quantum-optical correlation generation and dissipation

To study the possibilities of quantum-spectroscopy investigations in dissipative systems, the relation of quantum-optical correlation generation and dissipation is analyzed in this Section. Therefore, a Jaynes–Cummings-type QD system [60, 62] is studied, which allows for an exact computation of the correlation dynamics to all orders. More specifically, the

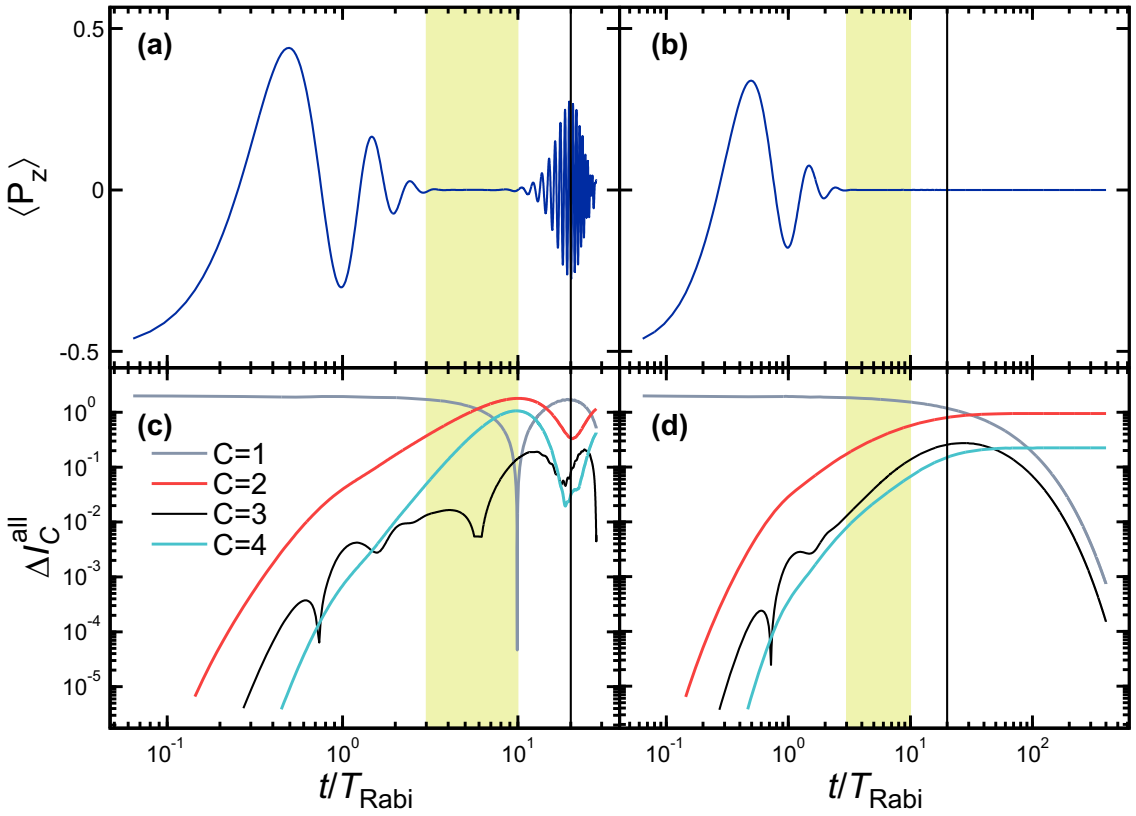

Figure 5.3: Dynamics of quantum-optical correlations. (a) The time evolution of the population inversion $\langle \hat{P}_z \rangle$ is shown in logarithmic time scale. The corresponding dynamics of collective C-particle correlations $\Delta I_C^{\mathrm{all}}$ is plotted in (c) for $C = 1$ up to $C = 4$ in double-logarithmic scale. In both frames, the shaded area indicates the collapse region while the vertical line denotes the revival time. The same quantities are presented in (b) and (d) for a dephasing of $\gamma = g$. (According to Paper (I)).

QD is described by an effective two-level system, i. e. $N = 1$ in the Hamiltonian (5.1), that is resonantly excited ($\omega = \omega_{21}$) with a coherent state $|\beta_0\rangle$ instead of the classical pumping, i. e. $\alpha_0 = 0$. In addition, only polarization dephasing is considered by setting $\gamma_{\mathrm{a}} = \kappa = 0$ in Eq. (5.4), which describes situations where the polarization decays much faster than populations [133]. This behavior is very typical in semiconductors where the polarization decay occurs on a much faster time scale than the carrier relaxation [18]. The resulting time evolution of the density matrix (5.4) allows then for the computation of the quantum-optical correlation dynamics, see Paper (I) for more details.

The dynamics of the systems is first studied in the strong-coupling regime, i. e. $\gamma = 0$, where the light–matter coupling is stronger compared to dissipative processes. Figure 5.3(a) shows the time evolution of the population inversion $\langle \hat{P}_z \rangle$ in logarithmic time scale. The system has been excited by a coherent state $|\beta_0\rangle$ that has $\langle B^\dagger B \rangle = |\beta_0|^2 = 10$ photons on average. The time is quoted in units of the Rabi period $T_{\mathrm{Rabi}} = \pi/(g|\beta_0|)$ [18]. The time evolution of $\langle \hat{P}_z \rangle$ shows the typical collapse and revival of Rabi oscillations [134] which has been first experimentally observed in Ref. [135]. In contrast to that, a semiclassical calculation yields permanent oscillations as a function of time such that the

collapse–revival behavior is indeed a true quantum-optical effect.

To study the generation of the quantum-optical correlations (2.4), the normalized collective C-particle correlations

$$\Delta I_C^{\mathrm{all}} \equiv \frac{1}{|\beta_0|^C} \sum_{J=0}^{C} \frac{|\Delta I_{C-J}^J|}{J!(C-J)!} \tag{5.6}$$

are analyzed. They contain all different C-particle correlations, see Sec. 3 of Paper (I) for a more detailed discussion. Figure 5.3(c) presents the time evolution of $\Delta I_C^{\mathrm{all}}$ on a double-logarithmic scale for $C = 1$ up to $C = 4$. At early times $t < T_{\mathrm{Rabi}}/2$, the quantum-optical correlations build up in a hierarchal order, i. e. C-particle correlations are only created after $(C-1)$-particle cluster are already present. As a result, one can efficiently apply the cluster-expansion approach in this time regime to truncate the hierarchy problem (2.8) because system's dynamics is accurately described by few lowest clusters while higher order clusters are negligible.

With increasing time, the higher order correlations start to dominate the dynamics. In particular, the higher order cluster become larger than the singlets $C = 1$ in the collapse region (shaded area). In this regime, a large number of clusters is needed to describe the dynamics of the system accurately. At the revival time $T_{\mathrm{rev}} = 2\pi|\beta_0|/g$ (vertical line), the correlation order is restored. More specifically, the correlations are weak in this regime indicating that the system's dynamics shows a more classical behavior. As a result, in the strong-coupling regime the dynamics of the system can be described by few lowest clusters only at early times and around the revival while many clusters are needed to reproduce the collapse and revival behavior of the Rabi oscillations.

The influence of dissipation on the correlation generation is analyzed next. For strong dephasing, the Jaynes–Cummings system enters the weak-coupling regime where obvious quantum features like the revivals vanish and the system can be described semiclassically [123]. Figure 5.3(b) and (d) show the same quantities as in Fig. 5.3(a) and (c) but now for a dephasing of $\gamma = g$ in the Lindbladian (5.5). The $\langle \hat{P}_z \rangle$ dynamics in Fig. 5.3(b) shows no revival indicating that the system has reached the weak-coupling regime. The build up of the quantum-optical correlations in Fig. 5.3(d) is hindered by the presence of dissipation. Consequently, the dynamics of the system can be described by a low number of clusters when the system has a dissipative coupling such that the cluster-expansion truncation scheme can be efficiently applied. This suggests that also the dynamics of many-body systems can be successfully described by the cluster expansion because many-body systems naturally contain dissipation.

However, the correlations become strong in the time region $[10, 25]T_{\mathrm{Rabi}}$. More precisely, a group of even $(2C)$- and odd $(2C+1)$-particle correlations shows the sequential order all the time. In particular, the odd correlations decay towards zero at elevated times as a direct consequence of dephasing while the even correlations still remain when the system relaxes into a steady state; the evolution towards the steady state is discussed in detail in Sec. 5 of Paper (I). As a result, even in the presence of strong dephasing appreciable correlations are generated, which indicates that quantum-spectroscopy studies are possible in systems with dissipation.

6 Conclusions and Outlook

In this Thesis, quantum-spectroscopy studies have been performed on semiconductor nanostructures. Besides purely theoretical studies, the optical properties of QW and QD systems have been analyzed with quantum spectroscopy by projecting high-precision measurements into quantum-optical responses. The findings of these experiment–theory investigations have been supported by applying systematic microscopic theories.

In the first part of this Thesis, experimental and theoretical evidence has been shown for a new quasiparticle, the dropleton, in direct-gap GaAs QWs. In classical spectroscopy, the new quasiparticle appeared as a gradual increasing binding energy of the naively identified biexciton resonance as the pump intensity is increased. To enhance the sensitivity of the quasiparticle identification, quantum spectroscopy has been applied to directly excite highly correlated many-body states. The study revealed quantized binding energy bands above the biexciton binding energy and quantum beats with frequency matching the energy difference between the energy bands. Additional control measurements have been performed to verify the physics expected for dropletons, providing additional evidence for the discovery of this new quasiparticle.

To compute the pair-excitation spectrum of dropletons, a new theoretical scheme has been developed which allows for the determination of the pair-excitation energetics of highly correlated many-body complexes in optically excited semiconductor QWs. As a new aspect, the pair-excitation spectrum is computed based on a pair-correlation function formulation of the many-body state. In general, the approach can be applied to determine and predict the pair-excitation energetics of a large range of quasiparticle states.

In conclusion, our study showed unambiguous evidence for the discovery of dropletons as a new stable configuration of charged particles in GaAs QWs. The dropletons contain four-to-seven electron–hole pairs confined inside a correlation bubble that is kept together by the Fermi pressure generated by the surrounding dense electron–hole plasma. Compared to polyexcitons, the electrons in the quantum droplets are not attached to an individual hole but they form a ring-like pattern around any given hole which is similar to the ordering observed in macroscopic liquids. Additionally, the dropletons show discrete energy bands due to their small size and exist on a picosecond time scale much before the system reaches the thermal equilibrium. Since the identification of stable many-body configurations is an important step in describing physical systems, the detection of dropletons will have a large impact on several research directions. For example, dropletons couple strongly to light source's quantum fluctuations such that they can be used

to study the interaction between quantized light and highly correlated matter in more detail. The gained physical understanding of these studies may be used to develop new optoelectronic devices.

In the second part of this Thesis, the biexciton resonance in the absorption spectra of GaAs QWs has been investigated with quantum spectroscopy. The results demonstrated that classical and quantum spectroscopy yield a significantly different QW absorption. More specifically, the excitation-induced dephasing of the biexciton resonance as a function of the pump intensity can be characterized with a much higher accuracy using quantum spectroscopy. In general, the accurate characterization capabilities of quantum spectroscopy are not restricted to the biexciton resonance. Due to the state-injection aspects, quantum spectroscopy can be used to sensitively monitor the properties of a large number of quasiparticle states in semiconductor QWs. The only requirement is that pump laser's quantum fluctuations have to be adjusted to match with the corresponding electron–hole correlations of the desired many-body state.

In another study, the I/O characteristics of optically pumped QD microcavities has been analyzed in the excitation power regime below the laser threshold. Surprisingly, the I/O curve showed unexpected oscillations. By applying a systematic three-step approach it has been shown that the oscillations correspond to a genuine quantum-memory effect originating from photon-density correlations which are simultaneously driven by coherences and squeezing in the pump field. The investigation also illustrated that quantum spectroscopy cannot only verify the nature of the quantum-memory effect, but can also be applied to enable or increase the I/O oscillations by adjusting pump laser's quantum statistics. As a result, the QD emission can be controlled by the quantum fluctuations of the pump laser. This discovery may be the first step in developing light sources with increased quantum-light emission, which will have a wide spectroscopic impact on solid-state physics.

A fundamental study about the general applicability of quantum spectroscopy in dissipative systems has been presented in the last part of this Thesis. Therefore, the connection of quantum-optical correlation generation and dissipation has been analyzed by modeling QD systems with the Jaynes–Cummings model. The results show that the photon correlations build up in a hierarchical order and survive significant amount of dissipation. Since many-body systems naturally contain dissipation, these results suggest that quantum-spectroscopy measurements can be applied to investigate new intriguing phenomena in a large range of systems. The study also revealed that the cluster-expansion truncation can be efficiently applied when the system has a dissipative coupling.

As a general outlook, it will be interesting to investigate which new classes of many-body states emerge when even stronger correlated quantum sources are used to excite many-body systems. Further investigations may also use other optical measurements like terahertz spectroscopy or two-dimensional Fourier transform spectroscopy in the experiment–theory analysis.

7 Short introduction to the papers

(I) We study how quantum-optical correlations are generated through the light–matter interaction and how they survive dissipative processes. The presented results show that quantum-spectroscopy studies are possible for a large range of systems. The analysis also indicates when the cluster-expansion truncation scheme can be efficiently applied to describe the dynamics of the system.

(II) A new intriguing theoretic approach has been developed to determine the excitation energetics of highly correlated quasiparticles in optically excited semiconductors. As a new aspect, the pair-excitation energetics is computed based entirely on a correlation-function formulation of the quasiparticle state. The approach is verified for several well-known many-body configurations and applied to compute the excitation spectrum of quantum droplets.

(III) We report experimental and theoretical evidence for the discovery of a new stable quasiparticle configuration, the dropleton, in direct-gap GaAs quantum wells. The dropleton is a microscopic bubble consisting of four-to-seven electron–hole pairs. It exists in plasma, exhibits energy quantization due to its microscopic size, and has an electron–hole pair-correlation function characteristic for liquids.

(IV) The properties of the biexciton resonance in the absorption spectra of GaAs quantum wells are analyzed with quantum spectroscopy. Our study shows that quantum spectroscopy reveals a completely new level of biexciton details that remain hidden to classical spectroscopy.

(V) We investigate the input/output characteristics of optically pumped quantum-dot microcavities which shows unexpected oscillations. A systematic microscopic analysis identifies the input/output nonlinearities as a genuine quantum-memory effect that can be control by shaping pump source's quantum fluctuations.

Bibliography

[1] Lvovsky, A. I. and Raymer, M. G. (2009) Continuous-variable optical quantum-state tomography. *Rev. Mod. Phys.*, **81**, 299–332.

[2] Cramer, M., Plenio, M. B., Flammia, S. T., Somma, R., Gross, D., Bartlett, S. D., Landon-Cardinal, O., Poulin, D., and Liu, Y.-K. (2010) Efficient quantum state tomography. *Nat. Commun.*, **1**, 149.

[3] Hofheinz, M., et al. (2009) Synthesizing arbitrary quantum states in a superconducting resonator. *Nature*, **459**, 546–549.

[4] Eichler, C., Bozyigit, D., Lang, C., Steffen, L., Fink, J., and Wallraff, A. (2011) Experimental State Tomography of Itinerant Single Microwave Photons. *Phys. Rev. Lett.*, **106**, 220503.

[5] Christandl, M. and Renner, R. (2012) Reliable Quantum State Tomography. *Phys. Rev. Lett.*, **109**, 120403.

[6] Vogel, K. and Risken, H. (1989) Determination of quasiprobability distributions in terms of probability distributions for the rotated quadrature phase. *Phys. Rev. A*, **40**, 2847–2849.

[7] Smithey, D. T., Beck, M., Raymer, M. G., and Faridani, A. (1993) Measurement of the Wigner distribution and the density matrix of a light mode using optical homodyne tomography: Application to squeezed states and the vacuum. *Phys. Rev. Lett.*, **70**, 1244–1247.

[8] Breitenbach, G., Schiller, S., and Mlynek, J. (1997) Measurement of the quantum states of squeezed light. *Nature*, **387**, 471–475.

[9] Lvovsky, A. I., Hansen, H., Aichele, T., Benson, O., Mlynek, J., and Schiller, S. (2001) Quantum State Reconstruction of the Single-Photon Fock State. *Phys. Rev. Lett.*, **87**, 050402.

[10] Bertet, P., Auffeves, A., Maioli, P., Osnaghi, S., Meunier, T., Brune, M., Raimond, J. M., and Haroche, S. (2002) Direct Measurement of the Wigner Function of a One-Photon Fock State in a Cavity. *Phys. Rev. Lett.*, **89**, 200402.

[11] Lundeen, J. S., Sutherland, B., Patel, A., Stewart, C., and Bamber, C. (2011) Direct measurement of the quantum wavefunction. *Nature*, **474**, 188–191.

[12] Leibfried, D., Meekhof, D. M., King, B. E., Monroe, C., Itano, W. M., and Wineland, D. J. (1996) Experimental Determination of the Motional Quantum State of a Trapped Atom. *Phys. Rev. Lett.*, **77**, 4281–4285.

[13] Lutterbach, L. G. and Davidovich, L. (1997) Method for Direct Measurement of the Wigner Function in Cavity QED and Ion Traps. *Phys. Rev. Lett.*, **78**, 2547–2550.

[14] Kurtsiefer, C., Pfau, T., and Mlynek, J. (1997) Measurement of the Wigner function of an ensemble of helium atoms. *Nature*, **386**, 150–153.

[15] Kira, M. and Koch, S. W. (2006) Quantum-optical spectroscopy of semiconductors. *Phys. Rev. A*, **73**, 013813.

[16] Gerry, C. and Knight, P. (2005) *Introductory Quantum Optics*. Cambridge University Press, 3rd edn.

[17] Vogel, W. and Welsch, D. G. (2006) *Quantum Optics*. Wiley, 3rd edn.

[18] Kira, M. and Koch, S. W. (2011) *Semiconductor Quantum Optics*. Cambridge University Press, 1st edn.

[19] Stenholm, S. (1984) *Foundations of Laser Spectroscopy*. 1st edn.

[20] Demtröder, W. (2008) *Laser Spectroscopy: Basic Concepts and Instrumentation*. 4th edn.

[21] Koch, S. W., Kira, M., Khitrova, G., and Gibbs, H. M. (2006) Semiconductor excitons in new light. *Nature Mater.*, **5**, 523–531.

[22] Walls, D. F. (1983) Squeezed states of light. *Nature*, **306**, 141–146.

[23] Slusher, R. E., Hollberg, L. W., Yurke, B., Mertz, J. C., and Valley, J. F. (1985) Observation of Squeezed States Generated by Four-Wave Mixing in an Optical Cavity. *Phys. Rev. Lett.*, **55**, 2409–2412.

[24] Vahlbruch, H., Mehmet, M., Chelkowski, S., Hage, B., Franzen, A., Lastzka, N., Goßler, S., Danzmann, K., and Schnabel, R. (2008) Observation of Squeezed Light with 10-dB Quantum-Noise Reduction. *Phys. Rev. Lett.*, **100**, 033602.

[25] Mehmet, M., Ast, S., Eberle, T., Steinlechner, S., Vahlbruch, H., and Schnabel, R. (2011) Squeezed light at 1550 nm with a quantum noise reduction of 12.3 db. *Opt. Express*, **19**, 25763–25772.

[26] Safavi-Naeini, A. H., Gröblacher, S., Hill, J. T., Chan, J., Aspelmeyer, M., and Painter, O. (2013) Squeezed light from a silicon micromechanical resonator. *Nature*, **500**, 185–189.

[27] Brattke, S., Varcoe, B. T. H., and Walther, H. (2001) Generation of Photon Number States on Demand via Cavity Quantum Electrodynamics. *Phys. Rev. Lett.*, **86**, 3534–3537.

[28] Hofheinz, M., Weig, E., Ansmann, M., Bialczak, R. C., Lucero, E., Neeley, M., Oconnell, A., Wang, H., Martinis, J. M., and Cleland, A. (2008) Generation of Fock states in a superconducting quantum circuit. *Nature*, **454**, 310–314.

[29] Ourjoumtsev, A., Tualle-Brouri, R., Laurat, J., and Grangier, P. (2006) Generating Optical Schrödinger Kittens for Quantum Information Processing. *Science*, **312**, 83–86.

[30] Ourjoumtsev, A., Jeong, H., Tualle-Brouri, R., and Grangier, P. (2007) Generation of optical Schrödinger cats from photon number states. *Nature*, **448**, 784–786.

[31] Kira, M., Koch, S. W., Smith, R. P., Hunter, A. E., and Cundiff, S. T. (2011) Quantum spectroscopy with Schrödinger-cat states. *Nature Phys.*, **7**, 799–804.

[32] Frenkel, J. (1931) On the Transformation of light into Heat in Solids. I. *Phys. Rev.*, **37**, 17–44.

[33] Wannier, G. (1937) The Structure of Electronic Excitation Levels in Insulating Crystals. *Phys. Rev.*, **52**, 191–197.

[34] Haug, H. and Koch, S. (2009) *Quantum Theory of the Optical and Electronic Properties of Semiconductors*. World Scientific, 5th edn.

[35] Miller, R. C., Kleinman, D. A., Gossard, A. C., and Munteanu, O. (1982) Biexcitons in GaAs quantum wells. *Phys. Rev. B*, **25**, 6545–6547.

[36] Kim, J. C., Wake, D. R., and Wolfe, J. P. (1994) Thermodynamics of biexcitons in a GaAs quantum well. *Phys. Rev. B*, **50**, 15099–15107.

[37] Wang, S. and Kittel, C. (1972) Excitonic molecules: A possible new form of chemical bonding. *Phys. Lett. A*, **42**, 189–190.

[38] Steele, A. G., McMullan, W. G., and Thewalt, M. L. W. (1987) Discovery of Polyexcitons. *Phys. Rev. Lett.*, **59**, 2899–2902.

[39] Yu, P. Y. and Kittel, C. (1988) Polyexcitons in ultrapure silicon. *Nature*, **332**, 783–784.

[40] Jeffries, C. (1975) Electron-Hole Condensation in Semiconductors. *Science*, **189**, 955–964.

[41] Wolfe, J. P., Hansen, W. L., Haller, E. E., Markiewicz, R. S., Kittel, C., and Jeffries, C. D. (1975) Photograph of an Electron-Hole Drop in Germanium. *Phys. Rev. Lett.*, **34**, 1292–1293.

[42] Suzuki, T. and Shimano, R. (2009) Time-Resolved Formation of Excitons and Electron-Hole Droplets in Si Studied Using Terahertz Spectroscopy. *Phys. Rev. Lett.*, **103**, 057401.

[43] Gross, E. K. and Dreizler, R. M. (1995) *Density functional theory*. Springer.

[44] Kohn, W., Becke, A. D., and Parr, R. G. (1996) Density Functional Theory of Electronic Structure. *J. Phys. Chem.*, **100**, 12974–12980.

[45] Sholl, D. and Steckel, J. (2009) *Density Functional Theory: A Practical Introduction*. Wiley.

[46] Kira, M. and Koch, S. W. (2006) Many-body correlations and excitonic effects in semiconductor spectroscopy. *Prog. Quantum Electron.*, **30**, 155 – 296.

[47] Kirkwood, J. G. and Boggs, E. M. (1942) The Radial Distribution Function in Liquids. *J. Chem. Phys.*, **10**, 394–402.

[48] Born, M. and Green, H. S. (1946) A General Kinetic Theory of Liquids. I. The Molecular Distribution Functions. *Proc. R. Soc. A*, **188**, 10–18.

[49] C. M. Davis, J. and Litovitz, T. A. (1965) Two-State Theory of the Structure of Water. *J. Chem. Phys.*, **42**, 2563–2576.

[50] Yarnell, J. L., Katz, M. J., Wenzel, R. G., and Koenig, S. H. (1973) Structure Factor and Radial Distribution Function for Liquid Argon at 85 K. *Phys. Rev. A*, **7**, 2130–2144.

[51] Soper, A. (2000) The radial distribution functions of water and ice from 220 to 673 K and at pressures up to 400 MPa. *Chem. Phys.*, **258**, 121 – 137.

[52] Narten, A. H. (1972) Liquid Water: Atom Pair Correlation Functions from Neutron and X-Ray Diffraction. *J. Chem. Phys.*, **56**, 5681–5687.

[53] Schommers, W. (1973) A pair potential for liquid rubidium from the pair correlation function. *Phys. Lett. A*, **43**, 157 – 158.

[54] Soper, A. K. and Silver, R. N. (1982) Hydrogen-Hydrogen Pair Correlation Function in Liquid Water. *Phys. Rev. Lett.*, **49**, 471–474.

[55] Jorgensen, W. L., Chandrasekhar, J., Madura, J. D., Impey, R. W., and Klein, M. L. (1983) Comparison of simple potential functions for simulating liquid water. *J. Chem. Phys.*, **79**, 926–935.

[56] Badolato, A., Hennessy, K., Atatre, M., Dreiser, J., Hu, E., Petroff, P. M., and Imamolu, A. (2005) Deterministic Coupling of Single Quantum Dots to Single Nanocavity Modes. *Science*, **308**, 1158–1161.

[57] Yoshie, T., Scherer, A., Hendrickson, J., Khitrova, G., Gibbs, H. M., Rupper, G., Ell, C., Shchekin, O. B., and Deppe, D. G. (2004) Vacuum rabi splitting with a single quantum dot in a photonic crystal nanocavity. *Nature*, **432**, 200–203.

[58] Reithmaier, J. P., Sek, G., Loffler, A., Hofmann, C., Kuhn, S., Reitzenstein, S., Keldysh, L. V., Kulakovskii, V. D., Reinecke, T. L., and Forchel, A. (2004) Strong coupling in a single quantum dot-semiconductor microcavity system. *Nature*, **432**, 197–200.

[59] Schuster, I., Kubanek, A., Fuhrmanek, A., Puppe, T., Pinkse, P. W. H., Murr, K., and Rempe, G. (2008) Nonlinear spectroscopy of photons bound to one atom. *Nature Mater.*, **4**, 382–385.

[60] Schneebeli, L., Kira, M., and Koch, S. W. (2008) Characterization of Strong Light-Matter Coupling in Semiconductor Quantum-Dot Microcavities via Photon-Statistics Spectroscopy. *Phys. Rev. Lett.*, **101**, 097401.

[61] Wiersig, J., et al. (2009) Direct observation of correlations between individual photon emission events of a microcavity laser. *Nature*, **460**, 245–249.

[62] Schneebeli, L., Kira, M., and Koch, S. W. (2009) Microscopic theory of squeezed-light emission in strong-coupling semiconductor quantum-dot systems. *Phys. Rev. A*, **80**, 033843.

[63] Carmele, A., Richter, M., Chow, W. W., and Knorr, A. (2010) Antibunching of Thermal Radiation by a Room-Temperature Phonon Bath: A Numerically Solvable Model for a Strongly Interacting Light-Matter-Reservoir System. *Phys. Rev. Lett.*, **104**, 156801.

[64] Reinhard, A., Volz, T., Winger, M., Badolato, A., Hennessy, K. J., Hu, E. L., and Imamoğlu, A. (2012) Strongly correlated photons on a chip. *Nature Photon.*, **6**, 93–96.

[65] Zeilinger, A. (1999) Experiment and the foundations of quantum physics. *Rev. Mod. Phys.*, **71**, 288–297.

[66] Englund, D., Faraon, A., Fushman, I., Stoltz, N., Petroff, P., and Vučković, J. (2007) Controlling cavity reflectivity with a single quantum dot. *Nature*, **450**, 857–861.

[67] Khitrova, G., Gibbs, H., Kira, M., Koch, S., and Scherer, A. (2006) Vacuum Rabi splitting in semiconductors. *Nature Phys.*, **2**, 81–90.

[68] Michler, P., Kiraz, A., Becher, C., Schoenfeld, W. V., Petroff, P. M., Zhang, L., Hu, E., and Imamoglu, A. (2000) A Quantum Dot Single-Photon Turnstile Device. *Science*, **290**, 2282–2285.

[69] Yuan, Z., Kardynal, B. E., Stevenson, R. M., Shields, A. J., Lobo, C. J., Cooper, K., Beattie, N. S., Ritchie, D. A., and Pepper, M. (2002) Electrically Driven Single-Photon Source. *Science*, **295**, 102–105.

[70] Press, D., Götzinger, S., Reitzenstein, S., Hofmann, C., Löffler, A., Kamp, M., Forchel, A., and Yamamoto, Y. (2007) Photon Antibunching from a Single Quantum-Dot-Microcavity System in the Strong Coupling Regime. *Phys. Rev. Lett.*, **98**, 117402.

[71] Kwiat, P. G., Mattle, K., Weinfurter, H., Zeilinger, A., Sergienko, A. V., and Shih, Y. (1995) New High-Intensity Source of Polarization-Entangled Photon Pairs. *Phys. Rev. Lett.*, **75**, 4337–4341.

[72] Akopian, N., Lindner, N. H., Poem, E., Berlatzky, Y., Avron, J., Gershoni, D., Gerardot, B. D., and Petroff, P. M. (2006) Entangled Photon Pairs from Semiconductor Quantum Dots. *Phys. Rev. Lett.*, **96**, 130501.

[73] Dousse, A., Suffczyński, J., Beveratos, A., Krebs, O., Lemaître, A., Sagnes, I., Bloch, J., Voisin, P., and Senellart, P. (2010) Ultrabright source of entangled photon pairs. *Nature*, **466**, 217–220.

[74] Bennett, C. H., Brassard, G., and Mermin, N. D. (1992) Quantum cryptography without Bells theorem. *Phys. Rev. Lett.*, **68**, 557–559.

[75] Bouwmeester, D., Pan, J.-W., Mattle, K., Eibl, M., Weinfurter, H., and Zeilinger, A. (1997) Experimental quantum teleportation. *Nature*, **390**, 575–579.

[76] Furusawa, A., Srensen, J. L., Braunstein, S. L., Fuchs, C. A., Kimble, H. J., and Polzik, E. S. (1998) Unconditional Quantum Teleportation. *Science*, **282**, 706–709.

[77] Jennewein, T., Simon, C., Weihs, G., Weinfurter, H., and Zeilinger, A. (2000) Quantum Cryptography with Entangled Photons. *Phys. Rev. Lett.*, **84**, 4729–4732.

[78] Tittel, W., Brendel, J., Zbinden, H., and Gisin, N. (2000) Quantum Cryptography Using Entangled Photons in Energy-Time Bell States. *Phys. Rev. Lett.*, **84**, 4737–4740.

[79] Awschalom, D. D., Bassett, L. C., Dzurak, A. S., Hu, E. L., and Petta, J. R. (2013) Quantum Spintronics: Engineering and Manipulating Atom-Like Spins in Semiconductors. *Science*, **339**, 1174–1179.

[80] Xie, Z. G., Götzinger, S., Fang, W., Cao, H., and Solomon, G. S. (2007) Influence of a Single Quantum Dot State on the Characteristics of a Microdisk Laser. *Phys. Rev. Lett.*, **98**, 117401.

[81] Walls, D. F. and Milburn, G. J. (2008) *Quantum Optics*. Springer-Verlag, New York, 2nd edn.

[82] Kira, M., Jahnke, F., Hoyer, W., and Koch, S. W. (1999) Quantum theory of spontaneous emission and coherent effects in semiconductor microstructures. *Prog. Quantum Electron.*, **23**, 189 – 279.

[83] Kira, M. and Koch, S. W. (2008) Cluster-expansion representation in quantum optics. *Phys. Rev. A*, **78**, 022102.

[84] Wyld Jr, H. and Fried, B. D. (1963) Quantum mechanical kinetic equations. *Ann. Phys.*, **23**, 374–389.

[85] Cizek, J. (1966) On the Correlation Problem in Atomic and Molecular Systems. Calculation of Wavefunction Components in Ursell-Type Expansion Using Quantum-Field Theoretical Methods. *J. Chem. Phys.*, **45**.

[86] Purvis III, G. D. and Bartlett, R. J. (1982) A full coupled-cluster singles and doubles model: The inclusion of disconnected triples. *J. Chem. Phys.*, **76**, 1910–1918.

[87] Fricke, J. (1996) Transport Equations Including Many-Particle Correlations for an Arbitrary Quantum System: A General Formalism. *Ann. Phys.*, **252**, 479 – 498.

[88] Usui, T. (1960) Excitations in a High Density Electron Gas. I. *Prog. Theor. Phys.*, **23**, 787–798.

[89] Jaynes, E. and Cummings, F. (1963) Comparison of quantum and semiclassical radiation theories with application to the beam maser. *Proc. IEEE*, **51**, 89 – 109.

[90] Kira, M. (2013) private communication.

[91] Kira, M. and Koch, S. W. (2004) Exciton-Population Inversion and Terahertz Gain in Semiconductors Excited to Resonance. *Phys. Rev. Lett.*, **93**, 076402.

[92] Zewail, A. H. (1988) Laser Femtochemistry. *Science*, **242**, 1645–1653.

[93] Steinmeyer, G., Sutter, D. H., Gallmann, L., Matuschek, N., and Keller, U. (1999) Frontiers in Ultrashort Pulse Generation: Pushing the Limits in Linear and Nonlinear Optics. *Science*, **286**, 1507–1512.

[94] Jones, D. J., Diddams, S. A., Ranka, J. K., Stentz, A., Windeler, R. S., Hall, J. L., and Cundiff, S. T. (2000) Carrier-Envelope Phase Control of Femtosecond Mode-Locked Lasers and Direct Optical Frequency Synthesis. *Science*, **288**, 635–639.

[95] Hentschel, M., et al. (2001) Attosecond metrology. *Nature Phys.*, **414**, 509–513.

[96] Sudarshan, E. C. G. (1963) Equivalence of Semiclassical and Quantum Mechanical Descriptions of Statistical Light Beams. *Phys. Rev. Lett.*, **10**, 277–279.

[97] Glauber, R. J. (1963) Coherent and incoherent states of the radiation field. *Phys. Rev.*, **131**, 2766–2788.

[98] Leo, K., Wegener, M., Shah, J., Chemla, D. S., Göbel, E. O., Damen, T. C., Schmitt-Rink, S., and Schäfer, W. (1990) Effects of coherent polarization interactions on time-resolved degenerate four-wave mixing. *Phys. Rev. Lett.*, **65**, 1340–1343.

[99] Weiss, S., Mycek, M.-A., Bigot, J.-Y., Schmitt-Rink, S., and Chemla, D. S. (1992) Collective effects in excitonic free induction decay: Do semiconductors and atoms emit coherent light in different ways? *Phys. Rev. Lett.*, **69**, 2685–2688.

[100] Chemla, D. and Shah, J. (2001) Many-body and correlation effects in semiconductors. *Nature*, **411**, 549–557.

[101] Kaindl, R. A., Carnahan, M. A., Hagele, D., Lovenich, R., and Chemla, D. S. (2003) Ultrafast terahertz probes of transient conducting and insulating phases in an electron-hole gas. *Nature*, **423**, 734–738.

[102] Turner, D. and Nelson, K. (2010) Coherent measurements of high-order electronic correlations in quantum wells. *Nature*, **466**, 1089–1092.

[103] Peyghambarian, N., Gibbs, H. M., Jewell, J. L., Antonetti, A., Migus, A., Hulin, D., and Mysyrowicz, A. (1984) Blue Shift of the Exciton Resonance due to Exciton-Exciton Interactions in a Multiple-Quantum-Well Structure. *Phys. Rev. Lett.*, **53**, 2433–2436.

[104] Khitrova, G., Gibbs, H. M., Jahnke, F., Kira, M., and Koch, S. W. (1999) Nonlinear optics of normal-mode-coupling semiconductor microcavities. *Rev. Mod. Phys.*, **71**, 1591–1639.

[105] Smith, R. P., Wahlstrand, J. K., Funk, A. C., Mirin, R. P., Cundiff, S. T., Steiner, J. T., Schafer, M., Kira, M., and Koch, S. W. (2010) Extraction of Many-Body Configurations from Nonlinear Absorption in Semiconductor Quantum Wells. *Phys. Rev. Lett.*, **104**, 247401.

[106] Li, X., Zhang, T., Borca, C. N., and Cundiff, S. T. (2006) Many-Body Interactions in Semiconductors Probed by Optical Two-Dimensional Fourier Transform Spectroscopy. *Phys. Rev. Lett.*, **96**, 057406.

[107] Siemens, M. E., Moody, G., Li, H., Bristow, A. D., and Cundiff, S. T. (2010) Resonance lineshapes in two-dimensional Fourier transform spectroscopy. *Opt. Express*, **18**, 17699–17708.

[108] Cundiff, S. T. (2012) Optical two-dimensional Fourier transform spectroscopy of semiconductor nanostructures. *J. Opt. Soc. Am. B*, **29**, A69–A81.

[109] Schmitt-Rink, S., Chemla, D. S., and Miller, D. A. B. (1985) Theory of transient excitonic optical nonlinearities in semiconductor quantum-well structures. *Phys. Rev. B*, **32**, 6601–6609.

[110] Fernández-Rossier, J., Tejedor, C., Muñoz, L., and Viña, L. (1996) Polarized interacting exciton gas in quantum wells and bulk semiconductors. *Phys. Rev. B*, **54**, 11582–11591.

[111] Rochat, G., Ciuti, C., Savona, V., Piermarocchi, C., Quattropani, A., and Schwendimann, P. (2000) Excitonic Bloch equations for a two-dimensional system of interacting excitons. *Phys. Rev. B*, **61**, 13856–13862.

[112] Barker, J. A. and Henderson, D. (1976) What is "liquid"? Understanding the states of matter. *Rev. Mod. Phys.*, **48**, 587–671.

[113] Sastry, S. and Angell, C. (2003) Liquid-liquid phase transition in supercooled silicon. *Nature Mater.*, **2**, 39–743.

[114] Kiraz, A., Michler, P., Becher, C., Gayral, B., Imamolu, A., Zhang, L., Hu, E., Schoenfeld, W. V., and Petroff, P. M. (2001) Cavity-quantum electrodynamics using a single InAs quantum dot in a microdisk structure. *Appl. Phys. Lett.*, **78**.

[115] Peter, E., Senellart, P., Martrou, D., Lemaitre, A., Hours, J., Gérard, J. M., and Bloch, J. (2005) Exciton-Photon Strong-Coupling Regime for a Single Quantum Dot Embedded in a Microcavity. *Phys. Rev. Lett.*, **95**, 067401.

[116] Sek, G., Hofmann, C., Reithmaier, J., Löffler, A., Reitzenstein, S., Kamp, M., Keldysh, L., Kulakovskii, V., Reinecke, T., and Forchel, A. (2006) Investigation of strong coupling between single quantum dot excitons and single photons in pillar microcavities. *Phys. E*, **32**, 471 – 475.

[117] Chu, Y., Mintairov, A., He, Y., Merz, J., Kalyuzhnyy, N., Lantratov, V., and Mintairov, S. (2009) Lasing of whispering-gallery modes in asymmetric waveguide GaInP micro-disks with InP quantum dots. *Phys. Lett. A*, **373**, 1185 – 1188.

[118] Chu, Y., Mintairov, A. M., He, Y., Merz, J. L., Kalugnyy, N. A., Lantratov, V. M., and Mintairov, S. A. (2011) Lasing of whispering-gallery modes in GaInP waveguide micro-discs and rings with InP quantum dots. *Phys. Status Solidi C*, **8**, 325–327.

[119] Tavis, M. and Cummings, F. W. (1968) Exact Solution for an N-Molecule-Radiation-Field Hamiltonian. *Phys. Rev.*, **170**, 379–384.

[120] Shore, B. W. and Knight, P. L. (1993) The Jaynes-Cummings Model. *J. Mod. Opt.*, **40**, 1195–1238.

[121] Lindblad, G. (1976) On the generators of quantum dynamical semigroups. *Commun. Math. Phys.*, **48**, 119–130.

[122] Dalibard, J., Castin, Y., and Mølmer, K. (1992) Wave-function approach to dissipative processes in quantum optics. *Phys. Rev. Lett.*, **68**, 580–583.

[123] Carmichael, H. J. (1993) Quantum trajectory theory for cascaded open systems. *Phys. Rev. Lett.*, **70**, 2273–2276.

[124] Kaluzny, Y., Goy, P., Gross, M., Raimond, J. M., and Haroche, S. (1983) Observation of Self-Induced Rabi Oscillations in Two-Level Atoms Excited Inside a Resonant Cavity: The Ringing Regime of Superradiance. *Phys. Rev. Lett.*, **51**, 1175–1178.

[125] Thompson, R. J., Rempe, G., and Kimble, H. J. (1992) Observation of normal-mode splitting for an atom in an optical cavity. *Phys. Rev. Lett.*, **68**, 1132–1135.

[126] Brune, M., Schmidt-Kaler, F., Maali, A., Dreyer, J., Hagley, E., Raimond, J. M., and Haroche, S. (1996) Quantum Rabi Oscillation: A Direct Test of Field Quantization in a Cavity. *Phys. Rev. Lett.*, **76**, 1800–1803.

[127] Raimond, J. M., Brune, M., and Haroche, S. (2001) Manipulating quantum entanglement with atoms and photons in a cavity. *Rev. Mod. Phys.*, **73**, 565–582.

[128] Riebe, M., et al. (2004) Deterministic quantum teleportation with atoms. *Nature*, **429**, 734–737.

[129] Barrett, M., et al. (2004) Deterministic quantum teleportation of atomic qubits. *Nature*, **429**, 737–739.

[130] Mootz, M. (2010) *Model Study of Quantum-Optical Spectroscopy in Dissipative Systems*. Diploma thesis, Philipps-Universität Marburg.

[131] Schwabl, F. (2006) *Statistical mechanics*. Springer-Verlag, 2. edn.

[132] Kira, M., Jahnke, F., and Koch, S. W. (1999) Quantum Theory of Secondary Emission in Optically Excited Semiconductor Quantum Wells. *Phys. Rev. Lett.*, **82**, 3544–3547.

[133] Schneebeli, L., Feldtmann, T., Kira, M., Koch, S. W., and Peyghambarian, N. (2010) Zeno-logic applications of semiconductor quantum dots. *Phys. Rev. A*, **81**, 053852.

[134] Eberly, J. H., Narozhny, N. B., and Sanchez-Mondragon, J. J. (1980) Periodic Spontaneous Collapse and Revival in a Simple Quantum Model. *Phys. Rev. Lett.*, **44**, 1323–1326.

[135] Rempe, G., Walther, H., and Klein, N. (1987) Observation of quantum collapse and revival in a one-atom maser. *Phys. Rev. Lett.*, **58**, 353–356.

Publications

Paper I

M. Mootz, M. Kira, and S. W. Koch
Sequential build-up of quantum-optical correlations
J. Opt. Soc. Am. B **29**, A17–A24 (2012)

Sequential build-up of quantum-optical correlations

M. Mootz,* M. Kira, and S. W. Koch

Department of Physics and Material Sciences Center, Philipps-University Marburg, Renthof 5, 35032 Marburg, Germany
**Corresponding author: martin.mootz@physik.uni-marburg.de*

Received September 30, 2011; revised November 22, 2011; accepted November 23, 2011;
posted November 23, 2011 (Doc. ID 155723); published January 25, 2012

The build-up dynamics of quantum-optical correlations in a Jaynes–Cummings model for semiconductor quantum-dot systems is characterized using the cluster-expansion scheme. Assuming an excitation with a coherent state source under strong- and weak-coupling conditions, it is found that higher-order correlations are sequentially generated. Even though the influence of dephasing hinders their development, significant correlations build up even in the presence of strong dissipation showing that quantum-spectroscopy studies are possible even in interacting many-body systems like semiconductors.

OCIS codes: 190.5970, 270.2500, 270.5580.

1. INTRODUCTION

Many of the central quantum-optical effects have either been suggested or measured using simple systems where an atom-like two-level system is strongly coupled with a single quantized light mode. In particular, one can then solve the exact wave-function dynamics for both light and matter degrees of freedom by using the Jaynes–Cummings model [1]. Such information has been vital in discovering photon antibunching [2,3], collapses and revivals of Rabi oscillations [4,5], squeezing of light [6], strong-coupling [7–10], and entanglement effects [11–13], few to mention.

Generally, there is no hope to obtain an equivalent level of information on the wave-function of an interacting many-body system because of the overwhelmingly large dimensionality of the problem. Besides the quantized light-matter coupling, many-body systems often exhibit a strong Coulomb interaction among the charged particles within the system. The full Coulomb and quantum-optical interactions can be successfully treated by applying the so-called cluster-expansion approach [14] that describes the quantum dynamics in terms of different C-particle correlations. Systematic approximations can be made by including all the correlations from singlets up to the C-particle level and solving the resulting closed set of equations. This approach has been applied to describe a great variety of many-body and quantum-optical effects in extended semiconductors [14–16] as well as quantum dots [17–19]. The cluster-expansion method has also been extended to describe quantum-optical fields in terms of clusters as an equivalent formulation for the density matrix [20].

In simple systems, the clearest quantum-optical effects are observed when the light-matter coupling is stronger than dissipative processes. Such strong-coupling conditions are difficult to realize in many-body systems. Nevertheless, [21] has demonstrated a new quantum-spectroscopy framework where the quantum fluctuations of light are applied to access desired many-body states, despite dissipation. It is important to know how and why quantum-optical effects can be measured even in the weak-coupling regime.

In this paper, we study this fundamental problem using a simple model based on a Jaynes–Cummings-type quantum-dot system [22,23]. In particular, since one can solve the full dynamics to all orders, we analyze how quantum-optical correlations develop in this system when dissipation is added. To characterize the build-up of quantum-optical correlations, we assume an uncorrelated light source provided by the coherent state which describes a perfect single-mode laser. We investigate the quantum state of light up to 14-particle correlations [20] and show that higher-order clusters are generated sequentially. We also show that the generation of quantum-optical correlations is hindered but not destroyed by dissipation. Especially, the higher-order correlations remain sensitive to changes in the dynamics of matter, which explains why quantum-spectroscopy measurements are possible in many-body systems. The analysis also yields insights how and when the cluster-expansion truncation can be applied to describe the relevant quantum dynamics.

2. QUANTUM-OPTICAL MODEL

To analyze the build-up of correlations, we use the simplest quantum-optical system provided by the well-known Jaynes-Cummings model. It describes a single quantized light mode coupled to a two-level system consisting of a ground state $|-\rangle$ and an excited state $|+\rangle$. The system Hamiltonian is

$$\hat{H}_{\mathrm{JC}} = \hbar\omega B^{\dagger}B + \hbar\omega_{21}\sigma_z - g(\sigma_- B^{\dagger} + \sigma_+ B), \tag{1}$$

where the operators σ_j are the usual Pauli spin matrices and g defines the strength of the light-matter coupling. The appearing $\sigma_{\pm} = \sigma_x \pm \mathrm{i}\sigma_y$ are the raising $(+)$ and lowering $(-)$ operators defining the polarization operator $\hat{P} \equiv \sigma_-$ of the two-level system dipole. The interaction part of $\hat{H}_{\mathrm{JC}}$ specifies the process where a single photon lifts the matter from the ground to the excited state $(\sigma_+ B)$ and the reverse case $(\sigma_- B^{\dagger})$.

The two-level system has a perfectly Fermionic nature because only a single occupation of the states is allowed. Besides, the polarization operator fulfills the Fermionic anticommutation relation

$$[\sigma_-, \sigma_-^{\dagger}]_+ = [\sigma_-, \sigma_+]_+ = 1. \tag{2}$$

A computation of the corresponding commutation relation yields

$$[\sigma_-, \sigma_+]_- = -2\sigma_z. \tag{3}$$

It is interesting to note that the system in the ground state shows an average Bosonic character where $\langle\sigma_z\rangle = -\frac{1}{2}$. All excitations create Fermionic contributions that increase with the excitation level.

To evaluate the dynamics of the quantum-optical correlations, we solve the time-evolution of the density matrix $\hat{\rho}$ which follows from the von Neumann equation [24]

$$i\hbar\frac{\partial}{\partial t}\hat{\rho} = [\hat{H}_{\mathrm{JC}}, \hat{\rho}]_-. \tag{4}$$

In the most realistic situations the system is influenced not only by optical interactions but also by its coupling to the outside world. Therefore, we include dissipation in our study by adding the Lindbladian [25],

$$i\hbar\frac{\partial}{\partial t}\hat{\rho} = [\hat{H}_{\mathrm{JC}}, \hat{\rho}]_- + i\gamma[2\hat{L}\hat{\rho}\hat{L}^\dagger - \hat{L}^\dagger\hat{L}\hat{\rho} - \hat{\rho}\hat{L}^\dagger\hat{L}], \tag{5}$$

to the von Neumann equation Eq. (4). The strength of dephasing is given by γ and $\hat{L}$ is an operator within the system studied. Choosing $\hat{L} = \sigma_-$, the population inversion relaxes toward its ground state which is characteristic for atomic systems. In this paper, however, we use $\hat{L} = \sigma_z$ which leads to the following additional contributions to the quantum dynamics of $\langle\sigma_z\rangle$ and $\langle\sigma_-\rangle$

$$i\hbar\frac{\partial}{\partial t}\langle\sigma_z\rangle|_{\mathrm{deph}} = 0, \qquad i\hbar\frac{\partial}{\partial t}\langle\sigma_-\rangle\Big|_{\mathrm{deph}} = -i\gamma\langle\sigma_-\rangle. \tag{6}$$

We can see that the dissipation mainly destroys the polarization whereas the population inversion is not directly influenced by dephasing. This model is appropriate for quantum-dot like systems whose polarization decay is much faster than the carrier relaxation.

The general density matrix for the quantized light-matter system is given by

$$\hat{\rho} = \sum_{n_1,n_2=0}^{N}\sum_{\sigma_1,\sigma_2=\pm}|\sigma_1\rangle|n_1\rangle\rho_{n_2,\sigma_2}^{n_1,\sigma_1}\langle n_2|\langle\sigma_2|, \tag{7}$$

where $|n\rangle$ is an n-photon Fock state. This is propagated numerically by truncating Eq. (7) up to Fock state $|N\rangle$ and solving Eq. (5) using the forth-order Runge–Kutta method. In the computations, we use $N = 30$.

2.A Quantum-Optical Hierarchy Problem

To explore the hierarchy problem, we study a generic interaction where a polarization operator $\hat{P}$ is coupled with a single light mode

$$\hat{H} = -g(\hat{P}\hat{B}^\dagger + \hat{P}^\dagger\hat{B}). \tag{8}$$

Since the cluster-expansion approach is based on deriving Heisenberg equation of motion for elementary operators, we compute the generic quantum dynamics for the interaction Eq. (8), resulting in

$$i\hbar\frac{\partial}{\partial t}\hat{B} = -g\hat{P}, \tag{9}$$

$$i\hbar\frac{\partial}{\partial t}\hat{P} = -g\hat{B}[\hat{P}, \hat{P}^\dagger]_-. \tag{10}$$

We note that the set of equations would be closed if the polarization has Bosonic statistics, i.e., $[\hat{P}, \hat{P}^\dagger]_- = 1$. However, for the Fermionic two-level system, we have

$$i\hbar\frac{\partial}{\partial t}\hat{B} = -g\hat{P}, \tag{11}$$

$$i\hbar\frac{\partial}{\partial t}\hat{P} = 2g\hat{P}_z\hat{B}, \tag{12}$$

where $\hat{P}_z = \sigma_z$ is the inversion operator based on Eq. (3). We see that the Fermionic $\hat{P}$ dynamics contains a new operator class $\hat{P}_z\hat{B}$ that is a product of single matter and photon operator. Deriving the equation of motion also for this new operator class, we quickly notice the generic hierarchy problem

$$i\hbar\frac{\partial}{\partial t}\langle N\rangle = F[\langle N\rangle] + \mathrm{Hi}[\langle N+1\rangle], \tag{13}$$

where $\langle N\rangle$ is an expectation-value with N operators. An analogous hierarchy is obtained in an electronic many-body system due to the Coulombic interaction. Therefore, solutions of the quantum-optical hierarchy problem provide qualitative insights how correlations build up in general. The specific form of the hierarchy problem is defined by functionals $F[\langle N\rangle]$ and $\mathrm{Hi}[\langle N+1\rangle]$.

The fundamental quantum-mechanical fluctuations of light, described by the quantum statistics, can be defined using equivalent representations such as the density matrix, the Wigner function, expectation values or correlations [26]. For a Bosonic $\hat{P}$, the hierarchy problem vanishes and Eqs. (9–10) can be solved analytically, yielding

$$I_K^J(t) \equiv \langle[\hat{B}^\dagger(t)]^J[\hat{B}(t)]^K\rangle = [c(t)]^{J+K}I_K^J(0), \qquad c(t) \equiv \cos(\omega_g t), \tag{14}$$

$$\tilde{I}_K^J(t) \equiv \langle[\hat{P}^\dagger(t)]^J[\hat{P}(t)]^K\rangle = e^{i\frac{\pi}{2}(K-J)}[s(t)]^{J+K}I_K^J(0), \quad s(t) \equiv \sin(\omega_g t), \tag{15}$$

for the expectation-value representation. Here, the temporal evolution is started at $t = 0$ and the transition rate is defined by the Rabi frequency $\omega_g = g/\hbar$. Especially, we find a strict conservation law

$$|I_K^J(t)|\frac{2}{J+K} + |\tilde{I}_K^J(t)|^{\frac{2}{J+K}} = |I_K^J(0)|^{\frac{2}{J+K}}, \tag{16}$$

between light and Bosonic matter, which means that the original quantum statistics of light is recycled unaltered between the light and matter states. This also means that the absolute value of $(J+K)$-operator expectation values is conserved within the order $J+K$, which eliminates the hierarchical

generation of higher-order contributions that is present in Eq. (13) for a nonbosonic $\hat{P}$.

For a Fermionic $\hat{P}$, the expectation values $\tilde{I}_K^J$ vanish for $J > 1$ or $K > 1$ due to the Pauli exclusion principle. Consequently, the coupling between Bosonic light and Fermionic matter can lead to strong modifications of the light's quantum statistics due to the large quantum-statistical difference between $\hat{B}$ and $\hat{P}$. As a result, the quantum statistics is not recycled anymore. Especially, the interaction with Fermionic matter distorts the overall optical quantum statistics leading to the generation of new quantum-optical correlations which is the main subject of this paper.

2.B. Cluster-Expansion Representation of Quantum-Optical Fields

The quantum statistics of any system can be described compactly in terms of clusters. Physically, the lowest order clusters are given by single-particle expectation values. The C-particle correlations $\Delta\langle C\rangle$ are defined by the difference between the C-particle expectation values and their systematic factorizations into all lower order clusters. Mathematically, $\Delta\langle 2\rangle$ corresponds to the variance while $\Delta\langle C \geq 3\rangle$ corresponds to higher-order culmulants of the distribution; for a textbook discussion, see [26].

We analyze the hierarchical generation of new correlations assuming that the two-level system is originally in its ground state and excited by light in the coherent state

$$|\beta\rangle = \sum_{n=0}^{\infty} e^{-\frac{|\beta|^2}{2}} \frac{\beta^n}{\sqrt{n!}} |n\rangle. \tag{17}$$

Initially, a coherent state is fully characterized by the displacement β because its quantum statistics,

$$I_K^J(0) = [\beta^\star]^J \beta^K, \tag{18}$$

is defined exactly by a classical factorization where the operators are simply replaced by the complex-valued amplitude $\beta \equiv \langle B\rangle$. In a cluster-expansion sense, coherent states are described by single-particle correlations, i.e. singlets $\langle B\rangle$, while all higher-order correlations vanish. All quantum-statistical modifications due to the light-matter interaction are then directly observable in the time-evolution of the light's quantum statistics I_K^J. To reveal the detailed correlation changes, we apply the cluster-expansion representation [20] that can be implemented with the following pragmatic steps: We first compute expectation values

$$\begin{aligned} I_K^J \equiv \langle (B^+)^J B^K\rangle &= \mathrm{Tr}[\hat{\rho}(B^+)^J B^K] \\ &= \sum_{n=0}^{\infty} \sum_{\sigma=\pm} \frac{\sqrt{(n+J)!(n+K)!}}{n!} \rho_{n+J,\sigma}^{n+K,\sigma}. \end{aligned} \tag{19}$$

As shown in [20], the connection of the cluster-expansion with I_K^J follows from the normally ordered characteristic function χ_N and the correlation-generating function ξ_N

$$\chi_N(\beta) \equiv \langle e^{\beta B^+} e^{-\beta^\star B}\rangle = \sum_{J,K=0}^{\infty} \frac{\beta^J(-\beta^\star)^K}{J!K!} I_K^J, \tag{20}$$

$$\xi_N(\beta) = \sum_{J,K=0}^{\infty} \frac{\beta^J(-\beta^\star)^K}{J!K!} \Delta I_K^J = \ln[\chi_N(\beta)]. \tag{21}$$

Finally, the $(J+K)$-particle clusters, ΔI_K^J are obtained via the differentiation

$$\Delta I_K^J = \left[(-1)^K \frac{\partial^{J+K}}{\partial\beta^J \partial(\beta^\star)^K} \xi_N(\beta)\right]_{\beta=0}. \tag{22}$$

In our forthcoming investigations, we denote the total cluster number $(J+K)$ by $C \equiv (J+K)$. As a generalization of the presented formalism, Eqs. (19–22) can also be extended to multimode light [20].

In general, the numerical computation of the expectation values Eq. (19) is straightforward whereas the evaluation of high-order correlations with the help of Eq. (22) is challenging because of the large number of elements included. For example, the computation of ΔI_{10}^{10} follows from 6×10^4 factorizations and the number of factorizations increases almost exponentially. In this paper, we have studied the correlations up to $C = 14$. The explicit expressions for the correlations ΔI_K^J with $J + K \leq 3$ are given in Appendix A.

3. CORRELATION DYNAMICS WITHOUT DISSIPATION

To first study the quantum-optical effects in the purest strong-coupling regime [7–10], we set the dissipation to zero and excite the two-level system resonantly ($\omega = \omega_{21}$) with a coherent state source having $\langle B^\dagger B\rangle = |\beta|^2 = 10$ photons on average. To gain some insights in the matter dynamics, we first analyze the time-evolution of the population inversion $\langle\sigma_z\rangle$. The result is shown in Fig. 1 on (a) linear and (b) logarithmic time scale. The dynamics of $\langle\sigma_z\rangle$ shows the well-known collapse and revival sequence [27] which has been experimentally verified [28].

In Fig. 1, the time is given in units of the Rabi period [29]

$$T_{\mathrm{Rabi}} = \frac{\pi}{g|\beta|}. \tag{23}$$

The first oscillation maxima and minima of $\langle\sigma_z\rangle$ are marked by vertical dashed and solid lines, respectively. The shaded area indicates the collapse region. The revival is centered at [29]

$$T_{\mathrm{rev}} = \frac{2\pi|\beta|}{g}. \tag{24}$$

The collapse-revival behavior is a genuine quantum effect because semiclassical calculations produce persistent oscillations at all times. Since the Fermionic signatures of matter are strongest as $\langle\sigma_z\rangle$ approaches $+1/2$ (vertical dashed lines) according to Eq. (3), we expect strong modifications of the light's quantum statistics at those times.

As a next step, we analyze how correlated clusters are generated under strong-coupling conditions. The physical relevance of correlations can be determined by analyzing the normalized correlations

$$\Delta\bar{I}_K^J \equiv \frac{\Delta I_K^J}{J!K!|\beta|^{J+K}}, \tag{25}$$

i.e. the Taylor-expansion coefficients in Eq. (21), normalized by the corresponding classical value $|\beta|^{J+K}$. In addition, we define

$$\Delta I_C^{\mathrm{all}} = \sum_{J=0}^{C} |\Delta \bar{I}_{C-J}^{J}|, \tag{26}$$

which are collective C-particle correlations because they contain all different C-particle correlations. In Fig. 1, the dynamics of $\Delta I_C^{\mathrm{all}}$ is presented on (c) a semilogarithmic and (d) a double-logarithmic scale for $C = 1$ up to $C = 4$. We notice at early times $t < T_{\mathrm{Rabi}}/2$ (up to the first dashed vertical line in Fig. 1) that the singlets dominate the quantum statistics whereas the other correlations build up *sequentially*. In other words, the $(C+1)$-particle correlation is generated only after the C-particle correlation already exists. In this regime, one can efficiently apply the cluster-expansion to describe the full quantum dynamics in terms of few lowest clusters, which simplifies the numerical effort considerably.

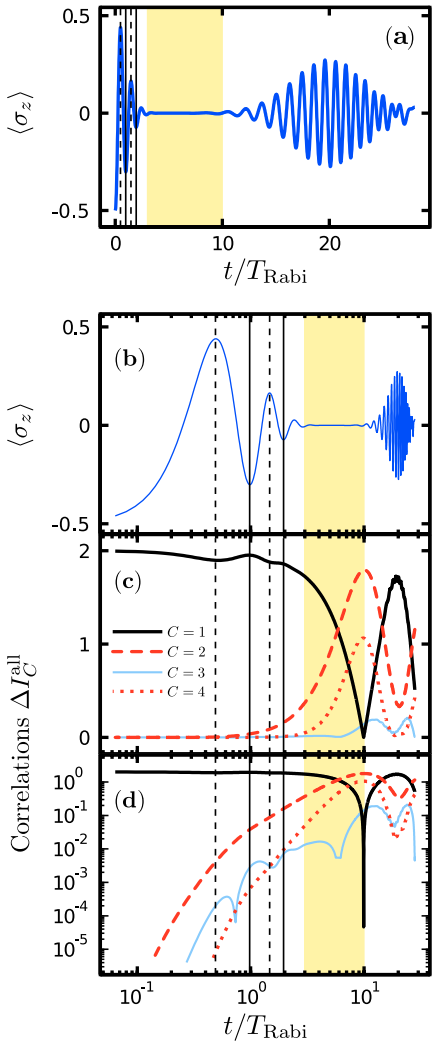

Fig. 1. (Color online) Dynamics of quantum statistics without dissipation. The time-evolution of the population inversion $\langle\sigma_z\rangle$ is presented in (a) linear and (b) semilogarithmic time scale. The corresponding dynamics of the collective C-particle correlations $\Delta I_C^{\mathrm{all}}$ is shown for $C = 1$ up to $C = 4$ in (c) semilogarithmic and (d) double-logarithmic scale. The times of interest are marked with vertical dashed and solid lines. The shaded area displays the collapse region.

However, the build-up of correlations remains fully sequential only up to about $t = 0.7\ T_{\mathrm{Rabi}}$ whereas some crossover between the correlations are generated around $t = 3\ T_{\mathrm{Rabi}}/4$. This observation can be related to the Fermion nature of the matter excitations when $\langle\sigma_z\rangle$ evolves through its inversion point, modifying the quantum-statistical transfer between Bosonic light and Fermionic matter. Even though the effect is initially very small, it develops to a strongly nonsequential form at later times.

For the current example, the system needs around 6 Rabi flops before higher-order clusters take over the singlets. This happens in the collapse region, $t \in [3, 10]T_{\mathrm{Rabi}}$ (shaded area) where $\langle\sigma_z\rangle$ approaches zero with the rate g. In the collapse region, the quantum-optical hierarchy produces correlations so rapidly that high-order correlations eventually dominate the quantum statistics. In this regime, the even correlations $2C$ are much larger than the odd ones $2C+1$ and the Jaynes–Cummings system can generate very high-order correlations. At the revival time $t = 20\ T_{\mathrm{Rabi}}$, the correlations return back to small values indicating that the system enters a regime of more classical behavior. The correlation order is restored resulting again in a sequential build-up.

Altogether, we see that even one revival cycle is enough to generate very high-order correlations in the strong-coupling regime. In particular, the recycling of the quantum statistics between the Boson and Fermion degrees of freedom triggers growth of high-order correlations and saturation of low-order correlations such that the original light's quantum statistics becomes strongly modified. As a general rule of thumb, the cluster-expansion must include the dominant $\Delta \bar{I}_K^J$ contributions to describe the quantum statistics accurately. Based on Fig. 1, one needs many clusters to describe the collapse-revival cycle correctly for nondissipative systems. The work in [22,23,30–32] has developed the cluster-expansion further to handle this complexity. Only at early times of the evolution and around the revival time low number of clusters, i.e. $C \leq 4$, capture the essential features of quantum-statistical changes generated.

4. CORRELATIONS DYNAMICS WITH DISSIPATION

It is rather natural that the generation of quantum-optical correlations becomes weaker when the system experiences dissipation. When dephasing becomes large enough, the Jaynes–Cummings system goes from strong-to-weak-coupling regime where the two-level system properties can be described semiclassically [33]. To test the effect of dissipation, we solve the coherent state excitation of Sec. 3 including the Lindblad from Eq. (5) with dephasing $\gamma = g$ that is commonly considered as the strong-to-weak-coupling border. Examples of the results are plotted in Fig. 2. We see that $\langle\sigma_z\rangle$ does not contain obvious quantum features because it simply decays to zero. Especially, the revival is washed out, indicating the typical weak-coupling behavior.

However, even under these conditions some amount of photon correlations are generated especially for times $t \in [10, 25]T_{\mathrm{Rabi}}$. If we compare even $(2C)$- and odd $(2C+1)$-particle correlations separately, we see that higher-order correlations build up after the lower ones emerge. Especially, the

decay of odd correlations at late times is a direct consequence of the dephasing whereas even correlations can exist even when the system reaches a steady state. Therefore, only a group of even or odd correlations maintain a sequential order during the whole evolution. As a result, quantum-optical effects up to C-particle correlations can be efficiently described by the cluster-expansion truncation made at the level of $(C+1)$-particle correlations when the system is in the weak-coupling regime. Since many-body systems contain some dissipation, this observation is clearly connected with the capability of the cluster-expansion truncation to describe the many-body dynamics accurately [14].

It is interesting to notice that the light-matter interaction can generate appreciable quantum-optical correlations even in the weak-coupling regime. To quantify the effect of dephasing more carefully, we define the maximum of correlations up to the first revival time

$$\Delta I_C^{\max} \equiv \max_{t\in[0,T_{\rm rev}]} [\Delta I_C^{\rm all}(t)]. \tag{27}$$

Figure 3(a) presents $\Delta I_C^{\max}$ as function of the cluster number C for the even $(2C)$-particle correlations without dephasing (squares) and a dephasing of $\gamma = g$ (circles). Without dissipation, $\Delta I_C^{\max}$ is dominated by terms beyond the 14-photon correlations. Therefore, strong-coupling conditions indeed generate strong quantum-optical correlations. With dissipation, $\Delta I_C^{\max}$ decays monotonously. However, light-matter interaction still generates appreciable amount of high-order correlations that is detectable.

Similar dissipation features as those investigated here, naturally exist in semiconductor many-body systems because any excited state is coupled to a continuum of other many-body states. Also in these systems, the correlations build up sequentially and quantum-optical effects can be sensitively monitored through correlation measurements. For example, [22] shows that strong-coupling features can be detected in photon-photon correlations even when the photon intensity shows only weak-coupling features. This principle works also in the opposite direction. One can apply quantum fluctuations of light to generate and monitor distinct many-body states in solids. The concept of quantum-spectroscopy was predicted in [34] and experimentally verified in [21] using semiconductor quantum wells.

To quantify how correlation effects survive dephasing, Fig. 3(b) plots $\Delta I_C^{\max}$ as function of dephasing for $C = 2$ (solid line), $C = 3$ (dashed line), and $C = 4$ (dotted line). As expected, the correlations decay as the dephasing is made larger. However, $\Delta I_C^{\max}$ decays fast only up to $\gamma = 0.5g$ while it decreases only weakly for $\gamma > g$ (shaded area), making quantum-optical effects relatively strong also in the weak-couping regime. This result corroborates that quantum-optical spectroscopy can be applied even when dissipative processes prevent strong-coupling, which suggests that also many-body systems possess intriguing quantum-optical effects.

5. STEADY STATE

As discussed in Sec. 4, the system evolves toward a steady state when dissipation is present. As shown in Appendix B, the corresponding density matrix becomes

$$\hat{\rho}_{\rm steady} = \frac{1}{2}\sum_{n=0}^{\infty} (|n\rangle|-\rangle\rho^{\rm ini}_{n,n}\langle -|\langle n| + |n\rangle|+\rangle\rho^{\rm ini}_{n+1,n+1}\langle +|\langle n|), \tag{28}$$

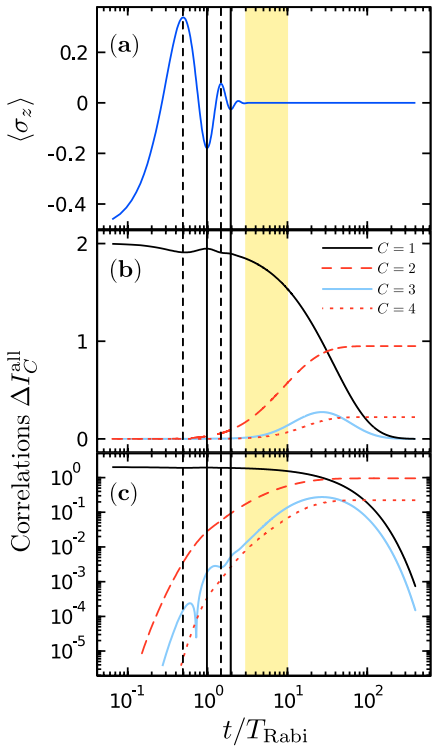

Fig. 2. (Color online) Dynamics of quantum statistics with dissipation. Same plots as in Fig. 1(b–d) but now with a dephasing of $\gamma = g$.

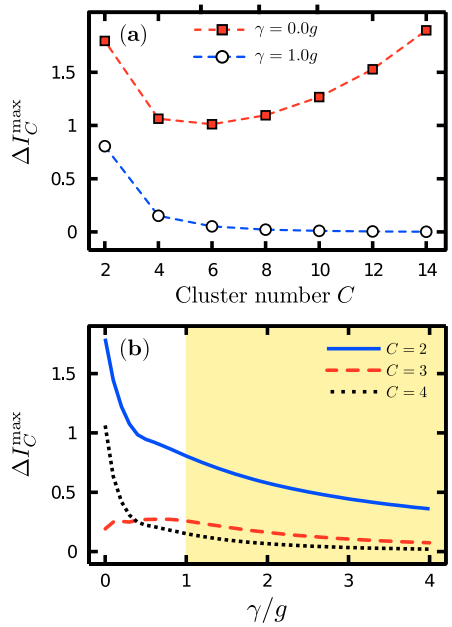

Fig. 3. (Color online) Effect of dissipation on build-up of correlations. (a) The maximum of correlations up to the first revival time $\Delta I_C^{\max}$ is plotted as function of the cluster number C for the even $(2C)$-particle correlations without dephasing (squares) and a dephasing of $\gamma = g$ (circles). The dashed lines are a guide to the eye. (b) The same quantity is presented as function of γ for $C = 2$ (solid line), $C = 3$ (dashed line), and $C = 4$ (dotted line). The shaded area indicates the weak-coupling regime.

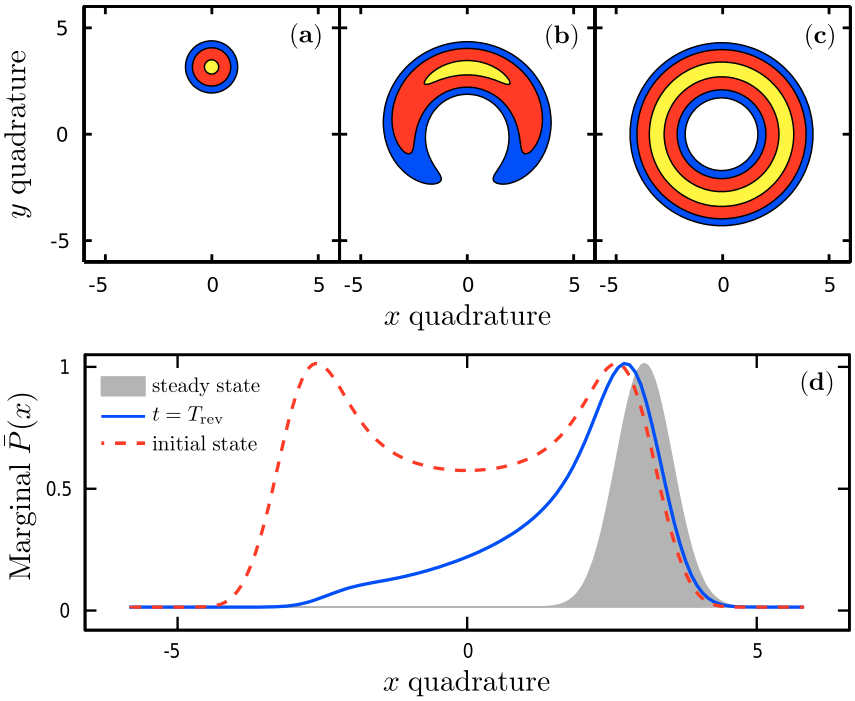

Fig. 4. (Color online) Evolution of light's quantum statistics toward the steady state. The Wigner function of light is shown at (a) the initial time, (b) an intermediate time ($t = T_{\rm rev}$), and (c) the final time. The contour lines are defined at 0.05, 0.2, and 0.8 normalized to the peak height of $W(x, y)$. A dephasing of $\gamma = g$ has been used. (d) The corresponding scaled marginal distributions $\bar{P}(x) = P(x)/\max[P(x)]$.

$$\hat{\rho}^{\rm light}_{\rm steady} \equiv {\rm Tr}_{\rm 2LS}[\hat{\rho}_{\rm steady}] = \sum_{n=0}^{\infty} |n\rangle S_n \langle n|, \qquad S_n \equiv \frac{1}{2}(\rho^{\rm ini}_{n,n} + \rho^{\rm ini}_{n+1,n+1}), \tag{29}$$

when $\hat{L} = \sigma_z$ is used in Eq. (5). For the coherent state, the reduced density matrix of the quantized light field is given by

$$\hat{\rho}^{\rm light}_{\rm steady} = \sum_{n=0}^{\infty} |n\rangle S_n^{|\beta\rangle} \langle n|, \qquad S_n^{|\beta\rangle} = \frac{1}{2}\left(1 + \frac{|\beta|^2}{n+1}\right)\frac{|\beta|^{2n}}{n!} e^{-|\beta|^2}, \tag{30}$$

which approaches the density matrix of a phase-randomized coherent state

$$\hat{\rho}^{\rm light}_{\rm rand} = \sum_{n=0}^{\infty} |n\rangle S_n^{\rm rand} \langle n|, \qquad S_n^{\rm rand} = \frac{|\beta|^{2n}}{n!} e^{-|\beta|^2}. \tag{31}$$

When $|\beta|$ becomes large enough, the actual difference of Eq. (30) and Eq. (31) scales as $1/|\beta|$.

To illustrate the dynamical evolution toward equilibrium, we visualize the quantum statistics at different times using the Wigner function $W(x, y)$. Figure 4 shows $W(x, y)$ at (a) the initial time, (b) an intermediate time ($t = T_{\rm rev}$), and (c) the final time for a dephasing of $\gamma = g$. The corresponding scaled marginal distributions $\bar{P}(x) = P(x)/\max[P(x)]$ are plotted in frame (d). We see that the original coherent state is a well-localized state in phase. As the scattering becomes important, the phase of $W(x, y)$ starts to diffuse around a ring such that the final state has a donut shape. The corresponding marginal distribution evolves nontrivially toward a double-peaked curve. The dissipation does not, however, destroy all quantum-optical aspects. For example, Eq. (28) shows that the steady state depends on the quantum statistics of the source. At the same time, the diffusion is accompanied with a sequential build-up of quantum-optical correlations generated by the light-matter interactions as shown in Figs. 2 and 3. Because of these two factors, the quantum dynamics of weak-coupling systems still contains detectable quantum-optical correlations.

6. CONCLUSIONS

We have applied the cluster-expansion scheme to characterize the quantum-optical hierarchy problem arising from the Fermionic properties of matter using a simple Jaynes–Cummings model for a quantum-dot system. The dynamics of the appearing quantum-optical correlations has been investigated in the strong- and weak-coupling regime excited by a coherent state source. Our results show that the correlated clusters build up sequentially which allows for a systematic truncation of the infinite hierarchy when the system has dissipative coupling. Since dissipation can be understood as a general many-body effect, one can understand the qualitative nature of many-body quantum optics through the simple model used.

Only under strong-coupling conditions the light-matter interaction generates very high-order correlations. Therefore, the cluster-expansion truncation can be applied efficiently when the system has dissipation or when matter is a many-body system. Nonetheless, even in the weak-coupling regime appreciable quantum-optical correlations are generated through the light-matter coupling. Consequently, quantum-optical investigations are possible also for systems with dissipation and/or many-body interactions. Hence, our work suggests that quantum-spectroscopy measurements can be applied to study novel phenomena in a broad range of systems.

APPENDIX A

The explicit expressions for the quantum-optical correlations are listed from ($C = 1$)- up to ($C = 3$)-particle correlations:

$$\Delta I^1_0 = I^1_0, \qquad \Delta I^0_1 = [\Delta I^1_0]^\star, \tag{A1}$$

$$\Delta I_0^2 = I_0^2 - (I_0^1)^2, \qquad \Delta I_2^0 = [\Delta I_0^2]^\star, \tag{A2}$$

$$\Delta I_1^1 = I_1^1 - I_0^1 I_1^0, \tag{A3}$$

$$\Delta I_0^3 = I_3^0 - 3I_1^0 I_2^0 + 2(I_1^0)^3, \qquad \Delta I_3^0 = [\Delta I_0^3]^\star, \tag{A4}$$

$$\Delta I_1^2 = I_1^2 - I_1^0 I_0^2 - 2I_0^1 I_1^1 + 2I_1^0 (I_0^1)^2, \qquad \Delta I_2^1 = [\Delta I_1^2]^\star. \tag{A5}$$

These are obtained by evaluating Eq. (22).

APPENDIX B

In this appendix, we derive the density matrix of the steady state. Starting from Eq. (5), we find a closed set of four coupled differential equations:

$$\frac{\partial}{\partial t}\rho_{n_2,-}^{n_1,-} = -i\frac{g}{\hbar}\left(\sqrt{n_1}\rho_{n_2,-}^{n_1-1,+} - \sqrt{n_2}\rho_{n_2-1,+}^{n_1,-}\right), \tag{B1}$$

$$\frac{\partial}{\partial t}\rho_{n_2,-}^{n_1-1,+} = -i\frac{g}{\hbar}\left(\sqrt{n_1}\rho_{n_2,-}^{n_1,-} - \sqrt{n_2}\rho_{n_2-1,+}^{n_1-1,+}\right) - \frac{\gamma}{\hbar}\rho_{n_2,-}^{n_1-1,+}, \tag{B2}$$

$$\frac{\partial}{\partial t}\rho_{n_2-1,+}^{n_1,-} = -i\frac{g}{\hbar}\left(\sqrt{n_1}\rho_{n_2-1,+}^{n_1-1,+} - \sqrt{n_2}\rho_{n_2,-}^{n_1,-}\right) - \frac{\gamma}{\hbar}\rho_{n_2-1,+}^{n_1,-}, \tag{B3}$$

$$\frac{\partial}{\partial t}\rho_{n_2-1,+}^{n_1-1,+} = -i\frac{g}{\hbar}\left(\sqrt{n_1}\rho_{n_2-1,+}^{n_1,-} - \sqrt{n_2}\rho_{n_2,-}^{n_1-1,+}\right). \tag{B4}$$

As initial condition we assume that a light field with quantum statistics $\rho_{n_1,n_2}^{\mathrm{ini}}$ excites an unexcited two-level system

$$\begin{aligned}&\rho_{n_2,-}^{n_1,-}(t=0) = \rho_{n1,n_2}^{\mathrm{ini}},\\ &\rho_{n_2,+}^{n_1,+}(t=0) = \rho_{n_2,+}^{n_1,-}(t=0) = \rho_{n_2,-}^{n_1,+}(t=0) = 0.\end{aligned} \tag{B5}$$

The differential equations Eqs. (B.1–B.4) together with the initial condition Eq. (B.5) can be solved analytically. A straightforward calculation eventually yields

$$\begin{aligned}\rho_{n_2,-}^{n_1,-}(t) = &\frac{e^{-\frac{\gamma t}{2\hbar}}}{4\Gamma^-_{n_1,n_2}\Gamma^+_{n_1,n_2}}\rho_{n_1,n_2}^{\mathrm{ini}}\\ &\times\left\{\Gamma^-_{n_1,n_2}\left[(\gamma+\Gamma^+_{n_1,n_2})e^{\frac{\Gamma^+_{n_1,n_2}t}{2\hbar}} - (\gamma-\Gamma^+_{n_1,n_2})e^{-\frac{\Gamma^+_{n_1,n_2}t}{2\hbar}}\right]\right.\\ &\left.+\Gamma^+_{n_1,n_2}\left[(\gamma+\Gamma^-_{n_1,n_2})e^{\frac{\Gamma^-_{n_1,n_2}t}{2\hbar}} - (\gamma-\Gamma^-_{n_1,n_2})e^{-\frac{\Gamma^-_{n_1,n_2}t}{2\hbar}}\right]\right\},\end{aligned} \tag{B6}$$

$$\begin{aligned}\rho_{n_2,-}^{n_1,+}(t) = &\frac{ige^{-\frac{\gamma t}{2\hbar}}}{2\Gamma^-_{n_1+1,n_2}\Gamma^+_{n_1+1,n_2}}\rho_{n_1+1,n_2}^{\mathrm{ini}}\\ &\times\left\{\Gamma^-_{n_1+1,n_2}\left[\left(\sqrt{n_1+1}-\sqrt{n_2}\right)e^{-\frac{\Gamma^+_{n_1+1,n_2}t}{2\hbar}}\right.\right.\\ &\left.-\left(\sqrt{n_1+1}-\sqrt{n_2}\right)e^{\frac{\Gamma^+_{n_1+1,n_2}t}{2\hbar}}\right]\\ &+\Gamma^+_{n_1+1,n_2}\left[\left(\sqrt{n_1+1}+\sqrt{n_2}\right)e^{-\frac{\Gamma^-_{n_1+1,n_2}t}{2\hbar}}\right.\\ &\left.\left.-\left(\sqrt{n_1+1}+\sqrt{n_2}\right)e^{\frac{\Gamma^-_{n_1+1,n_2}t}{2\hbar}}\right]\right\},\end{aligned} \tag{B7}$$

$$\begin{aligned}\rho_{n_2,+}^{n_1,-}(t) = &\frac{ige^{-\frac{\gamma t}{2\hbar}}}{2\Gamma^-_{n_1,n_2+1}\Gamma^+_{n_1,n_2+1}}\rho_{n_1,n_2+1}^{\mathrm{ini}}\\ &\times\left\{\Gamma^-_{n_1,n_2+1}\left[\left(\sqrt{n_1}-\sqrt{n_2+1}\right)e^{-\frac{\Gamma^+_{n_1,n_2+1}t}{2\hbar}}\right.\right.\\ &\left.-\left(\sqrt{n_1}-\sqrt{n_2+1}\right)e^{\frac{\Gamma^+_{n_1,n_2+1}t}{2\hbar}}\right]\\ &-\Gamma^+_{n_1,n_2+1}\left[\left(\sqrt{n_1}+\sqrt{n_2+1}\right)e^{-\frac{\Gamma^-_{n_1,n_2+1}t}{2\hbar}}\right.\\ &\left.\left.-\left(\sqrt{n_1}+\sqrt{n_2+1}\right)e^{\frac{\Gamma^-_{n_1,n_2+1}t}{2\hbar}}\right]\right\},\end{aligned} \tag{B8}$$

$$\begin{aligned}\rho_{n_2,+}^{n_1,+}(t) = &\frac{e^{-\frac{\gamma t}{2\hbar}}}{4\Gamma^-_{n_1+1,n_2+1}\Gamma^+_{n_1+1,n_2+1}}\rho_{n_1+1,n_2+1}^{\mathrm{ini}}\\ &\times\left\{\Gamma^-_{n_1+1,n_2+1}\left[(\gamma+\Gamma^+_{n_1+1,n_2+1})e^{\frac{\Gamma^+_{n_1+1,n_2+1}t}{2\hbar}}\right.\right.\\ &\left.-(\gamma-\Gamma^+_{n_1+1,n_2+1})e^{-\frac{\Gamma^+_{n_1+1,n_2+1}t}{2\hbar}}\right]\\ &+\Gamma^+_{n_1+1,n_2+1}\left[(\gamma-\Gamma^-_{n_1+1,n_2+1})e^{\frac{\Gamma^-_{n_1+1,n_2+1}t}{2\hbar}}\right.\\ &\left.\left.-(\gamma+\Gamma^-_{n_1+1,n_2+1})e^{-\frac{\Gamma^-_{n_1+1,n_2+1}t}{2\hbar}}\right]\right\},\end{aligned} \tag{B9}$$

where we have identified

$$\Gamma^\pm_{n_1,n_2} \equiv \left[\gamma^2 - 4g^2\left(\sqrt{n_1}\mp\sqrt{n_2}\right)^2\right]^{1/2}. \tag{B10}$$

Performing the steady state limit $t\to\infty$ leads to

$$\lim_{t\to\infty}\rho_{n_2,-}^{n_1,-}(t) = \frac{\delta_{n_1,n_2}}{2}\rho_{n_1,n_2}^{\mathrm{ini}}, \tag{B11}$$

$$\lim_{t\to\infty}\rho_{n_2,-}^{n_1,+}(t) = \lim_{t\to\infty}\rho_{n_2,+}^{n_1,-}(t) = 0, \tag{B12}$$

$$\lim_{t\to\infty}\rho_{n_2,+}^{n_1,+}(t) = \frac{\delta_{n_1,n_2}}{2}\rho_{n_1+1,n_2+1}^{\mathrm{ini}}. \tag{B13}$$

As a result, the density matrix of the steady state can be written as

$$\hat{\rho}_{\mathrm{steady}} = \frac{1}{2}\sum_{n=0}^{\infty}(|n\rangle|-\rangle\rho_{n,n}^{\mathrm{ini}}\langle-|\langle n| + |n\rangle|+\rangle\rho_{n+1,n+1}^{\mathrm{ini}}\langle+|\langle n|). \tag{B14}$$

The corresponding reduced density matrix of the quantized light field is given by

$$\begin{aligned}&\hat{\rho}_{\mathrm{steady}}^{\mathrm{light}} \equiv \mathrm{Tr}_{2\mathrm{LS}}[\hat{\rho}_{\mathrm{steady}}] = \sum_{n=0}^{\infty}|n\rangle S_n\langle n|,\\ &S_n \equiv \frac{1}{2}(\rho_{n,n}^{\mathrm{ini}} + \rho_{n+1,n+1}^{\mathrm{ini}}).\end{aligned} \tag{B15}$$

REFERENCES

1. E. Jaynes and F. Cummings, "Comparison of quantum and semiclassical radiation theories with application to the beam maser," Proc. IEEE **51**, 89–109 (1963).
2. H. J. Kimble, M. Dagenais, and L. Mandel, "Photon antibunching in resonance fluorescence," Phys. Rev. Lett. **39**, 691–695 (1977).
3. P. Michler, A. Kiraz, C. Becher, W. V. Schoenfeld, P. M. Petroff, L. Zhang, E. Hu, and A. Imamoglu, "A quantum dot single-photon turnstile device," Science **290**, 2282–2285 (2000).
4. J. H. Eberly, N. B. Narozhny, and J. J. Sanchez-Mondragon, "Periodic spontaneous collapse and revival in a simple quantum model," Phys. Rev. Lett. **44**, 1323–1326 (1980).
5. G. Rempe, H. Walther, and N. Klein, "Observation of quantum collapse and revival in a one-atom maser," Phys. Rev. Lett. **58**, 353–356 (1987).
6. H. J. Carmichael, "Photon antibunching and squeezing for a single atom in a resonant cavity," Phys. Rev. Lett. **55**, 2790–2793 (1985).
7. M. Brune, F. Schmidt-Kaler, A. Maali, J. Dreyer, E. Hagley, J. M. Raimond, and S. Haroche, "Quantum Rabi oscillation: A direct test of field quantization in a cavity," Phys. Rev. Lett. **76**, 1800–1803 (1996).
8. J. P. Reithmaier, G. Sek, A. Loffler, C. Hofmann, S. Kuhn, S. Reitzenstein, L. V. Keldysh, V. D. Kulakovskii, T. L. Reinecke, and A. Forchel, "Strong coupling in a single quantum dot-semiconductor microcavity system," Nature **432**, 197–200 (2004).
9. T. Yoshie, A. Scherer, J. Hendrickson, G. Khitrova, H. M. Gibbs, G. Rupper, C. Ell, O. B. Shchekin, and D. G. Deppe, "Vacuum Rabi splitting with a single quantum dot in a photonic crystal nanocavity," Nature **432**, 200–203 (2004).
10. I. Schuster, A. Kubanek, A. Fuhrmanek, T. Puppe, P. W. H. Pinkse, K. Murr, and G. Rempe, "Nonlinear spectroscopy of photons bound to one atom," Nature Mater. **4**, 382–385 (2008).
11. P. G. Kwiat, K. Mattle, H. Weinfurter, A. Zeilinger, A. V. Sergienko, and Y. Shih, "New high-intensity source of polarization-entangled photon pairs," Phys. Rev. Lett. **75**, 4337–4341 (1995).
12. A. Rauschenbeutel, G. Nogues, S. Osnaghi, P. Bertet, M. Brune, J.-M. Raimond, and S. Haroche, "Step-by-step engineered multiparticle entanglement," Science **288**, 2024–2028 (2000).
13. W. Hoyer, M. Kira, S. W. Koch, H. Stolz, S. Mosor, J. Sweet, C. Ell, G. Khitrova, and H. M. Gibbs, "Entanglement between a photon and a quantum well," Phys. Rev. Lett. **93**, 067401 (2004).
14. M. Kira and S. W. Koch, "Many-body correlations and excitonic effects in semiconductor spectroscopy," Prog. Quantum Electron. **30**, 155–296 (2006).
15. G. Khitrova, H. M. Gibbs, F. Jahnke, M. Kira, and S. W. Koch, "Nonlinear optics of normal-mode-coupling semiconductor microcavities," Rev. Mod. Phys. **71**, 1591–1639 (1999).
16. S. W. Koch, M. Kira, G. Khitrova, and H. M. Gibbs, "Semiconductor excitons in new light," Nature Mater. **5**, 523–531 (2006).
17. T. Feldtmann, L. Schneebeli, M. Kira, and S. W. Koch, "Quantum theory of light emission from a semiconductor quantum dot," Phys. Rev. B **73**, 155319 (2006).
18. N. Baer, C. Gies, J. Wiersig, and F. Jahnke, "Luminescence of a semiconductor quantum dot system," Eur. Phys. J. B **50**, 411–418 (2006).
19. K. J. Ahn, J. Förstner, and A. Knorr, "Resonance fluorescence of semiconductor quantum dots: signatures of the electron-phonon interaction," Phys. Rev. B **71**, 153309 (2005).
20. M. Kira and S. W. Koch, "Cluster-expansion representation in quantum optics," Phys. Rev. A **78**, 022102 (2008).
21. M. Kira, S. W. Koch, R. P. Smith, A. E. Hunter, and S. T. Cundiff, "Quantum spectroscopy with Schrödinger-cat states," Nature Phys. **7**, 799–804 (2011).
22. L. Schneebeli, M. Kira, and S. W. Koch, "Characterization of strong light-matter coupling in semiconductor quantum-dot microcavities via photon-statistics spectroscopy," Phys. Rev. Lett. **101**, 097401 (2008).
23. L. Schneebeli, M. Kira, and S. W. Koch, "Microscopic theory of squeezed-light emission in strong-coupling semiconductor quantum-dot systems," Phys. Rev. A **80**, 033843 (2009).
24. F. Schwabl, *Statistical Mechanics*, 2nd ed. (Springer-Verlag, 2006).
25. G. Lindblad, "On the generators of quantum dynamical semigroups," Commun. Math. Phys. **48**, 119–130 (1976).
26. M. Kira and S. W. Koch, *Semiconductor Quantum Optics*, 1st ed. (Cambridge University, 2011).
27. J. H. Eberly, N. B. Narozhny, and J. J. Sanchez-Mondragon, "Periodic spontaneous collapse and revival in a simple quantum model," Phys. Rev. Lett. **44**, 1323–1326 (1980).
28. G. Rempe, H. Walther, and N. Klein, "Observation of quantum collapse and revival in a one-atom maser," Phys. Rev. Lett. **58**, 353–356 (1987).
29. D. Walls and G. Milburn, *Quantum Optics*, 2nd ed. (Springer-Verlag, 2008).
30. M. Richter, A. Carmele, A. Sitek, and A. Knorr, "Few-photon model of the optical emission of semiconductor quantum dots," Phys. Rev. Lett. **103**, 087407 (2009).
31. J. Wiersig, C. Gies, F. Jahnke, M. Aszmann, T. Berstermann, M. Bayer, C. Kistner, S. Reitzenstein, C. Schneider, S. Hofling, A. Forchel, C. Kruse, J. Kalden, and D. Hommel, "Direct observation of correlations between individual photon emission events of a microcavity laser," Nature **460**, 245–249 (2009).
32. C. Gies, J. Wiersig, M. Lorke, and F. Jahnke, "Semiconductor model for quantum-dot-based microcavity lasers," Phys. Rev. A **75**, 013803 (2007).
33. Y. Zhu, D. J. Gauthier, S. E. Morin, Q. Wu, H. J. Carmichael, and T. W. Mossberg, "Vacuum Rabi splitting as a feature of linear-dispersion theory: analysis and experimental observations," Phys. Rev. Lett. **64**, 2499–2502 (1990).
34. M. Kira and S. W. Koch, "Quantum-optical spectroscopy of semiconductors," Phys. Rev. A **73**, 013813 (2006).

Paper II

M. Mootz, M. Kira, and S. W. Koch
Pair-excitation energetics of highly correlated many-body states
New J. Phys. **15**, 093040 (2013)

New Journal of Physics
The open access journal for physics

Pair-excitation energetics of highly correlated many-body states

M Mootz[1], **M Kira and S W Koch**
Department of Physics, Philipps-University Marburg, Renthof 5, D-35032 Marburg, Germany
E-mail: martin.mootz@physik.uni-marburg.de

New Journal of Physics **15** (2013) 093040 (31pp)
Received 19 July 2013
Published 26 September 2013
Online at http://www.njp.org/
doi:10.1088/1367-2630/15/9/093040

Abstract. A microscopic approach is developed to determine the excitation energetics of highly correlated quasi-particles in optically excited semiconductors based entirely on a pair-correlation function input. For this purpose, the Wannier equation is generalized to compute the energy per excited electron–hole pair of a many-body state probed by a weak pair excitation. The scheme is verified for the degenerate Fermi gas and incoherent excitons. In a certain range of experimentally accessible parameters, a new stable quasi-particle state is predicted which consists of four to six electron–hole pairs forming a liquid droplet of fixed radius. The energetics and pair-correlation features of these 'quantum droplets' are analyzed.

[1] Author to whom any correspondence should be addressed.

Contents

1. Introduction

Interactions may bind matter excitations into new stable entities, quasi-particles, that typically have very different properties than the non-interacting constituents. In semiconductors, electrons in the conduction band and vacancies, i.e. holes, in the valence band attract each other via the Coulomb interaction [1]. Therefore, the Coulomb attraction may bind different numbers of electron–hole pairs into a multitude of quasi-particle configurations. The simplest example is an exciton [2, 3] which consists of a Coulomb-bound electron–hole pair and exhibits many analogies to the hydrogen atom [1]. Two excitons can bind to a molecular state known as the biexciton [4, 5]. Both, exciton and biexciton resonances can be routinely accessed in present-day experiments by exciting a high quality direct-gap semiconductor optically from its ground state. Even the exciton formation can directly be observed in both optical [6] and terahertz [7] spectroscopy and their abundance can be controlled via the intensity of the optical excitation [8]. Also higher correlated quasi-particles can emerge in semiconductors. For instance, polyexcitons or macroscopic electron–hole droplets have been detected [9–12], especially in semiconductors with an indirect gap.

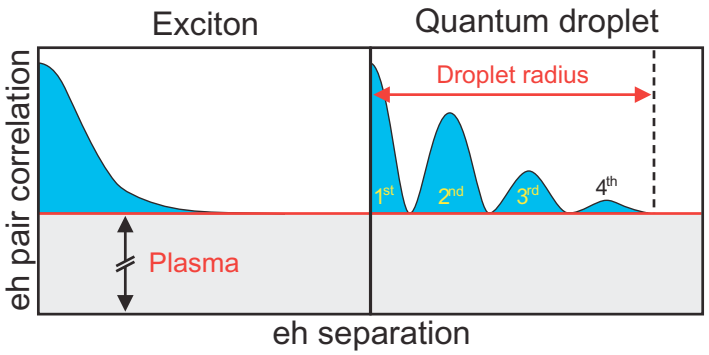

Figure 1. Schematic representation of the exciton (left) and the quantum droplet electron–hole (eh) pair-correlation function $g(\mathbf{r})$. The plasma contribution (gray shaded area) is shown together with the correlation contribution (blue shaded area). The radius of the quantum droplet is indicated by the vertical dashed line and each of the rings are labeled.

To determine the energetics of a given quasi-particle configuration, one can apply density-functional theory based on the functional dependence of the total energy on the electron density [13, 14]. This procedure is well established in particular for ground-state properties. However, whenever one wants to model experimental signatures of excited quasi-particle states in the excitation spectra, the applicability of density-functional theory becomes challenging, especially for highly correlated states.

In this paper, we develop a new scheme to determine the excitation energetics of highly correlated quasi-particle configurations. We start directly from the pair-correlation function, not from the density functional, and formulate a framework to compute the pair-excitation energetics. The electron–hole pair-correlation function $g(\mathbf{r})$ defines the conditional probability of finding an electron at the position $\mathbf{r}$ when the hole is at the origin. As an example, we show in figure 1 examples of $g(\mathbf{r})$ for excitons (left) and quantum droplets (right). Here, we refer to quantum droplets as a quasi-particle state where few electron–hole pairs, typically four to six, are in a liquid-like state bounded within a sphere of microscopic radius R.

In general, $g(\mathbf{r})$ always contains a constant electron–hole plasma contribution (gray shaded area) stemming from the mean-field aspects of the many-body states. The actual bound quasi-particles are described by the correlated part $\Delta g(\mathbf{r})$ (blue shaded area) which decays for increasing electron–hole separation. For 1s excitons, $\Delta g(\mathbf{r}) \propto |\phi_{1s}(\mathbf{r})|^2$ decreases monotonically and has the shape defined by the 1s-exciton wavefunction $\phi_{1s}(\mathbf{r})$ [15]. Since the electrons and holes in a quantum droplet are in a liquid phase, $\Delta g(\mathbf{r})$ must have the usual liquid structure where particles form a multi-ring-like pattern where the separation between the rings is defined by the average particle distance [16–18]. Due to the electron–hole attraction, one also observes a central peak, unlike for single-component liquids.

We derive the pair-excitation energetics for an arbitrary initial many-body state in section 2. In this connection, we first study the pair excitations of the semiconductor ground state before we extend the approach for an arbitrary initial many-body state. We then test our approach for the well-known cases of a degenerate Fermi gas and incoherent excitons in section 3. In section 4, we apply our scheme to study the energetics and structure of quantum droplets based on electron–hole correlations in a GaAs-type quantum well (QW). The effect of carrier–carrier correlations on the quantum droplet energetics is analyzed in section 5.

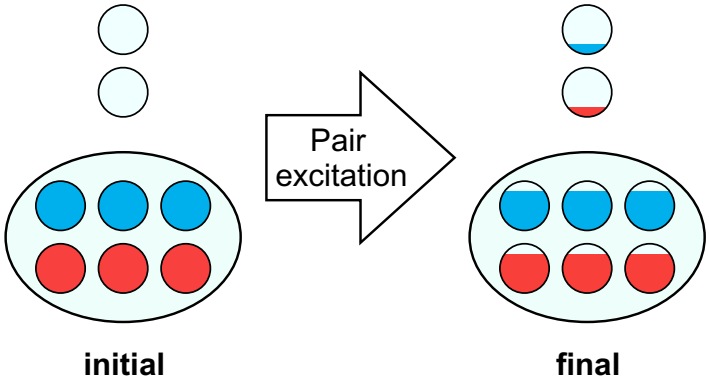

Figure 2. Schematic representation of a pair excitation. The quasi-particle configuration is shown before (left) and after (right) the pair excitation. Electron (holes) are symbolized by blue (red) circles while a yellow ellipse surrounds the correlated pairs. The level of filling indicates the fraction of electrons and holes bound as correlated pairs.

2. Energy and correlations in many-body systems

For resonant excitations, the excitation properties of many direct-gap semiconductor QW systems can be modeled using a two-band Hamiltonian [1, 19]

$$\hat{H} = \sum_{\mathbf{k},\lambda} \epsilon^{\lambda}_{\mathbf{k}} a^{\dagger}_{\lambda,\mathbf{k}} a_{\lambda,\mathbf{k}} + \frac{1}{2} \sum_{\mathbf{k},\mathbf{k}',\mathbf{q},\lambda,\lambda'} V_{\mathbf{q}}\, a^{\dagger}_{\lambda,\mathbf{k}+\mathbf{q}} a^{\dagger}_{\lambda',\mathbf{k}'-\mathbf{q}} a_{\lambda',\mathbf{k}'} a_{\lambda,\mathbf{k}}, \tag{1}$$

where the Fermionic operators $a^{\dagger}_{\mathrm{v(c)},\mathbf{k}}$ and $a_{\mathrm{v(c)},\mathbf{k}}$ create and annihilate an electron with crystal momentum $\hbar\,\mathbf{k}$ in the valence (conduction) band, respectively. We consider excitations close to the Γ point such that the kinetic energies can be treated as parabolic

$$\epsilon^{\mathrm{c}}_{\mathbf{k}} = \frac{\hbar^2\mathbf{k}^2}{2m_{\mathrm{e}}} + E_{\mathrm{g}}, \quad \epsilon^{\mathrm{v}}_{\mathbf{k}} = -\frac{\hbar^2\mathbf{k}^2}{2m_{\mathrm{h}}} \tag{2}$$

with the bandgap energy E_{g} and the effective masses for the electron m_{e} and hole m_{h}. The Coulomb interaction is characterized by the matrix element $V_{\mathbf{q}}$ of the quantum confined system [1]. We have formally set $V_{\mathbf{q}=0} = 0$ to eliminate the $\mathbf{q} = 0$ contribution from the Coulomb sum, which enforces the overall charge neutrality in the system [1].

For later use, we introduce Fermion field operators without the lattice-periodic functions

$$\hat{\Psi}_{\mathrm{e}}(\mathbf{r}) = \frac{1}{\sqrt{S}} \sum_{\mathbf{k}} a_{\mathrm{c},\mathbf{k}}\, \mathrm{e}^{\mathrm{i}\mathbf{k}\cdot\mathbf{r}}, \quad \hat{\Psi}_{\mathrm{h}}(\mathbf{r}) = \frac{1}{\sqrt{S}} \sum_{\mathbf{k}} a^{\dagger}_{\mathrm{v},\mathbf{k}}\, \mathrm{e}^{-\mathrm{i}\mathbf{k}\cdot\mathbf{r}} \tag{3}$$

for electrons and holes, respectively. These can be directly used to follow e.g. electron (hole) densities $\rho_{\mathrm{e(h)}}(\mathbf{r}) \equiv \langle \hat{\Psi}^{\dagger}_{\mathrm{e(h)}}(\mathbf{r}) \hat{\Psi}_{\mathrm{e(h)}}(\mathbf{r}) \rangle$ on macroscopic length scales because the unit-cell dependence is already averaged over. The corresponding normalization area is given by S.

2.1. Ground-state pair excitations

A schematic representation of a pair excitation is shown in figure 2 to illustrate the detectable energetics. The individual electrons and holes are symbolized by circles while the yellow ellipse

surrounds the correlated pairs. The level of blue (red) filling indicates the fraction of electrons (holes) bound as correlated pairs within the entire many-body system. This fraction can be changed continuously by applying, e.g. an optical field to generate pair excitations. If all pairs are bound to a single quasi-particle type, the initial energy of the system is

$$E_{\mathrm{ini}} = N E(N), \tag{4}$$

where N is the total number of pairs. Since N is typically much larger than the number of pairs within a quasi-particle, it is meaningful to introduce $E(N)$ as the binding energy per excited electron–hole pair. For stable quasi-particle configurations, a change in N does not alter $E(N)$, yielding the stability condition $\frac{\partial E(N)}{\partial N} = 0$.

We now assume that only a small number of pairs, δN, is excited from the quasi-particle into an unbound pair. An example of the excited configuration is presented in the right panel of figure 2. This state has the energy

$$\begin{aligned} E_{\mathrm{fin}} &= (N - \delta N)\, E(N - \delta N) + \delta N E_{\mathrm{pair}} \\ &= N E(N) + \delta N (E_{\mathrm{pair}} - E(N)) + \delta N \frac{\partial E(N)}{\partial N} + \mathcal{O}(\delta N^2), \end{aligned} \tag{5}$$

where E_{pair} is the energy of the unbound pair. After we apply the stability condition $\frac{\partial E(N)}{\partial N} = 0$, we find that the pair excitation produces an energy change $\Delta E \equiv E_{\mathrm{fin}} - E_{\mathrm{ini}} = \delta N (E_{\mathrm{pair}} - E(N)) + \mathcal{O}(\delta N^2)$ such that the energy per excited particle becomes

$$\bar{E} = \lim_{\delta N \to 0} \frac{\Delta E}{\delta N} = E_{\mathrm{pair}} - E(N). \tag{6}$$

This difference defines how much energy the electron–hole pair gains by forming the quasi-particle from unbound pairs.

To develop a systematic method describing the quasi-particle energetics, we start from the simplest situation where the unexcited semiconductor is probed optically, i.e. by inducing a weak pair excitation. The corresponding initial state is then the semiconductor's ground state $|G\rangle$ where all valence bands are fully occupied while all conduction bands are empty. Following the analysis in [15], we introduce the coherent displacement-operator functional [1, 15]

$$\hat{D}[\psi] = \mathrm{e}^{\varepsilon \hat{S}[\psi]}, \quad \hat{S}[\psi] = \sum_{\mathbf{k}} \left(\psi_{\mathbf{k}} a^{\dagger}_{\mathrm{c},\mathbf{k}} a_{\mathrm{v},\mathbf{k}} - \psi^{\star}_{\mathbf{k}} a^{\dagger}_{\mathrm{v},\mathbf{k}} a_{\mathrm{c},\mathbf{k}} \right) \tag{7}$$

to generate pair excitations. Here, ε is an infinitesimal constant and $\psi_{\mathbf{k}}$ is a function to be determined later using a variational approach. The probed ground state has a density matrix $\hat{\rho}_{\mathrm{G}}$ that determines the pair-excitation state via

$$\hat{\rho}[\psi] = \hat{D}[\psi]\, \hat{\rho}_{\mathrm{G}}\, \hat{D}^{\dagger}[\psi]. \tag{8}$$

We see from the definition (7) that $\hat{D}[\psi]$ generates pair excitations to the semiconductor ground state $\hat{\rho}_{\mathrm{G}}$ because $\hat{S}[\psi]$ contains all elementary, direct, pair-excitation processes $a^{\dagger}_{\mathrm{c},\mathbf{k}} a_{\mathrm{v},\mathbf{k}}$ ($a^{\dagger}_{\mathrm{v},\mathbf{k}} a_{\mathrm{c},\mathbf{k}}$) where an electron is moved from the valence (conduction) to the conduction (valence) band. The weak excitation of the probe is realized by making ε infinitesimal, i.e. $\varepsilon \ll 1$.

As shown in [15], the pair excitation (7) generates the electron–hole distribution and polarization

$$\begin{aligned} f_{\mathbf{k},\psi} &\equiv \mathrm{Tr}\left[a^{\dagger}_{\mathrm{c},\mathbf{k}} a_{\mathrm{c},\mathbf{k}}\, \hat{\rho}[\psi] \right] \equiv \mathrm{Tr}\left[a_{\mathrm{v},\mathbf{k}} a^{\dagger}_{\mathrm{v},\mathbf{k}}\, \hat{\rho}[\psi] \right] = \sin^2(\varepsilon |\psi_{\mathbf{k}}|), \\ P_{\mathbf{k},\psi} &\equiv \mathrm{Tr}\left[a^{\dagger}_{\mathrm{v},\mathbf{k}} a_{\mathrm{c},\mathbf{k}}\, \hat{\rho}[\psi] \right] = \mathrm{e}^{\mathrm{i}\varphi_{\mathbf{k}}} \sin(\varepsilon\, |\psi_{\mathbf{k}}|) \cos(\varepsilon\, |\psi_{\mathbf{k}}|), \end{aligned} \tag{9}$$

respectively. Here, $\psi_{\mathbf{k}} = |\psi_{\mathbf{k}}|e^{i\varphi_{\mathbf{k}}}$ has been defined in terms of a real-valued amplitude $|\psi_{\mathbf{k}}|$ and phase $\varphi_{\mathbf{k}}$. For the weak-excitation limit $\varepsilon \ll 1$, equation (9) reduces to

$$f_{\mathbf{k},\psi} = \varepsilon^2|\psi_{\mathbf{k}}|^2 + \mathcal{O}(\varepsilon^3), \quad P_{\mathbf{k},\psi} = \varepsilon\,\psi_{\mathbf{k}} + \mathcal{O}(\varepsilon^3) \tag{10}$$

to the leading order. Also the exact energy of state $\hat{\rho}[\psi]$ has already been computed in [15] with the result

$$\begin{aligned} E_{\mathrm{pro}}[\psi] &\equiv E[\psi] - E_{\mathrm{GS}} = \mathrm{Tr}\left[\hat{H}\hat{\rho}[\psi]\right] - \mathrm{Tr}\left[\hat{H}\hat{\rho}_{\mathrm{G}}\right] \\ &= \varepsilon^2\left(\sum_{\mathbf{k}}\frac{\hbar^2\mathbf{k}^2}{2\mu}|\psi_{\mathbf{k}}|^2 - \sum_{\mathbf{k},\mathbf{k}'}V_{\mathbf{k}-\mathbf{k}'}\psi_{\mathbf{k}}\psi^{\star}_{\mathbf{k}'}\right) + \mathcal{O}(\varepsilon^3), \quad \mu \equiv \frac{m_{\mathrm{e}}m_{\mathrm{h}}}{m_{\mathrm{e}}+m_{\mathrm{h}}}, \end{aligned} \tag{11}$$

where we removed the ground-state energy E_{GS} and introduced the reduced mass μ.

2.2. *Ordinary Wannier equation*

The lowest pair-excitation energy can be found by minimizing $E_{\mathrm{pro}}[\psi]$ with the constraint that the number of excited electron–hole pairs

$$N_{\mathrm{pro}} \equiv \sum_{\mathbf{k}} f_{\mathbf{k},\psi} = \varepsilon^2\sum_{\mathbf{k}}|\psi_{\mathbf{k}}|^2 \tag{12}$$

remains constant. This can be accounted for by the standard procedure of introducing a Lagrange multiplier E_λ to the functional

$$F[\psi] \equiv E_{\mathrm{pro}}[\psi] - E_\lambda\varepsilon^2\sum_{\mathbf{k}}|\psi_{\mathbf{k}}|^2. \tag{13}$$

By demanding $\delta F[\psi] = 0$ under any infinitesimal change $\psi_{\mathbf{k}} \to \psi_{\mathbf{k}} + \delta\psi_{\mathbf{k}}$, this extremum condition produces the Wannier equation [15]

$$\frac{\hbar^2\mathbf{k}^2}{2\mu}\psi_{\mathbf{k}} - \sum_{\mathbf{k}'}V_{\mathbf{k}-\mathbf{k}'}\psi_{\mathbf{k}'} = E_\lambda\psi_{\mathbf{k}}. \tag{14}$$

Fourier transform of equation (14) produces the real-space form

$$\left[-\frac{\hbar^2\nabla^2}{2\mu} - V(\mathbf{r})\right]\psi(\mathbf{r}) = E_\lambda\psi(\mathbf{r}), \tag{15}$$

where $V(\mathbf{r})$ and $\psi(\mathbf{r})$ are the Fourier transformations of $V_{\mathbf{k}}$ and $\psi_{\mathbf{k}}$, respectively. Since equations (14) and (15) are the usual Wannier equations for excitons, the exciton wavefunction defines those pair excitations that produce minimal energy E_λ. At the same time, equation (15) is fully analogous to the Schrödinger equation of atomic hydrogen [1]. Therefore, E_λ also defines the Coulombic binding energy of excitons.

For the identification of the quasi-particle energy, we use the result (6) and compute the energy per excited electron–hole pair

$$\bar{E}_{\mathrm{pro}} \equiv \frac{E_{\mathrm{pro}}}{N_{\mathrm{pro}}}. \tag{16}$$

By inserting solution (14) into equations (11) and (12), we find $\bar{E}_{\mathrm{pro}} = E_\lambda$ showing that the energetics of the pair-excitations from the ground state are defined by the exciton resonances. As a result, the energy per probe-generated electron–hole pair produces a series of exciton

resonances that can be detected, e.g. in the absorption spectrum. We will show next that this variational approach can be generalized to determine the quasi-particle energetics for any desired many-body state.

2.3. Average carrier-excitation energy

Here, we start from a generic many-body system defined by the density matrix $\hat{\rho}_{\mathrm{MB}}$ instead of the semiconductor ground state $\hat{\rho}_{\mathrm{G}}$. We assume that $\hat{\rho}_{\mathrm{MB}}$ contains spatially homogeneous excitations with equal numbers of electrons and holes, i.e.

$$N_{\mathrm{eh}} = \sum_{\mathbf{k}} f^{\mathrm{e}}_{\mathbf{k}} = \sum_{\mathbf{k}} f^{\mathrm{h}}_{\mathbf{k}}, \quad \text{with} \quad f^{\mathrm{e}}_{\mathbf{k}} \equiv \langle a^{\dagger}_{\mathrm{c},\mathbf{k}} a_{\mathrm{c},\mathbf{k}} \rangle, \quad f^{\mathrm{h}}_{\mathbf{k}} \equiv 1 - \langle a^{\dagger}_{\mathrm{v},\mathbf{k}} a_{\mathrm{v},\mathbf{k}} \rangle, \tag{17}$$

where the electron (hole) distribution $f^{\mathrm{e}}_{\mathbf{k}}$ ($f^{\mathrm{h}}_{\mathbf{k}}$) is defined within the electron–hole picture [1]. In general, each electron–hole pair excitation increases the energy by E_{g} because an electron is excited from the valence to the conduction band. To directly monitor the energetics of $\hat{\rho}_{\mathrm{MB}}$, we remove the trivial $E_{\mathrm{g}} N_{\mathrm{eh}}$ contribution, yielding the average carrier energy

$$\begin{aligned} E_{\mathrm{MB}} &\equiv \langle \hat{H} \rangle - E_{\mathrm{g}} N_{\mathrm{eh}} = \mathrm{Tr}\left[\hat{H}\,\hat{\rho}_{\mathrm{MB}}\right] - E_{\mathrm{g}} N_{\mathrm{eh}} \\ &= \sum_{\mathbf{k}} \left(\frac{\hbar^2 \mathbf{k}^2}{2 m_{\mathrm{e}}} f^{e}_{\mathbf{k}} + \frac{\hbar^2 \mathbf{k}^2}{2 m_{\mathrm{h}}} f^{\mathrm{h}}_{\mathbf{k}} \right) - \frac{1}{2} \sum_{\mathbf{k},\mathbf{k}'} V_{\mathbf{k}-\mathbf{k}'} \left(f^{\mathrm{e}}_{\mathbf{k}} f^{\mathrm{e}}_{\mathbf{k}'} + f^{\mathrm{h}}_{\mathbf{k}} f^{\mathrm{h}}_{\mathbf{k}'} \right) - \sum_{\mathbf{k},\mathbf{k}'} V_{\mathbf{k}-\mathbf{k}'} P^{\star}_{\mathbf{k}} P_{\mathbf{k}'} \\ &\quad + \frac{1}{2} \sum_{\mathbf{k},\mathbf{k}',\mathbf{q}} \left[V_{\mathbf{q}} \left(c^{\mathbf{q},\mathbf{k}',\mathbf{k}}_{\mathrm{v,v;v,v}} + c^{\mathbf{q},\mathbf{k}',\mathbf{k}}_{\mathrm{c,c;c,c}} \right) - 2\, V_{\mathbf{k}'+\mathbf{q}-\mathbf{k}}\, c^{\mathbf{q},\mathbf{k}',\mathbf{k}}_{\mathrm{eh}} \right], \end{aligned} \tag{18}$$

which is an exact result for homogeneous excitation conditions. Using the cluster expansion [15], we identified the incoherent two-particle correlations

$$\begin{aligned} c^{\mathbf{q},\mathbf{k}',\mathbf{k}}_{\mathrm{v,v;v,v}} &\equiv \Delta \langle a^{\dagger}_{\mathrm{v},\mathbf{k}} a^{\dagger}_{\mathrm{v},\mathbf{k}'} a_{\mathrm{v},\mathbf{k}'+\mathbf{q}} a_{\mathrm{v},\mathbf{k}-\mathbf{q}} \rangle, \quad c^{\mathbf{q},\mathbf{k}',\mathbf{k}}_{\mathrm{c,c;c,c}} \equiv \Delta \langle a^{\dagger}_{\mathrm{c},\mathbf{k}} a^{\dagger}_{\mathrm{c},\mathbf{k}'} a_{\mathrm{c},\mathbf{k}'+\mathbf{q}} a_{\mathrm{c},\mathbf{k}-\mathbf{q}} \rangle, \\ c^{\mathbf{q},\mathbf{k}',\mathbf{k}}_{\mathrm{eh}} &\equiv \Delta \langle a^{\dagger}_{\mathrm{c},\mathbf{k}} a^{\dagger}_{\mathrm{v},\mathbf{k}'} a_{c,\mathbf{k}'+\mathbf{q}} a_{\mathrm{v},\mathbf{k}-\mathbf{q}} \rangle, \end{aligned} \tag{19}$$

which represent the truly correlated parts of the respective two-particle expectation value. The first two correlations correspond to hole–hole and electron–electron correlations, respectively. Electron–hole correlations are described by $c^{\mathbf{q},\mathbf{k}',\mathbf{k}}_{\mathrm{eh}}$ where $\hbar\,\mathbf{q}$ defines the center-of-mass momentum of the correlated electron–hole pairs.

The only coherent quantity in equation (18) is the microscopic polarization

$$P_{\mathbf{k}} \equiv \langle a^{\dagger}_{\mathrm{v},\mathbf{k}} a_{\mathrm{c},\mathbf{k}} \rangle. \tag{20}$$

Consequently, the average carrier energy E_{MB} of any $\hat{\rho}_{\mathrm{MB}}$ is determined entirely by the single-particle expectation values $f^{\lambda}_{\mathbf{k}}$ and $P_{\mathbf{k}}$ and the incoherent two-particle correlations $c^{\mathbf{q},\mathbf{k}',\mathbf{k}}$. In other words, the system energy is *directly* influenced by contributions up to second-order correlations. We will show in section 2.4 that this fundamental property allows us to determine the pair-excitation energetics of a given state when we know its singlets and doublets. In other words, we do not need to identify the properties of the higher order clusters to compute the pair-excitation energetics.

Since we are interested in long-living quasi-particles in the incoherent regime, we consider only those states $\hat{\rho}_{\mathrm{MB}}$ which have vanishing coherences [1]. Therefore, we set $P_{\mathbf{k}}$ and all coherent correlations to zero from now on. Furthermore, we assume conditions where the

electron–hole correlations $c_{\mathrm{eh}}^{\mathbf{q},\mathbf{k}',\mathbf{k}}$ have a vanishing center-of-mass momentum $\hbar\,\mathbf{q}=0$, i.e. we assume that the correlated pairs are at rest. As a result, the electron–hole correlations can be expressed in terms of

$$c_{\mathrm{eh}}^{\mathbf{q},\mathbf{k}',\mathbf{k}} = \delta_{\mathbf{q},0}\, c_{\mathrm{eh}}^{\mathbf{q},\mathbf{k}',\mathbf{k}} \equiv \delta_{\mathbf{q},0}\, g_{\mathbf{k},\mathbf{k}'}. \tag{21}$$

For homogeneous and incoherent excitation conditions, the pair-correlation function can be written as

$$g(\mathbf{r}) \equiv \langle \hat{\Psi}_{\mathrm{e}}^{\dagger}(\mathbf{r})\hat{\Psi}_{\mathrm{h}}^{\dagger}(0)\hat{\Psi}_{\mathrm{h}}(0)\hat{\Psi}_{\mathrm{e}}(\mathbf{r})\rangle = \rho_{\mathrm{e}}\rho_{\mathrm{h}} + \Delta g(\mathbf{r}), \tag{22}$$

compare equation (3) [15]. The term $\rho_{\mathrm{e}}\rho_{\mathrm{h}}$ describes an uncorrelated electron–hole plasma contribution, whereas the quasi-particle clusters determine the correlated part

$$\Delta g(\mathbf{r}) = \frac{1}{S^2}\sum_{\mathbf{k},\mathbf{k}',\mathbf{q}} c_{\mathrm{eh}}^{\mathbf{q},\mathbf{k}',\mathbf{k}}\, \mathrm{e}^{\mathrm{i}(\mathbf{k}'+\mathbf{q}-\mathbf{k})\cdot\mathbf{r}} = \frac{1}{S^2}\sum_{\mathbf{k},\mathbf{k}'} g_{\mathbf{k},\mathbf{k}'}\, \mathrm{e}^{\mathrm{i}(\mathbf{k}'-\mathbf{k})\cdot\mathbf{r}}. \tag{23}$$

To describe, e.g. excitons and similar quasi-particles, we use an ansatz

$$\Delta g(\mathbf{r}) = |g_0\,\phi(\mathbf{r})|^2, \tag{24}$$

where g_0 defines the strength of the correlation while the specific properties of the quasi-particles determine the normalized wavefunction $\phi(\mathbf{r})$. In order to compute the quasi-particle energetics, we need to express $\Delta g(\mathbf{r})$ in terms of the electron–hole correlation $g_{\mathbf{k},\mathbf{k}'}$. By writing $\phi(\mathbf{r}) = \frac{1}{S}\sum_{\mathbf{k}} \phi_{\mathbf{k}}\, \mathrm{e}^{\mathrm{i}\mathbf{k}\cdot\mathbf{r}}$, we find the unique connection

$$g_{\mathbf{k},\mathbf{k}'} = g_0^2\, \phi_{\mathbf{k}}^{\star}\, \phi_{\mathbf{k}'}, \tag{25}$$

where $\phi(\mathbf{k})$ is the Fourier transformation of the wavefunction $\phi(\mathbf{r})$.

As shown in appendix A, the electron and hole distributions $f_{\mathbf{k}}^{\mathrm{e}}$ and $f_{\mathbf{k}}^{\mathrm{h}}$, together with the incoherent correlations $g_{\mathbf{k},\mathbf{k}'}$, $c_{\mathrm{v,v;v,v}}^{\mathbf{q},\mathbf{k}',\mathbf{k}}$, and $c_{\mathrm{c,c;c,c}}^{\mathbf{q},\mathbf{k}',\mathbf{k}}$ must satisfy the general conservation laws

$$\left(f_{\mathbf{k}}^{\mathrm{e}} - \tfrac{1}{2}\right)^2 + g_{\mathbf{k},\mathbf{k}} - \sum_{\mathbf{k}'} c_{\mathrm{c,c;c,c}}^{0,\mathbf{k}',\mathbf{k}} = \tfrac{1}{4}, \quad \left(f_{\mathbf{k}}^{\mathrm{h}} - \tfrac{1}{2}\right)^2 + g_{\mathbf{k},\mathbf{k}} - \sum_{\mathbf{k}'} c_{\mathrm{v,v;v,v}}^{0,\mathbf{k}',\mathbf{k}} = \tfrac{1}{4}. \tag{26}$$

As a consequence, we have to connect $f_{\mathbf{k}}^{\mathrm{e}}$ and $f_{\mathbf{k}}^{\mathrm{h}}$ with $g_{\mathbf{k},\mathbf{k}}$, $c_{\mathrm{c,c;c,c}}^{\mathbf{q},\mathbf{k}',\mathbf{k}}$, and $c_{\mathrm{v,v;v,v}}^{\mathbf{q},\mathbf{k}',\mathbf{k}}$ to have a self-consistent description of the many-body state. Therefore, equation (26) has a central role when the energetics of many-body states is solved self-consistently.

We show in section 5 that the effect of electron–electron and hole–hole correlations can be neglected when the energetics of new quasi-particle states is analyzed. Therefore, we set $c_{\mathrm{c,c;c,c}}^{\mathbf{q},\mathbf{k}',\mathbf{k}}$ and $c_{\mathrm{v,v;v,v}}^{\mathbf{q},\mathbf{k}',\mathbf{k}}$ to zero such that equation (26) reduces to

$$\left(f_{\mathbf{k}} - \tfrac{1}{2}\right)^2 + g_{\mathbf{k},\mathbf{k}} = \tfrac{1}{4}, \quad f_{\mathbf{k}} \equiv f_{\mathbf{k}}^{\mathrm{e}} = f_{\mathbf{k}}^{\mathrm{h}}. \tag{27}$$

From this result, we see that the electron and hole distributions become identical as long as correlations are dominated by $g_{\mathbf{k},\mathbf{k}'}$. A more general case with carrier–carrier correlations is studied in section 5. In the actual quasi-particle calculations, we solve equation (27)

$$f_{\mathbf{k}} = \tfrac{1}{2}\left(1 \pm \sqrt{1 - 4\, g_{\mathbf{k},\mathbf{k}}}\right) \tag{28}$$

that limits $g_{\mathbf{k},\mathbf{k}}$ to be below $\frac{1}{4}$. In other words, the maximum of $g_0|\phi(\mathbf{k})|$ is $\frac{1}{2}$, based on the connection (25). The '+' branch in equation (28) describes an inverted many-body system $\hat{\rho}_{\mathrm{MB}}$ corresponding to large electron–hole densities. Below inversion, only the '−' branch contributes.

Once the self-consistent pair $(f_{\mathbf{k}}, g_{\mathbf{k},\mathbf{k}'})$ is found, we determine the corresponding electron–hole density via

$$\rho_{\mathrm{eh}} = \frac{1}{S}\sum_{\mathbf{k}} f_{\mathbf{k}} \tag{29}$$

that becomes a functional of the electron–hole pair-correlation function due to its $g_{\mathbf{k},\mathbf{k}'}$ dependence via equation (28). In sections 3 and 4, we will use equation (27) to self-consistently determine $f_{\mathbf{k}}$ and $g_{\mathbf{k},\mathbf{k}'}$ for different quasi-particle configurations.

2.4. *Pair-excitation energetics*

To generalize the Wannier equation (14), we next analyze the pair-excitation energetics of an arbitrary homogeneous initial state $\hat{\rho}_{\mathrm{MB}}$. As shown in section 2.1, the simplest class of pair excitations can be generated by using the coherent displacement-operator functional (7). The pair-excitation state is then given by

$$\hat{\rho}[\psi] = \hat{D}[\psi]\,\hat{\rho}_{\mathrm{MB}}\,\hat{D}^{\dagger}[\psi], \tag{30}$$

which is properly normalized $\mathrm{Tr}[\hat{\rho}[\psi]] = \mathrm{Tr}[\hat{\rho}_{\mathrm{MB}}] = 1$, as any density matrix should be.

As shown in appendix B, the pair excitation generates the polarization and electron–hole distribution

$$P_{\mathbf{k},\psi} = \left(1 - f^{\mathrm{e}}_{\mathbf{k}} - f^{\mathrm{h}}_{\mathbf{k}}\right)\varepsilon\,\psi_{\mathbf{k}} + \mathcal{O}(\varepsilon^3), \qquad f_{\mathbf{k},\psi} = \left(1 - f^{\mathrm{e}}_{\mathbf{k}} - f^{\mathrm{h}}_{\mathbf{k}}\right)\varepsilon^2\,|\psi_{\mathbf{k}}|^2 + \mathcal{O}(\varepsilon^3), \tag{31}$$

respectively where we have applied the weak excitation limit $\varepsilon \ll 1$. For the sake of completeness, we keep the explicit dependences $f^{\mathrm{e}}_{\mathbf{k}}$, $f^{\mathrm{h}}_{\mathbf{k}}$ and $c^{\mathbf{q},\mathbf{k}',\mathbf{k}}_{\lambda,\lambda;\lambda,\lambda}$ and take the limit of dominant electron–hole correlation after the central results for the pair excitations have been derived. In analogy to equation (11), pair excitations add the average carrier energy $E_{\mathrm{pro}}[\psi] \equiv E[\psi] - E_{\mathrm{MB}}$ to the system. Technically, $E[\psi]$ is obtained by replacing ρ_{MB} in equation (18) by $\rho[\psi]$. The actual derivation is performed in appendix B, yielding again an exact relation for incoherent quasi-particles

$$\begin{aligned} E_{\mathrm{pro}}[\psi] = {} & \epsilon^2 \sum_{\mathbf{k}} E_{\mathbf{k}} |\psi_{\mathbf{k}}|^2 - \epsilon^2 \sum_{\mathbf{k},\mathbf{k}'} V^{\mathrm{eff}}_{\mathbf{k},\mathbf{k}'}\,\psi_{\mathbf{k}}\,\psi^{\star}_{\mathbf{k}'} \\ & + \epsilon^2 \sum_{\mathbf{k},\mathbf{k}',\mathbf{q}} V_{\mathbf{q}} \left(c^{\mathbf{q},\mathbf{k}',\mathbf{k}}_{\mathrm{v},\mathrm{v};\mathrm{v},\mathrm{v}}\,\psi_{\mathbf{k}-\mathbf{q}}\,\psi^{\star}_{\mathbf{k}} + c^{\mathbf{q},\mathbf{k}',\mathbf{k}}_{\mathrm{c},\mathrm{c};\mathrm{c},\mathrm{c}}\,\psi_{\mathbf{k}}\,\psi^{\star}_{\mathbf{k}-\mathbf{q}} - \mathrm{Re}[c^{\mathbf{q},\mathbf{k}',\mathbf{k}}_{\mathrm{v},\mathrm{v};\mathrm{v},\mathrm{v}} + c^{\mathbf{q},\mathbf{k}',\mathbf{k}}_{\mathrm{c},\mathrm{c};\mathrm{c},\mathrm{c}}]|\psi_{\mathbf{k}}|^2 \right) \\ & + \mathcal{O}(\varepsilon^3), \end{aligned} \tag{32}$$

where we identified the renormalized kinetic electron–hole pair energy

$$E_{\mathbf{k}} \equiv \left[\frac{\hbar^2\mathbf{k}^2}{2\mu} - \sum_{\mathbf{k}'} V_{\mathbf{k}-\mathbf{k}'}\left(f^{\mathrm{e}}_{\mathbf{k}'} + f^{\mathrm{h}}_{\mathbf{k}'}\right)\right]\left(1 - f^{\mathrm{e}}_{\mathbf{k}} - f^{\mathrm{h}}_{\mathbf{k}}\right) + 2\sum_{\mathbf{k}'} V_{\mathbf{k}-\mathbf{k}'}\,g_{\mathbf{k},\mathbf{k}'}. \tag{33}$$

The unscreened Coulomb interaction $V_{\mathbf{k}-\mathbf{k}'}$ is modified through the presence of electron–hole densities and correlations via

$$V^{\mathrm{eff}}_{\mathbf{k},\mathbf{k}'} \equiv \left(1 - f^{\mathrm{e}}_{\mathbf{k}} - f^{\mathrm{h}}_{\mathbf{k}}\right) V_{\mathbf{k}-\mathbf{k}'}\left(1 - f^{\mathrm{e}}_{\mathbf{k}'} - f^{\mathrm{h}}_{\mathbf{k}'}\right) + 2 g_{\mathbf{k},\mathbf{k}'} V_{\mathbf{k}-\mathbf{k}'}. \tag{34}$$

Since the phase-space filling factor $(1 - f^{\mathrm{e}}_{\mathbf{k}} - f^{\mathrm{h}}_{\mathbf{k}})$ becomes negative once inversion is reached, the excitation level changes the nature of the effective electron–hole Coulomb interaction

from attractive to repulsive. At the same time, $g_{\mathbf{k},\mathbf{k}'}$ can either enhance or decrease the Coulomb interaction depending on the nature of the pair correlation. The exact generalization of equation (32) for coherent quasi-particles is presented in appendix C.

2.5. *Generalized Wannier equation*

As in section 2.2, we minimize the functional $E_{\mathrm{pro}}[\psi]$ with the constraint that the excitation $\varepsilon^2 \sum_{\mathbf{k}} |\psi_{\mathbf{k}}|^2$ remains constant. Following the same variational steps as those producing equation (14), we obtain the *generalized Wannier equation* for incoherent quasi-particles:

$$E_{\mathbf{k}}\psi_{\mathbf{k}} - \sum_{\mathbf{k}'} V^{\mathrm{eff}}_{\mathbf{k},\mathbf{k}'}\psi_{\mathbf{k}'} + \sum_{\mathbf{k}',\mathbf{q}} V_{\mathbf{q}} \left(c^{\mathbf{q},\mathbf{k}',\mathbf{k}+\mathbf{q}}_{\mathrm{c,c;c,c}}\, \psi_{\mathbf{k}+\mathbf{q}} + c^{\mathbf{q},\mathbf{k}',\mathbf{k}}_{\mathrm{v,v;v,v}}\, \psi_{\mathbf{k}-\mathbf{q}} \right) - \sum_{\mathbf{k}',\mathbf{q}} V_{\mathbf{q}}\, \mathrm{Re}\left[c^{\mathbf{q},\mathbf{k}',\mathbf{k}}_{\mathrm{c,c;c,c}} + c^{\mathbf{q},\mathbf{k}',\mathbf{k}}_{\mathrm{v,v;v,v}} \right] \psi_{\mathbf{k}} = E_{\lambda}\psi_{\mathbf{k}}. \tag{35}$$

For vanishing electron–hole densities and correlations, equation (35) reduces to the ordinary exciton Wannier equation (14). Since the presence of two-particle correlations and densities modifies the effective Coulomb interaction, it is possible that new quasi-particles emerge. The generalized Wannier equation with all coherent and incoherent contributions is presented in appendix C.

For the identification of the quasi-particle energy, we compute the energy per excited electron–hole pair (16). The number of excited electron–hole pairs of the probed many-body system is

$$N_{\mathrm{pro}} \equiv \sum_{\mathbf{k}} f_{\mathbf{k},\psi} = \varepsilon^2 \sum_{\mathbf{k}} \left(1 - f^{\mathrm{e}}_{\mathbf{k}} - f^{\mathrm{h}}_{\mathbf{k}}\right) |\psi_{\mathbf{k}}|^2 \tag{36}$$

according to equation (31). By inserting equation (35) into equation (32) and using the definitions (16) and (36), the energy per excited electron–hole pairs follows from

$$\bar{E}_{\mathrm{pro}} = E_{\lambda} \frac{\sum_{\mathbf{k}} |\psi_{\mathbf{k}}|^2}{\sum_{\mathbf{k}} |\psi_{\mathbf{k}}|^2 \left(1 - f^{\mathrm{e}}_{\mathbf{k}} - f^{\mathrm{h}}_{\mathbf{k}}\right)} \tag{37}$$

that defines the quasi-particle energy, based on the discussion in section 2.1.

3. Pair-excitation spectrum of the degenerate Fermi gas and of incoherent excitons

For all our numerical evaluations, we use the parameters of a typical 10 nm GaAs-QW system. Here, the reduced mass is $\mu = 0.0581 m_0$, where m_0 is the free-electron mass and the 1s-exciton binding energy is $E_{\mathrm{B}} = 9.5$ meV. This is obtained by using the dielectric constant $\varepsilon_{\mathrm{r}} = 13.74$ of GaAs in the Coulomb interaction.

To compute the quasi-particle energetics for a given electron–hole density ρ_{eh}, we always start from the conservation law (27) to generate a self-consistent many-body state $\hat{\rho}_{\mathrm{MB}}$. We then use the found self-consistent pair ($f_{\mathbf{k}}$, $g_{\mathbf{k},\mathbf{k}'}$) as an input to the generalized Wannier equation (35) and numerically solve the pair excitation $\psi_{\mathbf{k}}$ and E_{λ}. As shown in section 5, the effect of electron–electron and hole–hole correlations on the quasi-particle energetics is negligible such that we set $c^{\mathbf{q},\mathbf{k}',\mathbf{k}}_{\mathrm{c,c;c,c}}$ and $c^{\mathbf{q},\mathbf{k}',\mathbf{k}}_{\mathrm{v,v;v,v}}$ to zero in equation (35).

The variational computations rigorously determine only the lowest energy E_0. However, it is useful to analyze also the characteristics of the excited states E_{λ} to gain additional information

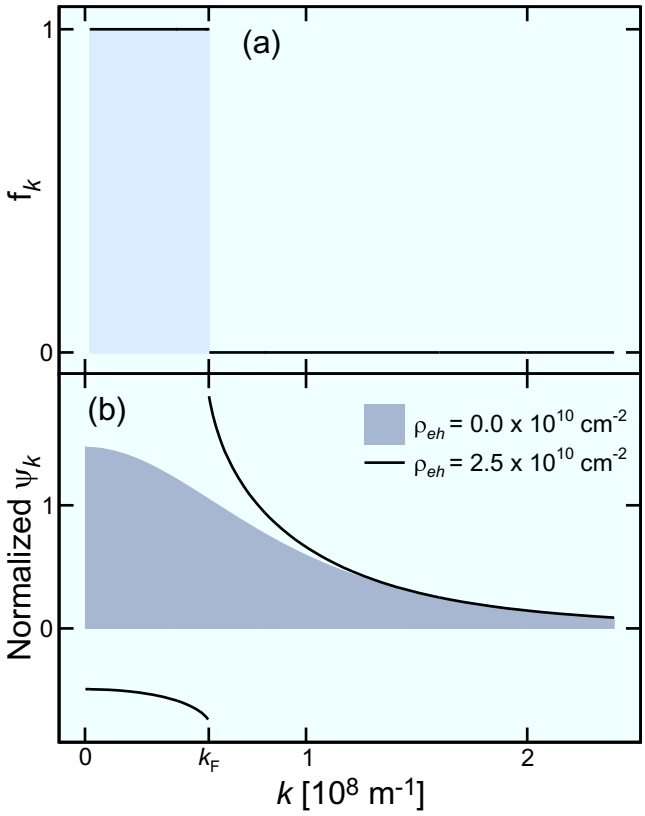

Figure 3. Solutions of the generalized Wannier equation for degenerate Fermi gas. (a) The electron–hole distribution $f_{\mathbf{k}}$ is shown as function of k for $\rho_{\mathrm{eh}} = 2.5 \times 10^{10}\,\mathrm{cm}^{-2}$ and $k_{\mathrm{F}} = 0.56 \times 10^{8}\,\mathrm{m}^{-1}$. (b) Normalized ground-state wavefunction $\psi_{\mathbf{k}}$ for vanishing electron–hole density (shaded area) and $\rho_{\mathrm{eh}} = 2.5 \times 10^{10}\,\mathrm{cm}^{-2}$ (solid line).

about the energetics of the pair excitation acting upon $\hat{\rho}_{\mathrm{MB}}$. To deduce the quasi-particle energetics, we normalize the energy E_λ via equation (37). The resulting energy per excited electron–hole pair $\bar{E}_{\mathrm{pro}}$ defines then the detectable energy resonances.

3.1. Degenerate Fermi gas

The simplest form of $\hat{\rho}_{\mathrm{MB}}$ for an excited state is provided by the degenerate Fermi gas [20–23]

$$f_{\mathbf{k}} = \theta(k - k_{\mathrm{F}}), \quad g_{\mathbf{k},\mathbf{k}'} = 0 \tag{38}$$

because the two-particle correlations vanish. It is straightforward to show that the pair $(f_{\mathbf{k}}, g_{\mathbf{k},\mathbf{k}'})$ satisfies the conservation law (27) even though the system is inverted for all k below the Fermi wave vector $k_{\mathrm{F}} = \sqrt{4\pi\rho_{\mathrm{eh}}}$. Due to this inversion, the degenerate Fermi gas provides a simple model to study quasi-particle excitations under optical gain conditions.

Figure 3(a) presents the electron–hole distribution $f_{\mathbf{k}}$ as function of k for the electron–hole density $\rho_{\mathrm{eh}} = 2.5 \times 10^{10}\,\mathrm{cm}^{-2}$. The distribution has a Fermi edge at $k_{\mathrm{F}} = 0.56 \times 10^{8}\,\mathrm{m}^{-1}$ while $g_{\mathbf{k},\mathbf{k}}$ is zero for all k values (not shown). The numerically computed ground-state wavefunction

$\psi_{\mathbf{k}}$ is plotted in figure 3(b) as solid line. We have applied the normalization $\sum_{\mathbf{k}} |\psi_{\mathbf{k}}|^2 = 1$. As a comparison, we also show the corresponding zero-density result ($f_{\mathbf{k}} = 0$, $g_{\mathbf{k},\mathbf{k}'} = 0$) as shaded area. While the zero-density wavefunction decays monotonically from the value 1.47, the degenerate Fermi gas has a $\psi_{\mathbf{k}}$ that is negative-valued up to the Fermi edge k_{F}. Exactly at $k = k_{\mathrm{F}}$, $\psi_{\mathbf{k}}$ abruptly jumps from the value -0.74 to 1.89. Above roughly $k = 1.3 \times 10^8\,\mathrm{m}^{-1}$, both wavefunctions show a similar decay. The energetics of the related pair excitations is discussed later in section 3.3.

3.2. Incoherent excitons

According to the ansatz (25), the exciton state is determined by the electron–hole pair-correlation function

$$g_{\mathbf{k},\mathbf{k}'} = \phi_{1\mathrm{s},\mathbf{k}} \phi_{1\mathrm{s},\mathbf{k}'} \tag{39}$$

with the 1s-exciton wavefunction $\phi_{1\mathrm{s},\mathbf{k}}$ defining the initial many-body state $\hat{\rho}_{\mathrm{MB}}$, not the pair-excitation state. Here, we have included the strength of the electron–hole correlation g_0 into the 1s-exciton wavefunction to simplify the notation. To compute $\phi_{1\mathrm{s},\mathbf{k}}$, we have to solve the ordinary density-dependent Wannier equation [1, 15]

$$\tilde{E}_{\mathbf{k}}\, \phi_{1\mathrm{s},\mathbf{k}} - (1 - 2\, f_{\mathbf{k}}) \sum_{\mathbf{k}'} V_{\mathbf{k}-\mathbf{k}'}\, \phi_{1\mathrm{s},\mathbf{k}'} = E_{1\mathrm{s}}\, \phi_{1\mathrm{s},\mathbf{k}}, \qquad \tilde{E}_{\mathbf{k}} = \frac{\hbar^2 \mathbf{k}^2}{2\mu} - 2 \sum_{\mathbf{k}'} V_{\mathbf{k}-\mathbf{k}'}\, f_{\mathbf{k}'}\,, \tag{40}$$

with the constraint imposed by the conservation law (27). In practice, we solve equations (27) and (40) iteratively. Since the specific choice $E_{1\mathrm{s}}$ defines the electron–hole density (29) uniquely, we can directly identify the self-consistent pair ($f_{\mathbf{k}}$, $g_{\mathbf{k},\mathbf{k}'}$) as function of ρ_{eh}. The explicit steps of the iteration cycle are presented in appendix D.

Figure 4(a) shows the resulting normalized electron–hole pair-correlation function $\Delta\bar{g}(r) \equiv \Delta g(r)/\rho_{\mathrm{eh}}^2$ for an electron–hole density of $\rho_{\mathrm{eh}} = 2.5 \times 10^{10}\,\mathrm{cm}^{-2}$. For the incoherent excitons, $\Delta\bar{g}(r)$ is a monotonically decaying function. The corresponding iteratively solved $f_{\mathbf{k}}$ (black line) and $g_{\mathbf{k},\mathbf{k}}$ (red line) are plotted in figure 4(b). The pair correlation $g_{\mathbf{k},\mathbf{k}}$ decays monotonically from the value 0.21. Also the electron–hole distribution $f_{\mathbf{k}}$ function decreases monotonically, peaking at 0.30. This implies that the phase-space filling already reduces the strength of the effective Coulomb potential (34) for small momentum states which typically dominate the majority of ground-state configurations.

The corresponding normalized ground-state wavefunction $\psi_{\mathbf{k}}$ of the pair excitation is shown in figure 4(c) (solid line) together with the zero-density result (shaded area). Both functions show a similar decay for k values larger than $2 \times 10^8\,\mathrm{m}^{-1}$. In contrast to the zero-density result, we observe that $\psi_{\mathbf{k}}$ has a peak at $k = 0.59 \times 10^8\,\mathrm{m}^{-1}$. Interestingly, the maximum of $\psi_{\mathbf{k}}$ is close to k_{F} of the degenerate Fermi gas analyzed in figure 3 because both cases have the same density giving rise to sufficiently strong phase-space filling effects.

3.3. Energetics of pair excitations

We next analyze the influence of the electron–hole density ρ_{eh} on the pair-excitation energetics for the degenerate Fermi gas and for incoherent excitons. The result for the degenerate Fermi gas is presented in figure 5(a) where the ground-state energy E_0 (solid line), the continuum (shaded area) and the ground-state energy per excited electron–hole pair $\bar{E}_{\mathrm{pro}}$ (dashed line)

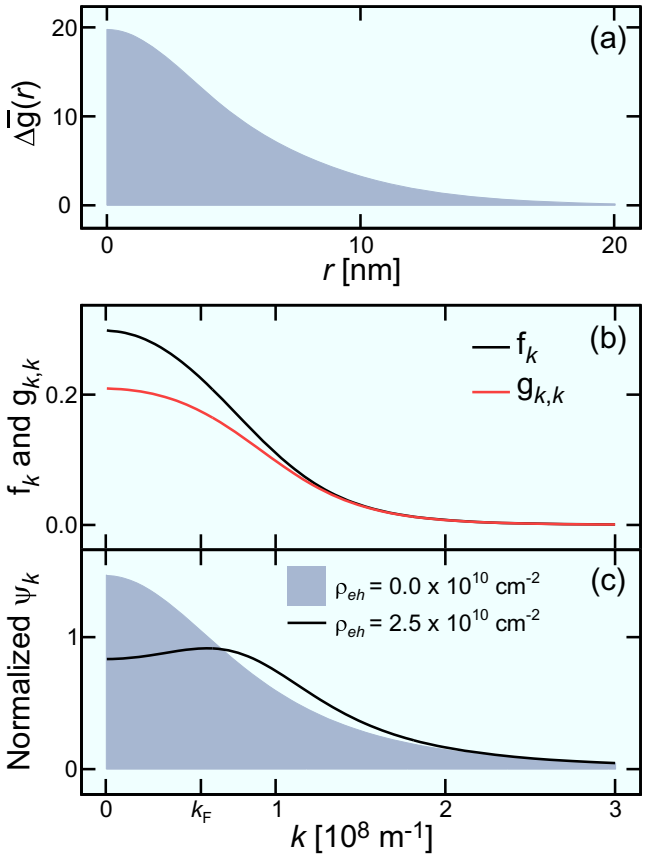

Figure 4. Solutions of the generalized Wannier equation for incoherent excitons. (a) The normalized electron–hole pair-correlation function $\Delta\bar{g}(r)$ is shown for $\rho_{\mathrm{eh}} = 2.5 \times 10^{10}\,\mathrm{cm}^{-2}$. (b) The corresponding electron–hole distribution $f_{\mathbf{k}}$ (black line) and the correlation $g_{\mathbf{k},\mathbf{k}}$ (red line) as function of k. (c) Normalized ground-state wavefunction for vanishing electron–hole density (shaded area) and $\rho_{\mathrm{eh}} = 2.5 \times 10^{10}\,\mathrm{cm}^{-2}$ (solid line).

are plotted as function of ρ_{eh}. We see that the energy difference between E_0 and the ionized states is considerably reduced from 9.5 to 6.1 meV as the density is increased from zero to $\rho_{\mathrm{eh}} = 3.6 \times 10^{10}\,\mathrm{cm}^{-2}$. This decrease is already an indication that none of the excited states remain bound for elevated densities. At the same time, the ground-state energy shows only a slight red shift while the continuum is strongly red shifted such that the first excited state becomes ionized for electron–hole densities above $\rho_{\mathrm{eh}} = 2 \times 10^{9}\,\mathrm{cm}^{-2}$. The detectable pair-excitation energy is defined by $\bar{E}_{\mathrm{pro}}$, according to equation (37). As a general trend, $\bar{E}_{\mathrm{pro}}$ is slightly smaller than E_0. We also observe that $\bar{E}_{\mathrm{pro}}$ remains relatively stable as the density is increased. This implies that the semiconductor absorption and gain peaks appear at roughly the same position independent of electron–hole density. This conclusion is consistent with fully microscopic absorption [8] and gain calculations [24, 25] and measurements [26, 27].

The pair-excitation energetics of the exciton state (39)–(40) is presented in figure 5(b) for the initial exciton state analyzed in figure 4. The black line compares the ground state E_0 with the first excited state E_1 (red line) while the shaded area indicates the ionized solutions.

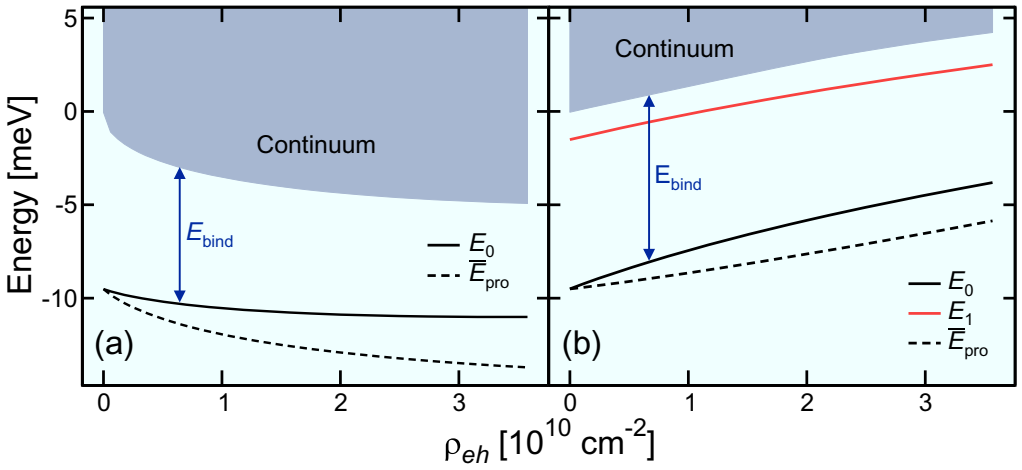

Figure 5. Pair-excitation energetics for the degenerate Fermi gas versus incoherent excitons. (a) The ground-state energy E_0 (black solid line), the continuum (shaded area) and the energy per excited electron–hole pair $\bar{E}_{\rm pro}$ (dashed line) are presented as function of the electron–hole density $\rho_{\rm eh}$ for the degenerate Fermi gas. The same analysis is plotted in (b) for the exciton state. Additionally, the red solid line shows the energy of the first excited state E_1.

In contrast to the degenerate Fermi gas, the ground-state energy blue shifts. This blue shift remains present in $\bar{E}_{\rm pro}$ (dashed line) and is consistent with the blue shift of the excitonic absorption when excitons are present in the system, as detected in several measurements [6, 8, 28, 29]. The nearly linear dependence of $\bar{E}_{\rm pro}$ on the electron–hole density is consistent with earlier theoretical studies [30–32]. In particular, E_0 blue shifts faster than the continuum does. If we interpret the energy difference of E_0 and continuum as the exciton-binding energy, we find that the exciton-binding energy decreases from 9.5 to 8.0 meV as the density is increased to $\rho_{\rm eh} = 3.6 \times 10^{10}\,{\rm cm}^{-2}$, which shows that excitons remain bound even at elevated densities. For later reference, the density $2.5 \times 10^{10}\,{\rm cm}^{-2}$ produces $\bar{E}_{\rm pro} = -7.1$ meV energy per excited electron–hole pair.

4. Pair-excitation spectrum of quantum droplets

To define a quantum droplet state, we assume that the electron–hole pairs form a liquid confined within a small droplet with a radius R as discussed in connection with figure 1. Since the QW is two dimensional, the droplet is confined inside a circular disc with radius R. We assume that the droplet has a hard shell created by the Fermi pressure of the plasma acting upon the droplet. As a result, the solutions correspond to standing waves. Therefore, we define the quantum droplet state via the standing-wave ansatz

$$\phi(r) = J_0\left(x_n \frac{r}{R}\right) {\rm e}^{-\kappa r}\theta(R-r) \tag{41}$$

to be used in equation (24). Here, x_n is the nth zero of the Bessel function $J_0(x)$. The Heaviside $\theta(x)$ function confines the droplet inside a circular disc with radius R. The additional decay constant κ is used for adjusting the electron–hole density (29) when the quantum droplet has radius R and n rings.

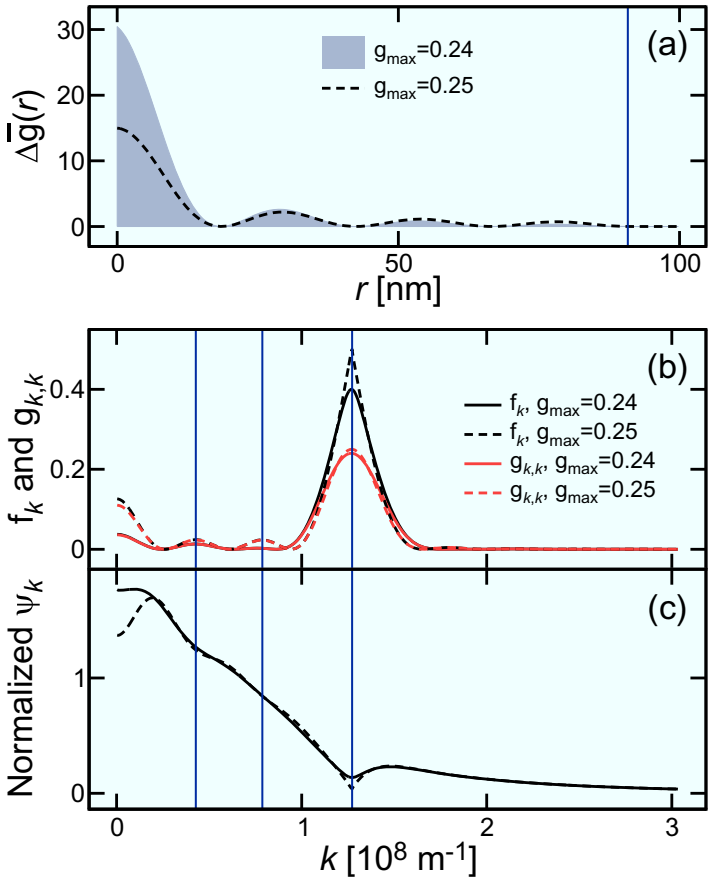

Figure 6. Solutions of the generalized Wannier equation for quantum droplets. (a) The normalized electron–hole pair-correlation function $\Delta\bar{g}(r)$ is shown for $g_{\max} = 0.24$ (shaded area) and $g_{\max} = \frac{1}{4}$ (dashed line). The quantum droplet has $n = 4$ rings, $R = 90.8$ nm (vertical line) and $\rho_{\rm eh} = 2.5 \times 10^{10}\,{\rm cm}^{-2}$. (b) The corresponding electron–hole distribution $f_{\mathbf{k}}$ (black lines) and correlation $g_{\mathbf{k},\mathbf{k}}$ (red lines) as function of k for $g_{\max} = 0.24$ (solid lines) and $g_{\max} = \frac{1}{4}$ (dashed lines). (c) The resulting normalized ground-state wavefunctions $\psi_{\mathbf{k}}$.

For a given quantum droplet radius R, ring number n and electron–hole density $\rho_{\rm eh}$, we fix the peak amplitude of $g_{\mathbf{k},\mathbf{k}}$ to $g_{\max} = \max[g_{\mathbf{k},\mathbf{k}}]$ which defines the strength of the electron–hole correlations. This settles g_0 for any given $(R, n, \rho_{\rm eh})$ combination. Based on the discussion following equation (28), the largest possible peak amplitude of $g_{\mathbf{k},\mathbf{k}}$ is $\frac{1}{4}$ which yields vanishing $(1 - 2f_{\mathbf{k}})$ at the corresponding momentum.

Once g_0 produces a fixed $g_{\max}$, we only need to find which κ value produces the correct density for a given (R, n) combination. In other words, κ alters $\rho_{\rm eh}$ because it changes the width of $g_0\,\phi_{\mathbf{k}}$ whose peak amplitude is already fixed. Since we want to solve $\bar{E}_{\rm pro}$ for a given $(R, n, \rho_{\rm eh})$ combination, we solve the specific κ value iteratively. In more detail, we construct $f_{\mathbf{k}}$ by using $g_0\,\phi_{\mathbf{k}}$ as input to equation (28) for a fixed (R, n) as function of κ. We then find iteratively which κ satisfies the density condition (29).

Figure 6(a) presents the normalized electron–hole pair-correlation function $\Delta\bar{g}(r)$ for an electron–hole correlation strength of $g_{\max} = 0.24$ (shaded area) and $g_{\max} = \frac{1}{4}$ (dashed line).

The quantum droplet has $n = 4$ rings and a radius of $R = 90.8\,\text{nm}$ indicated by a vertical line. We assume that the electron–hole density is $\rho_{\text{eh}} = 2.5 \times 10^{10}\,\text{cm}^{-2}$ such that the iteration yields $\kappa = 1.1 \times 10^{7}\,\text{m}^{-1}$ ($\kappa = 1.7 \times 10^{6}\,\text{m}^{-1}$) for $g_{\max} = 0.24$ ($g_{\max} = \frac{1}{4}$), which settles the consistent quantum droplet configuration. We observe that $\Delta\bar{g}(r)$ has four rings including the half oscillation close to the origin which appears due to the Coulomb attraction between electrons and holes. Additionally, the electron–hole pair-correlation function is only non-zero up to the hard shell at $r = R$, according to equation (41). By comparing the results of $g_{\max} = 0.24$ and $\frac{1}{4}$, we note that the oscillation amplitude decreases slower as function of r with increasing $g_{\max}$ because the decay parameter κ is smaller for elevated $g_{\max}$.

The corresponding self-consistently computed electron–hole distribution $f_{\mathbf{k}}$ and correlation $g_{\mathbf{k},\mathbf{k}}$ are plotted in figure 6(b) as black and red lines, respectively for $g_{\max} = 0.24$ (solid lines) and $g_{\max} = \frac{1}{4}$ (dashed lines). The electron–hole distribution $f_{\mathbf{k}}$ peaks to 0.4 (0.5) at $k = 1.3 \times 10^{8}\,\text{m}^{-1}$ for $g_{\max} = 0.24$ ($g_{\max} = \frac{1}{4}$). We see that the peak of $f_{\mathbf{k}}$ sharpens as $g_{\max}$ is increased. Interestingly, $f_{\mathbf{k}}$ and $g_{\mathbf{k},\mathbf{k}}$ show small oscillations indicated by vertical lines whose amplitude becomes larger with increasing electron–hole correlation strength.

As we compare the $f_{\mathbf{k}}$ of the quantum droplets with that of the excitons (figure 4(b)), we note that quantum droplets exhibit a significant reduction of the Pauli blocking, i.e. $(1 - 2f_{\mathbf{k}})$, at small momenta. As a result, quantum droplets produce a stronger electron–hole attraction than excitons for low $\mathbf{k}$, which makes the formation of these quasi-particle states possible once the carrier density becomes large enough. Figure 6(c) presents the corresponding normalized ground-state wavefunctions $\psi_{\mathbf{k}}$. The wavefunction $\psi_{\mathbf{k}}$ is qualitatively different from the state obtained for both, the degenerate Fermi gas and excitons, presented in figures 3(b) and 4(c), respectively. In particular, the quantum droplet produces a $\psi_{\mathbf{k}}$ that has small oscillations for small k (vertical lines) which are synchronized with the oscillations of $f_{\mathbf{k}}$. Additionally, $f_{\mathbf{k}}$ shows a strong dip close to the inversion $k = 1.3 \times 10^{8}\,\text{m}^{-1}$. The dip becomes more pronounced as $g_{\max}$ is increased.

As discussed above, the largest possible peak amplitude of $g_{\mathbf{k},\mathbf{k}}$ is $\frac{1}{4}$. By approaching $g_{\max} = \frac{1}{4}$, the energy per excited electron–hole pair $\bar{E}_{\text{pro}}$ decreases slightly from $\bar{E}_{\text{pro}} = -10.12$ to $-10.14\,\text{meV}$ as $g_{\max}$ is changed from 0.24 to $\frac{1}{4}$. In general, for a fixed quantum-droplet radius R, ring number n and electron–hole density ρ_{eh}, we find that $\bar{E}_{\text{pro}}$ is minimized when the amplitude of $g_{\mathbf{k},\mathbf{k}}$ is maximized. Consequently, we use $g_{\max} = \frac{1}{4}$ in our calculations to study the energetics of quantum droplets. For this particular case, the quantum droplet's ground state is 3.0 meV below the exciton energy, based on the analysis in section 3.2. Therefore, the quantum droplets are quasi-particles where electron–hole pairs are stronger bound than in excitons, as concluded above.

4.1. Density dependence

The quantum droplet ansatz (41) is based on a postulated radius R for the correlation bubble. Even though we find the self-consistent configuration ($f_{\mathbf{k}}$, $g_{\mathbf{k},\mathbf{k}}$) for each R, we still need to determine the stable quantum droplet configurations. As the main condition, the quantum droplet's pair-excitation energy must be lower than that of the excitons and the biexcitons.

In the formation scheme of macroscopic electron–hole droplets, these droplets emerge only after a critical density is exceeded [11]. In addition, stable droplets grow in size as the overall particle density is increased. Therefore, it is reasonable to assume that also quantum droplets share these properties. We use the simplest form where the area of the quantum droplet scales

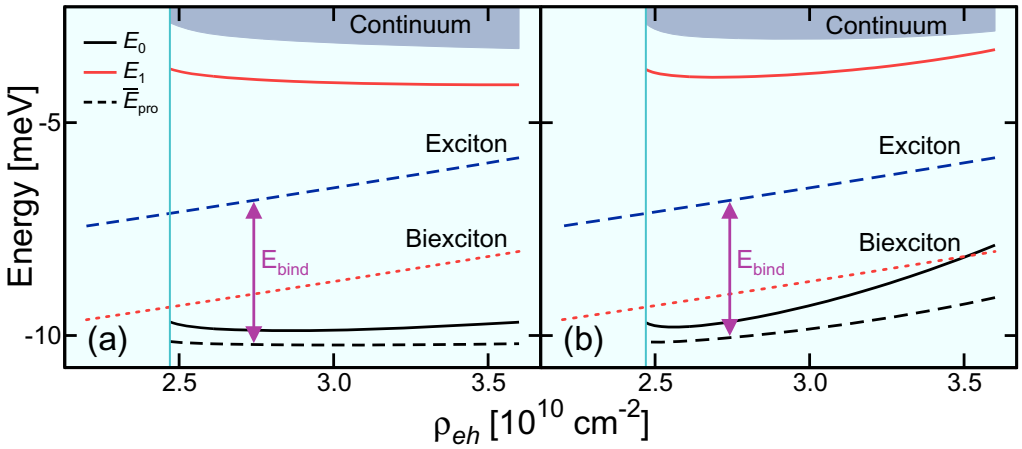

Figure 7. Energetics of quantum droplets. (a) The ground-state energy E_0 (black solid line), the first excited state E_1 (red solid line), the continuum (shaded area) and the energy per excited electron–hole pair (black dashed line) are presented as function of ρ_{eh}. The quantum droplet has $n = 4$ rings and $R = 90.8$ nm. The density-dependent exciton (dashed blue line) and biexciton-binding energy (dotted red line) are also plotted. (b) The corresponding result for quantum droplets with the density-dependent R defined in equation (42).

linearly with density. This condition connects the radius and density via

$$R = R_0\sqrt{\frac{\rho_{eh}}{\rho_0}}, \tag{42}$$

where R_0 is the radius at reference density ρ_0. To determine the effect of the droplet's ρ_{eh}-dependent size, we also compute the quantum droplet properties for a fixed $R = R_0$. In the actual calculations, we use $R_0 = 90.8$ nm and $\rho_0 = 2.5 \times 10^{10}\,\mathrm{cm}^{-2}$.

In both cases, we find the fully consistent pair ($f_{\mathbf{k}}$, $g_{\mathbf{k},\mathbf{k}'}$) as described in section 4 and compute the pair-excitation energy for different ρ_{eh}. Figure 7(a) shows the ground-state energy E_0 (solid black line), the first excited state E_1 (solid red line), the continuum (shaded area) and the energy per excited electron–hole pair (black dashed line) as function of ρ_{eh} when a constant-R quantum droplet has $n = 4$ rings. The corresponding result for the density-dependent R, defined by equation (42), is shown in figure 7(b). In both frames, the position of the density-dependent exciton (dashed blue line) and biexciton energy (dotted red line) are indicated, based on the calculation shown in figure 5 and the experimentally deduced biexciton binding energy 2.2 meV in [29].

For both R models, the quantum droplet's pair-excitation energy $\bar{E}_{pro}$ (black dashed line) is significantly lower than both the exciton and the biexciton energy, which makes the $(n = 4)$-ring quantum droplet energetically stable for densities exceeding $\rho_{eh} = 2.5 \times 10^{10}\,\mathrm{cm}^{-2}$. We also see that all excited states of the quantum droplets have a higher energy than the exciton. Therefore, only the quantum droplet's ground state is energetically stable enough to exist permanently. However, the quantum droplet state with $n = 4$ rings does not exist for an electron–hole density below $\rho_{eh} = 2.47 \times 10^{10}\,\mathrm{cm}^{-2}$ (vertical line) because this case corresponds to the smallest possible $\kappa = 0$. In other words, one cannot lower κ to make $f_{\mathbf{k}}$ narrower in order to produce ρ_{eh} smaller than $2.47 \times 10^{10}\,\mathrm{cm}^{-2}$. More generally, one can compute the threshold ρ_{eh} of a quantum

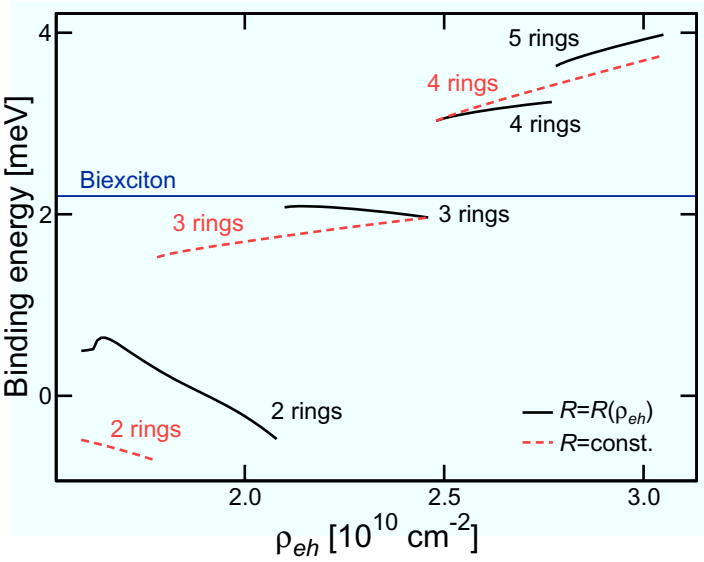

Figure 8. Ground-state energy of quantum droplets. The ground-state energy is presented as function of $\rho_{\rm eh}$ for a constant (dashed line) and density-dependent R (solid line). The biexciton-binding energy is indicated by the horizontal line.

droplet with n rings by setting κ to zero in equation (41) and by generating the corresponding $\phi_{\mathbf{k}}$, $g_{\mathbf{k},\mathbf{k}}$ and $f_{\mathbf{k}}$ via equation (27). Since $\phi_{\mathbf{k}}$ and $f_{\mathbf{k}}$ peak at k that is proportional to x_n, it is clear that $\rho_{\rm eh} \propto \int_0^\infty {\rm d}k\, k f_{\mathbf{k}}$ increases monotonically as function of n. Therefore, one finds quantum droplets with a higher ring number only at elevated densities.

4.2. *Ground-state energy*

To determine the quantum droplet's binding energy, we define

$$E_{\rm bind} \equiv \bar{E}_{\rm pro}(1{\rm s}) - \bar{E}_{\rm pro}({\rm droplet}), \tag{43}$$

where $\bar{E}_{\rm pro}(1{\rm s})$ and $\bar{E}_{\rm pro}({\rm droplet})$ are the ground-state energies of the exciton and the quantum droplet, respectively. Figure 8 presents $E_{\rm bind}$ for all possible ring numbers for both constant R (dashed line) and $\rho_{\rm eh}$-dependent R (solid line), as function of $\rho_{\rm eh}$. Here, we follow the lowest $E_{\rm bind}$ among all n-ring states as the ground state of the quantum droplet. As explained in section 4.1, each n-ring state appears as an individual threshold density is crossed. The horizontal line indicates the binding energy of the biexciton. We see that both droplet-radius configurations produce discrete energy bands. As the electron–hole density is increased, new energy levels appear as sharp transitions. Each transition increases the ring number n by one such that the ring number directly defines the quantum number for the discrete energy levels. We see that only quantum droplets with more or equal than four rings have a larger binding than biexcitons do, making one-, two- and three-ring quantum droplets instable. The constant R and the density-dependent R produce a qualitatively similar energy structure. As main differences, the constant R produces ring-to-ring transitions at higher densities and the energy bands spread to a wider energy range. For example, the energy range of the $n = 4$ energy band is [3.0, 3.8] meV for constant R while it is [3.0, 3.2] meV for the density-dependent R. In general, the actual stable droplet configuration has to be determined by experiments. Since the

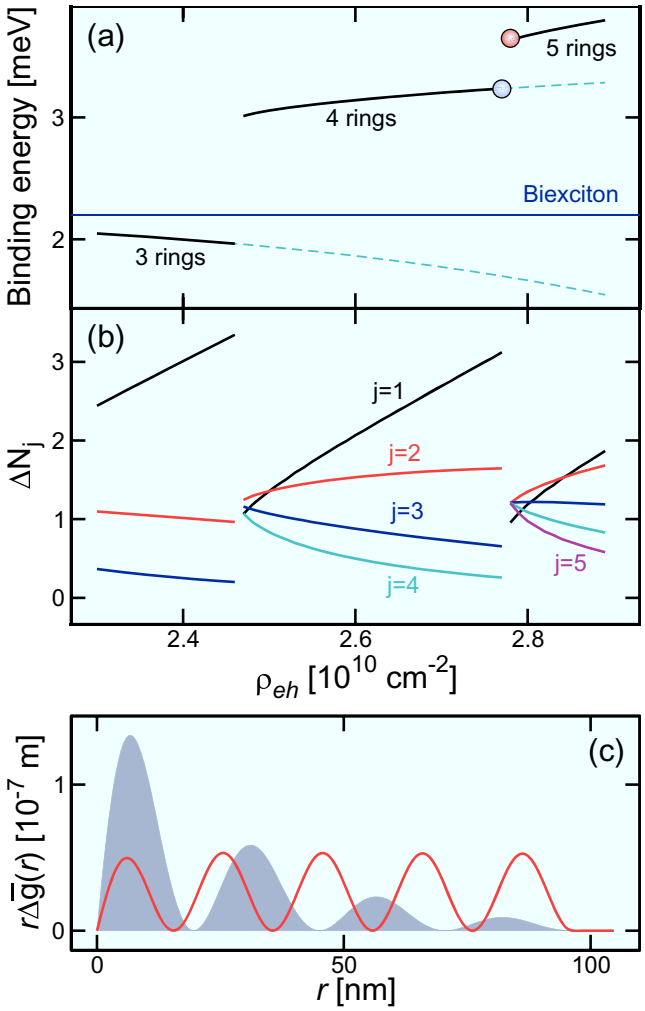

Figure 9. Properties of quantum droplets. (a) The ground-state energy (solid line) is presented as function of $\rho_{\rm eh}$ for the density-dependent R. The dashed lines denote excited states and the biexciton-binding energy is marked by the horizontal line. (b) Number of correlated electron–hole pairs within the jth ring as function $\rho_{\rm eh}$ from the first ($j = 1$) up to the fifth ($j = 5$) ring. (c) The electron–hole pair-correlation function $r\Delta\bar{g}(r)$ is shown before (shaded area) and after (solid line) the four-to-five-ring droplet transition. These cases are indicated by circles in frame (a).

density-dependent droplet radius is consistent with the properties of macroscopic electron–hole droplets, we use equation (42) to study the properties of quantum droplets.

Figure 9(a) shows again the ground-state energy of the quantum droplet as function of electron–hole density $\rho_{\rm eh}$ for the density-dependent R. The dashed lines continue the energy levels after the next higher quantum droplet state becomes the ground state. The biexciton-binding energy is indicated by a horizontal line. We see that the binding energy of the unstable ($n = 3$)-liquid state remains smaller than the biexciton-binding energy even at elevated $\rho_{\rm eh}$ making it instable at all densities. In contrast to that, $E_{\rm bind}$ of the ($n = 4$)- and ($n = 5$)-liquid

state is stronger than the biexciton value while it remains relatively stable as the electron–hole density is increased.

4.3. Ring structure of quantum droplets

We also can analyze the number of correlated electron–hole pairs within the jth ring of the quantum droplet. Since $S_{\rm drop}\int {\rm d}^2 r\,\Delta g(r) = S_{\rm drop}\,2\pi\int {\rm d}r\,r\Delta g(r)$ defines the total number of correlated pairs [15]:

$$\Delta N_j = S_{\rm drop}\,2\pi\int_{x_{j-1}}^{x_j} {\rm d}r\,r\Delta g(r) \tag{44}$$

is the number of correlated pairs within the jth ring when $S_{\rm drop} = \pi R^2$ is the area of the quantum droplet. Figure 9(b) shows ΔN_j as function of $\rho_{\rm eh}$ from the first up to the fifth ring. We see that the number of electron–hole pairs within the innermost rings becomes larger, while it decreases within the outermost rings, as $\rho_{\rm eh}$ is made larger. Interestingly, each ring has roughly the same number of electron–hole pairs after the n-ring droplet has become the ground state via a sharp transition, compare with figure 9(a). More precisely, ΔN_j is close to one such that the nth quantum droplet state has about n electron–hole pairs after the transition. Consequently, the n-ring quantum droplet has roughly n electron–hole pairs. Therefore, already the first stable quantum droplet with $n = 4$ rings has four correlated electrons and holes showing that it is a highly correlated quasi-particle. As derived in appendix E, one can solve analytically that for ring numbers up to $n = 3$ the nth quantum droplet state has very close n correlated electron–hole pairs while the ratio $\Delta N/n$ converges toward 1.2 for a very large ring number.

Figure 9(c) presents examples for the electron–hole pair-correlation function $r\Delta\bar{g}(r)$ before (shaded area) and after (solid line) the four-to-five-ring droplet transition. The corresponding binding energies and electron–hole densities are indicated with circles in figure 9(a). Before the transition, the oscillation amplitude of $r\Delta\bar{g}(r)$ decreases as function of r while after the transition the oscillation amplitude stays almost constant indicating that the decay parameter κ is close to zero, just after the transition. This is consistent with our earlier observation that a n-ring quantum droplet emerges only above a threshold density matching the density of the $\kappa = 0$ state.

5. Influence of electron–electron and hole–hole correlations

So far, we have analyzed the properties of quantum droplets without electron–electron and hole–hole correlations based on the assumption that electron–hole correlations dominate the energetics. We will next show that this scenario is plausible also in dense interacting electron–hole systems. We start by reorganizing the carrier–carrier correlations $c^{\mathbf{q},\mathbf{k}',\mathbf{k}}_{\lambda,\lambda;\lambda,\lambda}$, defined in equation (19), into $\Delta\langle a^\dagger_{\lambda,\mathbf{K}+\mathbf{p}} a^\dagger_{\lambda,\mathbf{K}-\mathbf{p}} a_{\lambda,\mathbf{K}-\mathbf{p}'} a_{\lambda,\mathbf{K}+\mathbf{p}'}\rangle$ using $\mathbf{k} = \mathbf{K}+\mathbf{p}$, $\mathbf{k}' = \mathbf{K}-\mathbf{p}$ and $\mathbf{q} = \mathbf{p}-\mathbf{p}'$. In this form, we see that two annihilation (or creation) operators assign a correlated carrier pair that has a center-of-mass momentum of $2\hbar\,\mathbf{K}$. Like for electron–hole correlations, we concentrate on the case where the center-of-mass momentum of the correlated pairs vanishes

$$\Delta\langle a^\dagger_{\lambda,\mathbf{K}+\mathbf{p}} a^\dagger_{\lambda,\mathbf{K}-\mathbf{p}} a_{\lambda,\mathbf{K}-\mathbf{p}'} a_{\lambda,\mathbf{K}+\mathbf{p}'}\rangle \equiv -\delta_{\mathbf{K},0}\,F^\lambda_{\mathbf{p},\mathbf{p}'} \quad\Leftrightarrow\quad c^{\mathbf{q},\mathbf{k}',\mathbf{k}}_{\lambda,\lambda;\lambda,\lambda} = -\delta_{\mathbf{k}',-\mathbf{k}} F^\lambda_{\mathbf{k},\mathbf{k}-\mathbf{q}} \tag{45}$$

that follows from a straightforward substitution $\mathbf{K} = \frac{1}{2}(\mathbf{k}+\mathbf{k}')$, $\mathbf{p} = \frac{1}{2}(\mathbf{k}-\mathbf{k}')$ and $\mathbf{p}' = \frac{1}{2}(\mathbf{k}-\mathbf{k}')-\mathbf{q}$. Since the transformations $\mathbf{p}\to-\mathbf{p}$ and $\mathbf{p}'\to-\mathbf{p}'$ correspond to exchanging creation

and annihilation operators in $c_{\lambda,\lambda;\lambda,\lambda}$, respectively, the $F^{\lambda}_{\mathbf{p},\mathbf{p}'}$ function must change its sign with these transformations due to the Fermionic antisymmetry. In other words, $F^{\lambda}_{\mathbf{p},\mathbf{p}'}$ must satisfy

$$F^{\lambda}_{-\mathbf{p},\mathbf{p}'} = F^{\lambda}_{\mathbf{p},-\mathbf{p}'} = -F^{\lambda}_{\mathbf{p},\mathbf{p}'} = -F^{\lambda}_{-\mathbf{p},-\mathbf{p}'}, \tag{46}$$

when the sign of the momentum is changed.

Like for electron–hole correlations, carrier–carrier effects can be described through the corresponding pair-correlation function

$$g_{\lambda}(\mathbf{r}) \equiv \langle \Psi^{\dagger}_{\lambda}(\mathbf{r})\Psi^{\dagger}_{\lambda}(0)\Psi_{\lambda}(0)\Psi_{\lambda}(\mathbf{r})\rangle = \rho^2_{\lambda} - f^2_{\lambda}(\mathbf{r}) + \Delta g_{\lambda}(\mathbf{r}), \tag{47}$$

$$f_{\lambda}(\mathbf{r}) \equiv \frac{1}{S}\sum_{\mathbf{k}} f^{\lambda}_{\mathbf{k}}\, \mathrm{e}^{-\mathrm{i}\mathbf{k}\cdot\mathbf{r}} \quad \text{with} \quad \lambda = \mathrm{e}, \mathrm{h}, \tag{48}$$

where we have applied homogeneous conditions, used the definition (3), and introduced $f_{\lambda}(\mathbf{r})$ as the Fourier transformation of $f^{\lambda}_{\mathbf{k}}$. The first term describes again a plasma contribution analogously to the first part in the electron–hole pair-correlation function (22). The correlated contribution is defined by

$$\begin{aligned}\Delta g_{\lambda}(\mathbf{r}) &\equiv \frac{1}{S^2}\sum_{\mathbf{K},\mathbf{p},\mathbf{p}'} \Delta\langle a^{\dagger}_{\lambda,\mathbf{K}+\mathbf{p}} a^{\dagger}_{\lambda,\mathbf{K}-\mathbf{p}} a_{\lambda,\mathbf{K}-\mathbf{p}'} a_{\lambda,\mathbf{K}+\mathbf{p}'}\rangle\, \mathrm{e}^{-\mathrm{i}(\mathbf{p}-\mathbf{p}')\cdot\mathbf{r}} \\ &= -\frac{1}{S^2}\sum_{\mathbf{p},\mathbf{p}'} F^{\lambda}_{\mathbf{p},\mathbf{p}'}\, \mathrm{e}^{-\mathrm{i}(\mathbf{p}-\mathbf{p}')\cdot\mathbf{r}},\end{aligned} \tag{49}$$

where we have applied the condition (45). We note that $\Delta g_{\lambda}(\mathbf{r})$ vanishes at $\mathbf{r} = 0$ due to the Pauli-exclusion principle among Fermions, enforced by equation (46).

Due to the conservation law (26), the electron and hole distributions $f^{\mathrm{e}}_{\mathbf{k}}$ and $f^{\mathrm{h}}_{\mathbf{k}}$ become different only when the electron–electron and hole–hole correlations are different. To study how the carrier–carrier correlations modify the overall energetics, we assume identical electron–electron and hole–hole correlations $F^{\mathrm{e}}_{\mathbf{p},\mathbf{p}'} = F^{\mathrm{h}}_{\mathbf{p},\mathbf{p}'}$ to simplify the book-keeping. With this choice, equations (26) and (45) imply identical distributions that satisfy

$$\left(f_{\mathbf{k}} - \tfrac{1}{2}\right)^2 + g_{\mathbf{k},\mathbf{k}} + F_{\mathbf{k},\mathbf{k}} = \tfrac{1}{4}, \qquad F_{\mathbf{k},\mathbf{k}} \equiv F^{\mathrm{e}}_{\mathbf{k},\mathbf{k}} = F^{\mathrm{h}}_{\mathbf{k},\mathbf{k}}. \tag{50}$$

We see that also carrier–carrier correlations modify $f_{\mathbf{k}}$ via a diagonal $F_{\mathbf{k},\mathbf{k}}$, just like $g_{\mathbf{k},\mathbf{k}}$.

In the same way, the generalized Wannier equation (35) is modified through the presence of carrier–carrier correlations in the form of equation (46). By inserting equations (45) and (50) into equation (35), the original $E_{\mathbf{k}}$ and $V^{\mathrm{eff}}_{\mathbf{k},\mathbf{k}'}$ can simply be replaced by

$$E_{\mathbf{k}} \equiv \left[\frac{\hbar^2\mathbf{k}^2}{2\mu} - 2\sum_{\mathbf{k}'} V_{\mathbf{k}-\mathbf{k}'} f_{\mathbf{k}'}\right](1-2f_{\mathbf{k}}) + 2\sum_{\mathbf{k}'} V_{\mathbf{k}-\mathbf{k}'}\left(g_{\mathbf{k},\mathbf{k}'} + F_{\mathbf{k},\mathbf{k}'}\right), \tag{51}$$

$$V^{\mathrm{eff}}_{\mathbf{k},\mathbf{k}'} \equiv (1-2f_{\mathbf{k}})\, V_{\mathbf{k}-\mathbf{k}'}\, (1-2f_{\mathbf{k}'}) + 2\left(g_{\mathbf{k},\mathbf{k}'} + F_{\mathbf{k},\mathbf{k}'}\right) V_{\mathbf{k}-\mathbf{k}'} \tag{52}$$

to fully account for the carrier–carrier contributions.

As a general property, the repulsive Coulomb interaction tends to extend the $\mathbf{r}$-range where the presence of multiple carriers is Pauli blocked. In other words, carrier–carrier correlations build up to form a correlation hole to $g_{\lambda}(\mathbf{r})$. To describe this principle effect, we use an ansatz

$$F_{\mathbf{k},\mathbf{k}'} \equiv F^2_0 \cos(\theta_{\mathbf{k}} - \theta_{\mathbf{k}'})\, \mathrm{e}^{-l_{\mathrm{c}}(|\mathbf{k}|-|\mathbf{k}'|)} \tag{53}$$

that satisfies the antisymmetry relations (46). The strength of the correlation is determined by F_0 and l_c corresponds to a correlation length. As equation (53) is inserted to equation (49), a straightforward integration yields

$$\Delta g_\lambda(r) = -\frac{F_0^2}{(2\pi)^2}\frac{r^2}{(l_c^2+r^2)^3}, \tag{54}$$

which is rotational symmetric and vanishes at $\mathbf{r} = 0$, as it should for homogeneous Fermions.

To compute the quasi-particle energetics with carrier–carrier correlations, we use the same quantum droplet state (41) as computed for vanishing carrier–carrier correlations in section 4, i.e. we keep the quantum droplet radius R, ring number n and decay parameter κ unchanged. For a given combination (F_0, l_c), we then adjust the strength of the electron–hole correlations g_0 such that $g_{\mathbf{k},\mathbf{k}} + F_{\mathbf{k},\mathbf{k}}$ is maximized, i.e. $\max[g_{\mathbf{k},\mathbf{k}} + F_{\mathbf{k},\mathbf{k}}] = \frac{1}{4}$, according to equation (50). In analogy to section 4, this yields a vanishing $(1-2f_{\mathbf{k}})$ at one momentum state. Since $F_{\mathbf{k},\mathbf{k}}$ is positive, the presence of carrier–carrier correlations must be compensated by reducing the magnitude of the electron–hole correlations $g_{\mathbf{k},\mathbf{k}}$. Additionally, equation (50) modifies the electron–hole distribution $f_{\mathbf{k}}$ and the electron–hole density in comparison to the case with vanishing $F_{\mathbf{k},\mathbf{k}}$.

Figure 10(a) shows the normalized electron–hole pair-correlation function $\Delta\bar{g}(r)$ for vanishing carrier–carrier correlations ($F_0 = 0$, black line). The vertical lines indicate the maxima of $\Delta\bar{g}(r)$ identifying the centers of the liquid-state rings. The quantum droplet state has a radius of $R = 90.8\,\text{nm}$, $n = 4$ rings and an electron–hole density of $\rho_{\text{eh}} = 2.5\times10^{10}\,\text{cm}^{-2}$. The corresponding result for non-vanishing carrier–carrier correlations with $F_0 = 0.3$ and $l_c = 12.5\,\text{nm}$ is plotted as red line. The presence of carrier–carrier correlations increases the electron–hole density to $\rho_{\text{eh}} = 2.7\times10^{10}\,\text{cm}^{-2}$ due to the normalization procedure described above. We see that the presence of carrier–carrier correlations reduces the amplitude of the ring-state oscillations in $\Delta\bar{g}(r)$ only slightly. This suggests that carrier–carrier correlations play a minor role in the build up of electron–hole correlations in quantum droplets.

The corresponding normalized carrier–carrier pair-correlation function $\bar{g}_\lambda(r) \equiv g_\lambda(r)/\rho_{\text{eh}}^2$ is presented in figure 10(b) without ($F_0 = 0$, black line) and with ($F_0 = 0.3$, red line) carrier–carrier correlations. Additionally, the pure correlated contribution $-\Delta\bar{g}_\lambda(r) \equiv -\Delta g_\lambda(r)/\rho_{\text{eh}}^2$ for $F_0 = 0.3$ is shown as a shaded area. Even without carrier–carrier correlations, $\bar{g}_\lambda(r)$ shows a range of Pauli blocked carriers at short distances followed by the Friedel oscillations [33]. Interestingly, $\bar{g}_\lambda(r)$ dips at exactly the same positions where $\Delta\bar{g}(r)$ peaks indicated by vertical lines in figure 10. Consequently, the carriers try to avoid each other within the rings of the quantum droplets, which is clearly related to the Fermion character of electrons. We observe that the presence of $\Delta\bar{g}_\lambda(r)$ increases the range of Pauli-blocked carriers. To show the range of Pauli blocking, the inset of figure 10(b) plots the same data up to the first Friedel oscillation $r = 26.6\,\text{nm}$. To quantify Pauli blocking, we determine the half-width value where $g_\lambda(r_{1/2}) = \frac{1}{2}\rho_{\text{eh}}^2$. We find that $r_{1/2}$ increases from 8.8 nm for $F_0 = 0$ to 11.2 nm for $F_0 = 0.3$, i.e. the correlation hole increases the range of Pauli blocking by roughly 27% which is significant.

In the next step, we compute the ground-state energy of pair excitations from the generalized Wannier equation (35) with the $f_{\mathbf{k}}$, $g_{\mathbf{k},\mathbf{k}'}$ and $F_{\mathbf{k},\mathbf{k}'}$ entries (51) and (52). The actual energy per excited particle follows from equation (37) and this is compared against the exciton binding deduced as in section 3.2. The results produce a quantum droplet energy that grows from 2.99 to 3.08 meV as the carrier–carrier correlations are included. The small increase shows that the correlated arrangement of the carriers saves energy. However, carrier–carrier correlations

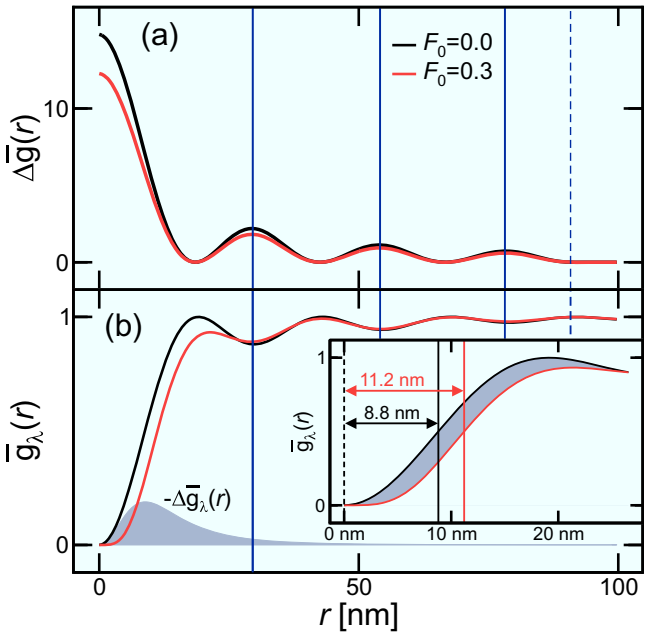

Figure 10. Effect of carrier–carrier correlations on the quantum-droplet energetics. (a) Normalized electron–hole pair-correlation function without ($F_0 = 0$, black line) and with ($F_0 = 0.3$, $l_c = 12.5$ nm, red line) carrier–carrier correlations. The quantum-droplet state has $R = 90.8$ nm, $n = 4$ rings and $\rho_{eh} = 2.5 \times 10^{10}$ nm ($\rho_{eh} = 2.7 \times 10^{10}$ nm) for $F_0 = 0$ ($F_0 = 0.3$). The maxima of $\Delta\bar{g}(r)$ are indicated by the vertical lines. (b) The corresponding normalized carrier–carrier pair-correlation function $\bar{g}_\lambda(r)$. The pure correlated contribution $-\Delta\bar{g}_\lambda(r)$ for $F_0 = 0.3$ is shown as a shaded area. Inset: same data as in (b) up to the first Friedel oscillation $r = 26.6$ nm together with the half-widths.

change the quantum droplet binding only by 3.3%, for the studied case. In other words, even a large correlation hole $\Delta g_\lambda(\mathbf{r})$ cannot affect much the energetics of the quantum droplet, which justifies the assumption of neglecting carrier–carrier correlations for quantum droplets.

6. Discussion

We have developed a systematic method to compute the pair-excitation energetics of many-body states based on the correlation-function formulation of quasi-particles. In particular, we have generalized the Wannier equation to compute the energy per excited electron–hole pair of a many-body state probed by a weak pair excitation of a quasi-particle. As an unconventional aspect, we determine the many-body state via the pair-correlation function $g(\mathbf{r})$ and work out the lower-order expectation values self-consistently, based on $g(\mathbf{r})$, not the other way around. As a major benefit, $g(\mathbf{r})$ characterizes the many-body state and its energetics, which allows us to identify the properties of different quasi-particles directly.

We have applied the scheme to study especially the energetics and properties of quantum droplets as a new quasi-particle. Our computations show that the pair-excitation energetics of quantum droplets has discrete bands that appear as sharp transitions. Additionally, each ring

contains roughly one electron–hole pair and only quantum droplets with more than four rings, i.e. electron–hole pairs are stable. We also show that the energy structure of quantum droplets originates dominantly from electron–hole correlations because the carrier–carrier correlations increase the binding energy of quantum droplets only slightly.

We also have checked that having a soft wall for the quantum droplet changes the energetics only slightly. More specifically, we allowed the pair-correlation function to tunnel into the wall region where it decayed exponentially, as is characteristic for a soft wall. For tunneling depths of 5 nm, the binding energy of the electron–hole droplet decreases only by 1%. Therefore, the explicit nature of the electron–hole confinement does not play a significant role for quantum droplets.

The developed method can be used more generally to determine the characteristic quasi-particle energies based on the correlation function. As further examples, we successfully analyze the energetics of the degenerate Fermi gas and high-density excitons. We also have extended the method to analyze coherent quasi-particles. As possible new directions, one can study different pair-excitation schemes to analyze the role of, e.g. spin. In this connection, one expects to detect bonding and antibonding branches for quasi-particles such as biexcitons. In general, the approach is limited only by the user's knowledge of the pair-correlation function. It also might be interesting to develop the approach to the direction where quasi-particles are identified via N-particle correlations to systematically analyze how the details of highly correlated states affect the excitation energetics and the response in general.

Acknowledgment

MK acknowledges support from the Deutsche Forschungsgemeinschaft.

Appendix A. Connection of correlations and expectation values

We first analyze a normally ordered $(N+1)$-particle expectation value

$$\langle \hat{N}+1\rangle \equiv \langle a^{\dagger}_{\lambda_1,\mathbf{k}_1}\ldots a^{\dagger}_{\lambda_N,\mathbf{k}_N}\,\hat{N}_{\mathrm{tot}}\,a_{\lambda_N,\mathbf{k}_N}\ldots a_{\lambda_1,\mathbf{k}_1}\rangle \tag{A.1}$$

that contains the total number operator $\hat{N}_{\mathrm{tot}} \equiv \sum_{\mathbf{k},\lambda} a^{\dagger}_{\lambda,\mathbf{k}} a_{\lambda,\mathbf{k}}$. Since $\hat{N}_{\mathrm{tot}}$ contains *all* electronic states, it produces

$$\hat{N}_{\mathrm{tot}}\hat{\rho}_{\mathcal{N}} = \mathcal{N}\hat{\rho}_{\mathcal{N}} \tag{A.2}$$

for all states $\hat{\rho}_{\mathcal{N}}$ containing $\mathcal{N}$ carriers within all bands of the system. Since we may consider only cases where the total number of carriers is conserved, we may limit the analysis to the states $\hat{\rho}_{\mathcal{N}}$ from here on.

By applying the commutator relation $[\hat{N}_{\mathrm{tot}}, a_{\lambda,\mathbf{k}}]_- = -a_{\lambda,\mathbf{k}}$ N times, equation (A.1) becomes

$$\langle \hat{N}+1\rangle = -N\langle \hat{O}_N\rangle + \langle \hat{O}_N\hat{N}_{\mathrm{tot}}\rangle \quad \text{with} \quad \hat{O}_N \equiv a^{\dagger}_{\lambda_1,\mathbf{k}_1}\ldots a^{\dagger}_{\lambda_N,\mathbf{k}_N} a_{\lambda_N,\mathbf{k}_N}\ldots a_{\lambda_1,\mathbf{k}_1}. \tag{A.3}$$

Using the property (A.2), we find

$$\langle \hat{O}_N\hat{N}_{\mathrm{tot}}\rangle = \mathrm{Tr}[\hat{O}_N\hat{N}_{\mathrm{tot}}\hat{\rho}_{\mathcal{N}}] = \mathrm{Tr}[\hat{O}_N\mathcal{N}\hat{\rho}_{\mathcal{N}}] = \mathcal{N}\langle \hat{O}_N\rangle. \tag{A.4}$$

By combining the result (A.4) with (A.1) and (A.3), we obtain a general reduction formula [34]

$$\sum_{\mathbf{k}',\lambda'}\langle a^\dagger_{\lambda_1,\mathbf{k}_1}\ldots a^\dagger_{\lambda_N,\mathbf{k}_N}a^\dagger_{\lambda',\mathbf{k}'}a_{\lambda',\mathbf{k}'}a_{\lambda_N,\mathbf{k}_N}\ldots a_{\lambda_1,\mathbf{k}_1}\rangle=(\mathcal{N}-N)\langle\hat{O}_N\rangle \tag{A.5}$$

that directly connects N and $(N+1)$-particle expectation values.

For $N=1$, equation (A.5) becomes

$$\sum_{\mathbf{k}',\lambda'}\langle a^\dagger_{\lambda,\mathbf{k}}a^\dagger_{\lambda',\mathbf{k}'}a_{\lambda',\mathbf{k}'}a_{\lambda,\mathbf{k}}\rangle=(\mathcal{N}-1)\langle a^\dagger_{\lambda,\mathbf{k}}a_{\lambda,\mathbf{k}}\rangle\,. \tag{A.6}$$

We then express the two-particle contribution exactly in terms of the Hartree–Fock factorization [1] and the two-particle correlations (19) and assume homogeneous conditions where all coherences vanish. By using a two-band model, equation (A.6) yields then

$$\begin{aligned}\left(f^{\mathrm{e}}_{\mathbf{k}}-\frac{1}{2}\right)^2+\sum_{\mathbf{k}'}\left(c^{\mathbf{k}-\mathbf{k}',\mathbf{k}',\mathbf{k}}_{\mathrm{eh}}-c^{0,\mathbf{k}',\mathbf{k}}_{\mathrm{c,c;c,c}}\right)&=\frac{1}{4},\\ \left(f^{\mathrm{h}}_{\mathbf{k}}-\frac{1}{2}\right)^2+\sum_{\mathbf{k}'}\left(c^{\mathbf{k}'-\mathbf{k},\mathbf{k},\mathbf{k}'}_{\mathrm{eh}}-c^{0,\mathbf{k}',\mathbf{k}}_{\mathrm{v,v;v,v}}\right)&=\frac{1}{4}\end{aligned} \tag{A.7}$$

for electrons ($\lambda=c$) and holes ($\lambda=v$), respectively. With the help of equation (21), equation (A.7) casts into the form

$$\left(f^{\mathrm{e}}_{\mathbf{k}}-\frac{1}{2}\right)^2+g_{\mathbf{k},\mathbf{k}}-\sum_{\mathbf{k}'}c^{0,\mathbf{k}',\mathbf{k}}_{c,c;c,c}=\frac{1}{4},\quad\left(f^{\mathrm{h}}_{\mathbf{k}}-\frac{1}{2}\right)^2+g_{\mathbf{k},\mathbf{k}}-\sum_{\mathbf{k}'}c^{0,\mathbf{k}',\mathbf{k}}_{v,v;v,v}=\frac{1}{4}, \tag{A.8}$$

that connects the density distributions with the pair-wise correlations.

Appendix B. Probe-induced quantities

To compute the probe-induced electron–hole density and polarization, we use the following general properties of the displacement operator (7) [1, 15]:

$$\begin{aligned}D^\dagger[\psi]a_{\mathrm{v},\mathbf{k}}D[\psi]&=\cos(\varepsilon\,|\psi_{\mathbf{k}}|)a_{\mathrm{v},\mathbf{k}}-\mathrm{e}^{-\mathrm{i}\varphi_{\mathbf{k}}}\sin(\varepsilon\,|\psi_{\mathbf{k}}|)a_{\mathrm{c},\mathbf{k}},\\ D^\dagger[\psi]a_{\mathrm{c},\mathbf{k}}D[\psi]&=\cos(\varepsilon\,|\psi_{\mathbf{k}}|)a_{\mathrm{c},\mathbf{k}}+\mathrm{e}^{\mathrm{i}\varphi_{\mathbf{k}}}\sin(\varepsilon\,|\psi_{\mathbf{k}}|)a_{\mathrm{v},\mathbf{k}}.\end{aligned} \tag{B.1}$$

Transformation (B.1) allows us to construct the density- and polarization-induced pair excitations exactly. More specifically, we start from the expectation value

$$\langle a^\dagger_{\lambda,\mathbf{k}}a_{\lambda',\mathbf{k}}\rangle_\psi\equiv\mathrm{Tr}\left[a^\dagger_{\lambda,\mathbf{k}}a_{\lambda',\mathbf{k}}\hat{D}[\psi]\hat{\rho}_{\mathrm{MB}}\hat{D}^\dagger[\psi]\right]=\mathrm{Tr}\left[\hat{D}^\dagger[\psi]a^\dagger_{\lambda,\mathbf{k}}\hat{D}[\psi]\hat{D}^\dagger[\psi]a_{\lambda',\mathbf{k}}\hat{D}[\psi]\hat{\rho}_{\mathrm{MB}}\right], \tag{B.2}$$

where we have utilized cyclic permutations under the trace and the unitary of the displacement operator (7).

To compute the pair-excitation energy, we have to compute how all those single-particle expectation values and two-particle correlations that appear in equation (18) are modified by the pair excitation. By inserting transformation (B.1) into equation (B.2), we can express any modified single-particle expectation value in terms of ε, $\psi_{\mathbf{k}}$ and $f_{\mathbf{k}}$. The change in density and polarization becomes then

$$\begin{aligned} f_{\mathbf{k},\psi} &\equiv \langle a^{\dagger}_{\mathrm{c},\mathbf{k}} a_{\mathrm{c},\mathbf{k}} \rangle_{\psi} - f^{\mathrm{e}}_{\mathbf{k}} = \langle a_{\mathrm{v},\mathbf{k}} a^{\dagger}_{\mathrm{v},\mathbf{k}} \rangle_{\psi} - f^{\mathrm{h}}_{\mathbf{k}} = \sin^2(\varepsilon\,|\psi_{\mathbf{k}}|)\left(1 - f^{\mathrm{e}}_{\mathbf{k}} - f^{\mathrm{h}}_{\mathbf{k}}\right), \\ P_{\mathbf{k},\psi} &\equiv \langle a^{\dagger}_{\mathrm{v},\mathbf{k}} a_{\mathrm{c},\mathbf{k}} \rangle_{\psi} = \mathrm{e}^{\mathrm{i}\varphi_{\mathbf{k}}} \sin(\varepsilon\,|\psi_{\mathbf{k}}|)\cos(\varepsilon\,|\psi_{\mathbf{k}}|)\left(1 - f^{\mathrm{e}}_{\mathbf{k}} - f^{\mathrm{h}}_{\mathbf{k}}\right), \end{aligned} \tag{B.3}$$

respectively. Since the many-body state $\hat{\rho}_{\mathrm{MB}}$ is probed by a weak laser pulse, we apply the weak-excitation limit $\varepsilon \ll 1$, producing

$$P_{\mathbf{k},\psi} = \left(1 - f^{\mathrm{e}}_{\mathbf{k}} - f^{\mathrm{h}}_{\mathbf{k}}\right)\varepsilon\,\psi_{\mathbf{k}} + \mathcal{O}(\varepsilon^3), \qquad f_{\mathbf{k},\psi} = \left(1 - f^{\mathrm{e}}_{\mathbf{k}} - f^{\mathrm{h}}_{\mathbf{k}}\right)\varepsilon^2\,|\psi_{\mathbf{k}}|^2 + \mathcal{O}(\varepsilon^3) \tag{B.4}$$

to the leading order.

Following the same derivation steps as above, we find that the pair excitations change the electron–hole correlation by

$$\begin{aligned} c^{\mathbf{q},\mathbf{k}',\mathbf{k}}_{\mathrm{eh},\psi} &\equiv \Delta\langle a^{\dagger}_{\mathrm{c},\mathbf{k}} a^{\dagger}_{\mathrm{v},\mathbf{k}'} a_{\mathrm{c},\mathbf{k}'+\mathbf{q}} a_{\mathrm{v},\mathbf{k}-\mathbf{q}} \rangle_{\psi} - c^{\mathbf{q},\mathbf{k}',\mathbf{k}}_{\mathrm{eh}} \\ &= \varepsilon\left[c^{-\mathbf{q},\mathbf{k},\mathbf{k}'}_{\mathrm{v},\mathrm{v};\mathrm{v},\mathrm{c}}\,\psi^{\star}_{\mathbf{k}} + \left(c^{-\mathbf{q},\mathbf{k}'-\mathbf{q},\mathbf{k}+\mathbf{q}}_{\mathrm{v},\mathrm{v};\mathrm{v},\mathrm{c}}\right)^{\star}\psi_{\mathbf{k}'+\mathbf{q}} - c^{-\mathbf{q},\mathbf{k},\mathbf{k}'}_{\mathrm{v},\mathrm{c};\mathrm{c},\mathrm{c}}\,\psi^{\star}_{\mathbf{k}-\mathbf{q}} - \left(c^{-\mathbf{q},\mathbf{k}'-\mathbf{q},\mathbf{k}+\mathbf{q}}_{\mathrm{v},\mathrm{c};\mathrm{c},\mathrm{c}}\right)^{\star}\psi_{\mathbf{k}'}\right] \\ &\quad + \varepsilon^2\left[c^{-\mathbf{q}+\mathbf{k}-\mathbf{k}',\mathbf{k}',\mathbf{k}}_{\mathrm{eh}}\psi_{\mathbf{k}'+\mathbf{q}}\psi^{\star}_{\mathbf{k}-\mathbf{q}} + \left(c^{\mathbf{q}-\mathbf{k}+\mathbf{k}',\mathbf{k}'-\mathbf{q},\mathbf{k}+\mathbf{q}}_{\mathrm{eh}}\right)^{\star}\psi_{\mathbf{k}'}\psi^{\star}_{\mathbf{k}}\right. \\ &\quad -\tfrac{1}{2}c^{\mathbf{q},\mathbf{k}',\mathbf{k}}_{\mathrm{eh}}\left(|\psi_{\mathbf{k}}|^2 + |\psi_{\mathbf{k}'}|^2 + |\psi_{\mathbf{k}-\mathbf{q}}|^2 + |\psi_{\mathbf{k}'+\mathbf{q}}|^2\right) + c^{\mathbf{q},\mathbf{k}',\mathbf{k}}_{\mathrm{c},\mathrm{c};\mathrm{c},\mathrm{c}}\psi_{\mathbf{k}'}\psi^{\star}_{\mathbf{k}-\mathbf{q}} + c^{\mathbf{q},\mathbf{k}',\mathbf{k}}_{\mathrm{v},\mathrm{v};\mathrm{v},\mathrm{v}}\psi_{\mathbf{k}'+\mathbf{q}}\psi^{\star}_{\mathbf{k}} \\ &\quad \left. - c^{\mathbf{q},\mathbf{k}',\mathbf{k}}_{\mathrm{v},\mathrm{v};\mathrm{c},\mathrm{c}}\psi^{\star}_{\mathbf{k}}\psi^{\star}_{\mathbf{k}-\mathbf{q}} - \left(c^{-\mathbf{q},\mathbf{k}'-\mathbf{q},\mathbf{k}+\mathbf{q}}_{\mathrm{v},\mathrm{v};\mathrm{c},\mathrm{c}}\right)^{\star}\psi_{\mathbf{k}'}\psi_{\mathbf{k}'+\mathbf{q}}\right] + \mathcal{O}(\varepsilon^3) \end{aligned} \tag{B.5}$$

out of the initial many-body correlation $c^{\mathbf{q},\mathbf{k}',\mathbf{k}}_{\mathrm{eh}}$. Besides the correlations (19), equation (B.5) contains also coherent two-particle correlations:

$$\begin{aligned} c^{\mathbf{q},\mathbf{k}',\mathbf{k}}_{\mathrm{v},\mathrm{c};\mathrm{c},\mathrm{c}} &\equiv \Delta\langle a^{\dagger}_{\mathrm{v},\mathbf{k}} a^{\dagger}_{\mathrm{c},\mathbf{k}'} a_{\mathrm{c},\mathbf{k}'+\mathbf{q}} a_{\mathrm{c},\mathbf{k}-\mathbf{q}} \rangle, \quad c^{\mathbf{q},\mathbf{k}',\mathbf{k}}_{\mathrm{v},\mathrm{v};\mathrm{v},\mathrm{c}} \equiv \Delta\langle a^{\dagger}_{\mathrm{v},\mathbf{k}} a^{\dagger}_{\mathrm{v},\mathbf{k}'} a_{\mathrm{v},\mathbf{k}'+\mathbf{q}} a_{\mathrm{c},\mathbf{k}-\mathbf{q}} \rangle, \\ c^{\mathbf{q},\mathbf{k}',\mathbf{k}}_{\mathrm{v},\mathrm{v};\mathrm{c},\mathrm{c}} &\equiv \Delta\langle a^{\dagger}_{\mathrm{v},\mathbf{k}} a^{\dagger}_{\mathrm{v},\mathbf{k}'} a_{\mathrm{c},\mathbf{k}'+\mathbf{q}} a_{\mathrm{c},\mathbf{k}-\mathbf{q}} \rangle. \end{aligned} \tag{B.6}$$

From these, $c^{\mathbf{q},\mathbf{k}',\mathbf{k}}_{\mathrm{v},\mathrm{c};\mathrm{c},\mathrm{c}}$ and $c^{\mathbf{q},\mathbf{k}',\mathbf{k}}_{\mathrm{v},\mathrm{v};\mathrm{v},\mathrm{c}}$ describe correlations between polarization and density while $c^{\mathbf{q},\mathbf{k}',\mathbf{k}}_{\mathrm{v},\mathrm{v};\mathrm{c},\mathrm{c}}$ corresponds to the coherent biexciton amplitude. Therefore, also the coherent two-particle correlations (B.6) contribute to the pair-excitation spectroscopy even though they do not influence the initial many-body energy (18). The remaining $c^{\mathbf{q},\mathbf{k}',\mathbf{k}}_{\mathrm{c},\mathrm{c};\mathrm{c},\mathrm{c}}$ and $c^{\mathbf{q},\mathbf{k}',\mathbf{k}}_{\mathrm{v},\mathrm{v};\mathrm{v},\mathrm{v}}$ transform analogously. With the help of equations (B.4)–(B.5) we can then construct exactly the energy change (32) induced by the pair-wise excitations.

Appendix C. Generalized Wannier equation with coherences

As the exact relations (B.4) and (B.5) are inserted to the system energy (32), we obtain the pair-excitation energy exactly

$$E_{\rm pro}[\psi] = E^{\rm coh}_{\rm pro}[\psi] + E^{\rm inc}_{\rm pro}[\psi] + \mathcal{O}(\varepsilon^3),$$

$$E^{\rm coh}_{\rm pro} \equiv 2\varepsilon \sum_{\mathbf{k}} \left[\tilde{E}_{\mathbf{k}} {\rm Re}[P_{\mathbf{k}}\psi^{\star}_{\mathbf{k}}] - \sum_{\mathbf{k}'} V_{\mathbf{k}-\mathbf{k}'} \left(1 - f^{\rm e}_{\mathbf{k}} - f^{\rm h}_{\mathbf{k}}\right) {\rm Re}[P_{\mathbf{k}'}\psi^{\star}_{\mathbf{k}}] + {\rm Re}[\Gamma_{\mathbf{k}}\psi^{\star}_{\mathbf{k}}] \right]$$

$$-2\varepsilon^2 \sum_{\mathbf{k},\mathbf{k}'} V_{\mathbf{k}-\mathbf{k}'} \left({\rm Re}[P_{\mathbf{k}}P_{\mathbf{k}'}\psi^{\star}_{\mathbf{k}}(\psi^{\star}_{\mathbf{k}'} - \psi^{\star}_{\mathbf{k}})] - {\rm Re}[P_{\mathbf{k}}P^{\star}_{\mathbf{k}'}]|\psi_{\mathbf{k}}|^2 + {\rm Re}[P_{\mathbf{k}'}P^{\star}_{\mathbf{k}}\psi_{\mathbf{k}}\psi^{\star}_{\mathbf{k}'}] \right)$$

$$+\varepsilon^2 \sum_{\mathbf{k},\mathbf{k}',\mathbf{q}} V_{\mathbf{q}}\, {\rm Re}\left[\left(c^{\mathbf{q},\mathbf{k}',\mathbf{k}+\mathbf{q}}_{\rm v,v;c,c} + c^{\mathbf{q},\mathbf{k}',\mathbf{k}}_{\rm v,v;c,c} - 2c^{\mathbf{q},\mathbf{k}'-\mathbf{q},\mathbf{k}}_{\rm v,v;c,c} \right) \psi^{\star}_{\mathbf{k}}\psi^{\star}_{\mathbf{k}'} \right],$$

$$E^{\rm inc}_{\rm pro} \equiv \varepsilon^2 \sum_{\mathbf{k}} \bar{E}_{\mathbf{k}}|\psi_{\mathbf{k}}|^2 - \varepsilon^2 \sum_{\mathbf{k},\mathbf{k}'} \bar{V}^{\rm eff}_{\mathbf{k},\mathbf{k}'}\psi_{\mathbf{k}}\psi^{\star}_{\mathbf{k}'} + \varepsilon^2 \sum_{\mathbf{k},\mathbf{k}',\mathbf{q}} V_{\mathbf{q}} \left(c^{\mathbf{q},\mathbf{k}',\mathbf{k}}_{\rm c,c;c,c}\psi_{\mathbf{k}}\psi^{\star}_{\mathbf{k}-\mathbf{q}} + c^{\mathbf{q},\mathbf{k}',\mathbf{k}}_{\rm v,v;v,v}\psi_{\mathbf{k}-\mathbf{q}}\psi^{\star}_{\mathbf{k}} \right), \tag{C.1}$$

where we have divided $E_{\rm pro}[\psi]$ into coherent (coh) and incoherent (inc) contributions. The coherent contribution $E^{\rm coh}_{\rm pro}[\psi]$ includes

$$\Gamma_{\mathbf{k}} \equiv \sum_{\mathbf{k}',\mathbf{q},\lambda} V_{\mathbf{q}} \left[c^{\mathbf{q},\mathbf{k}',\mathbf{k}}_{\rm v,\lambda;\lambda,c} - \left(c^{\mathbf{q},\mathbf{k}',\mathbf{k}}_{\rm c,\lambda;\lambda,v} \right)^{\star} \right] \tag{C.2}$$

that is exactly the same as the microscopically described Coulomb scattering term in the semiconductor Bloch equations [15]. The incoherent part $E^{\rm inc}_{\rm pro}[\psi]$ and the coherent energy contain different renormalized kinetic energies

$$\bar{E}_{\mathbf{k}} \equiv \tilde{E}_{\mathbf{k}}\left(1 - f^{\rm e}_{\mathbf{k}} - f^{\rm h}_{\mathbf{k}}\right) + \sum_{\mathbf{k}',\mathbf{q}} V_{\mathbf{q}}\, {\rm Re}\left[c^{\mathbf{q},\mathbf{k}',\mathbf{k}}_{\rm c,c;c,c} + c^{\mathbf{q},\mathbf{k}',\mathbf{k}}_{\rm v,v;v,v} \right] + \sum_{\mathbf{k}',\mathbf{q}} V_{\mathbf{k}'+\mathbf{q}-\mathbf{k}} \left({\rm Re}\left[c^{\mathbf{q},\mathbf{k}',\mathbf{k}}_{\rm eh} \right] + {\rm Re}\left[c^{-\mathbf{q},\mathbf{k},\mathbf{k}'}_{\rm eh} \right] \right),$$

$$\tilde{E}_{\mathbf{k}} = \frac{\hbar^2\mathbf{k}^2}{2\mu} - \sum_{\mathbf{k}'} V_{\mathbf{k}-\mathbf{k}'} \left(f^{\rm e}_{\mathbf{k}'} + f^{\rm h}_{\mathbf{k}'} \right), \tag{C.3}$$

respectively. We also have identified the effective Coulomb matrix element

$$\bar{V}^{\rm eff}_{\mathbf{k},\mathbf{k}'} \equiv \left(1 - f^{\rm e}_{\mathbf{k}} - f^{\rm h}_{\mathbf{k}}\right) V_{\mathbf{k}-\mathbf{k}'} \left(1 - f^{\rm e}_{\mathbf{k}'} - f^{\rm h}_{\mathbf{k}'}\right) - \sum_{\mathbf{k}',\mathbf{q}} V_{\mathbf{k}-\mathbf{k}'} \left(c^{\mathbf{q},\mathbf{k}'-\mathbf{q},\mathbf{k}}_{\rm eh} + c^{\mathbf{q},\mathbf{k}',\mathbf{k}+\mathbf{q}}_{\rm eh} \right)$$

$$- \sum_{\mathbf{k}',\mathbf{q}} V_{\mathbf{q}} \left(c^{\mathbf{q},\mathbf{k}'-\mathbf{q},\mathbf{k}}_{\rm eh} + c^{\mathbf{q},\mathbf{k}',\mathbf{k}+\mathbf{q}}_{\rm eh} - c^{\mathbf{q},\mathbf{k}'-\mathbf{q},\mathbf{k}+\mathbf{q}}_{\rm eh} - c^{\mathbf{q},\mathbf{k}',\mathbf{k}}_{\rm eh} \right) \tag{C.4}$$

that contains the unscreened Coulomb interaction together with the phase-space filling contribution $(1 - f^{\rm e}_{\mathbf{k}} - f^{\rm h}_{\mathbf{k}})$ and electron–hole correlations $c^{\mathbf{q},\mathbf{k}',\mathbf{k}}_{\rm eh}$.

We then minimize the energy functional (C.1) as described in section 2 to find a condition for the ground-state excitations. As a result, we obtain

$$s_{\rm coh}+\varepsilon E_{\rm coh}[\psi]+\varepsilon E_{\rm inc}[\psi]=\varepsilon E_\lambda \psi_{\mathbf{k}},$$
$$s_{\rm coh}\equiv \tilde{E}_{\mathbf{k}}P_{\mathbf{k}}-\left(1-f^{\rm e}_{\mathbf{k}}-f^{\rm h}_{\mathbf{k}}\right)\sum_{\mathbf{k}'}V_{\mathbf{k}-\mathbf{k}'}P_{\mathbf{k}'}+\Gamma_{\mathbf{k}},$$

$$E_{\rm coh}[\psi]\equiv 2\sum_{\mathbf{k}'}V_{\mathbf{k}-\mathbf{k}'}\left(P_{\mathbf{k}}P_{\mathbf{k}'}\psi^\star_{\mathbf{k}}+{\rm Re}[P_{\mathbf{k}}P^\star_{\mathbf{k}'}]\psi_{\mathbf{k}}\right)-2\sum_{\mathbf{k}'}V_{\mathbf{k}-\mathbf{k}'}\left(P_{\mathbf{k}}P_{\mathbf{k}'}\psi^\star_{\mathbf{k}'}+P_{\mathbf{k}}P^\star_{\mathbf{k}'}\psi_{\mathbf{k}'}\right) \tag{C.5}$$
$$+\sum_{\mathbf{k}',\mathbf{q}}V_{\mathbf{q}}\left(c^{\mathbf{q},\mathbf{k}',\mathbf{k}}_{\rm v,v;c,c}-c^{\mathbf{q},\mathbf{k}',\mathbf{k}+\mathbf{q}}_{\rm v,v;c,c}\right)\left(\psi^\star_{\mathbf{k}'}-\psi^\star_{\mathbf{k}'+\mathbf{q}}\right),$$

$$E_{\rm inc}[\psi]\equiv \bar{E}_{\mathbf{k}}\psi_{\mathbf{k}}-\sum_{\mathbf{k}'}\bar{V}^{\rm eff}_{\mathbf{k},\mathbf{k}'}\psi_{\mathbf{k}'}+\sum_{\mathbf{k}',\mathbf{q}}V_{\mathbf{q}}\left(c^{\mathbf{q},\mathbf{k}',\mathbf{k}+\mathbf{q}}_{\rm c,c;c,c}\psi_{\mathbf{k}+\mathbf{q}}+c^{\mathbf{q},\mathbf{k}',\mathbf{k}}_{\rm v,v;v,v}\psi_{\mathbf{k}-\mathbf{q}}\right).$$

We see that the presence of coherences generates the coherent source term $s_{\rm coh}$ to the generalized Wannier equation which is the dominant contribution in equation (C.5). However, since $s_{\rm coh}$ corresponds exactly to the homogeneous part of the semiconductor Bloch equations [15], it vanishes for stationary $P_{\mathbf{k}}$. Therefore, the ground state of excitation must satisfy the generalized Wannier equation

$$E_{\rm coh}[\psi]+E_{\rm inc}[\psi]=E_\lambda\psi_{\mathbf{k}}. \tag{C.6}$$

In the main part, we analyze the pair excitations of incoherent many-body systems such that $E_{\rm coh}[\psi]$ is not present.

Appendix D. Self-consistent exciton solver

To find the wavefunction $\phi_{1{\rm s},\mathbf{k}}$ and the electron–hole distribution $f_{\mathbf{k}}$ that satisfy the ordinary density-dependent Wannier equation (40) and the conservation law (27), we define a gap equation as in [35]

$$\Delta_{\mathbf{k}}\equiv\sum_{\mathbf{k}'}V_{\mathbf{k}-\mathbf{k}'}\phi_{1{\rm s},\mathbf{k}'},\quad \epsilon_{\mathbf{k}}\equiv\frac{1}{2}\left(\tilde{E}_{\mathbf{k}}-E_{1{\rm s}}\right),\quad \Omega_{\mathbf{k}}=\sqrt{\epsilon^2_{\mathbf{k}}+\Delta^2_{\mathbf{k}}}. \tag{D.1}$$

As a result, we obtain the integral equations

$$\phi_{1{\rm s},\mathbf{k}}=\frac{1}{2}\frac{\Delta_{\mathbf{k}}}{\Omega_{\mathbf{k}}},\quad f_{\mathbf{k}}=\frac{1}{2}\left(1-\frac{\epsilon_{\mathbf{k}}}{\Omega_{\mathbf{k}}}\right) \tag{D.2}$$

which simultaneously satisfy the ordinary density-dependent Wannier equation (40) and the conservation law (27). Equations (D.1) and (D.2) are solved numerically by using the iteration steps

$$\Delta^{(n+1)}_{\mathbf{k}}=\sum_{\mathbf{k}'}V_{\mathbf{k}-\mathbf{k}'}\phi^{(n)}_{1{\rm s},\mathbf{k}'},\quad \epsilon^{(n+1)}_{\mathbf{k}}=\frac{1}{2}\left(\frac{\hbar^2\mathbf{k}^2}{2\mu}-E_{1{\rm s}}\right),$$
$$\Omega^{(n+1)}_{\mathbf{k}}=\sqrt{(\epsilon^{(n+1)}_{\mathbf{k}})^2+(\Delta^{(n+1)}_{\mathbf{k}})^2}, \tag{D.3}$$
$$\phi^{(n+1)}_{1{\rm s},\mathbf{k}}=\frac{1}{2}\frac{\Delta^{(n+1)}_{\mathbf{k}}}{\Omega^{(n+1)}_{\mathbf{k}}},\quad f^{(n+1)}_{\mathbf{k}}=\frac{1}{2}\left(1-\frac{\epsilon^{(n+1)}_{\mathbf{k}}}{\Omega^{(n+1)}_{\mathbf{k}}}\right).$$

One typically needs 40 iteration steps to reach convergence.

Appendix E. Number of correlated electron–hole pairs within droplet

To compute the number of correlated pairs within the droplet close to the transition, we start from the quantum droplet pair-correlation function defined by (41). Since the decay constant κ is negligible small after each transition, see section 4.2, we set $\kappa = 0$ in equation (41), yielding

$$\phi(\mathbf{r}) = J_0\left(x_n \frac{r}{R}\right)\theta(R-r). \tag{E.1}$$

The correlated electron–hole density is then given by [15]

$$\Delta n \equiv \int \mathrm{d}^2 r\, \Delta g(\mathbf{r}) = 2\pi g_0^2 \int_0^R \mathrm{d}r\, r |J_0(x_n \frac{r}{R})|^2 = \pi g_0^2 R^2 [J_1(x_n)]^2, \tag{E.2}$$

where we have introduced polar coordinates and used the properties of the Bessel functions [36] in the last step.

To determine the parameter g_0 as function of the ring number n and the droplet radius R, we compute the Fourier transformation of $g_0\phi(\mathbf{r})$, producing

$$g_0\phi_{\mathbf{k}} = g_0 \int \mathrm{d}^2 r\, \phi(\mathbf{r})\, \mathrm{e}^{-\mathrm{i}\mathbf{k}\cdot\mathbf{r}} = 2\pi g_0 \int_0^R \mathrm{d}r\, r J_0(kr) J_0\left(x_n \frac{r}{R}\right), \tag{E.3}$$

where we have again introduced polar coordinates and identified $J_0(kr) = 2\pi \int_0^{2\pi} \mathrm{d}\theta\, \mathrm{e}^{\mathrm{i}kr\cos\theta}$ [36]. For a maximally excited quantum droplet state, the maximum of $g_0\phi_{\mathbf{k}}$ is $\max[g_0\phi_{\mathbf{k}}] = \frac{1}{2}$, based on the discussion in section 4. At the same time, the integral in equation (E.3) is maximized for $k = x_n/R$. By applying the orthogonality of Bessel functions, we obtain

$$\max[g_0\phi_{\mathbf{k}}] = \pi g_0 R^2 [J_1(x_n)]^2 = \tfrac{1}{2}, \tag{E.4}$$

such that g_0 can be written as

$$g_0 = \left[2\pi R^2 [J_1(x_n)]^2\right]^{-1}. \tag{E.5}$$

By inserting equation (E.5) into equation (E.2) and multiplication of Δn with the droplet area $S_{\mathrm{drop}} \equiv \pi R^2$, the number of correlated pairs within the droplet close to the transition becomes

$$\Delta N \equiv \pi R^2 \Delta n = \frac{1}{4[J_1(x_n)]^2}. \tag{E.6}$$

This formula predicts that quantum droplets contain $\Delta N = 3.4$, 4.6 and 5.9 correlated electron–hole pairs for $n = 3$, 4 and 5 rings, respectively. For ring numbers larger than $n = 10$, ΔN approaches $1.2\,n$.

References

[1] Kira M and Koch S W 2011 *Semiconductor Quantum Optics* 1st edn (Cambridge: Cambridge University Press)
[2] Frenkel J 1931 On the transformation of light into heat in solids: I. *Phys. Rev.* **37** 17–44
[3] Wannier G 1937 The structure of electronic excitation levels in insulating crystals *Phys. Rev.* **52** 191–7
[4] Miller R C, Kleinman D A, Gossard A C and Munteanu O 1982 Biexcitons in GaAs quantum wells *Phys. Rev.* B **25** 6545–7

[5] Kim J C, Wake D R and Wolfe J P 1994 Thermodynamics of biexcitons in a GaAs quantum well *Phys. Rev.* B **50** 15099–107
[6] Khitrova G, Gibbs H M, Jahnke F, Kira M and Koch S W 1999 Nonlinear optics of normal-mode-coupling semiconductor microcavities *Rev. Mod. Phys.* **71** 1591–639
[7] Kaindl R A, Carnahan M A, Hagele D, Lovenich R and Chemla D S 2003 Ultrafast terahertz probes of transient conducting and insulating phases in an electron–hole gas *Nature* **423** 734–8
[8] Smith R P, Wahlstrand J K, Funk A C, Mirin R P, Cundiff S T, Steiner J T, Schafer M, Kira M and Koch S W 2010 Extraction of many-body configurations from nonlinear absorption in semiconductor quantum wells *Phys. Rev. Lett.* **104** 247401
[9] Steele A G, McMullan W G and Thewalt M L W 1987 Discovery of polyexcitons *Phys. Rev. Lett.* **59** 2899–902
[10] Turner D B and Nelson K A 2010 Coherent measurements of high-order electronic correlations in quantum wells *Nature* **466** 1089–92
[11] Jeffries C D 1975 Electron–hole condensation in semiconductors *Science* **189** 955–64
[12] Wolfe J P, Hansen W L, Haller E E, Markiewicz R S, Kittel C and Jeffries C D 1975 Photograph of an electron–hole drop in germanium *Phys. Rev. Lett.* **34** 1292–3
[13] Perdew J P and Kurth S 2003 *A Primer in Density Functional Theory* (*Lecture Notes in Physics*) ed C Fiolhais, F Nogueira and M A L Marques (Berlin: Springer) pp 1–51
[14] Sholl D and Steckel J A 2009 *Density Functional Theory: A Practical Introduction* (New York: Wiley)
[15] Kira M and Koch S W 2006 Many-body correlations and excitonic effects in semiconductor spectroscopy *Prog. Quantum Electron.* **30** 155–296
[16] Narten A H 1972 Liquid water: atom pair correlation functions from neutron and x-ray diffraction *J. Chem. Phys.* **56** 5681–7
[17] Jorgensen W L, Chandrasekhar J, Madura J D, Impey R W and Klein M L 1983 Comparison of simple potential functions for simulating liquid water *J. Chem. Phys.* **79** 926–35
[18] Fois E S, Sprik M and Parrinello M 1994 Properties of supercritical water: an *ab initio* simulation *Chem. Phys. Lett.* **223** 411–5
[19] Kira M, Jahnke F, Hoyer W and Koch S W 1999 Quantum theory of spontaneous emission and coherent effects in semiconductor microstructures *Prog. Quantum Electron.* **23** 189–279
[20] DeMarco B and Jin D S 1999 Onset of Fermi degeneracy in a trapped atomic gas *Science* **285** 1703–6
[21] Holland M, Kokkelmans S J J M F, Chiofalo M L and Walser R 2001 Resonance superfluidity in a quantum degenerate Fermi gas *Phys. Rev. Lett.* **87** 120406
[22] O'Hara K M, Hemmer S L, Gehm M E, Granade S R and Thomas J E 2002 Observation of a strongly interacting degenerate Fermi gas of atoms *Science* **298** 2179–82
[23] Greiner M, Regal C A and Jin D S 2003 Emergence of a molecular Bose–Einstein condensate from a Fermi gas *Nature* **426** 537–40
[24] Gerhardt N C, Hofmann M R, Hader J, Moloney J V, Koch S W and Riechert H 2004 Linewidth enhancement factor and optical gain in (GaIn)(NAs)/GaAs lasers *Appl. Phys. Lett.* **84** 1–3
[25] Koukourakis N *et al* 2012 High room-temperature optical gain in Ga(NAsP)/Si heterostructures *Appl. Phys. Lett.* **100** 092107
[26] Ellmers C *et al* 1998 Measurement and calculation of gain spectra for (GaIn)As/(AlGa)As single quantum well lasers *Appl. Phys. Lett.* **72** 1647–9
[27] Hofmann M R *et al* 2002 Emission dynamics and optical gain of 1.3-μm (GaIn)(NAs)/GaAs lasers *IEEE J. Quantum Electron.* **38** 213–21
[28] Peyghambarian N, Gibbs H M, Jewell J L, Antonetti A, Migus A, Hulin D and Mysyrowicz A 1984 Blue shift of the exciton resonance due to exciton–exciton interactions in a multiple-quantum-well structure *Phys. Rev. Lett.* **53** 2433–6
[29] Kira M, Koch S W, Smith R P, Hunter A E and Cundiff S T 2011 Quantum spectroscopy with Schrödinger-cat states *Nature Phys.* **7** 799–804

[30] Schmitt-Rink S, Chemla D S and Miller D A B 1985 Theory of transient excitonic optical nonlinearities in semiconductor quantum-well structures *Phys. Rev.* B **32** 6601–9
[31] Fernández-Rossier J, Tejedor C, Muñoz L and Viña L 1996 Polarized interacting exciton gas in quantum wells and bulk semiconductors *Phys. Rev.* B **54** 11582–91
[32] Rochat G *et al* Excitonic Bloch equations for a two-dimensional system of interacting excitons *Phys. Rev.* B **61** 13856–62
[33] Friedel J 1956 On some electrical and magnetic properties of metallic solid solutions *Can. J. Phys.* **34** 1190–211
[34] Hoyer W, Kira M and Koch S W 2004 Cluster expansion in semiconductor quantum optics *Nonequilibrium Physics at Short Time Scales* ed K Morawetz (Berlin: Springer) pp 309–35
[35] Littlewood P B and Zhu X 1996 Possibilities for exciton condensation in semiconductor quantum-well structures *Phys. Scr.* **1996** 56
[36] Arfken G B, Weber H J and Harris F E 2012 *Mathematical Methods for Physicists: A Comprehensive Guide* 7th edn (New York: Academic/Elsevier)

Paper III

A. E. Almand-Hunter, H. Li, S. T. Cundiff, **M. Mootz**, M. Kira, and S. W. Koch

Quantum droplets of electrons and holes

Nature **506**, 471–475 (2014)

LETTER

doi:10.1038/nature12994

Quantum droplets of electrons and holes

A. E. Almand-Hunter[1,2], H. Li[1], S. T. Cundiff[1,2], M. Mootz[3], M. Kira[3] & S. W. Koch[3]

Interacting many-body systems are characterized by stable configurations of objects—ranging from elementary particles to cosmological formations[1–3]—that also act as building blocks for more complicated structures. It is often possible to incorporate interactions in theoretical treatments of crystalline solids by introducing suitable quasiparticles that have an effective mass, spin or charge[4,5] which in turn affects the material's conductivity, optical response or phase transitions[2,6,7]. Additional quasiparticle interactions may also create strongly correlated configurations yielding new macroscopic phenomena, such as the emergence of a Mott insulator[8], superconductivity or the pseudogap phase of high-temperature superconductors[9–11]. In semiconductors, a conduction-band electron attracts a valence-band hole (electronic vacancy) to create a bound pair, known as an exciton[12,13], which is yet another quasiparticle. Two excitons may also bind together to give molecules, often referred to as biexcitons[14], and even polyexcitons may exist[15,16]. In indirect-gap semiconductors such as germanium or silicon, a thermodynamic phase transition may produce electron–hole droplets whose diameter can approach the micrometre range[17,18]. In direct-gap semiconductors such as gallium arsenide, the exciton lifetime is too short for such a thermodynamic process. Instead, different quasiparticle configurations are stabilized dominantly by many-body interactions, not by thermalization. The resulting non-equilibrium quantum kinetics is so complicated that stable aggregates containing three or more Coulomb-correlated electron–hole pairs remain mostly unexplored. Here we study such complex aggregates and identify a new stable configuration of charged particles that we call a quantum droplet. This configuration exists in a plasma and exhibits quantization owing to its small size. It is charge neutral and contains a small number of particles with a pair-correlation function that is characteristic of a liquid. We present experimental and theoretical evidence for the existence of quantum droplets in an electron–hole plasma created in a gallium arsenide quantum well by ultrashort optical pulses.

The new quasiparticle that we call a quantum droplet has a pair-correlation function that is characteristic of a liquid; thus it is a droplet and not a polyexciton. However, it contains a small number of electron–hole pairs and the pair-correlation function exhibits the effects of quantization; thus it is distinct from a macroscopic droplet. It can form via Coulomb interaction in direct-gap semiconductors such as gallium arsenide (GaAs) on an ultrafast timescale, long before a thermodynamic equilibrium is reached. To be stable, a quantum droplet's binding energy must be higher than that of other quasiparticles, including excitons and biexcitons. Figure 1a sketches the hierarchy of the most relevant quasiparticle states in semiconductors. As for any liquid-like state, we expect quantum droplets to emerge only above a certain density threshold. Because quantum droplets should have discrete eigenenergies, it should be possible to detect quantum beats in suitable time-resolved experiments. Such quantum-dynamic evolution is absent for thermodynamic transitions.

We present experimental evidence for quantum electron–hole droplets in the absorption spectrum of a GaAs quantum well that has been excited by an ultrafast laser pulse. Absorption of light from the excitation pulse creates electron–hole pairs with a density that increases monotonically with the pulse intensity and puts the system in a non-equilibrium state. Thus, the number of injected quasiparticles can be controlled by the excitation-pulse intensity and additionally by the photon energy. If the excitation is tuned well above the exciton resonance, it initially generates an electron–hole plasma that may evolve into excitons only via relatively slow equilibration[19]. If the excitation is resonant with the exciton, it is rapidly converted into a mixture of excitons and electron–hole plasma[20] and only further equilibration may then bind excitons into biexcitons[14]. However, biexcitons can be generated more efficiently by tuning the photon energy below that of the exciton in order to match the biexciton binding.

In our experiments, absorption spectra are recorded using a weak time-delayed probe pulse that is spectrally resolved after passing through the sample (see Supplementary Information). The pump–probe delay Δt is defined as the temporal separation of pump and probe pulse centres. For $\Delta t > 0$, the pump pulse arrives at the sample before the probe pulse. The absorption spectra at a fixed pump–probe delay of $\Delta t = 2$ ps are shown in Fig. 1b as a function of probe-photon energy and number of photons in the pump pulse, N_{pump}. We quote the photon number because the number of generated quasiparticles is not necessarily linearly proportional to N_{pump} owing to saturation effects, and because the mixture of quasiparticles varies[20] with N_{pump}. At very low excitation density, the absorption spectrum shows a clear heavy-hole exciton resonance 9 meV below the bandgap (not shown) that also defines an exciton's binding

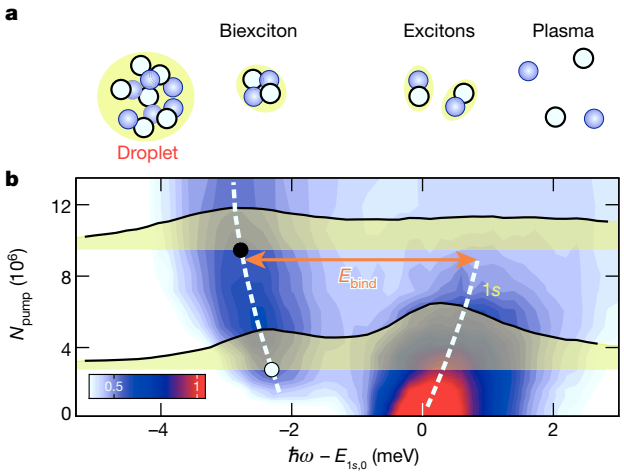

Figure 1 | Quasiparticles in classical spectroscopy. **a**, Schematic quasiparticles in direct-gap semiconductors. Open circles, holes; grey filled circles, electrons. See text for details. **b**, Measured absorption spectra as a function of the number of photons in the pump pulse, N_{pump}, for pump–probe delay $\Delta t = 2$ ps; the pump and probe have opposite circular polarization. The dark (white) colours denote the regions with strong (weak) absorption (see colour scale; peak absorption is normalized to one); the transparent yellow shaded areas with black lines on top show actual spectra corresponding to $N_{\mathrm{pump}} = 2.8 \times 10^6$ (lower) and $N_{\mathrm{pump}} = 9.5 \times 10^6$ (upper). The dashed lines indicate the shifts of the resonances, $\hbar\omega$ defines the photon energy, $E_{1s,0}$ is the low-density exciton energy, and E_{bind} denotes the binding energy.

[1]JILA, University of Colorado and National Institute of Standards and Technology, Boulder, Colorado 80309-0440, USA. [2]Department of Physics, University of Colorado, Boulder, Colorado 80309-0390, USA. [3]Department of Physics, Philipps-University Marburg, Renthof 5, 35032 Marburg, Germany.

energy with respect to the electron–hole plasma. For increasing pump intensity, the Coulomb renormalizations move the bandgap to a lower energy[2]. At the same time, the exciton binding energy is reduced due to the weakening of the Coulomb interaction by screening[21] and Pauli blocking of low-energy states. Interplay of these three effects yields an overall blue shift of the exciton energy, as expected[20,22,23].

Additionally, a second resonance appears below the exciton resonance for pump strengths exceeding 1.5×10^6 photons. The binding energy of this state, E_{bind}, is defined with respect to the exciton resonance (arrow in Fig. 1b). It has a value of just over 2 meV at low excitation levels and grows to about 3 meV as N_{pump} increases. Because excitons may lower their energy by forming a molecule, one expects E_{bind} to indicate the existence of a bound biexciton state. However, this assignment conflicts with the increase of E_{bind} with elevated N_{pump} because the biexciton's binding energy should track the exciton's binding energy. In other words, the biexcitonic E_{bind} should decrease as the Coulomb interaction weakens at elevated N_{pump}. Furthermore, we see that the second resonance remains much more pronounced than the high-N_{pump} exciton resonance. We have confirmed the increase of E_{bind} as a function of N_{pump} not only by using another sample but also by using a different experimental technique, two-dimensional Fourier transform spectroscopy, which produces more detailed information about the quasiparticles[24], as presented in Supplementary Information.

Because the behaviour of E_{bind} is inconsistent with the low-energy resonance remaining biexcitonic, it is reasonable to surmise that although this resonance initially corresponds to the biexciton, it cannot be due to the biexciton at higher excitation levels, but rather must be due to the excitation of a different quasiparticle, which we hypothesize to be a quantum droplet. To test this assignment, we analyse the properties of the experimentally detected resonance and check if they are consistent with a many-body state where electrons and holes form a liquid confined within a small droplet with radius R. As the principal hallmark of liquids, the particle-position correlations form a ring pattern where the ring separation corresponds roughly to the average particle separation[25–27]. This fundamental property can be formulated using the pair-correlation function $g(r) = \rho_e\rho_h + \Delta g(r)$ that determines the conditional distribution of electrons when a hole is at the origin and vice versa. The product of electron and hole densities, $\rho_e\rho_h$, describes the evenly spread plasma contribution in a homogeneous system. The quasiparticle clusters are determined by the correlated part, $\Delta g(r)$, that contains the r dependence.

A quantum droplet has a well-defined radius R such that the $\Delta g(r)$ correlation vanishes for distances greater than R. Physically, a quantum droplet can be viewed as a correlation bubble that is held together by the Fermi pressure created by the surrounding high-density plasma. Because electron–hole pairs are quantum confined inside a bubble, the pair wavefunction exhibits a standing wave within a circular shell because the quantum well is two-dimensional. Therefore, for simplicity, we start by assuming that the droplet has a hard shell at $r = R$ and implement a standing-wave ansatz $\Delta g(r) = |g_0\phi(r)|^2$ defined by

$$\phi(r) = J_0\left(x_n \frac{r}{R}\right) e^{-\kappa r}\theta(R-r) \qquad (1)$$

where x_n is the nth zero of the Bessel function $J_0(x)$, κ is an additional decay constant, the Heaviside $\theta(x)$ function confines $\Delta g(r)$ inside the shell, and g_0 determines the strength of the correlations. As discussed in the Supplementary Information, the specific (g_0, κ, R) values also fix $\rho_{eh} \equiv \rho_e = \rho_h$ within the quantum droplet. We adjust the density to match the external ρ_{eh} of the plasma, and fix κ and g_0 coefficients for a given carrier density when the droplet has radius R and n rings.

Figure 2a illustrates the pair-correlation function $g(r)$ of a quantum droplet with $R = 91$ nm, $n = 4$, and electron–hole density $\rho_{eh} = 2.5 \times 10^{10}$ cm^{-2}. The shell of the droplet is indicated by the cylinder. Outside the shell, $g(r)$ has a constant value $\rho_e\rho_h$ (grey area) and $\Delta g(r)$ (yellow area) is non-zero only within the shell. Here, $\Delta g(r)$ has four rings, including the central part that appears because the electrons and holes attract each other. This behaviour is different from typical liquids that show a correlation hole at the centre of $g(r)$ (refs 25–27) because particles in a typical liquid repel each other at short distances.

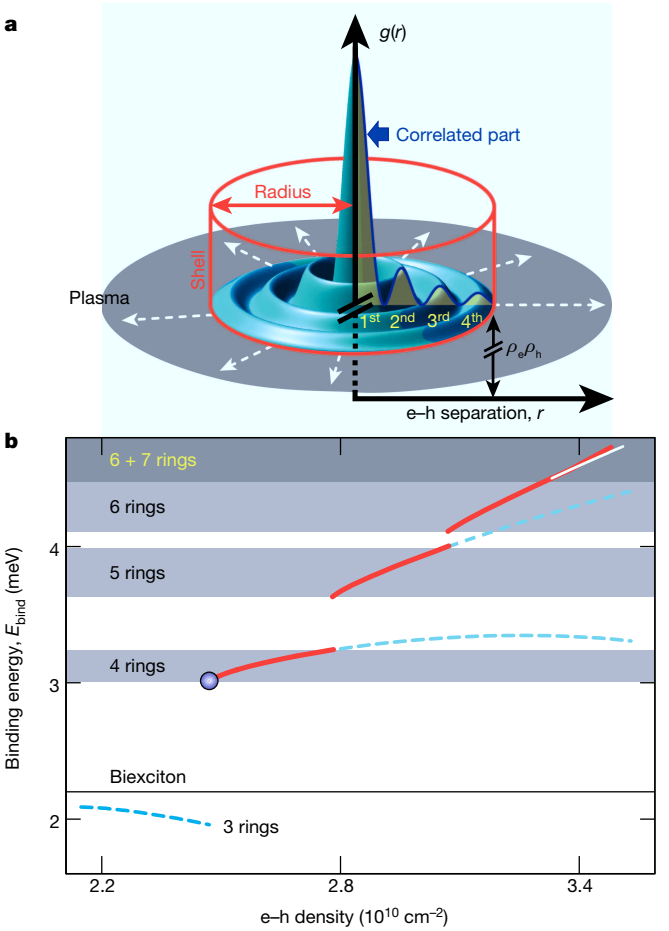

Figure 2 | Quantum droplet properties. **a**, Computed $g(r)$ of a quantum droplet having radius $R = 91$ nm, $n = 4$ and $\rho_{eh} \equiv \rho_e = \rho_h = 2.5 \times 10^{10}$ cm^{-2}. The cylinder represents the droplet shell, the correlated part ($\Delta g(r)$) is indicated by a yellow area, and the grey area corresponds to the plasma ($\rho_e\rho_h$). **b**, Computed binding energy as a function of ρ_{eh}. Energy dispersion for each droplet is continued as a dashed line after the next higher quantum droplet becomes the lowest-energy state; the white line continues the 6-ring E_{bind}. The horizontal line indicates the biexciton binding energy. The shaded areas denote the ground-state bands. The filled circle defines the binding energy for the configuration presented in **a**.

To determine the energetics of quantum droplets, we generalize the Wannier equation[13,28] to compute the energy per electron–hole pair probed by an infinitesimally weak pair excitation when the system initially contains an n-ring quantum droplet (see Supplementary Information). The red solid lines in Fig. 2b define the highest E_{bind} as a function of ρ_{eh} found among quantum droplets with a different number of rings. The dashed curves continue the energy dispersion of the n-ring droplet for higher densities where it is no longer the lowest-energy state. In general, we always find a discrete droplet–energy relation where new energy levels appear as sharp transitions when ρ_{eh} is increased; allowed energy ranges are indicated by the shaded bands. Because each jump in the ground state E_{bind} increases n by one, the number of rings also defines the quantum number for the discrete energy levels. We show in Supplementary Information that quantum droplets confined inside a finite wall produce essentially the same energetics as the hard-wall ansatz, equation (1); we also find that the skin depth of the quantum droplet's edge is then 7 nm, which is comparable with the exciton Bohr radius of $a_B = 12$ nm, whereas the quantum-droplet radius itself is roughly 8 times larger than a_B.

The relative excitation level can be estimated from the Pauli-blocking (or the phase-space filling) factor of the zero-momentum electrons and holes in the excitonic system. It is unity at vanishing density and 0.41 (0.32) when the $n = 4$ (6)-ring quantum droplet emerges. Therefore, the exciton resonance is already strongly broadened in Fig. 1b, indicating that the quantum rings appear at elevated electron–hole densities ρ_{eh}. This conclusion is consistent with the need for a sufficiently large Fermi pressure to create conditions favourable for the correlation bubbles surrounded by the plasma. As shown in Supplementary Information, we also find that the n-ring quantum droplet has essentially n electron–hole pairs just after the sharp transition in the E_{bind}–ρ_{eh} diagram.

Both the magnitude and excitation-induced increase of the calculated quantum-droplet binding energy agree with the experimental results presented in Fig. 1b. However, the calculated E_{bind} shows a series of abrupt jumps whenever a ring is added. As such jumps are not directly evident in the experimental results, we reanalyse the data through differential absorption $\Delta\alpha$ that excels at revealing the effect of many-body correlations. However, a simple differential absorption $\Delta\alpha_{class}$ (with respect to classical changes in the pump) monitors all effects down to the single-particle level[2], which masks the effect of the individual many-body states. To overcome this obstacle, we use the projection protocol described in ref. 23 to directly access the effect of the distinct many-body states via the projected differential absorption $\Delta\alpha_{MB}$. Technically, one only needs to measure the quantum-well absorption for a large ensemble of N_{pump} values, as is done in Fig. 1b, and apply the projection protocol to generate $\Delta\alpha_{MB}$ that becomes a differential to the quantum-optical fluctuations in the pump source[23]. As elaborated in the Supplementary Information, we follow this protocol and project $\Delta\alpha_{MB}$ to 'slanted' Schrödinger cat states that are superpositions of two different coherent states with unequal amplitudes. The resulting $\Delta\alpha_{MB}$ is designed (see Supplementary Information) to access the response from many-body correlations involving three or more electron–hole pairs. Therefore, one gains a significant enhancement of sensitivity to highly correlated quasiparticles when analysing $\Delta\alpha_{MB}$ instead of $\Delta\alpha_{class}$.

A contour plot of the $\Delta\alpha_{MB}$ spectra generated from the experimental results is presented in Fig. 3a as a function of N_{pump} and E_{bind} for $\Delta t = 16$ ps. The binding energy is defined with respect to the N_{pump}-dependent 1*s* energy. Spectra at three different values of N_{pump}, indicated by the circles, are shaded. For low N_{pump}, there is a clear resonance at the biexciton energy (horizontal line). The position of the biexciton resonance is stationary, in contrast to the experimental results presented in Fig. 1b. However, the resonance jumps abruptly at $N_{pump} = 1.3 \times 10^6$ while maintaining its width. As N_{pump} is increased further, we find two more sharp transitions at $N_{pump} = 3.5 \times 10^6$ and 5.0×10^6 such that three quantized energy levels are resolved. More specifically, these energy levels have E_{bind} that exceeds the biexciton binding by 0.9 meV, 1.60 meV or 2.4 meV.

The shaded bands in Fig. 3a indicate each quantized energy level, deduced from the computation in Fig. 2b. The positions of the measured quantized energy levels agree well with the calculated energies for the 4-ring, 5-ring and 6 (7)-ring quantum droplets, which is consistent with the assignment of the low-energy resonance to quantum droplets at excitation levels above $N_{pump} = 1.3 \times 10^6$. Also, the predicted merging of 6- and 7-ring features seems to appear in $\Delta\alpha_{MB}$ (see Supplementary Information), even though our signal-to-noise ratio starts to deteriorate in this weak absorption range. Quantum droplets with two and three rings (not shown) have a binding energy smaller than the biexciton, which make them undetectable in the cross-circular pump–probe measurement. Because the quantum droplets are highly correlated, these quantized levels become clearly visible only in the $\Delta\alpha_{MB}$ spectra that are sensitive to three-pair effects and beyond. Classical spectroscopy cannot resolve the individual quantum droplet levels as seen in Fig. 1b. Instead, quantum droplets appear in classical spectra as a gradual increase in E_{bind}, because classical light yields a mixture of biexcitons and quantum droplets via Coulomb and phonon scattering[2], preventing sharp resonances.

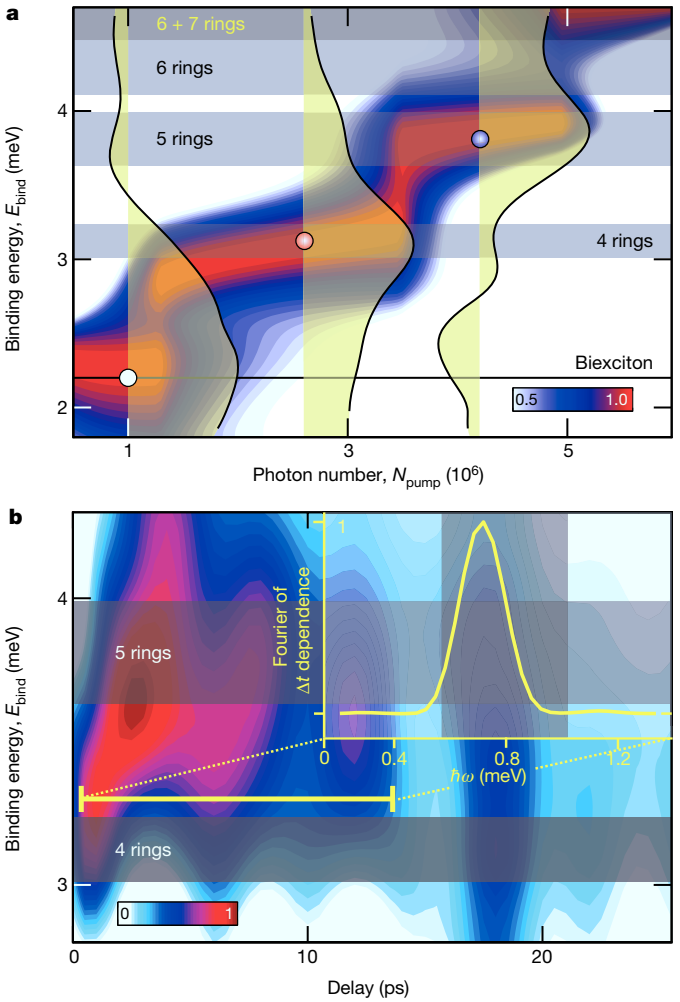

Figure 3 | Detection of quantum droplets via quantum spectroscopy. **a**, Contour plot of $\Delta\alpha_{MB}$ (on colour scale) as a function of N_{pump} and E_{bind}. The dark (white) contours indicate the regions with large (small) increase in $\Delta\alpha_{MB}$. The biexciton E_{bind} (horizontal line) matches the low-density binding in Fig. 1b. Grey shaded horizontal bands denote the computed energy ranges of 4-, 5-, 6- and 7-ring droplets. The yellow areas with black traces show $\Delta\alpha_{MB}$ at $N_{pump} = 1.0 \times 10^6$ (left, open circle), 2.6×10^6 (middle, red sphere) and 4.2×10^6 (right, blue sphere). **b**, Temporal evolution of $\Delta\alpha_{MB}$ for $N_{pump} = 3.8 \times 10^6$. Grey shaded horizontal bands denote the 4- and 5-ring bands. Inset, Fourier-transformed $\Delta\alpha_{MB}$ at $E_{bind} = 3.3$ meV (horizontal yellow line in **b**). The vertical grey shaded rectangle determines the expected range for 4–5 ring splitting.

We also show in Supplementary Information that the quantum-droplet levels cannot be explained by polyexcitons. More specifically, we have performed a control measurement in which the generation of polyexcitons is excluded owing to antibonding of the excited states, and yet the control measurement produces identical quantum-droplet bands. Hence, the constituents of quantum droplets are not excitons, but collectively bound electron–hole complexes. We note that a polyexciton is also forbidden in direct-gap systems at low densities[29].

To track the quantum dynamics of quantum droplets, we measure and generate $\Delta\alpha_{MB}$ as a function of the pump–probe delay Δt. Because each value of Δt labels an independent N_{pump}-measurement ensemble that is projected into $\Delta\alpha_{MB}$, the Δt dependence of $\Delta\alpha_{MB}$ reveals the quantum dynamics of the quantum droplets independently from the pure energetics deduced from the N_{pump} dependence alone (Fig. 3a). The accuracy of the $\Delta\alpha_{MB}$ projection is 6% from the spectral peak height. Figure 3b shows the Δt dependence of $\Delta\alpha_{MB}$ spectra for a fixed $N_{pump} = 3.8 \times 10^6$. The spectral peak is first created at the 4-ring quantum

droplet energy and it then moves vertically towards the 5-ring energy. This is followed by oscillations that are also visible in a horizontal cut at fixed $E_{bind} = 3.3$ meV (horizontal thick yellow line), as a function of time. The Fourier transform of this horizontal cut is presented in the inset, where the vertical shaded area indicates the expected transition energy range between the 4- and 5-ring states, based on Fig. 2b. The $\Delta\alpha_{MB}$ resonance not only oscillates between the 4- and 5-ring droplets, but the oscillation frequency matches the energy splitting between these levels. The observed quantum beats provide independent evidence for the existence of quantum droplets with discrete energy states.

The $\Delta\alpha_{MB}$ dynamics provide further insight into the properties of the quantum droplets. Three-photon correlations create the quantum droplet essentially instantly, as seen in Fig. 3b from the immediate emergence of the resonance at the first quantized level just after $\Delta t = 0$. The results also show that the quantum droplet has a lifetime of roughly 25 ps. These transient features, as well as the quantum beats, cannot appear for thermodynamic transitions.

Although we cannot directly measure $\Delta\alpha_{MB}$ because suitable quantum-light sources do not yet exist, the projected measurements analysed in Fig. 3b suggest that one might still detect the quantum-droplet beats as a function of pump–probe delay directly in absorption measurements at an appropriate excitation level. Furthermore, we can enhance the effect of higher-order correlations by measuring the differential $\Delta\alpha_{class}$ due to modulation of the pump intensity, rather than just the absorption itself. The details of the experiment are given in the Supplementary Information. The measured values of $\Delta\alpha_{class}$ at the first quantum-droplet energy are shown in Fig. 4. We note pronounced beats that match the splitting between the 4- and 5-ring droplets, and also note beats that match the splitting between the 4- and 6-ring droplets, providing further independent evidence for the existence of quantum droplets. The simultaneous presence of multiple droplet resonances is also consistent with the incapability of the classical spectroscopy to resolve the individual quantum-droplet states. In the Supplementary Information, we report an additional control measurement that we have performed, where we study quantum droplets at 70 K, which is expected to be a high enough temperature that the quantum droplets are ionized by phonon scattering. We find that the 70 K measurement indeed does not produce quantum droplets.

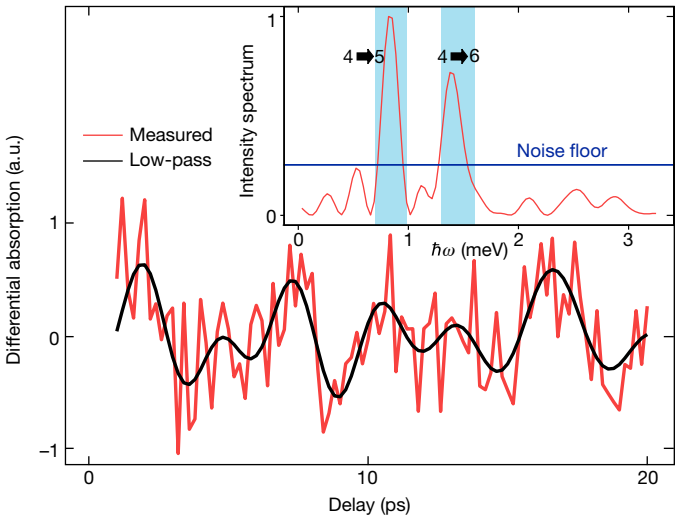

Figure 4 | Direct measurement of quantum-droplet signatures. Main figure, differential absorption trace recorded at 3 meV binding energy as a function of pump–probe delay. The measured (red line) and low-pass filtered (black line) traces are shown. Inset, corresponding intensity spectra (red line) together with the experimental noise floor (blue horizontal line) and energy ranges (vertical cyan shaded rectangles) expected for transitions between the 4- and 5-ring droplet and the 4- and 6-ring droplet, identified in Fig. 2b. a.u., arbitrary units.

Because a quantum droplet of electrons and holes has a microscopic size, quantized energy and quantized transitions, we suggest this new quasiparticle be called simply a dropleton. Conceptually, a dropleton is in between a quantum version of the Thomson atom[30] and the real multi-electron atom, because the positive charge is not uniform, as in the Thomson atom, but is localized around the electrons, although it is not as extremely localized as in an atomic nucleus due to the strong force. Our analysis shows that the individual dropleton levels can be accessed using ultrafast light pulses whose quantum fluctuations are tailored to match the particle correlations within the dropleton. Owing to the dropleton's relatively long life time, it appears to be stable enough for systematic studies on interactions between quantum light and highly correlated matter states.

METHODS SUMMARY

We excite various quasiparticles in the GaAs quantum well by varying the intensity of an ultrafast high-quality pump pulse. The resulting quasiparticles are characterized by measuring linear absorption with a weak probe pulse that is delayed with respect to the pump. This part of the process records a systematic set of high-precision absorption spectra as a function of pump intensity, for each fixed pump–probe delay. The high precision of our measurements allows each of these sets to be independently projected into a differential absorption spectrum with respect to changes only in the pump field's three-photon fluctuations. We use an experimentally robust protocol demonstrated in ref. 23. As the central feature of quantum-optical spectroscopy[2], such a differential absorption is exclusively sensitive to correlations of three electron–hole pairs excited in the system. Consequently, we can then directly follow how correlations among three electron–hole pairs evolve, which allows us to detect quasiparticles that remain virtually hidden to classical spectroscopies. The Supplementary Information elaborates both the experimental set-up and the exact projection algorithm used.

Received 29 July; accepted 12 December 2013.

1. Lissauer, J. Chaotic motion in the solar system. *Rev. Mod. Phys.* **71,** 835–845 (1999).
2. Kira, M. & Koch, S. W. *Semiconductor Quantum Optics* 1st edn (Cambridge Univ. Press, 2011).
3. Oganessian, Y. *et al.* Synthesis of nuclei of the superheavy element 114 in reactions induced by ^{48}Ca. *Nature* **400,** 242–245 (1999).
4. Kittel, C. *Introduction to Solid State Physics* 7th edn (Wiley, 2004).
5. Laughlin, R. Anomalous quantum Hall effect: an incompressible quantum fluid with fractionally charged excitations. *Phys. Rev. Lett.* **50,** 1395–1398 (1983).
6. Datta, S. *Electronic Transport in Mesoscopic Systems* 1st edn (Cambridge Univ. Press, 1997).
7. Papon, P., Leblond, J. & Meijer, P. *The Physics of Phase Transitions: Concepts and Applications* 2nd edn (Springer, 2006).
8. Endres, M. *et al.* Observation of correlated particle-hole pairs and string order in low-dimensional Mott insulators. *Science* **334,** 200–203 (2011).
9. Vershinin, M. *et al.* Local ordering in the pseudogap state of the high-T_C superconductor $Bi_2Sr_2CaCu_2O_{8+\delta}$. *Science* **303,** 1995–1998 (2004).
10. Kanigel, A. *et al.* Evolution of the pseudogap from Fermi arcs to the nodal liquid. *Nature Phys.* **2,** 447–451 (2006).
11. Daou, R. *et al.* Broken rotational symmetry in the pseudogap phase of a high-T_c superconductor. *Nature* **463,** 519–522 (2010).
12. Frenkel, J. On the transformation of light into heat in solids. *Phys. Rev.* **37,** 17–44 (1931).
13. Wannier, G. The structure of electronic excitation levels in insulating crystals. *Phys. Rev.* **52,** 191–197 (1937).
14. Kim, J. C., Wake, D. R. & Wolfe, J. P. Thermodynamics of biexcitons in a GaAs quantum well. *Phys. Rev. B* **50,** 15099–15107 (1994).
15. Steele, A., McMullan, W. & Thewalt, M. Discovery of polyexcitons. *Phys. Rev. Lett.* **59,** 2899–2902 (1987).
16. Turner, D. & Nelson, K. Coherent measurements of high-order electronic correlations in quantum wells. *Nature* **466,** 1089–1092 (2010).
17. Jeffries, C. Electron–hole condensation in semiconductors. *Science* **189,** 955–964 (1975).
18. Suzuki, T. & Shimano, R. Time-resolved formation of excitons and electron–hole droplets in Si studied using terahertz spectroscopy. *Phys. Rev. Lett.* **103,** 057401 (2009).
19. Kaindl, R. A., Carnahan, M. A., Hagele, D., Lovenich, R. & Chemla, D. S. Ultrafast terahertz probes of transient conducting and insulating phases in an electron–hole gas. *Nature* **423,** 734–738 (2003).
20. Smith, R. P. *et al.* Extraction of many-body configurations from nonlinear absorption in semiconductor quantum wells. *Phys. Rev. Lett.* **104,** 247401 (2010).
21. Huber, R. *et al.* How many-particle interactions develop after ultrafast excitation of an electron–hole plasma. *Nature* **414,** 286–289 (2001).

22. Khitrova, G., Gibbs, H. M., Jahnke, F., Kira, M. & Koch, S. W. Nonlinear optics of normal-mode-coupling semiconductor microcavities. *Rev. Mod. Phys.* **71,** 1591–1639 (1999).
23. Kira, M., Koch, S. W., Smith, R. P., Hunter, A. E. & Cundiff, S. T. Quantum spectroscopy with Schrödinger-cat states. *Nature Phys.* **7,** 799–804 (2011).
24. Cundiff, S. T. Optical two-dimensional Fourier transform spectroscopy of semiconductor nanostructures. *J. Opt. Soc. Am. B* **29,** A69–A81 (2012).
25. Barker, J. A. & Henderson, D. What is "liquid"? Understanding the states of matter. *Rev. Mod. Phys.* **48,** 587–671 (1976).
26. Jorgensen, W. L., Chandrasekhar, J., Madura, J. D., Impey, R. W. & Klein, M. L. Comparison of simple potential functions for simulating liquid water. *J. Chem. Phys.* **79,** 926–935 (1983).
27. Sastry, S. & Angell, C. Liquid–liquid phase transition in supercooled silicon. *Nature Mater.* **2,** 739–743 (2003).
28. Mootz, M., Kira, M. & Koch, S. W. Pair-excitation energetics of highly correlated many-body states. *New J. Phys.* **15,** 093040 (2013).
29. Hirschfelder, J. O. The energy of the triatomic hydrogen molecule and ion, V. *J. Chem. Phys.* **6,** 795–806 (1938).
30. Thomson, J. On the structure of the atom. *Phil. Mag.* **7,** 237–265 (1904).

Supplementary Information is available in the online version of the paper.

Acknowledgements We thank R. Mirin at NIST-Boulder for growing the quantum well samples. The work at Philipps-University Marburg was supported by the Deutsche Forschungsgemeinschaft under grant KI 917/2-1, and the work at JILA was supported by the NSF under grant 1125844 and by NIST. S.T.C. acknowledges support from the Alexander von Humboldt Foundation.

Author Contributions All authors contributed substantially to this work. The experiments were performed by the JILA group whereas the Philipps-University Marburg group was predominantly responsible for the theory.

Author Information Reprints and permissions information is available at www.nature.com/reprints. The authors declare no competing financial interests. Readers are welcome to comment on the online version of the paper. Correspondence and requests for materials should be addressed to M.K. (mackillo.kira@physik.uni-marburg.de).

Supplementary Information to Paper III

SUPPLEMENTARY INFORMATION

doi:10.1038/nature12994

Quantum droplets of electrons and holes

A.E. Hunter[1,2], H. Li[1], S.T. Cundiff[1,2], M. Mootz[3], M. Kira[3,*], and S.W. Koch[3]

[1] *JILA, University of Colorado & National Institute of Standards and Technology, Boulder, CO 80309-0440, USA*

[2] *Department of Physics, University of Colorado, Boulder, CO 80309-0390 USA and*

[3] *Department of Physics, Philipps-University Marburg, Renthof 5, D-35032 Marburg, Germany*

We present here the details of our theoretic approach and experiments we apply to detect *dropletons*, i.e. quantum droplets of electrons and holes. More explicitly, we go through the relevant details of our spectrally resolved transient absorption setup and present our pre-pulse 2DFT spectroscopy measurements in Sec. I. In Secs. II – V, we then introduce the mathematical form of the slanted Schrödingers cat state and explain how it directly accesses three-particle correlations of quasi-particles when we utilize the framework of quantum-optical spectroscopy. In Sec. VI, we explain how we compute the excitation spectrum of dropletons as functional of their pair-correlation function. The control measurements are also presented in Sec. VII in order to show that dropletons are genuine plasma configurations, not polyexcitons, and that dropletons ionize at elevated temperatures.

I. EXPERIMENTAL DETAILS

Experiments were performed on two multiple quantum well (QW) samples. Both samples contained GaAs QWs with $Al_{0.3}Ga_{0.7}As$ barriers, where both wells and barriers are 10 nm thick. These barriers are sufficiently thick that the individual QWs are quantum mechanically isolated. The sample used for the spectrally resolved transient absorption experiments contained 10 QWs, whereas the one used for two-dimensional coherent spectroscopy contained only 4 QWs. The lower number of wells was used to reduce the peak absorption and the resulting distortion of the 2D spectra.

Both samples were grown by molecular-beam epitaxy. A buffer layer of GaAs is grown on a GaAs substrate to create a smooth growth front, followed by as stop-etch layer. After the stop etch layer, a 300 nm GaAs bulk layer is grown restore a smooth growth front. This layer is followed by a 300 nm $Al_{0.3}Ga_{0.7}As$ barrier and then either 4 or 10 periods of alternating 10 nm $Al_{0.3}Ga_{0.7}As$ and 10 nm GaAs layers. A final 300 nm $Al_{0.3}Ga_{0.7}As$ barrier is followed by a 10 nm GaAs capping layer to prevent oxidation. Both samples are mounted on a sapphire disk, and the substrate removed by a combination of mechanical grinding and chemical etching.

To determine the resolution limits due to disorder, we make use of our earlier work in Ref.[S1], where we found that an equivalent sample has a heavy-hole 1*s*-exciton linewidth of 0.75 meV (half-width half-maximum). A *quantitative* experiment-theory comparison revealed that half of the linewidth originates from the radiative decay, such that the disorder related dephasing in our sample is less than 0.4 meV. This is confirmed in complementary 2D spectroscopy that deduced 0.45 inhomogeneous line for this type of sample[S2]. Since the inhomogeneous linewidth does not depend on the excitation power[S3], the excitation-induced effects in the dropleton investigations cannot be generated by disorder effects. Instead, disorder can blur the detected excitation-induced features. However, disorder does not influence the identification of the dropleton resonances, because the dropleton's quantization energy of roughly 0.7 meV is far greater than the upper limit (0.4 meV) of disorder blurring. Thus the dropleton resonances can be clearly resolved.

For both measurements, the sample is cooled to 10 K in a cold-finger cryostat. At this temperature, the heavy-hole (HH) 1*s* resonance is approximately 9 meV below the gap at 1546.7 meV.

A. Spectrally Resolved Transient Absorption

We measure the spectrally resolved response of the sample to classical (coherent state) excitation with a pump–probe absorption setup. The pump and probe come from a mode-locked Ti:Sapphire laser with the spectrum centered around the HH 1*s* resonance (see Fig. S2(a)). The pulses have an approximately Gaussian temporal profile with a temporal width of 320 fs for the pump, and 160 fs for the probe (see Fig. S2(b)).

Figure S1 shows the layout of the experiment. A beamsplitter divides the laser output into a strong pump pulse and weak probe pulse. With a pulse shaper, the pump pulse is filtered to narrow the spectrum around the HH 1*s* resonance. This spectral filtering helps to avoid exciting population at the light-hole (LH) resonances, higher-order HH resonances, and continuum. The number of photons in the pump pulse is set with a computer-controlled variable attenuator, then the polarization is set with a half-wave plate and quarter-wave plate in series. To monitor the pump, part of the pump beam is picked off and sent to a biased photodiode, which is calibrated to convert average photodiode voltage to the number of photons in each pump pulse. Finally, the pump is focused to a 100 μm spot on the sample.

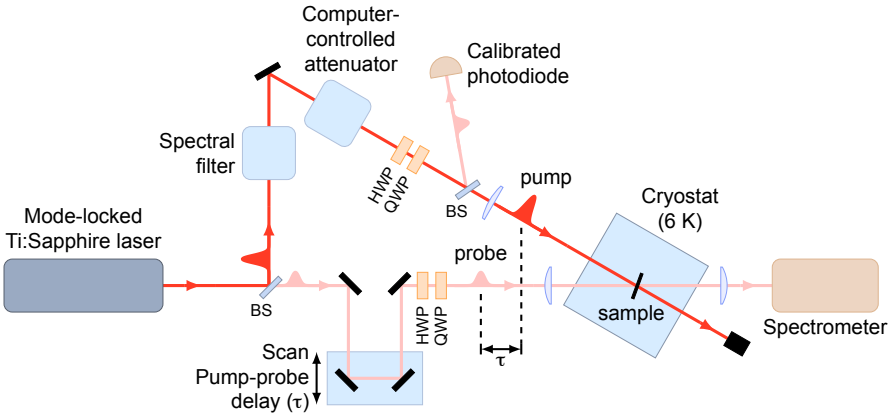

Figure S1: **Setup for spectrally resolved transient absorption measurement.** The 160 fs pulse from a mode-locked Ti:Sapphire laser is split into a strong pump pulse and a weak probe pulse. The pump pulse is filtered to narrow the spectrum around the heavy-hole (HH) 1*s* resonance. A computer-controlled attenuator sets the average pump power. Both the pump pulse and the probe pulse pass through wave plates to produce arbitrary polarization states. A small portion of the pump beam is monitored with a calibrated photodiode.

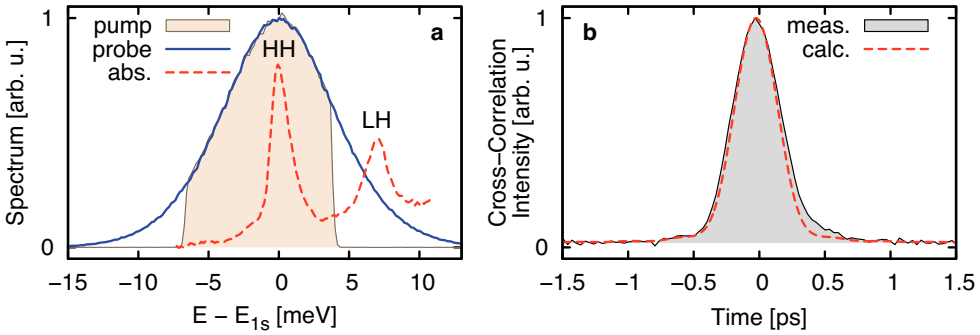

Figure S2: **Spectral and time-domain characterization of pump and probe.** (a) Pump spectrum (orange, filled) and probe spectrum (blue) measured directly by scanning the grating of a monochromator. Quantum-well absorption spectrum (dashed red) shown for comparison. The laser spectrum has a full width half max (FWHM) of 12.0 meV, and the wings of the pump spectrum are filtered out, as shown, to avoid exciting the light-hole (LH) exciton or the electron–hole continuum. (b) Intensity cross correlation of pump and probe measured directly (gray, filled) and calculated via Fourier transform of the pump and probe spectra, assuming no chirp (dashed red). The close fit shows that the pulses are nearly transform limited. The transform-limited temporal FWHM is 320 fs for the pump, and 160 fs for the probe.

The probe pulse is delayed with a mechanical stage, its polarization set using waveplates, and focused to a 10 μm spot on the sample. The probe spot size is much smaller than the pump so that it measures the absorption for a region with reasonably uniform excitation density. For this experiment, the pump and probe have opposite circular polarizations. The probe is spectrally resolved after the sample.

For detection, the pump and probe beams are chopped at different frequencies, ω_{PUMP} and ω_{PROBE}, and the signal split to two lock-in amplifiers referenced to ω_{PROBE} and $\omega_{\mathrm{SUM}} = \omega_{\mathrm{PUMP}} + \omega_{\mathrm{PROBE}}$. In real time, linear combinations of the ω_{PROBE} and ω_{SUM} signals are taken to recover the probe spectrum with and without the pump present. The spectrum without the pump is compared to careful absorption measurements taken with the pump blocked. This comparison gives a conversion factor to calibrate the absorption spectra, with the pump present, in absolute units.

B. Differential Spectrally Resolved Transient Absorption

We also use the transient-absorption setup to measure differential transmission due to a small change in the number of photons in the classical (coherent state) pump pulse. The results of this measurement are shown in Fig. 4 of the main text. We modulate the pump amplitude at 500 Hz using an AOM, and then detect the resulting probe transmission at a specific wavelength with a photodiode and lock-in amplifier referenced to the 500 Hz modulation signal.

To understand the signal measured by the lock-in amplifier in this setup, we express the modulated pump photon number in terms of mean pump photon number $\bar{N}_{\mathrm{PU}}$, modulation amplitude $N_{\mathrm{PU}}^{(0)}$, and modulation frequency ω_{PU}:

$$\begin{aligned} N_{\mathrm{PU}}(t) &\equiv \bar{N}_{\mathrm{PU}} + \delta N_{\mathrm{PU}}(t) \\ &= \bar{N}_{\mathrm{PU}} + N_{\mathrm{PU}}^{(0)} \cos(\omega_{\mathrm{PU}} t). \end{aligned} \tag{1}$$

Assuming the probe transmittance is an analytic function of the pump photon number,

$$T(N_{\mathrm{PU}}) = T(\bar{N}_{\mathrm{PU}}) + \frac{\mathrm{d}T}{\mathrm{d}\bar{N}_{\mathrm{PU}}}\delta N_{\mathrm{PU}} + \frac{\mathrm{d}^2T}{\mathrm{d}\bar{N}_{\mathrm{PU}}^2}\delta N_{\mathrm{PU}}^2 + \mathcal{O}(\delta N_{\mathrm{PU}}^3), \tag{2}$$

the signal sent from the photodiode to the lock-in amplifier is,

$$\begin{aligned} V_{\mathrm{PD}}(t) &\propto N_{\mathrm{PR}} T[N_{\mathrm{PU}}(t)] \\ &= N_{\mathrm{PR}} \Bigg(T(\bar{N}_{\mathrm{PU}}) + \frac{\mathrm{d}T}{\mathrm{d}\bar{N}_{\mathrm{PU}}} N_{\mathrm{PU}}^{(0)} \cos(\omega_{\mathrm{PU}} t) \\ &\quad + \frac{\mathrm{d}^2T}{\mathrm{d}\bar{N}_{\mathrm{PU}}^2} (N_{\mathrm{PU}}^{(0)} \cos(\omega_{\mathrm{PU}} t))^2 + \mathcal{O}[(N_{\mathrm{PU}}^{(0)} \cos(\omega_{\mathrm{PU}} t))^3] \Bigg). \end{aligned} \tag{3}$$

The lock-in amplifier selects the component of this signal that oscillates at ω_{PU}:

$$V_{\text{lock-in}}(t) \propto N_{\mathrm{PR}} N_{\mathrm{PU}}^{(0)} \frac{\mathrm{d}T}{\mathrm{d}\bar{N}_{\mathrm{PU}}}. \tag{4}$$

Thus, the signal measured by the lock-in amplifier is proportional to $\mathrm{d}T/\mathrm{d}\bar{N}_{\mathrm{PU}}$, the first derivative of the probe transmission with respect to pump photon number. Since we are only looking for oscillations in this value with respect to probe time delay, we have not calibrated this value in absolute units.

C. Two-dimensional coherent spectroscopy with pre-pulse excitation

As we discuss in the main text, the transient absorption data show an unexpected red shift in the biexciton binding energy. To verify this and obtain more detailed information, we performed a similar experiment using two-dimensional Fourier transform (2DFT) spectroscopy[S3] in place of the weak probe pulse. In 2DFT spectroscopy, a sequence of three pulses is used to create a coherent third-order nonlinear optical signal. This signal is then Fourier transformed with respect to the time delay between the first two pulses, giving the absorption energy, and with respect to the time after the third pulse, giving emission energy. By spreading the spectrum over both absorption and emission energy, 2DFT spectroscopy can disentangle congested spectra, separate homogeneous and inhomogeneous broadening, identify coherent coupling between resonances and identify microscopic many-body processes.

The pulse sequence for pre-pulse two-dimensional coherent spectroscopy is shown in Fig. S3. After the sample is optically excited by the pre pulse, 2DFT spectroscopy is performed with the remaining three pulses to probe the optical response of the excited many-body state in the sample. The pre pulse is spectrally shaped to excite only on the HH excitonic resonance. We can vary the pre-pulse intensity from 0 to $\sim 1.5 \times 10^{13}$ photons $\cdot$ cm^{-2} $\cdot$ pulse^{-1} to create different carrier densities in the sample. The 2DFT excitation pulse spectrum is tuned to excite both HH and LH excitons. The intensity of each 2DFT excitation beam is $\sim 4.7 \times 10^{11}$photons $\cdot$ cm^{-2} $\cdot$ pulse^{-1}. The first 2DFT pulse (pulse A) arrives 4 ps after the pre pulse. The pre-pulse beam is focused to a 211 μm (FWHM) spot on the sample, and the 2DFT beams are focused to a 54 μm (FWHM) spot in the center of the pre-pulse spot to probe only the area where the excitation is relatively uniform. The polarization of each beam can be individually controlled. In the current experiment, the polarizations of the pre pulse, A, B, C, and the detection are set to $\sigma^-\sigma^+\sigma^+\sigma^+\sigma^+$ respectively.

Insets to Fig. S4 show two representative 2D spectra for $N_{\mathrm{pump}} = 2.1 \times 10^6$ (left) and $N_{\mathrm{pump}} = 7.1 \times 10^6$ (right). For these spectra, the vertical axis corresponds to the Fourier transform with respect to delay between the first two pulses (absorption energy) and the horizontal axis to the time after the third pulse (emission energy). The diagonal peaks can be partially explained by considering the energy levels shown in Fig. S5(a), which includes the ground state g, the HH exciton states X_+ and X_-, and the biexciton state B. The higher-energy on-diagonal peak is contributed by the $g \rightarrow X_+$ transition. Starting from the ground state g, there are two possible quantum pathways for the given pulse

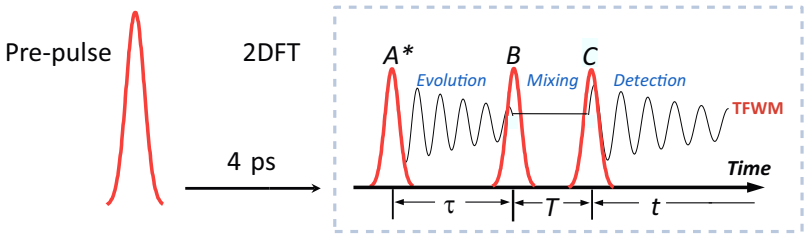

Figure S3: **The time ordering of the pulse sequence in pre-pulse 2D coherent spectroscopy.** The pre-pulse is followed by 2D pulses.

time ordering, the phase matching condition, and the polarizations. These two quantum pathways, show in Fig. S5(b) as double-sided Feynman diagrams, result in the higher-energy diagonal peak. With the presence of the pre pulse, a population is created in the X$_-$ state, which modifies the many-body configuration of the system and also provides access to the B states. Starting from the exciton state X$_-$, the 2DFT experiment can access the X$_-$ $\rightarrow$ B transition. The corresponding quantum pathways are shown in Fig. S5(c). They give rise to the lower-energy on-diagonal peak. Thus, the binding energy of the B states can be measured by comparing the emission energies of the two diagonal peaks. The extracted binding energy at different pre-pulse excitation intensity is shown in Fig. S4.

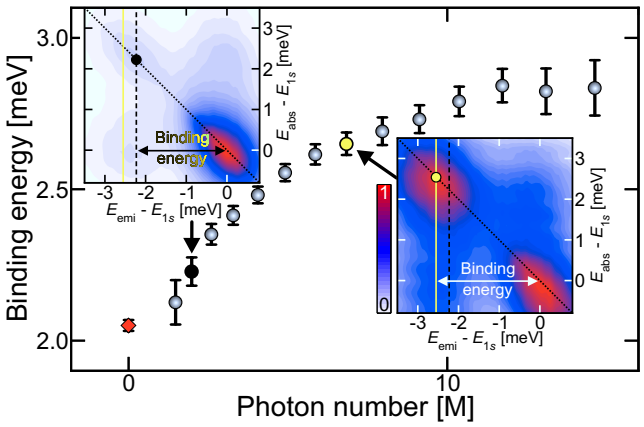

Figure S4: **Binding energy of low energy resonance measured using 2DFT spectroscopy as function of N_{pump}, with confidence intervals.** Diamond measured in cross-linearly polarized configuration to determine the zero-density biexciton energy. Insets: Examples of 2DFT spectra at $N_{\mathrm{pump}} = 2.1 \times 10^6$ (left) and $N_{\mathrm{pump}} = 7.1 \times 10^6$ (right). Emission (E_{emi}) and absorption (E_{abs}) energies determined with respect to N_{pump}-dependent E_{1s}. The filled circles indicate the low energy resonance and vertical lines identify the change of binding between the compared spectra.

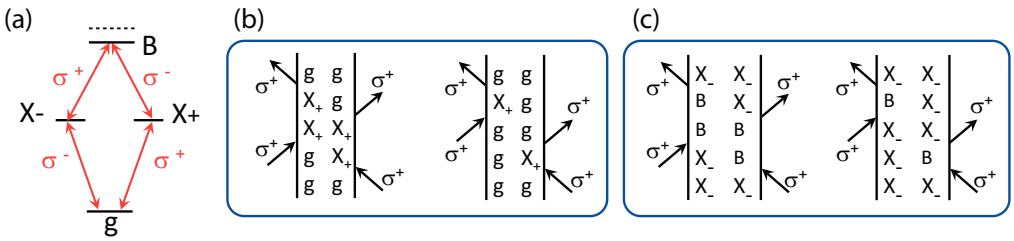

Figure S5: (a) The energy level diagram showing the heavy-hole exciton states (X$_+$ and X$_-$) and biexciton state B. (b) The quantum pathways contributing to the higher-energy on-diagonal peak. (c) The quantum pathways contributing to the biexciton component of the lower-energy on-diagonal peak.

As observed in the absorption spectra of Fig. 1a in the main text, the exciton resonance shifts to higher energy while the low-energy resonance shifts to lower energy, suggesting that the description of the lower energy state as a pure biexciton is incorrect. The binding energy starts at roughly the expected biexciton binding energy of just over

2 meV and increases to about 2.8 meV as the pump intensity increases, which confirms the unexpected increase of the biexciton binding energy observed in the pump-probe measurements.

II. QUANTUM THEORY OF PUMP-INDUCED CARRIER EXCITATIONS

To analyze our experiment, we give a brief overview of our full many-body theory describing all relevant interactions among carrier excitations[S4,S5], including the quantum-optical light–matter interaction. The elementary carrier excitations are described by the Fermion operators $a^\dagger_{\lambda,\mathbf{k}}$ and $a_{\lambda,\mathbf{k}}$ that create and annihilate an electron, respectively, in the valence $\lambda = v$ (conduction $\lambda = c$) band with crystal momentum $\hbar\,\mathbf{k}$. The quantized properties of the pump laser are characterized using the mode expansion for the electric field

$$\mathbf{E}(\mathbf{r}) = \sum_{\mathbf{q}} \mathcal{E}_{\mathbf{q}} \left[\mathbf{u}_{\mathbf{q}}(\mathbf{r}) B_{\mathbf{q}} + \mathbf{u}^\star_{\mathbf{q}}(\mathbf{r}) B^\dagger_{\mathbf{q}}\right] , \tag{5}$$

where $\mathbf{q}$ is the photon-wave vector and $\mathcal{E}_{\mathbf{q}}$ is the so-called vacuum-field amplitude connected with the mode function $\mathbf{u}_{\mathbf{q}}(\mathbf{r})$ having frequency $\omega_{\mathbf{q}} = c|\mathbf{q}|$. The Bosonic creation and annihilation operator $B^\dagger_{\mathbf{q}}$ and $B_{\mathbf{q}}$ define the quantum statistics of the light mode.

A. System Hamiltonian

The resonant excitations of direct gap semiconductor QWs can be described with a two-band Hamiltonian

$$\begin{aligned} \hat{H} &= \hat{H}_{\rm eh} + \hat{H}_{\rm lm} , \qquad \hat{H}_{\rm eh} = \sum_{\mathbf{k},\lambda} \epsilon^\lambda_{\mathbf{k}} a^\dagger_{\lambda,\mathbf{k}} a_{\lambda,\mathbf{k}} + \frac{1}{2} \sum_{\mathbf{k},\mathbf{k}',\mathbf{q},\lambda,\lambda'} V_{\mathbf{q}}\, a^\dagger_{\lambda,\mathbf{k}+\mathbf{q}} a^\dagger_{\lambda',\mathbf{k}'-\mathbf{q}} a_{\lambda',\mathbf{k}'} a_{\lambda,\mathbf{k}} , \\ \hat{H}_{\rm lm} &= \sum_{\mathbf{q}} \hbar\omega_{\mathbf{q}} \left(B^\dagger_{\mathbf{q}} B_{\mathbf{q}} + \tfrac{1}{2}\right) - \mathrm{i}\hbar \sum_{\mathbf{k},\mathbf{q}} \mathcal{F}_{\mathbf{q}} \left(a^\dagger_{c,\mathbf{k}} a_{v,\mathbf{k}} + a^\dagger_{v,\mathbf{k}} a_{c,\mathbf{k}}\right) B_{\mathbf{q}} + \mathrm{h.c.} , \end{aligned} \tag{6}$$

that is derived e.g. in Refs.[S5,S6]. Here, the electronic part, $\hat{H}_{\rm eh}$, contains the kinetic energies

$$\epsilon^c_{\mathbf{k}} = \frac{\hbar^2\mathbf{k}^2}{2m_e} + \mathrm{E_g} , \qquad \epsilon^v_{\mathbf{k}} = -\frac{\hbar^2\mathbf{k}^2}{2m_h} , \tag{7}$$

that are parabolic near the bandgap energy $E_{\rm g}$ as function of $\mathbf{k}$, introducing an effective electron (hole) mass m_e (m_h). The second part of $\hat{H}_{\rm eh}$ describes the Coulomb interaction with the Coulomb matrix element $V_{\mathbf{q}}$ of the confined system[S5], inducing all many-body effects. Free photons with wave vector $\mathbf{q}$ have energy $\hbar\omega_{\mathbf{q}}$ while the strength of light–matter interaction, $\mathcal{F}_{\mathbf{q}} = \mathbf{d}\,\mathcal{E}_{\mathbf{q}} \cdot \mathbf{u}_{\mathbf{q}}(0)$, consists of a product between the dipole-matrix element $\mathbf{d}$ for the interband transitions, the vacuum-field amplitude $\mathcal{E}_{\mathbf{q}}$, and the mode function at the QW position ($\mathbf{r} = 0$). The overall charge neutrality between the lattice and electrons eliminates the $\mathbf{q} = 0$ term in the Coulomb sum in Eq. (6)[S5]: We include this fact by implicitly setting $V_{\mathbf{q}=0} = 0$.

B. Correlations in light and electron–hole excitations

When the laser is resonant with the 1s-exciton state, the electron–hole pair excitations are defined by an exciton operator[S5]

$$\hat{X}^\dagger = \sum_{\mathbf{k}} \phi_{1s}(\mathbf{k})\, a^\dagger_{c,\mathbf{k}} a_{v,\mathbf{k}} , \tag{8}$$

where $\phi_{1s}(\mathbf{k})$ is the exciton wave function that is determined explicitly in Sec. VI B. The exciton operator always has nonbosonic corrections due to its composite Fermion-operator nature[S7].

A single-mode laser is described by a single B operator. The corresponding photon correlations can be uniquely defined in the correlation representation[S8]

$$\left[\Delta I^J_K\right]_{\rm B} = \Delta\langle \left[B^\dagger\right]^J B^K \rangle , \tag{9}$$

that contains the truly correlated parts of the expectation values

$$I_K^J = \langle \left[B^\dagger\right]^J B^K \rangle = \mathrm{Tr}\left[\left(B^\dagger\right)^J B^K \hat{\rho}\right] , \tag{10}$$

where $\hat{\rho}$ is the density matrix of the system. The correlations can be deduced uniquely by applying the cluster-expansion approach[S5,S8]. Electron–hole correlations can be determined analogously[S5], yielding

$$\left[\Delta I_K^J\right]_{\mathrm{X}} = \Delta\langle \left[\hat{X}^\dagger\right]^J \hat{X}^K \rangle . \tag{11}$$

Note, that these correlations fully include the Fermionic substructure of excitons.

C. Quantum-statistical state injection

On a general level, a fully quantized light–matter interaction (6) couples Bosonic light to Fermionic quasi-particle excitations. Investigations in Ref.[S9] have revealed that the interband-dipole transitions transfer correlation by mapping photon correlations (9) directly into electron–hole correlations (11). More specifically, the pump field injects electron–hole correlations[S9,S10]

$$\Delta\langle \left[\hat{X}^\dagger\right]^J \hat{X}^K \rangle = \eta^{\frac{J+K}{2}} \Delta\langle \left[B^\dagger\right]^J B^K \rangle , \tag{12}$$

before the onset of Coulomb and phonon scattering when fraction η of photons is absorbed as electron–hole pairs. In other words, when the pump laser pulse is short enough, one can inject the desired electron–hole correlation simply by adjusting the quantum statistics of the pump laser. This principle generalizes ultrafast laser spectroscopy into quantum-optical spectroscopy[S4,S9,S11] because one needs to shape the quantum fluctuations of the pump laser, instead of its classical aspects, i.e. amplitude, phase, duration, and spectrum. Quantum-optical spectroscopy offers an ideal search tool for finding new quasi-particles because quantum spectroscopy can individually access them through quantum-optical state injection.

III. PROJECTION TO QUANTUM RESPONSE

We have shown that new quasi-particles emerge when the pump pulse has roughly $N_{\mathrm{pump}} = 1.5 \times 10^6$ photons. Unfortunately, one cannot yet realize high-N_{pump} laser pulses whose quantum fluctuations can be shaped freely. Nonetheless, we have developed in Ref.[S11] an alternative solution to this problem by developing a robust algorithm tat converts a large set of *experimental* data, measured with present day lasers, into quantum-optical response. As a starting point of such investigations, the pump is defined by a coherent state $|\beta\rangle$[S12–S14] where β defines its complex-valued amplitude in a phasor diagram. With this information, we may use a general projection relation[S15]

$$R_{\mathrm{QM}} = \int \mathrm{d}^2\beta P(\beta) R_{|\beta\rangle} , \tag{13}$$

between *quantum-optical* response R_{QM} and *classical* response $R_{|\beta\rangle}$. The Glauber–Sudarshan function $P(\beta)$[S15,S16] is a phase-space distribution that defines the quantum statistics of the quantum-light source in the same way as the correlation representation (9). We see from Eq. (13) that a properly chosen $P(\beta)$ allows us to project the effect of correlation injection (12) to R_{QM} using a complete set of classically measured $R_{|\beta\rangle}$ data. Unfortunately, $P(\beta)$ is pathological for many interesting quantum sources, which makes the projection (13) challenging. However, we have already developed and demonstrated in Ref.[S8] a robust algorithm for an accurate projection of any desired R_{QM} from classical laser spectroscopy. The algorithm is summarized in Sec. V.

Once $R_{\mathrm{QM}}^{(\lambda)}$ is projected for a quantum source $P_\lambda(\beta)$ labeled here by λ, we can determine the effect of individual particle clusters from a generic differential response

$$R_{1,2} = R_{\mathrm{QM}}^{(1)} - R_{\mathrm{QM}}^{(2)} = \int \mathrm{d}^2\beta\, P_{1,2}(\beta) R_{|\beta\rangle} , \qquad P_{1,2}(\beta) \equiv P_1(\beta) - P_2(\beta) , \tag{14}$$

that follows directly from the projection relation (13) when we identify $P_{1,2}(\beta)$ as the quantum-statistics difference

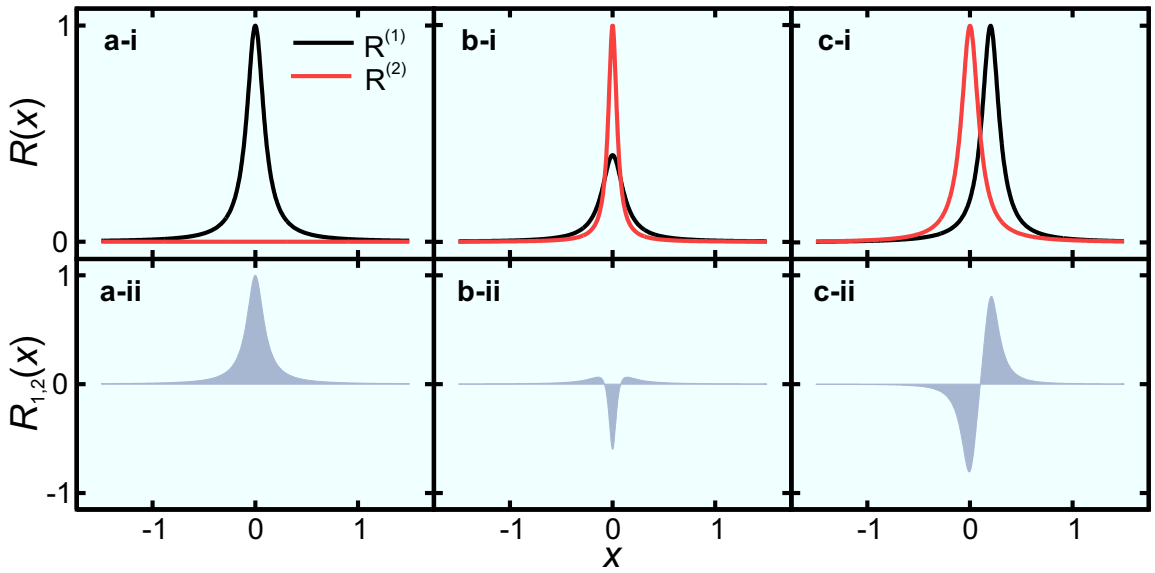

Figure S6: **Archetypes of differential spectra.** Initial spectrum $R^{(2)}$ (red line) changes into $R^{(1)}$ (black line) via resonance (a) creation/changed oscillator strength, (b) broadening, and (c) shift. Frame ii shows the corresponding differential $R_{1,2} = R^{(1)} - R^{(2)}$.

of two quantum sources. At the same time, $P_{1,2}(\beta)$ also defines the quantum-statistics difference,

$$\left[I_K^J\right]_{1,2} \equiv \left[I_K^J\right]_1 - \left[I_K^J\right]_2 = \int \mathrm{d}^2\beta \, (\beta^\star)^J \, \beta^K \, P_{1,2}(\beta) \,, \tag{15}$$

of two sources used in the projection (or in actual experiments) after we use the general connection between I_K^J and the phase-space integrals of the Glauber–Sudarshan function. In case of the difference $\left[I_K^J\right]_{1,2}$ vanishes for $J+K \leq (C-1)$, also the correlation differences

$$\left[\Delta I_K^J\right]_{1,2} \equiv \left[\Delta I_K^J\right]_1 - \left[\Delta I_K^J\right]_2 \tag{16}$$

vanish for $J+K \leq (C-1)$ because they are uniquely defined by the expectation values $\left[I_K^J\right]_{1,2}$ with $J+K \leq (C-1)$[S8]. As a result, the quantum sources $P_1(\beta)$ and $P_2(\beta)$ can then differ in C-particle correlations and above. Since quantum-state injection Eq. (12) matches the correlations of the pump and electron–hole system, the sources $P_1(\beta)$ and $P_2(\beta)$ inject two different states whose correlation difference is directly defined by Eq. (16).

In case $\left[\Delta I_K^J\right]_{1,2}$ difference vanishes up to $(C-1)$-particle correlations, the injected states can differ only starting from C-particle electron–hole configurations, based on the injection relation (12). The corresponding differential response (14) records then directly the effect of electron–hole clusters that have more or equal than C particles. We have utilized this generic property in our Letter to identify and demonstrate the existence of new quasi-particles because if a C particle cluster is stable, the direct injection shows up as new resonance in the $R_{1,2}$ response.

A. Archetypes of differential spectra

Positive and negative features in differential spectra can be identified via archetypes of responses. Figure S6 shows three relevant examples due to change from the initial spectrum $R^{(2)}$ (red line) into the final $R^{(1)}$ (black line). The corresponding differential, according to Eq. (14), is shown below as frame ii. More specifically, $R^{(1)}$ describes (a-i) the emergence of a resonance or the increase of oscillator strength, (b-i) broadening, or (c-i) shift of the resonance.

An exclusively positive signal only appears when either a new resonance emerges to the spectrum or the oscillator strength of an exciting resonance increases. Excitation-induced dephasing (Fig. S6(b)) or an energetic shift (Fig. S6(c)) always yields to a negative signal at least in some parts of the differential spectrum. In general, multiple of the principle forms appear simultaneously in $R_{1,2}$, which complicates the interpretation of the differential spectrum. However, we may detect the emergence of new quasi-particles clearly when quantum spectroscopy is applied, because it yields direct injection of new quasi-particles.

IV. SLANTED SCHRÖDINGER'S CAT STATE

We project the quantum-optical differential absorption $\Delta\alpha_{\rm MB}$ as a response that directly monitors quasi-particles with $C = 3$ correlated electron–hole clusters or more. To construct the corresponding differential from measurements, we generalize the Schrödinger's cat state of our earlier study[S11] by introducing a *slanted-cat state* that we define as the superposition of two coherent states with unequal amplitudes:

$$|\beta,\gamma,\theta\rangle = \mathcal{N}_{\gamma,\theta}\left[\cos\left(\theta+\tfrac{\pi}{4}\right)\mathrm{e}^{\mathrm{iIm}[\beta\gamma^\star]}|\Gamma_+\rangle + \sin\left(\theta+\tfrac{\pi}{4}\right)\mathrm{e}^{-\mathrm{iIm}[\beta\gamma^\star]}|\Gamma_-\rangle\right],$$
$$\mathcal{N}_{\gamma,\theta} \equiv \left(1+\cos 2\theta\ \mathrm{e}^{-2|\gamma|^2}\right)^{-\frac{1}{2}}, \qquad \Gamma_\pm \equiv \beta \pm \gamma, \tag{17}$$

where $\mathcal{N}_{\gamma,\theta}$ defines the norm. We use the angle θ to adjust the ratio of the amplitudes between the coherent states $|\Gamma_+\rangle$ and $|\Gamma_-\rangle$. With this parametrization, both coherent states have the same amplitude for $\theta = 0$ while only the state $|\Gamma_-\rangle$ is occupied for $\theta = \pi/4$. In order to find which $|\beta,\gamma,\theta\rangle$ states produce the $\Delta\alpha_{\rm MB}$ differential, we must first find those $|\beta,\gamma,\theta\rangle$ states that have identical single- and two-particle expectation values. Once $|\beta_1,\gamma_1,\theta_1\rangle$ and $|\beta_2,\gamma_2,\theta_2\rangle$ are found, the differential response (14) directly monitors the QW response resulting from the injection of three-particle correlations and beyond.

In general, the state Eq. (17) produces the single- and two-particle expectation values:

$$\langle B\rangle = \beta - \gamma\mathcal{N}^2_{\gamma,\theta}\sin 2\theta, \qquad \langle B^\dagger B\rangle = |\langle B\rangle|^2 + |\gamma|^2\mathcal{N}^4_{\gamma,\theta}\cos^2 2\theta\left(1-\mathrm{e}^{-4|\gamma|^2}\right),$$
$$\langle BB\rangle = \langle B\rangle^2 + \gamma^2\left(1-\mathcal{N}^4_{\gamma,\theta}\sin^2 2\theta\right), \tag{18}$$

that are obtained straight forwardly from the fundamental properties among coherent states[S5]. Obviously, many different $|\beta,\gamma,\theta\rangle$ combinations yield identical single- and two-particle expectation values such that the slanted-cat states establish the possibility to inject quasi-particles with $C \geq 3$ correlated electron–hole pairs.

In our study, we consider slanted-cat states that are small quantum perturbations around the classical pump laser, defined by the coherent state $|\beta_0\rangle$, because we can then monitor those quasi-particles that exist under conditions created by the classical pump. More specifically, we choose β so that the slanted-cat state has exactly the same displacement as the classical pump laser, i.e. $\langle B\rangle = \beta_0$, that yields $\beta = \beta_0 + \gamma\mathcal{N}^2_{\gamma,\theta}\sin 2\theta$ based on Eq. (18). Equation (18) also implies that the states with inverted angles, i.e. θ or $-\theta$, produce identical $\langle B^\dagger B\rangle$, $\langle BB\rangle$, and $\langle B^\dagger B^\dagger\rangle$. Therefore, we can construct $\Delta\alpha_{\rm MB}$ from the differential absorption of two states:

$$|\beta_1,\gamma_1,\theta_1\rangle \quad\text{with}\quad \beta_1 = \beta_0 - |\gamma|\mathcal{N}^2_{\gamma,\theta}\sin 2\theta, \quad \gamma_1 = |\gamma|, \quad \theta_1 = -\theta,$$
$$|\beta_2,\gamma_2,\theta_2\rangle \quad\text{with}\quad \beta_2 = \beta_0 + |\gamma|\mathcal{N}^2_{\gamma,\theta}\sin 2\theta, \quad \gamma_2 = |\gamma|, \quad \theta_2 = \theta, \tag{19}$$

that we use in constructing $\Delta\alpha_{\rm MB}$ from measurements; the precise algorithm is described in Sec. V.

Since the states (19) have identical single- and two-particle expectation values, only their $C \geq 3$ photon correlations can be different. More specifically, we find that the three-particle correlation differentials become

$$\left[\Delta I^0_3\right]_{1,2} = \left[I^0_3\right]_{1,2} = 4|\gamma|^3\mathcal{N}^2_{\gamma,\theta}\sin 2\theta\left(1-\mathcal{N}^4_{\gamma,\theta}\sin^2 2\theta\right), \qquad \left[\Delta I^1_2\right]_{1,2} = \left[I^1_2\right]_{1,2} = 4|\gamma|\mathcal{N}^2_{\gamma,\theta}\sin 2\theta, \tag{20}$$

and their magnitude can be adjusted via θ.

Equation (18) shows that slanted-cat states, defined in Eq. (19), have a photon number that is increased by

$$\delta N \equiv |\gamma|^2\mathcal{N}^4_{\gamma,\theta}\cos^2 2\theta\left(1-\mathrm{e}^{-4|\gamma|^2}\right), \tag{21}$$

with respect to the classical pump laser. Since we want to analyze small perturbations around $|\beta_0\rangle$, we find γ numerically for a fixed θ by demanding $\delta N = 1$, so that the slanted-cat states produce a single-photon increment with respect to $|\beta_0\rangle$. Since the classical laser has $N_{\rm pump}$ photons in the order of million, the single-photon increment in slanted-cat states generates only a small perturbation to the system. Therefore, the scale of slanted cat's higher-order correlations should be compared with $\delta N = 1$, i.e. the single-photon scale.

To study the three-particle correlation differential in more detail, Fig. S7 shows $\left[\Delta I^0_3\right]_{1,2}$ as function of θ for a fixed $\delta N = 1$. We see that $\left[\Delta I^0_3\right]_{1,2}$ diverges as θ approaches $\frac{\pi}{4}$ making the desired three-particle correlations very

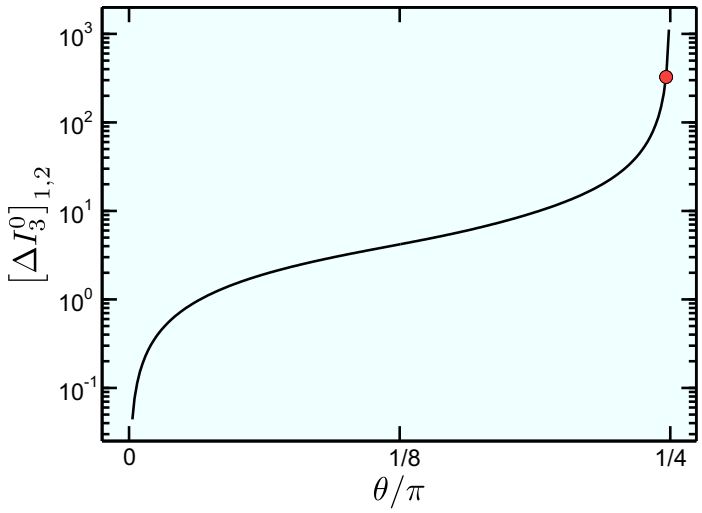

Figure S7: **Three-particle correlation differential.** Three-particle correlation differential $\left[\Delta I_3^0\right]_{1,2}$ as function of θ for a fixed $\delta N = 1$. The circle indicates θ and $\left[\Delta I_3^0\right]_{1,2}$ used in the Letter.

strong. Consequently, the magnitude of the injected many-body correlations involving three electron–hole pairs can be enhanced by choosing θ close to $\frac{\pi}{4}$. However, the $\theta \to \frac{\pi}{4}$ limit also produces a diverging γ displacement, according to Eq. (21), such that the coherent states within $|\beta, \gamma, \theta\rangle$ become spread infinitely far from each other. Since the experiment is projected within a finite phase-space, see Sec. V, one cannot approach $\theta \to \frac{\pi}{4}$ and $\gamma \to \infty$ limit in practice. As a compromise of large ΔI_3^0 and projection feasibility, we have used $\theta = 127\pi/512$ (circle) in our Letter yielding $\left[\Delta I_3^0\right]_{1,2} = \left[\Delta I_2^1\right]_{1,2} = 325.9$ for $\gamma = 81.5$. These values are large compared to the single-photon scale of the state but rather small compared to pump pulse's photon number which is in the range of millions. Therefore, the choice $\theta = 127\pi/512$ produces strong ΔI_3^0 correlations but yet rather small displacements within the cat states (19) making the projection of dropletons from measurement feasible.

To illustrate the general phase-space properties of slanted-cat states, we study the Wigner function

$$W^{|\beta,\gamma,\theta\rangle}(\beta') = \frac{\mathcal{N}_{\gamma,\theta}^2}{\pi}\left[(1-\sin 2\theta)\,\mathrm{e}^{-2|\beta'-\Gamma_+|^2} + (1+\sin 2\theta)\,\mathrm{e}^{-2|\beta'-\Gamma_-|^2} + 2\cos 2\theta\,\mathrm{e}^{-2|\beta'-\beta|^2}\cos\left(4|\gamma|\mathrm{Im}[\beta'-\beta]\right)\right], \tag{22}$$

of state (17). Figure S8 shows the Wigner function of $|\beta_1, \gamma_1, \theta_1\rangle$ (left) and $|\beta_2, \gamma_2, \theta_2\rangle$ (middle) and the difference $W_{1,2} \equiv W^{|\beta_1,\gamma_1,\theta_1\rangle} - W^{|\beta_2,\gamma_2,\theta_2\rangle}$ (right) for $\theta_1 = -3\pi/16$ ($\theta_2 = -\theta_1$), $\gamma_{1,2} = 2.6$, and $\beta_{1,(2)} = 997.6$ (1.002.4) as defined by Eq. (19). For sake of clarity, we have reduced $\theta_{1,2}$ further from the actual projection value to obtain a reduced displacement and enhanced visibility of the phase-space features. These modified states correspond to single-photon increments with respect to a coherent state with $\beta_0 = 1000$ having $|\beta_0|^2 = 10^6$ photons on average.

The Wigner functions of $|\beta_1, \gamma_1, \theta_1\rangle$ and $|\beta_2, \gamma_2, \theta_2\rangle$ contain Gaussians centered at $\Gamma_\pm$ indicated by vertical lines and an interference pattern between them. The amplitudes of the Gaussians are very different due to the different weighting so that the Gaussian located at Γ_- (Γ_+) of the state $|\beta_1, \gamma_1, \theta_1\rangle$ ($|\beta_2, \gamma_2, \theta_2\rangle$) is not visible on the shown scale. These slanted-cat states are truly quantum because the interference pattern shows pronounced negative regions such that one cannot interpret $W^{|\beta,\gamma,\theta\rangle}$ as a classical phase-space distribution. The state $|\beta, \gamma, \theta\rangle$ earns its name — slanted-cat state — due to its obvious quantum interference and the distinct asymmetry between $|\Gamma_-\rangle$ and $|\Gamma_+\rangle$ superposition.

The difference $W_{1,2}$ in Fig. S8(c) is antisymmetric with respect to the $x = \beta_0$ center. We observe that $W_{1,2}$ has a large negative (positive) peak centered at $x - \beta_0 = -0.2$ (0.2) and two interference patterns located around $x - \beta_0 = \pm 2.4$. In general, the positions and oscillation strengths of the two appearing interference patterns can be controlled by θ for states producing a single-photon increment with respect to $|\beta_0\rangle$. As a general trend, the interference patterns oscillate faster and the separation becomes larger with increasing θ for the single-photon increment states. In particular, the number of oscillations increases by a factor of 20 when θ is increased from $\theta = 3\pi/16$ to $\theta = 127\pi/512$ which is the value used in our Letter. At the same time, the central position of the interference patterns changes from $(x - \beta_0 = \pm 2.4)$ for $\theta = 3\pi/16$ to $(x - \beta_0 = \pm 81.5)$ for $\theta = 127\pi/512$.

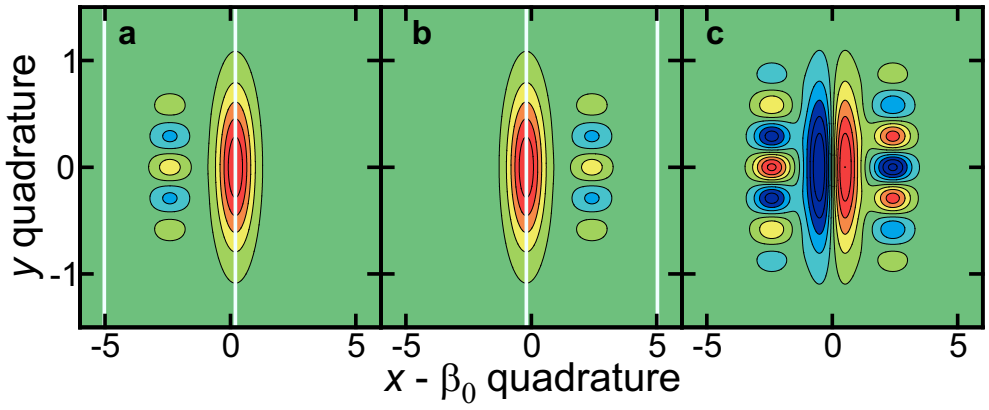

Figure S8: **Wigner function of slanted-cat states.** Contour plots of the Wigner functions for the states, (a), $|\beta_1, \gamma_1, \theta_1\rangle$ and, (b), $|\beta_2, \gamma_2, \theta_2\rangle$ are shown for $\theta_1 = -3\pi/16$ ($\theta_2 = -\theta_1$), $\gamma_{1,2} = 2.6$, and $\beta_{1,(2)} = 997.6$ (1.002.4). The states correspond to a single-photon increment with respect to the classical laser with $\beta_0 = 1000$. The displacement β_0 of the states is chosen to be along the x axis. The $\Gamma_\pm$ displacement centers are indicated by vertical lines. (c) The corresponding difference $W_{1,2}$.

V. CLUSTER-EXPANSION TRANSFORMATION (CET)

We have developed in Ref.[S11] an algorithm that converts a large set of classical measurements into quantum-optical differential responses (14), using projection (13). In particular, the method is robust against experimental noise and the projection can be computed from high-quality measurements for any quantum $P(\beta)$, even when $P(\beta)$ is nonanalytic. We next briefly summarize the algorithm used.

We first measure the probe absorption spectra $\alpha(E, \beta)$ as function of pump-laser's coherent displacement β and probe-photon energy E. In other words, we record a large set of $\alpha(E, \beta)$ absorption spectra within a phase-space region $\beta \in \Omega$, by adjusting the amplitude β of the pump laser. With respect to its β-dependence, $\alpha(E, \beta)$ can be perceived as an unnormalized phase-space distribution. The corresponding normalized phase-space distribution becomes then

$$W_R(E, \beta) \equiv \frac{\alpha(E, \beta)}{\mathcal{N}_R(E)}\,, \qquad \mathcal{N}_R(E) = \int_\Omega \mathrm{d}^2\beta\, \alpha(E, \beta)\,, \tag{23}$$

where $\mathcal{N}_\mathrm{R}$ defines the norm for measurements performed within a phase-space region Ω. Each probe E labels a separate phase-space distribution. In other words, two different E values yield two completely separate phase-space analyses. In the following, we follow one distinct E value and do not express the parametric E dependence explicitly, i.e. we implicitly have $W_R(\beta) \equiv W_R(\beta, E)$ and $\mathcal{N}_R \equiv \mathcal{N}_R(E)$.

Since our measured QW absorption depends only on pump laser's photon number, the phase-space distribution $W_R(\beta) = W_R(|\beta|)$ becomes rotationally symmetric. As a result, the relevant phase-space expectation values follow from

$$I(J) = \int_\Omega \mathrm{d}^2\beta\, |\beta|^{2J}\, W_R(|\beta|)\,. \tag{24}$$

These can be computed with a high accuracy from the measurement. In particular,

$$\Delta I = I(1) = \int_\Omega \mathrm{d}^2\beta\, |\beta|^2\, W_R(|\beta|)\,, \tag{25}$$

characterizes the intensity variance of the $W_R(\beta)$ distribution.

Once ΔI and $I(J)$ are determined from the β-measurement ensemble, we apply the cluster-expansion transformation (CET)[S8]

$$a_R(J) = \frac{J!J!}{[2\Delta I]^J} \sum_{L=0}^{J} \frac{[-\Delta I]^L I(J-L)}{L!(J-L)!(J-L)!}\,, \tag{26}$$

and its inverse

$$\alpha_{\mathrm{CET}}(\beta)=\frac{\mathcal{N}_R}{2\Delta I}\sum_{J=0}^{\frac{C}{2}}(-1)^J a_R(J)\,W_J\left(\tfrac{|\beta|^2}{2\Delta I}\right),\qquad W_J(x)=\frac{2}{\pi}\mathrm{e}^{-2x}\sum_{k=0}^{J}\frac{2^{2J-k}(-x)^{J-k}}{k!(J-k)!(J-k)!}, \tag{27}$$

in order to represent the measured response via an analytic function when C correlated, phase-space, clusters are included to the CET.

In order to construct $\alpha_{\mathrm{CET}}(E,\beta)$, we must perform an independent CET cycle from (23) to (27) for each E value separately. The data presented in our Letter contains 22 energy points such that a full CET spectrum is constructed using 22 separate CET transformations from a β ensemble that contains 21 pump intensities. As a general trend, the experimental noise influences only the $a_R(J)$ coefficients with a high J while already low-J coefficients contain the physical response, see Ref.[S11] for an explicit demonstration. Therefore, we can both eliminate the experimental scatter and access the physical response by choosing the C truncation appropriately. For the experimental data analyzed in our Letter, we use an average of $C=113$ clusters to reproduce the measured response accurately.

After $\alpha_{\mathrm{CET}}(E,\beta)$ reproduces the measured $\alpha(E,\beta)$ accurately enough, we may proceed with the actual projection of classical measurements into quantum response by replacing $R_{|\beta\rangle}$ by $\alpha_{\mathrm{CET}}(E,\beta)$ in Eq. (13). As a major benefit of the CET approach, the classical response is defined by an analytic function, given by Eq. (27), that is a product of a polynomial and a Gaussian. The coefficients within the polynomial and Gaussian decay are accurately deduced from the experimental β ensemble. The Gaussian factor within $\alpha_{\mathrm{CET}}(E,\beta)$ makes the phase-space integral (13) highly convergent to a degree that the input $P(\beta)$ can be chosen to be a nonanalytic Glauber–Sudarshan function of any quantum-light source. As a result, we can integrate projection (13) for any quantum source.

To project the slanted-cat response from measurements, we insert its Glauber–Sudarshan function:

$$\begin{aligned}P^{|\beta,\gamma,\theta\rangle}(\beta')=&\frac{\mathcal{N}_{\gamma,\theta}^2}{2}\left[(1-\sin 2\theta)\,\delta^{(2)}(\beta'-\Gamma_+)+(1+\sin 2\theta)\,\delta^{(2)}(\beta'-\Gamma_-)\right]\\&+\mathcal{N}_{\gamma,\theta}^2\lim_{\varepsilon\to 0}\frac{\cos 2\theta}{\pi\varepsilon}\mathrm{e}^{\left(\frac{1}{\varepsilon}-2\right)|\gamma|^2}\mathrm{e}^{-\frac{|\beta'-\beta|^2}{\varepsilon}}\cos\left(\frac{2|\gamma|}{\varepsilon}\mathrm{Im}\left[\beta'-\beta\right]\right),\end{aligned} \tag{28}$$

to the projection integral (13). We observe that the last term of Eq. (28) is nonanalytic and results from the interference pattern observed in Fig. S8, which again identifies $|\beta,\gamma,\theta\rangle$ as a quantum source. As we insert Eqs. (27) – (28) into Eq. (13) and integrate it, we find the quantum-optical QW absorption

$$\begin{aligned}\alpha_{|\beta,\gamma,\theta\rangle}(E,\Delta t,|\beta_0\rangle)=&\frac{\mathcal{N}_R}{4\Delta I}\sum_{J=0}^{\frac{C}{2}}(-1)^J a_R(J)\mathcal{N}_{\gamma,\theta}^2\\&\times\left[(1-\sin 2\theta)\,W_J\left(\frac{|\Gamma_+|^2}{2\Delta I}\right)+(1+\sin 2\theta)\,W_J\left(\frac{|\Gamma_-|^2}{2\Delta I}\right)+2\cos 2\theta\,\mathrm{e}^{-2|\gamma|^2}\mathrm{Re}\left[W_J\left(\frac{\Gamma_-^\star\Gamma_+}{2\Delta I}\right)\right]\right],\end{aligned} \tag{29}$$

to a slanted-cat state. All appearing $a_R(J)$ and ΔI coefficients are determined from an ensemble of β-dependent measurements so that we can indeed project the measurements into quantum-optical responses.

To search for new quasi-particles in semiconductor QWs, we project classical absorption measurements into the quantum differential between two slanted-cat states defined by Eq. (19):

$$\Delta\alpha_{\mathrm{MB}}(E,\Delta t,|\beta_0\rangle)\equiv\alpha_{|\beta_1,\gamma_1,\theta_1\rangle}(E,\Delta t,|\beta_0\rangle)-\alpha_{|\beta_2,\gamma_2,\theta_2\rangle}(E,\Delta t,|\beta_0\rangle), \tag{30}$$

which characterizes the absorption resonances resulting directly from three pair states on, as shown in Sec. IV. Since we measure the probe absorption as function of probe-photon energy and pump-probe delay Δt, we can construct the quantum kinetics of highly correlated quasi-particles. Technically, we measure 20 Δt values at roughly 2 ps time stepping.

VI. ENERGETICS OF DROPLETONS

To connect the new resonances in $\Delta\alpha_{\rm QM}$ (see Fig. 3 in our Letter) to new quasi-particles, we determine which many-body configurations have the same quantized energies as $\Delta\alpha_{\rm MB}$. We start from the many-body system defined by the density matrix $\hat{\rho}_{\rm MB}$ and the system Hamiltonian (6), yielding the average carrier-excitation energy

$$E_{\rm MB} \equiv \langle \hat{H}_{\rm eh} \rangle - E_{\rm g} N_{\rm eh} = {\rm Tr}\left[\hat{H}_{\rm eh}\,\hat{\rho}_{\rm MB}\right] - E_{\rm g} N_{\rm eh}\,, \tag{31}$$

for the many-body state $\hat{\rho}_{\rm MB}$ containing $N_{\rm eh}$ excited electron–hole pairs. Since each excited pair increases $\langle \hat{H}_{\rm eh} \rangle$ roughly by the bandgap energy $E_{\rm g}$, it is meaningful to choose the zero level such that the trivial $E_{\rm g} N_{\rm eh}$ dependency is removed from the energy average. By doing this, $E_{\rm MB}$ directly reveals the energetics of the studied $\rho_{\rm MB}$. We investigate a situation where the QW is homogeneously excited and it contains an equal amount of electrons and holes. As a result, the electron–hole pair number becomes

$$N_{\rm eh} = \sum_{\mathbf{k}} f^e_{\mathbf{k}} = \sum_{\mathbf{k}} f^h_{\mathbf{k}}\,, \qquad \text{with} \qquad f^e_{\mathbf{k}} \equiv \langle a^\dagger_{c,\mathbf{k}} a_{c,\mathbf{k}} \rangle\,, \qquad f^h_{\mathbf{k}} \equiv 1 - \langle a^\dagger_{v,\mathbf{k}} a_{v,\mathbf{k}} \rangle\,, \tag{32}$$

where we have introduced an electron (hole) distributions $f^e_{\mathbf{k}}$ ($f^h_{\mathbf{k}}$) using the usual electron–hole picture[S5].

Since we find the new quasi-particles also at the incoherent regime (see Letter), we consider those $\hat{\rho}_{\rm MB}$ states whose polarization and all other coherent quantities vanish and excitations are spatially homogeneous. For such conditions, inserting Hamiltonian (6) into Eq. (31) yields an exact result

$$\begin{aligned} E_{\rm MB} = &\sum_{\mathbf{k}} \left(\frac{\hbar^2 \mathbf{k}^2}{2m_e} f^e_{\mathbf{k}} + \frac{\hbar^2 \mathbf{k}^2}{2m_h} f^h_{\mathbf{k}} \right) - \frac{1}{2} \sum_{\mathbf{k},\mathbf{k}'} V_{\mathbf{k}-\mathbf{k}'} \left(f^e_{\mathbf{k}} f^e_{\mathbf{k}'} + f^h_{\mathbf{k}} f^h_{\mathbf{k}'} \right) \\ &+ \frac{1}{2} \sum_{\mathbf{k},\mathbf{k}',\mathbf{q}} \left[V_{\mathbf{q}} \left(c^{\mathbf{q},\mathbf{k}',\mathbf{k}}_{v,v;v,v} + c^{\mathbf{q},\mathbf{k}',\mathbf{k}}_{c,c;c,c} \right) - 2\, V_{\mathbf{k}'+\mathbf{q}-\mathbf{k}}\, c^{\mathbf{q},\mathbf{k}',\mathbf{k}}_{\rm eh} \right]. \end{aligned} \tag{33}$$

We have applied here the cluster expansion[S4] to identify the following incoherent two-particle correlations

$$\begin{aligned} &c^{\mathbf{q},\mathbf{k}',\mathbf{k}}_{v,v;v,v} \equiv \Delta\langle a^\dagger_{v,\mathbf{k}} a^\dagger_{v,\mathbf{k}'} a_{v,\mathbf{k}'+\mathbf{q}} a_{v,\mathbf{k}-\mathbf{q}} \rangle\,, \quad c^{\mathbf{q},\mathbf{k}',\mathbf{k}}_{c,c;c,c} \equiv \Delta\langle a^\dagger_{c,\mathbf{k}} a^\dagger_{c,\mathbf{k}'} a_{c,\mathbf{k}'+\mathbf{q}} a_{c,\mathbf{k}-\mathbf{q}} \rangle\,, \\ &c^{\mathbf{q},\mathbf{k}',\mathbf{k}}_{\rm eh} \equiv \Delta\langle a^\dagger_{c,\mathbf{k}} a^\dagger_{v,\mathbf{k}'} a_{c,\mathbf{k}'+\mathbf{q}} a_{v,\mathbf{k}-\mathbf{q}} \rangle\,. \end{aligned} \tag{34}$$

These describe truly correlated two-particle correlations of a two-particle expectation value. It is interesting to notice that $E_{\rm MB}$ is exactly described in terms of single-particle distributions $f^\lambda_{\mathbf{k}}$ and two-particle correlations $c^{\mathbf{q},\mathbf{k}',\mathbf{k}}$. Physically, $c^{\mathbf{q},\mathbf{k}',\mathbf{k}}_{v,v;v,v}$ and $c^{\mathbf{q},\mathbf{k}',\mathbf{k}}_{c,c;c,c}$ describe hole–hole and electron–electron correlations, respectively. The remaining $c^{\mathbf{q},\mathbf{k}',\mathbf{k}}_{\rm eh}$ determines electron–hole correlations within $\hat{\rho}_{\rm MB}$ and $\hbar\,\mathbf{q}$ defines the center-of-mass momentum of correlated electron–hole pairs.

In the density functional theory[S17], $E_{\rm MB}$ is expressed as a functional of the density. However, the interesting many-body quasi-particles are directly identifiable via their pair-correlation function, as shown in our Letter. Therefore, we have developed an alternative approach in Ref. [S18] that expresses $E_{\rm MB}$ completely in terms of pair-wise correlation functionals. We will next summarize the technical steps needed to compute the pair-excitation energetics of highly correlated states based on this approach.

A. Relevant electron–hole correlations

Since electron–hole-pair effects dominate our experiments, we concentrate on a situation where $c^{\mathbf{q},\mathbf{k}',\mathbf{k}}_{\rm eh}$ exists while $c^{\mathbf{q},\mathbf{k}',\mathbf{k}}_{c,c;c,c}$ and $c^{\mathbf{q},\mathbf{k}',\mathbf{k}}_{v,v;v,v}$ contributions can be neglected from energetic considerations. In addition, we assume that the detected quasi-particles are at rest by demanding

$$c^{\mathbf{q},\mathbf{k}',\mathbf{k}}_{\rm eh} = \delta_{\mathbf{q},0}\, c^{\mathbf{q},\mathbf{k}',\mathbf{k}}_{\rm eh} \equiv \delta_{\mathbf{q},0}\, g_{\mathbf{k},\mathbf{k}'}\,, \tag{35}$$

because $\hbar\,\mathbf{q}$ defines the center-of-mass momentum of correlations[S4]. As shown in Ref.[S18], a known pair-correlation function $\Delta g(\mathbf{r}) = |g_0 \phi(\mathbf{r})|^2$ with $\phi(\mathbf{r}) = \sum_{\mathbf{k}} \phi_{\mathbf{k}}\, {\rm e}^{{\rm i}\mathbf{k}\cdot\mathbf{r}}$ uniquely defines the excitation configuration[S18]

$$g_{\mathbf{k},\mathbf{k}'} = g_0^2\, \phi^\star(\mathbf{k}) \phi(\mathbf{k}')\,, \qquad f_{\mathbf{k}} = \tfrac{1}{2}\left(1 - \sqrt{1 - 4\, g_{\mathbf{k},\mathbf{k}}}\right). \tag{36}$$

As a general feature, electron and hole distributions become identical $f_{\mathbf{k}} \equiv f^e_{\mathbf{k}} = f^h_{\mathbf{k}}$ for quasi-particles where electron–hole correlations dominate over electron–electron and hole–hole correlations. But most importantly, Eq. (36) makes it possible to compute $E_{\rm MB}$ directly from the $g_{\mathbf{k},\mathbf{k}'}$ input.

B. Pair-excitation spectroscopy

As in the experiment, we consider that the many-body state is weakly excited to determine its characteristic energy resonances. We take Eq. (36) as an initial many-body state and compute the excess energy $E_{\rm pro}$ and particle number $N_{\rm pro}$ created by pair excitations. We then seek the ground state many-body configurations $(f_{\mathbf{k}}, g_{\mathbf{k},\mathbf{k}'})$ with variational calculation by finding that configuration which minimizes $E_{\rm pro}$ for a constant $N_{\rm pro}$. In analogy to the density functional theory, we express the system energy in terms of functionals, with the exception that they are expressed *exactly* in terms of the pair-correlation function $g_{\mathbf{k},\mathbf{k}'}$, not densities. We then find that the energy functional is minimized by the pair-excitation wavefunction that follows exactly from the generalized Wannier equation[S18,S19]

$$E_{\mathbf{k}}\,\psi_{\mathbf{k}} - \sum_{\mathbf{k}'} V^{\rm eff}_{\mathbf{k},\mathbf{k}'}\,\psi_{\mathbf{k}'} = E_\lambda\,\psi_{\mathbf{k}}\,, \tag{37}$$

with an effective eigenvalue E_λ and renormalized kinetic electron–hole pair energy

$$E_{\mathbf{k}} \equiv \left[\frac{\hbar^2\mathbf{k}^2}{2\mu} - 2\sum_{\mathbf{k}'} V_{\mathbf{k}-\mathbf{k}'}\,f_{\mathbf{k}'}\right](1-2f_{\mathbf{k}}) + 2\sum_{\mathbf{k}'} V_{\mathbf{k}-\mathbf{k}'}\,g_{\mathbf{k},\mathbf{k}'}\,, \qquad \mu = \frac{m_e m_h}{m_e+m_h}\,, \tag{38}$$

containing the reduced mass μ of electron–hole pairs. The presence of electron–hole densities and correlations also modifies the unscreened Coulomb interaction $V_{\mathbf{k}-\mathbf{k}'}$ in form

$$V^{\rm eff}_{\mathbf{k},\mathbf{k}'} \equiv (1-2f_{\mathbf{k}})\,V_{\mathbf{k}-\mathbf{k}'}\,(1-2f_{\mathbf{k}'}) + 2g_{\mathbf{k},\mathbf{k}'}V_{\mathbf{k}-\mathbf{k}'}\,. \tag{39}$$

At vanishing density and $g_{\mathbf{k},\mathbf{k}'}$, Eq. (37) defines the usual exciton problem that has hydrogen-like eigen solutions, explaining the series of exciton resonances in the absorption spectrum. For elevated densities and nonvanishing electron–hole correlations, the Coulomb interaction is modified such that new quasi-particle resonances may emerge.

Once $\psi_{\mathbf{k}}$ and E_λ are known, the energy per excited electron–hole pair follows from

$$\bar{E}_{\rm pro} = E_\lambda \frac{\sum_{\mathbf{k}} |\psi_{\mathbf{k}}|^2}{\sum_{\mathbf{k}} |\psi_{\mathbf{k}}|^2\,(1-2f_{\mathbf{k}})}\,. \tag{40}$$

This defines the energy per probe-generated electron–hole pair at the variational ground state that is analyzed in Fig. 2b in our Letter.

According to Eq. (1) in our Letter, the dropleton state is determined by

$$\phi(r) = J_0\left(x_n\,\tfrac{r}{R}\right)\mathrm{e}^{-\kappa r}\theta(R-r)\,. \tag{41}$$

We also assume that the area of the dropleton is proportional to the electron–hole density $\rho_{\rm eh} = \frac{1}{S}\sum_{\mathbf{k}} f_{\mathbf{k}}$ because the dropletons should grow in size as the electron–hole density is increased. The measured dropleton energetics is explained when the dropleton radius is chosen to be

$$R = 91\,\mathrm{nm}\,\sqrt{\rho_{\rm eh}/\rho_0}\,, \tag{42}$$

where $\rho_0 = 2.5 \times 10^{10}$ cm^{-2} is a reference density.

The $1s$-exciton pair-correlation function is defined by[S4,S5]

$$g_{\mathbf{k},\mathbf{k}'} = \phi_{1s}(\mathbf{k})\phi_{1s}(\mathbf{k}')\,, \tag{43}$$

based one Eq. (36) where we have included the g_0 coefficient into the $1s$-exciton wavefunction $\phi_{1s}(\mathbf{k})$. Since $\phi_{1s}(\mathbf{k})$ defines the initial many-body state and not the probed pair excitations, we need to solve it from the ordinary density-dependent Wannier equation[S4,S5]

$$\tilde{E}_{\mathbf{k}}\,\phi_{1s}(\mathbf{k}) - (1-2f_{\mathbf{k}})\sum_{\mathbf{k}'} V_{\mathbf{k}-\mathbf{k}'}\,\phi_{1s}(\mathbf{k}') = E_{1s}\,\phi_{1s}(\mathbf{k})\,, \qquad \tilde{E}_{\mathbf{k}} \equiv \frac{\hbar^2\mathbf{k}^2}{2\mu} - 2\sum_{\mathbf{k}'} V_{\mathbf{k}-\mathbf{k}'} f_{\mathbf{k}'} \tag{44}$$

that is solved iteratively.

To compute the quasi-particle energy via the energy per excited electron–hole pair (40), we solve the generalized Wannier equation (37) where we insert the self-consistent $(f_{\mathbf{k}}, g_{\mathbf{k},\mathbf{k}'})$ configuration and solve ϕ_{1s}, ψ_λ, E_λ, and $\bar{E}_{\rm pro}$ numerically. In general, this procedure yields multiple eigenstates and energies. From these, the lowest energy defines the variational ground state of the pair excitations. In our Letter, we compute the binding energy

$$E_{\rm bind} = \bar{E}_{\rm pro}(1s) - \bar{E}_{\rm pro}({\rm dropleton})\,, \tag{45}$$

for all ring numbers n as function of the electron–hole density $\rho_{\rm eh}$ where $\bar{E}_{\rm pro}(1s)$ and $\bar{E}_{\rm pro}({\rm dropleton})$ are the lowest-energy states for the exciton and dropleton, respectively.

Figure 3a compares the measured quantized energy levels in $\Delta\alpha_{\rm MB}$ with the computed $E_{\rm bind}$. The positions of the measured quantized energy levels agree well with the calculated binding energies for the 4- and 5-ring dropletons. Also the predicted merging of 6- and 7-ring features appears in the projected $\Delta\alpha_{\rm MB}$ because $\Delta\alpha_{\rm MB}$ starts to show first a transition to a broad 6-ring tail and then an added hump appears corresponding to the 7-ring dropletons, as observable in the left slice in Fig. 3a. In addition, one expects that the 6- and 7-ring produces much broader features than the 4- and 5- ring dropleton because they are created via further scattering from the injected 3-particle correlations, in agreement with Fig. 3a. Dropletons with one up to three ring dropletons are not detectable in Fig. 3a because they have a binding energy smaller than the biexciton, which makes them undetectable in the cross-circular measurement.

To estimate the effect of the Fermi pressure on the formation of dropletons, we determine the phase-space filling factor $(1-2f_{\mathbf{k}})$ for zero-momentum electrons. This value essentially defines how much other electrons are blocked from entering zero-momentum states due to Pauli exclusion. Therefore, $(1-2f_{\mathbf{k}=0})$ is directly related to the Fermi pressure for low-momentum electrons; when the phase-space filling is one (-1) electrons can enter freely (are blocked from entering) low-momentum states.

The resonant excitation conditions of our experiments excite the electron and hole distributions very close to the shape of the exciton wavefunction squared. Therefore, only the low-momentum states become occupied. As shown in Ref.[S1], resonant excitation generates electrons (holes) to an energy range that is comparable with 40 K (10 K) carrier temperature. This means that even a seemingly small carrier density can make the system quantum degenerate; compared to this situation, nonresonant and electronic excitations spread the electrons and holes to a much wider range than a resonant optical excitation does. Based on the computations presented in Fig. 2b, we find that the Pauli-blocking factor reduces to 0.41 at $\rho_{\rm eh} = 2.5 \times 10^{10}$ cm^{-2} where the 4-ring dropleton emerges. This implies a significant Pauli blocking, and hence Fermi pressure, for situations where dropletons exist. Therefore, dropletons can indeed be confined by Fermi pressure.

We also can compute the number of correlated electron–hole pairs within the droplet which is defined by $S_{\rm drop}\int {\rm d}^2r\Delta g(r) = S_{\rm drop}2\pi\int {\rm d}r\, r\Delta g(r)$ where $S_{\rm drop} = \pi R^2$ is the area of the dropleton as shown in Ref.[S18]. We find that the n-ring dropleton state has essentially n electron–hole pairs after the sharp ring-to-ring transition.

C. Generalizing the dropleton ansatz

The hard-wall ansatz (41) follows by assuming that the Fermi pressure acting upon the dropleton can be described with an infinite potential wall. More realistically, the particles can also move from inside to outside of the dropleton with cost of energy. The energy difference between the liquid-like inner part and plasma-like outer part may be described more precisely by assuming a soft, finite potential wall. We will next show that using soft-vs. hard-wall model does not change the dropleton.

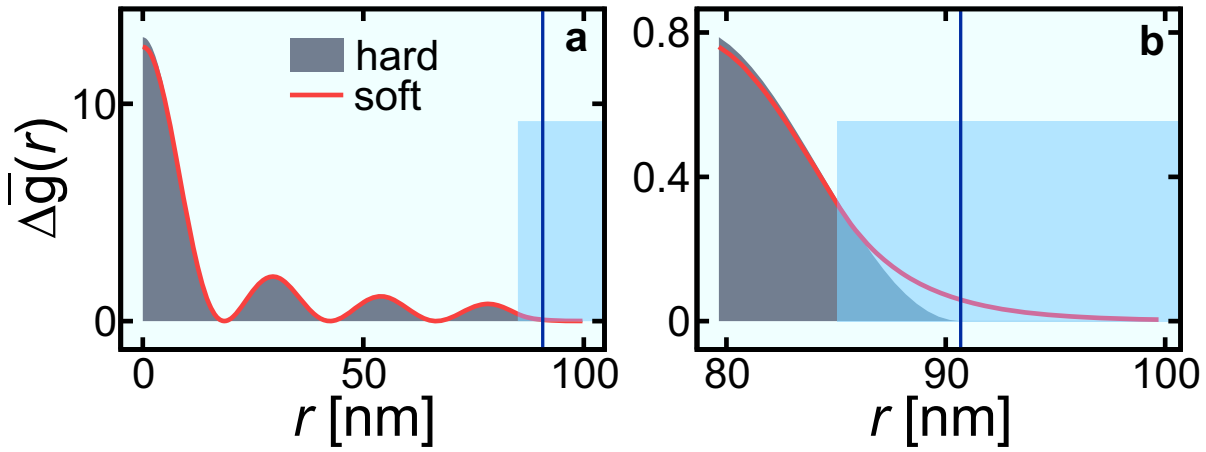

Figure S9: **Hard- vs. soft-wall dropleton properties.** (a) Normalized electron–hole pair-correlation function $\Delta\bar{g}(r)$ for hard- (gray shaded area) and soft-wall dropleton (solid line). The hard-wall (soft-wall) dropleton state has $R = 90.8\,\mathrm{nm}$ ($R_{\mathrm{soft}} = 85.1\,\mathrm{nm}$), $n = 4$ rings, and $\rho_{\mathrm{eh}} = 2.46 \times 10^{10}\,\mathrm{cm}^{-2}$ ($\rho_{\mathrm{eh}} = 2.52 \times 10^{10}\,\mathrm{cm}^{-2}$). The hard-wall radius is indicated by a vertical solid line while the soft-wall radius is shown as a transparent area. (b) Magnification of (a) close to the wall.

We model the soft-wall effects with an effective two-dimensional Hamiltonian

$$\hat{H} = -\frac{\hbar^2}{2m_{\mathrm{D}}}\nabla^2 + V(r)\,, \qquad V(r) = \begin{cases} 0, & r < R_{\mathrm{soft}} \\ V_0, & r \geq R_{\mathrm{soft}} \end{cases} \tag{46}$$

with an eigenfunction $\phi(r)$ that determines the dropleton pair-correlation via Eq. (36). For the soft-wall analysis, dropleton's radius is R_{soft} and V_0 is the height of the soft-wall potential $V(r)$. Since dropletons emerge at high densities, the single-particle energies also become renormalized by densities and correlations alike. To take this into account, the kinetic energy part of Eq. (46) contains an effective mass m_{D}. As a typical tendency, the renormalizations make m_{D} heavier than the low-density particle mass because particles tend to move slower inside the liquid.

Since Eq. (46) has radial symmetry, the Schrödinger equation $\hat{H}\phi(\mathbf{r}) = E\,\phi(\mathbf{r})$ can be solved exactly. The radially symmetric solutions cast then into the form:

$$\phi(r) = \mathcal{N}\begin{cases} J_0(kr)\,, & r < R_{\mathrm{soft}} \\ \frac{J_0(kR)}{K_0(\kappa R)}K_0(\kappa r)\,, & r \geq R_{\mathrm{soft}}\,, \end{cases} \tag{47}$$

where we have used the following parametrization: $E = \frac{\hbar^2 k^2}{2m_{\mathrm{D}}}$, $V_0 = \frac{\hbar^2 k_0^2}{2m_{\mathrm{D}}}$, and $\kappa = \sqrt{k_0^2 - k^2}$. For high enough potential wall ($k_0 > k$), the solution consists of an oscillating Bessel function $J_0(kr)$ inside the dropleton and exponentially decaying Bessel function $K_0(\kappa r)$ outside the dropleton. The physically allowed bound-state solutions follow from the usual boundary conditions, yielding the quantization condition

$$\frac{J_0(kR_{\mathrm{soft}})}{J_1(kR_{\mathrm{soft}})} = \frac{k}{\kappa}\frac{K_0(\kappa R_{\mathrm{soft}})}{K_1(\kappa R_{\mathrm{soft}})}\,, \tag{48}$$

that is satisfied only for a discrete set of k values. This quantization yields $\phi(r)$ that has n oscillations within the dropleton, which also defines the ring number. For an infinite wall, κ diverges such that Eq. (48) is satisfied only if $J_0(kR_{\mathrm{soft}})$ vanishes, reproducing the hard-wall result (41). For a finite V_0, Eq. (48) must be solved iteratively.

To directly compare the soft- and hard-wall results, we study a case where the soft-wall $\phi(r)$ is identical to the hard-wall wavefunction shape up to the radius of the soft wall R_{soft}. In other words, both the hard- and soft-wall wave vector is $k = x_n/R_{\mathrm{hard}}$, following from ansatz (41) with hard-wall radius $R = R_{\mathrm{hard}}$. As a general trend, the soft-wall R_{soft} is slightly smaller than R_{hard} because the particles tunnel into the wall region. We then seek for which soft-wall radius $R_{\mathrm{soft}} < R_{\mathrm{hard}}$ satisfies the quantization condition (48) for a given k_0. Once the corresponding $\phi(r)$ is known for both soft- and hard-wall dropleton, we can directly compute the pair-correlation function $\Delta g(r)$, the electron–hole density ρ_{eh}, and the pair-excitation energetics, as described in Sec. VI B.

Figure S9(a) shows the normalized $\Delta\bar{g}(r) \equiv \Delta g(r)/\rho_{\mathrm{eh}}^2$ for a quantum droplet confined within an infinite wall (gray shaded area). The dropleton has a hard-wall radius of $R_{\mathrm{hard}} = 90.8\,\mathrm{nm}$, $n = 4$ rings, and an electron–hole density

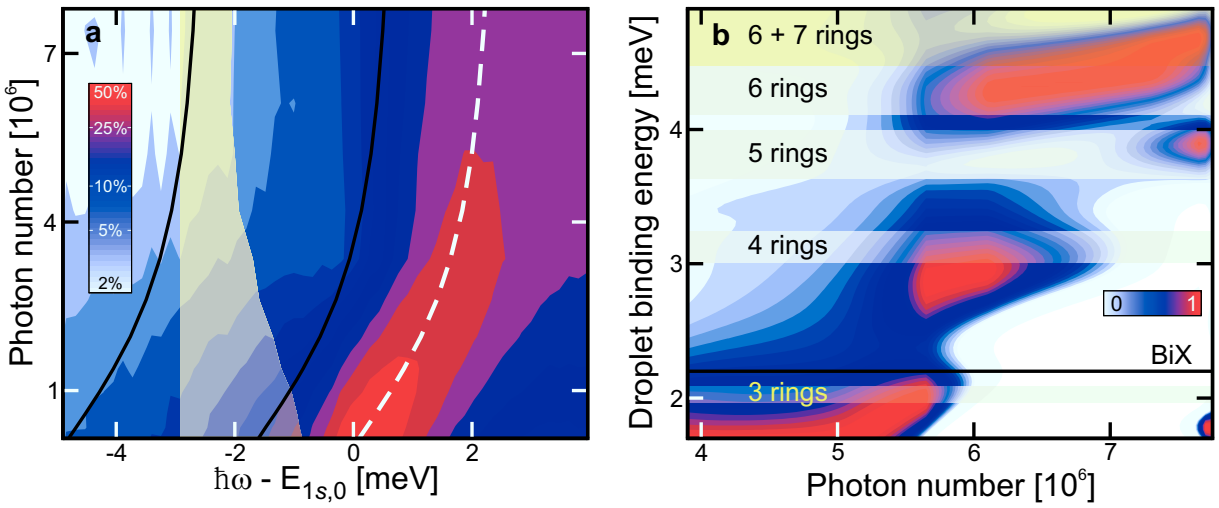

Figure S10: **Detection of dropletons with co-circular pump–probe configuration.** (a) Measured probe-absorption spectra as function of probe-photon energy and number of photons N_{pump} in the pump pulse for a pump–probe delay of 8 ps. The pump and probe have the same circular polarization. Transparent shaded area shows actual N_{pump} slice corresponding to $\hbar\omega - E_{1s,0} = -3$ meV. The dashed line indicates the shift of the heavy-hole exciton resonance and $E_{1s,0}$ is the low-density exciton energy. (b) Normalized $\Delta\alpha_{\mathrm{MB}}$ as function of N_{pump} and binding energy E_{bind}. The computed energies of 3-to-7-ring dropletons are indicated with shaded bands while the biexciton E_{bind} is marked by a solid line. The presented E_{bind} region is indicated by black lines in (a).

of $\rho_{\mathrm{eh}} = 2.46 \times 10^{10}\,\mathrm{cm}^{-2}$. The corresponding result for the soft-wall computation is plotted as solid line. We have used a soft-wall $k_0 = 2.0 \times 10^8\,\mathrm{m}^{-1}$ that yields $R_{\mathrm{soft}} = 85.1\,\mathrm{nm}$ which is 6.2 % smaller than R_{hard}. The position of the hard wall is indicated by a solid line while the position of the soft wall is presented as a transparent area. A magnification of $\Delta\bar{g}(r)$ is shown in Fig. S9(b), close to the wall. We see that the soft-wall produces $\Delta\bar{g}(r)$ that tunnels into the wall region with a 6.9 nm skin depth. This skin depth is comparable with the low-density exciton Bohr radius $a_0 = 12.5\,\mathrm{nm}$. Since a_0 defines the typical length scale of particle–particle interactions, the used soft wall confines dropletons on a typical interaction length scale. Therefore, it is plausible that the Fermi pressure of other particles can act upon the dropleton via the soft wall used here.

We also observe that the soft-wall $\Delta\bar{g}(r)$ has only a slightly smaller amplitude than the hard-wall result, which suggests that the dropleton-binding energy is only slightly modified. The actual computation produces 2.98 meV and 2.95 meV dropleton-binding energy for the hard- and soft-wall cases, respectively. The change is only 1 %, which confirms that the dropleton energetics we measure can be well described using also the hard-wall dropletons.

To gain more intuition how strong a wall is needed to confine dropletons, we estimate the magnitude of the confining potential. For this, one would need to know the effective, renormalized mass m_{D}. An accurate determination of m_{D} is beyond the scope of this report because it would require solving at least a 8-body many-body problem. However, we can make a reasonable estimate for the m_{D} without further many-body computations. Obviously, the dropleton liquid should slow down the particles, which effectively increases the particle mass. Therefore, we take the conduction-band electron mass m_e as the lower limit of m_{D}. Due to the liquid phase, these particles can equally well be 10 times heavier, i.e. slower. Therefore, we estimate m_{D} to be within $[m_e, 10\,m_e]$. For the used $k_0 = 2.0 \times 10^8\,\mathrm{m}^{-1}$, we find that the potential wall has height $V_0 \in [2.2, 22]$ meV. This value is comparable with the 10 meV exciton binding energy. Thus, the many-body state can easily rearrange itself to create the corresponding potential wall for dropletons whenever a dropleton state is available. Obviously, the carrier density must be significant because few particles cannot form the wall, both geometrically and energetically because the energy increase of the potential wall is shared by the carriers surrounding the dropleton. In other words, the wall creation should become energetically easier as more carriers participate to it.

VII. CONTROL MEASUREMENTS

To rule out alternative explanations for the dropleton resonances, we have performed two additional control measurements. In the first, we eliminate the possibility of creating or detecting polyexcitons by using a co-circular pump and probe. In the second, we study the result of the projection when no quasi-particles except electrons, holes,

and excitons are expected to be seen. This is realized by using high enough temperatures that all weakly bound quasi-particles become ionized.

A. Control measurement 1: Co-circular pump–probe configuration

In general, the probe adds (or removes) an electron–hole pair to the system, and the added pairs have the spin state defined by the probe. If the many-body system already has quasi-particles with opposite spin, the probe may detect both bound polyexciton states (including biexcitons) added to the system as well as resonances related directly to quasi-particle binding (such as dropletons) already existing in the system. In case the probing and many-body system have quasi-particles with the same spin, polyexcitons are strictly forbidden, due to antibonding, such that all new resonances must originate from single-spin quasi-particles (such as dropletons). In the main text, we exclusively study the cross-circular case, but it is clearly interesting to test the existence of dropletons with a control measurement that uses a co-circular pump–probe configuration (where the pump and probe have the same circular polarization). This configuration eliminates completely the possibility of detecting bound polyexcitons, including biexcitons, because the excitation and probing involve only parallel-spin excitations, which cannot be bound due to antibonding. Therefore, any detected resonance, below the exciton, cannot be attributed to polyexcitons. Although this reasoning suggests that the co-circular detection is more suitable for dropleton identification than the cross-circular setup used in the Letter, we will show below that the opposite is true, because the co-circular excitation produces much larger excitation-induced shifts (as seen earlier e.g. in Ref.[S1]).

Figure S10(a) shows a contour plot of the measured QW absorption as a function of probe-photon energy and number of photons N_{pump} in the pump pulse for a fixed pump–probe delay of 8 ps. The transparent shaded area shows actual N_{pump} slice at $\hbar\omega - E_{1s,0} = -3$ meV. At low pump intensities, the absorption spectrum shows a clear heavy-hole exciton resonance which broadens as the pump-photon number is increased. This data does not exhibit any biexciton feature 2.2 meV below the exciton, which is expected based on the discussion above. Instead, we observe that increasing N_{pump} blue shifts the heavy-hole exciton (dashed line) by 2.5 meV, i.e., 2.5 times more than for the cross-circular measurement in Fig. 1b, in agreement with previous experiments[S1]. This leads to a strong dispersive excitonic feature in the corresponding differential probe absorption that is appreciable across a wide spectral range. We also notice that the pump-induced exciton saturation emerges at $N_{\mathrm{pump}} = 6 \times 10^6$, compared with $N_{\mathrm{pump}} = 9.5 \times 10^6$ in Fig. 1b in our Letter. We attribute this difference to changes in spot sizes between the different measurements. Therefore, the N_{pump} of the co-circular case should be multiplied by 1.58 for a direct comparison.

To study the properties of dropletons in the measured probe-absorption spectra, we project the quantum differential $\Delta\alpha_{\mathrm{MB}}$ from the measured probe absorption presented in Fig. S10(a) using Eq. (30). A contour plot of the normalized $\Delta\alpha_{\mathrm{MB}}$ spectra is shown in Fig. S10(b) as a function of N_{pump} and the dropleton-binding energy E_{bind} defined with respect to the N_{pump}-dependent $1s$ energy. The computed energies of 3-to-7-ring dropletons are indicated by the shaded bands. The presented E_{bind} region is indicated by black lines in Fig. S10(a). Just as in the input data, the biexciton resonance (horizontal line) is absent from the $\Delta\alpha_{\mathrm{MB}}$ for all N_{pump}. Instead, only the dispersive excitonic tail close to 1.9 meV is visible for N_{pump} below 5×10^6. At $N_{\mathrm{pump}} = 5.5 \times 10^6$, the exciton resonance in Fig. S10(a) is already strongly bleached. Since there is no biexciton feature in the co-circular spectroscopy, $\Delta\alpha_{\mathrm{MB}}$ exhibits a clear resonance corresponding to 3-ring dropletons. This feature is completely absent in the cross-circular configuration due to the presence of the biexciton state.

As the pump intensity is further increased, we find a sharp transition to the 4-ring dropleton at $N_{\mathrm{pump}} = 5.6 \times 10^6$. Using the scaling factor above, the 4-ring dropleton appears at 8.8×10^6, compared to 1.3×10^6 in the cross-circular measurement (see Fig. 3). This apparent increase of the threshold stems from masking of dropleton features by the $1s$ blue-shift tails in the differential. Only when the dropleton resonances become strong, and the $1s$ resonance weak, do the dropletons become clearly visible. At the same time, the 4-ring dropleton appears at a density that is so high that multiple dropleton resonances should be present, based on the quantum-beats study in Fig. 3b. Indeed, the emergence of the 4-ring dropleton is soon accompanied with the emergence of 6/7-ring dropletons at $N_{\mathrm{pump}} = 5.7 \times 10^6$ and 5-ring dropleton at $N_{\mathrm{pump}} = 7 \times 10^6$. Obviously, the unusual order and appearance of the 5-ring dropleton is related to the high densities where the dropletons become visible compared with the cross-circular study. Also, the dropleton quantum beats can scramble the dropleton appearance order.

We have confirmed that both co- and cross-circular excitations produce identical energetics for the dropleton bands. Since co-circular excitation cannot excite polyexcitons, including biexcitons, we have unambiguously verified that the dropleton resonances cannot be polyexcitons. As the main difference between cross- and co-circular measurements, cross-circular measurements detect dropletons more sensitively due to the reduced excitation-induced shift of the exciton resonance.

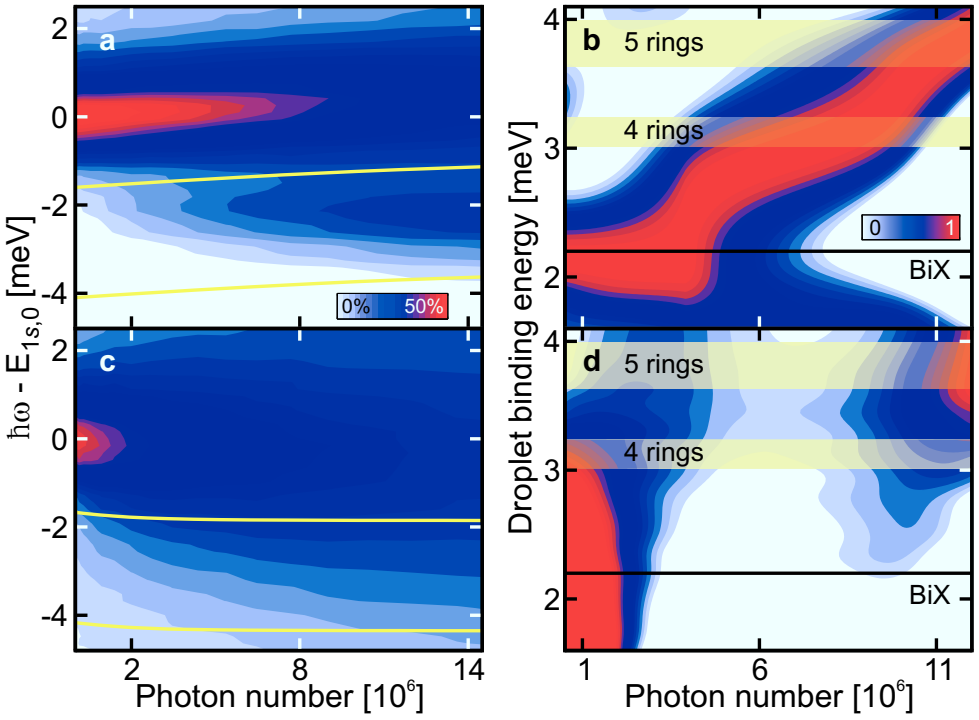

Figure S11: **Detection of dropletons at low and high sample temperatures.** (a) Measured probe-absorption spectra as a function of probe-photon energy and N_{pump} for $\Delta t = 8\,\mathrm{ps}$ and $T = 10\,\mathrm{K}$. The pump and probe have opposite circular polarization and $E_{1s,0}$ is the low-density exciton energy. (b) Normalized $\Delta\alpha_{\mathrm{MB}}$ as a function of N_{pump} and E_{bind}. The computed energies of 4- and 5-ring dropletons are indicated by shaded bands, while the biexciton E_{bind} is marked with a solid line. The presented E_{bind} region is indicated with yellow lines in (a). The corresponding 70 K results are shown in (c) and (d). Each $\Delta\alpha_{\mathrm{MB}}$ spectrum at 70 K is normalized to the maximum of the corresponding 10 K spectrum.

B. Control measurement 2: Temperature dependence

In general, raising the sample temperature increases the effect of phonon scattering such that weakly bound many-body states like biexcitons and dropletons dissociate. As a result, the dropleton signatures should be significantly lower for elevated temperatures. Therefore, we have performed cross-circular transient absorption measurements using two different sample temperatures to verify that dropletons vanish due to thermal ionization. More specifically, we have measured the QW absorption for a low ($T = 10\,\mathrm{K}$) and high ($T = 70\,\mathrm{K}$) sample temperature. (We note that the 10K data are a repetition of the results present in Figs. 1 and 3 of the main paper. We have repeated these measurements to avoid any quantitative discrepancies between the 10K and 70K results due to changes in experimental parameters such and the spot size or pump spectra.) The corresponding thermal energies are 0.9 meV (10 K) and 6.0 meV (70 K). Compared with the dropleton binding energy of around 3 meV, the 70 K measurement should not show clear dropleton signatures.

Figure S11(a) shows a contour plot of the measured QW absorption as a function of N_{pump} and probe-photon energy, at 8 ps pump–probe delay and with a sample temperature of $T = 10\,\mathrm{K}$. The absorption spectra show a heavy-hole exciton resonance for low N_{pump} which broadens and blue shifts as the pump intensity is increased. At roughly 2×10^6 photon-number excitation, a new biexciton-like resonance emerges 2 meV below the exciton, as in Fig. 1b. We note that the heavy-hole exciton resonance saturates at $N_{\mathrm{pump}} = 13.5 \times 10^6$ compared with $N_{\mathrm{pump}} = 9.5 \times 10^6$ in Fig. 1b in our Letter. This difference results from a change in the spot size between the different measurements. To directly compare both measurements, N_{pump} of the temperature-control measurement should be multiplied by 0.70. The corresponding measurement with a sample temperature of 70 K is presented in Fig. S11(c). As we compare 10 K with 70 K measurement, we see that the heavy-hole exciton resonance broadens significantly at 70 K due to increased phonon scattering. In addition, the biexciton-like peak is absent because phonon scattering ionizes all weakly bound states.

To resolve dropletons in the measured probe-absorption spectra, we project the differential absorption $\Delta\alpha_{\mathrm{MB}}$ from the measured absorption spectra of Figs. S11(a) and S11(c). The results are presented in Figs. S11(b) and S11(d), where the normalized $\Delta\alpha_{\mathrm{MB}}$ is shown as a function of dropleton binding energy and N_{pump} for $T = 10\,\mathrm{K}$ and $T = 70\,\mathrm{K}$,

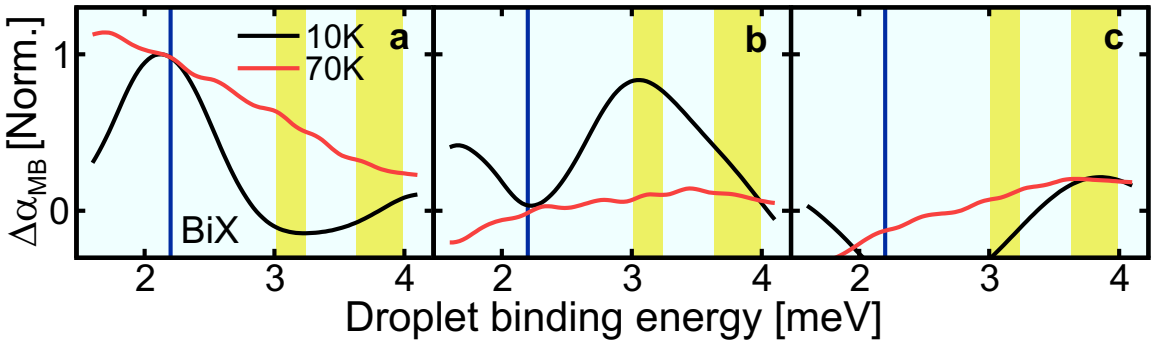

Figure S12: **Projected $\Delta\alpha_{\mathrm{MB}}$ spectra for $T = 10\,\mathrm{K}$ vs. $T = 70\,\mathrm{K}$.** Projected $\Delta\alpha_{\mathrm{MB}}$ spectra for $T = 10\,\mathrm{K}$ (black line) and $T = 70\,\mathrm{K}$ (red line) at (a) 2×10^6, (b) 8×10^6, and (c) 12×10^6 photon-number excitation. Spectra are normalized to the maximum of the 10 K $\Delta\alpha_{\mathrm{MB}}$ at $N_{\mathrm{pump}} = 2 \times 10^6$. The computed energies of 4- and 5-ring droplets are indicated with shaded bands, while the biexciton E_{bind} is marked by a solid line.

respectively. The shaded bands indicate the computed energies of 4- and 5-ring dropletons, while the biexciton binding energy is marked with a horizontal line. The presented E_{bind} region is indicated with yellow lines in Figs. S11(a) and S11(c). To directly compare the 10 K and 70 K measurement, we have normalized each 70 K spectrum to the maximum of the corresponding 10 K spectrum, while each 10 K spectrum itself is normalized to one. At $T = 10\,\mathrm{K}$, 4- and 5-ring dropletons appear after sharp transitions at $N_{\mathrm{pump}} = 4.0 \times 10^6$ and $N_{\mathrm{pump}} = 9.5 \times 10^6$, respectively, and the positions of the measured energy levels are explained well by the computed dropleton energies, in agreement with Fig. 3a. The corresponding 70 K result in Fig. S11(d) is dominated by the excitonic tail for N_{pump} below 2.5×10^6 that appears as an extended red-color contour. With increasing N_{pump}, a broad and weak feature appears between the 4- and 5-ring dropleton energies, whose amplitude becomes larger with respect to the 10 K measurement. However, this is not a dropleton, as discussed below.

To study the differences between the 10 K and 70 K measurements in more detail, Fig. S12 compares 10 K (black line) vs. 70 K (red line) spectra at (a) 2×10^6, (b) 8×10^6, and (c) 12×10^6 photon-number excitation. Each spectrum is normalized to the maximum of the 10 K $\Delta\alpha_{\mathrm{MB}}$ at $N_{\mathrm{pump}} = 2 \times 10^6$. The computed energies of 4- and 5-ring dropletons are indicated by shaded bands, while the biexciton E_{bind} is marked with a solid line. At $N_{\mathrm{pump}} = 2 \times 10^6$, the 10 K $\Delta\alpha_{\mathrm{MB}}$ spectrum has a pronounced resonance at the biexciton-binding energy, while the corresponding 70 K spectrum shows only the excitonic tail. For the intermediate photon number presented in Fig. S12(b), the 10 K measurement produces a resonance at the 4-ring dropleton while the 70 K $\Delta\alpha_{\mathrm{MB}}$ is featureless and about an order of magnitude smaller. The weak oscillations originate from the noise in the input. At elevated pump intensities (Fig. S12(c)), the signals of both measurements are weak (10 times smaller than at 2×10^6). Nevertheless, the 10 K $\Delta\alpha_{\mathrm{MB}}$ shows a resonance at the 5-ring dropleton, while the 70 K spectrum is again an extended featureless tail, such that no clear dropleton resonance is observable. In conclusion, we have demonstrated that the dropleton signatures vanish with increasing temperature, because no dropletons are detectable at 70 K. Thus, this control measurement confirms the expected physics for dropletons.

S1. Smith, R. P. *et al.* Extraction of many-body configurations from nonlinear absorption in semiconductor quantum wells. *Phys. Rev. Lett.* **104,** 247401 (2010).

S2. Siemens, M. E., Moody, G., Li, H., Bristow, A. D., & Cundiff, S. T. Resonance lineshapes in two-dimensional Fourier transform spectroscopy. *Opt. Express* **18**, 17699–17708 (2010).

S3. Cundiff, S. T. Optical two-dimensional Fourier transform spectroscopy of semiconductor nanostructures . *J. Opt. Soc. Am. B* **29**, A69–A81 (2012).

S4. Kira, M. & Koch, S. W. Many-body correlations and excitonic effects in semiconductor spectroscopy. *Prog. Quantum Electron.* **30**, 155 – 296 (2006).

S5. Kira, M. & Koch, S. W. *Semiconductor Quantum Optics* (Cambridge University Press, 2011), 1. edn.

S6. Kira, M., Jahnke, F., Hoyer, W. & Koch, S. W. Quantum theory of spontaneous emission and coherent effects in semiconductor microstructures. *Prog. Quantum Electron.* **23**, 189 – 279 (1999).

S7. Usui, T. Excitations in a high density electron gas. i. *Prog. Theor. Phys.* **23**, 787–798 (1960).

S8. Kira, M. & Koch, S. W. Cluster-expansion representation in quantum optics. *Phys. Rev. A* **78**, 022102 (2008).

S9. Kira, M. & Koch, S. W. Quantum-optical spectroscopy of semiconductors. *Phys. Rev. A* **73**, 013813 (2006).

S10. Koch, S. W., Kira, M., Khitrova, G. & Gibbs, H. M. Semiconductor excitons in new light. *Nature Mater.* **5**, 523–531

(2006).
S11. Kira, M., Koch, S. W., Smith, R. P., Hunter, A. E. & Cundiff, S. T. Quantum spectroscopy with Schrödinger-cat states. *Nature Phys.* **7**, 799–804 (2011).
S12. Gerry, C. & Knight, P. *Introductory Quantum Optics* (Cambridge University Press, 2005), 3. edn.
S13. Vogel, W. & Welsch, D. G. *Quantum Optics* (Wiley, 2006), 3. edn.
S14. Walls, D. F. & Milburn, G. J. *Quantum Optics* (Springer-Verlag, New York, 2008), 2. edn.
S15. Sudarshan, E. C. Equivalence of semiclassical and quantum mechanical descriptions of statistical light beams. *Phys. Rev. Lett.* **10**, 277–279 (1963).
S16. Glauber, R. J. Coherent and incoherent states of the radiation field. *Phys. Rev.* **131**, 2766–2788 (1963).
S17. Sholl, D. & Steckel, J. *Density Functional Theory: A Practical Introduction* (Wiley, 2009).
S18. Mootz, M., Kira, M. & Koch, S. W. Pair-excitation energetics of highly correlated many-body states *New J. Phys.* **15,** 093040 (2013).
S19. Wannier, G. The structure of electronic excitation levels in insulating crystals. *Phys. Rev.* **52**, 191–197 (1937).

Paper IV

M. Mootz, M. Kira, S. W. Koch, A. E. Almand-Hunter, and S. T. Cundiff

Characterizing biexciton coherences with quantum spectroscopy

Phys. Rev. B **89**, 155301 (2014)

Characterizing biexciton coherences with quantum spectroscopy

M. Mootz,[1,*] M. Kira,[1] S. W. Koch,[1] A. E. Almand-Hunter,[2,3] and S. T. Cundiff[2,3]
[1]*Department of Physics, Philipps University Marburg, Renthof 5, D-35032 Marburg, Germany*
[2]*JILA, University of Colorado and National Institute of Standards and Technology, Boulder, Colorado 80309-0440, USA*
[3]*Department of Physics, University of Colorado, Boulder, Colorado 80309-0390, USA*
(Received 22 November 2013; revised manuscript received 21 January 2014; published 2 April 2014)

The biexciton resonance in the absorption spectra of semiconductor quantum wells is analyzed with quantum-optical spectroscopy by projecting experimental pump-probe measurements into quantum-optical absorption spectra. More specifically, the measurements are converted into phase-space distributions using the cluster-expansion transformation. The quantum-optical responses can then be projected with full convergence, despite the unavoidable experimental noise. The calculations show that classical and quantum excitations produce significantly different results for the biexciton resonance. In particular, quantum-optical spectroscopy monitors the excitation-induced broadening of the biexciton resonance as a function of pump intensity much more sensitively than classical spectroscopy does.

DOI: 10.1103/PhysRevB.89.155301 PACS number(s): 42.50.−p, 78.40.Fy, 78.67.De

I. INTRODUCTION

Quantum mechanics inevitably implies that only a wave-function measurement enables the full characterization of matter's quantum state. This level of characterization is already achieved for simple systems such as a quantized light mode [1–5], trapped atom [6], or moving atoms [7] where the wave function or equivalently, the phase-space distributions have been measured. At the same time, the ascent of nanotechnology—built on semiconductors, molecules, and organics alike—depends critically on how well one can characterize and control the many-body states involved. Yet, it seems nearly impossible to realize such a "quantum-state tomography" for interacting many-body systems.

Nonetheless, it has been predicted [8,9] that the light-matter interaction has an inherent capability to directly excite targeted many-body states through the laser's nonclassical quantum fluctuations, which extends laser spectroscopy to quantum-optical spectroscopy. An experimental realization of this prospect requires quantum-light sources that are strong and flexibly adjustable in their quantum-optical fluctuations to control and access specific many-body states. In present-day experiments, there are no such quantum sources available. However, we have developed an alternative approach in Ref. [10] to deduce the quantum-optical response of many-body systems. In that article, we demonstrated with actual experimental data that a large set of classical measurements can be projected into the measured system's quantum-optical response to light sources with nonclassical quantum statistics. This particular work exposes a completely new level of many-body physics in semiconductor quantum wells (QWs) which remains otherwise hidden. Specifically, quantum-optical excitation produces an anomalous narrowing of the excitonic absorption, accompanied by a selective excitation of many-body states such as biexcitons and electron-hole complexes. It also has been shown [11,12] that quantum-optical spectroscopy has intriguing consequences for photon-statistics investigations of semiconductor emission. These aspects may become indispensable in light-matter strong-coupling investigations [13–20].

In this paper, we extend these quantum-optical spectroscopy studies to analyze how the biexciton resonance develops and broadens as a function of pump intensity, pump-probe delay, and the pump source's quantum-optical fluctuations. We show that quantum fluctuations, having the form of Schrödinger's cat state, help to resolve the excitation-induced dephasing [21,22] of biexciton coherences much more sensitively than classical excitations. More specifically, we find that the biexciton resonance survives to much higher pump intensities and larger pump-probe delays with quantum rather than with classical excitations. This result verifies the state-injection aspects of quantum-optical spectroscopy and thus shows that excitation with quantum-light sources improves the spectroscopy of complicated many-body systems.

In Sec. II, we briefly summarize the theoretical approach presented in Ref. [10] to project quantum-optical responses from a large set of classical measurements. The excitation-induced dephasing and the dynamics of the biexciton resonance in the absorption spectra of semiconductor QWs are analyzed in Sec. III as function of the pump laser's quantum-optical fluctuations.

II. FROM CLASSICAL TO QUANTUM-OPTICAL SPECTROSCOPY

At the moment, the lack of quantum sources with flexibly adjustable quantum statistics is a major obstacle for a complete experimental realization of quantum-optical spectroscopy. Nevertheless, one can measure the classical response that naturally includes all the aspects of many-body correlations. Interestingly, a comprehensive set of classical measurements also contains the information of all possible quantum-optical effects, even though this information is highly convolved. However, the projection of the quantum-optical system response is possible from a set of classical measurements, as we have shown recently in Ref. [10]. We briefly overview the central concepts of quantum-optical spectroscopy before we apply it to study biexciton-absorption resonances.

*martin.mootz@physik.uni-marburg.de

A. Quantum-optical response

Quantum statistics is the central concept of quantum-optical spectroscopy because it provides a complete description of the quantized light field, including the quantum-optical fluctuations. For example, a perfect laser outputs a coherent state [23] whose quantum statistics are characterized by a wave function $|\beta\rangle$. Physically, β is the complex amplitude of the laser; for normally ordered expectation values, one can simply replace photon operators by this amplitude, as if the coherent state behaved completely classically [22]. Even though $|\beta\rangle$ describes the most classical field possible, this simple relation does not hold for general expectation values. Therefore, even coherent states have some inherent quantum features.

General quantum statistics can be represented by using the density-matrix representation

$$\hat{\rho} \equiv \int d^2\beta \; P(\beta)|\beta\rangle\langle\beta|, \tag{1}$$

where $P(\beta)$ is the Glauber-Sudarshan function [24,25]. $P(\beta)$ is a phase-space distribution that also defines quantum statistics. One may equivalently represent the quantum statistics with the Wigner or the Husimi functions [22]. From these, the Glauber-Sudarshan function identifies the simplest criterion for the quantum-classical border: the quantum-light states are defined by those $P(\beta)$ functions that are partially negative. In other words, quantum-light states cannot be expressed as a probabilistic average over coherent states because the corresponding $P(\beta)$ in Eq. (1) is partially negative valued, producing quantum-optical effects such as antibunching [26,27] or squeezing [28,29].

One can now consider a situation where the optical response of the sample is measured with a set of coherent states, i.e., classical excitations. Let us denote the response to a coherent state $|\beta\rangle$ by $R_{|\beta\rangle}$. For example, the measured $R_{|\beta\rangle}$ can be transient absorption, photoluminescence, or four-wave mixing measurements, to mention a few. Based on the original observation by Sudarshan [25], the classical responses can be projected to a quantum response by using a convolution integral

$$R_P = \int d^2\beta \; P(\beta)\, R_{|\beta\rangle}. \tag{2}$$

The quantum response R_P is defined by $P(\beta)$ and the projection relation is general regardless of how complicated the many-body interactions are [10].

In principle, Eq. (2) can be used to project a large set of quantitative classical measurements $R_{|\beta\rangle}$ onto all possible quantum-source responses. Nevertheless, the computation of the quantum-optical response is challenging because one, in principle, needs to know $R_{|\beta\rangle}$ throughout the entire phase space. Even more so, one cannot measure $R_{|\beta\rangle}$ continuously but only at a discrete number of β points. In addition, any measurement exhibits some noise and the Glauber-Sudarshan function $P(\beta)$ is often nonanalytic for quantum sources, which complicates the computation of the convolution integral. As a result, the direct numerical integration becomes impossible.

Lobino *et al.* [30] have solved this challenging problem for simple systems if the density matrix behind $R_{|\beta\rangle}$ can be deduced with a maximum likelihood method. Nevertheless, this approach is not applicable for complicated many-body systems because their density matrix has an overwhelmingly large dimensionality. At the same time, we have developed an alternative method in Ref. [10] based on a straightforward idea: both of the functions within the projective integral (2) can be perceived as generalized phase-space distributions. The response $R_{|\beta\rangle}$ is then just an un-normalized phase-space distribution and we can use the cluster-expansion transformation (CET) [31] to remove the noise and extend it throughout the phase space. The formal aspects of the CET are presented in Appendix A, while the specific CET algorithm is given in Appendix B.

In general, the CET defines mean, variance, and higher-order clusters of the $R_{|\beta\rangle}$ distribution. As a typical trend, low-order clusters define the physical behavior of $R_{|\beta\rangle}$, while the technical noise of $R_{|\beta\rangle}$ influences mainly the very high-order clusters because they describe fast fluctuations corresponding to noise. Therefore, we can construct a CET form $R_{\mathrm{CET}}(\beta)$ of the measured $R_{|\beta\rangle}$ by truncating the clusters to the physical ones. Consequently, the CET can be used to filter out some noise from the measurement.

In addition, the resulting $R_{\mathrm{CET}}(\beta)$ is known continuously throughout the phase space. In particular, the CET-constructed response (B6) is a sum over polynomials multiplied by a Gaussian. This Gaussian decay guarantees the full integrability of the projection (2) when $R_{|\beta\rangle}$ is replaced $R_{\mathrm{CET}}(\beta)$; the accuracy of the method is thoroughly tested in Ref. [10] where the quantum response of the analytically solvable Jaynes-Cummings model [32] is studied. As a result, we can integrate the projection (2) for any quantum source so that we can determine the quantum-optical responses from measurements, as demonstrated in Ref. [10]. We use this approach to convert pump-probe measurements into quantum-optical absorption.

III. QUANTUM SPECTROSCOPY OF SEMICONDUCTOR-QUANTUM WELLS

To realize quantum-optical spectroscopy, we perform transient pump-probe absorption measurements as a function of pump intensity on a sample containing ten GaAs QWs. More details of the setup are given in Ref. [10]. The pump and probe pulse have opposite circular polarizations. As a result, our system response $R_{|\beta\rangle}$ is explicitly defined by the probe absorption $\alpha_{\mathrm{QW}}(E,\Delta t,|\beta_0\rangle)$ that is recorded in absolute units as a function of probe photon energy E, pump-probe delay Δt, and pump intensity $|\beta_0|^2$ defined by a coherent state $|\beta_0\rangle$. The orthogonal circular polarizations of pump and probe prevent pump-generated coherences from inducing phase-sensitive contributions to the probe response, i.e., the orthogonality eliminates the possibility for coherent interferences between the pump and the probe. Consequently, the measured QW absorption depends only on the photon number $N_0 = |\beta_0|^2$ such that we can apply the CET in a reduced form, as discussed in Appendix B.

An example of the measured QW absorption $\alpha_{\mathrm{QW}}(E,\Delta t,|\beta_0\rangle)$ is shown in Fig. 1(a) for six representative pump intensities, given in terms of the photon number N_0 of the pump pulse within the probed excitation spot. We quote N_0 in units of million ($10^6 = \mathrm{M}$) photons. We probe the

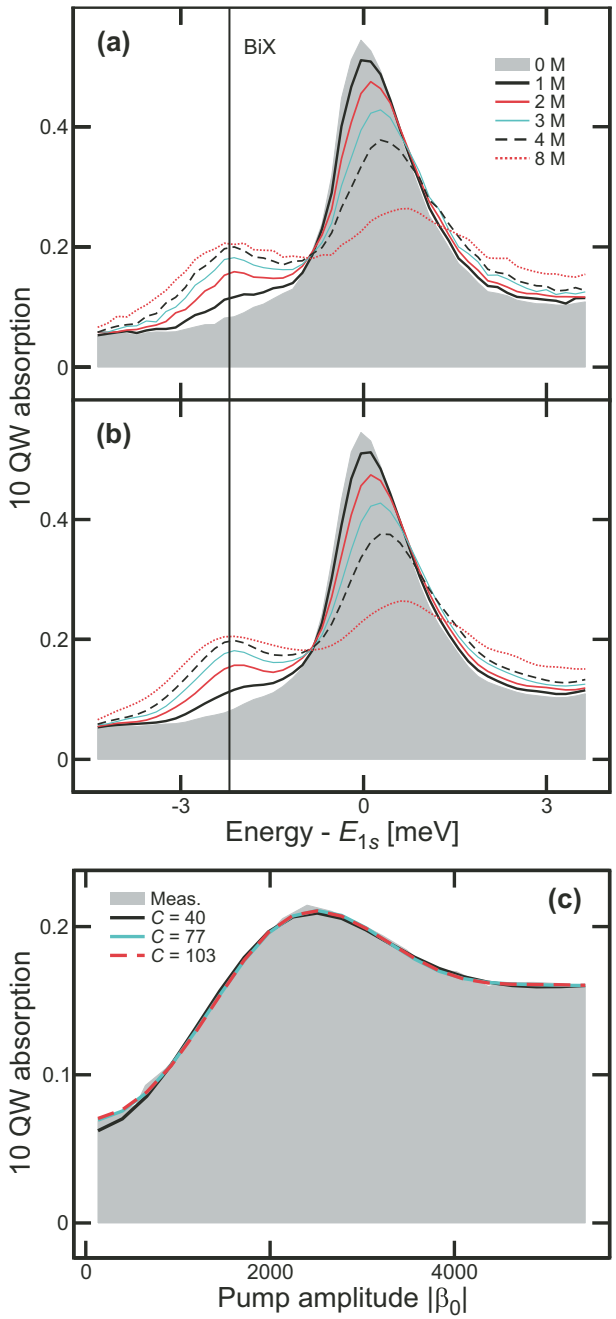

FIG. 1. (Color online) Input data for CET. (a) The measured ten QW absorption $\alpha_{\mathrm{QW}}(E,\Delta t = 12\ \mathrm{ps},|\beta_0\rangle)$ (defined in absolute units) is shown for six representative pump intensities. The vertical line denotes the spectral position of the biexciton resonance. (b) The corresponding low-pass filtered ten QW absorption $\alpha^{\mathrm{filt}}_{\mathrm{QW}}(E,\Delta t = 12\ \mathrm{ps},|\beta_0\rangle)$. (c) The measured ten QW absorption $\alpha_{\mathrm{QW}}(E_{\mathrm{BiX}},\Delta t = 12\ \mathrm{ps},|\beta_0\rangle)$ (shaded area) as function of pump amplitude $|\beta_0|$ is compared with the CET-constructed absorption $\alpha_{\mathrm{CET}}(E_{\mathrm{BiX}},\Delta t = 12\ \mathrm{ps},|\beta_0\rangle)$ for $C = 40$ (black line), $C = 77$ (cyan line), and $C = 103$ (dashed line). The measurement is performed at the biexciton resonance that is 2.2 meV below E_{1s}.

evenly excited part of the spot that has a 50 μm diameter. The pump-probe delay is $\Delta t = 12$ ps.

At the lowest intensities, the absorption spectra contain a resonance only at the $1s$ heavy-hole energy $E_{1s} = 1.547$ eV. We observe the typical excitation-induced broadening [33] of the $1s$ resonance as the pump N_0 is increased. At the same time, a second resonance emerges 2.2 meV below E_{1s} (vertical line) for a pump photon number above $N_0 = 1 \times 10^6 = 1$ M. This corresponds to the biexciton (BiX) resonance that is visible due to the opposite polarization directions of pump and probe. In general, circular polarized light generates an excitonic polarization of a single spin state in GaAs-type QW systems. Since a bound biexciton state contains excitons with opposite spins, one needs a pump and probe with opposite circular polarization in order to detect the biexciton resonance, as it is done in our experiment. We see that in classical spectroscopy, the biexciton line is broad for all intensities and it also broadens due to excitation-induced dephasing as the pump intensity is increased.

The measured $\alpha_{\mathrm{QW}}(E,\Delta t,|\beta_0\rangle)$ exhibits only a small amount of noise as a function of probe photon energy E. To increase the accuracy of characterization of the biexciton resonance, we low-pass filter the data to remove the spectral noise from the measurement. Technically, we low-pass filter $\alpha_{\mathrm{QW}}(E,\Delta t,|\beta_0\rangle)$ in energy for each fixed $|\beta_0\rangle$ and Δt separately to produce the low-pass filtered QW absorption spectrum $\alpha^{\mathrm{filt}}_{\mathrm{QW}}(E,\Delta t,|\beta_0\rangle)$. The resulting filtered QW absorption spectra are shown in Fig. 1(b) for the same pump photon numbers and pump-probe delay as in Fig. 1(a). Clearly, the low-pass filtering efficiently removes the residual noise from the measurement such that only smooth absorption spectra remain.

A. CET of measured QW absorption

To CET project the data, we measure the $\alpha_{\mathrm{QW}}(E,\Delta t,|\beta_0\rangle)$ spectra at 21 pump photon numbers $N_0 = |\beta_0|^2$ and 56 energy values. The shaded area in Fig. 1(c) presents the measured β_0 scan $\alpha_{\mathrm{QW}}(E_{\mathrm{BiX}},\Delta t,|\beta_0\rangle)$ at the biexciton energy $E_{\mathrm{BiX}} = -2.2$ meV $+ E_{1s}$ and fixed pump-probe delay $\Delta t = 12$ ps as a function of the pump amplitude $|\beta_0|$. We see that the biexciton resonance grows until about $\beta_0 = 2500$, i.e., $N_0 = |\beta_0|^2 = 6.25$ M, and then saturates as the amplitude is increased above $\beta_0 = 4000$, i.e., $N_0 = 16$ M.

The measured $\alpha_{\mathrm{QW}}(E_{\mathrm{BiX}},\Delta t = 12\ \mathrm{ps},|\beta_0\rangle)$ is indeed a slowly varying phase-space distribution as function of β_0, and its β_0 dependence is nonlinear. Based on these observations, we may expect that the biexciton resonance has strong sensitivity to the quantum-optical fluctuations because they exclusively modify the nonlinear properties [9].

As discussed in Sec. II, the response $\alpha_{\mathrm{QW}}(E,\Delta t,|\beta_0\rangle)$ can be perceived as an un-normalized phase-space distribution in the pump amplitude $|\beta_0|$ [10]. For fixed E and Δt, we can apply the CET to convert $\alpha_{\mathrm{QW}}(E,\Delta t,|\beta_0\rangle)$ into an analytical phase-space distribution $\alpha_{\mathrm{CET}}(E,\Delta t,|\beta_0\rangle)$ with the explicit steps defined in Appendix B. The resulting CET-reconstructed QW absorption $\alpha_{\mathrm{CET}}(E,\Delta t,|\beta_0\rangle)$ is a Gaussian times a polynomial. The Gaussian is determined by the variance $\Delta x_R(E,\Delta t)$ of the $\alpha_{\mathrm{QW}}(E,\Delta t,|\beta_0\rangle)$-response distribution, whereas the deviations of $\alpha_{\mathrm{QW}}(E,\Delta t,|\beta_0\rangle)$ from the Gaussian shape determine the higher-order correlation coefficients $a_R(J,E,\Delta t)$, where J is the cluster number. Technically, we have to compute the variance $\Delta x_R(E,\Delta t)$ and the correlations $a_R(J,E,\Delta t)$ for each probe photon energy E and pump-probe delay Δt

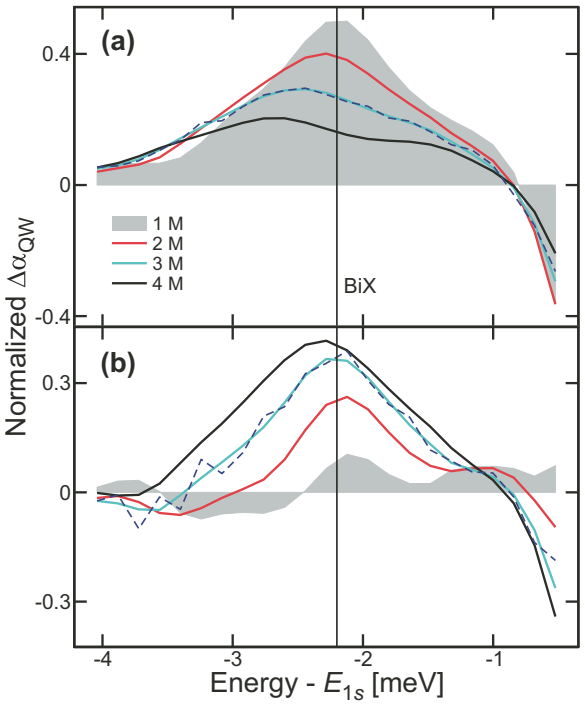

FIG. 2. (Color online) Projected classical and quantum-optical differential absorption. (a) The normalized classical differential-absorption spectrum $\Delta\bar{\alpha}_{\rm cl}(E,\Delta t=12\ {\rm ps},|\beta_0\rangle)$ is shown for 1 M (shaded area), 2 M (red line), 3 M (cyan line), and 4 M (black line) photon-number excitation. The corresponding 3-M photon excitation result, projected from the unprocessed measured QW absorption [Fig. 1(a)], is presented as a dashed line. The spectral position of the biexciton resonance is indicated by a vertical line. (b) The corresponding squeezing-cat differential absorption spectra.

separately, yielding the response $\alpha_{\rm CET}(E,\Delta t,|\beta_0\rangle)$, based on Eq. (B6). Figure 1(c) presents also the CET-reconstructed QW absorption $\alpha_{\rm CET}(E_{\rm BiX},\Delta t=12\ {\rm ps},|\beta_0\rangle)$ at the biexciton energy $E_{\rm BiX}$, where $C=40$ (black line), $C=77$ (cyan line), or $C=103$ (dashed line) clusters have been used in the reconstruction formula (B6). The CET result converges very well with increasing cluster number C while it removes the small experimental noise. In fact, the measured and low-pass filtered data yield essentially the same $\alpha_{\rm CET}(E,\Delta t,|\beta_0\rangle)$ result. We confirm, in connection with Figs. 2–4, that the measured and low-pass filtered input data also project into essentially the same quantum-optical responses.

B. Differential quantum response

Once the CET reconstruction best matches the experimental data as presented in Fig. 1(c), we may start projecting the quantum-optical responses with the projection formula (2), where $R_{|\beta\rangle}$ is simply replaced by $\alpha_{\rm CET}(E,\Delta t,|\beta_0\rangle)$. In this paper, we analyze quantum sources whose $P(\beta)$ corresponds to a quantum-light perturbation from the input coherent state $|\beta_0\rangle$; without a loss of generality, we analyze the response in the vicinity of a coherent state whose displacement is real-valued, i.e., $\beta_0={\rm Re}[\beta_0]$. In Ref. [10], we found that the biexciton state can be directly accessed by the so-called squeezing-cat state

$$|\beta_0,\gamma\rangle=\mathcal{N}(e^{i|\gamma|\beta_0}|\Gamma_-\rangle+e^{-i|\gamma|\beta_0}|\Gamma_+\rangle),$$
$$\mathcal{N}\equiv\frac{1}{\sqrt{2+2\,e^{-2|\gamma|^2}}},\quad \Gamma_\pm\equiv\beta_0\pm i|\gamma|, \tag{3}$$

which is a variant of the Schrödinger cat state [34]. More specifically, the squeezing cat is a superposition of two coherent states where the $\pm i|\gamma|$ displacements are perpendicular to the real-valued central displacement β_0. Currently, no quantum-light source is available that has quantum-optical fluctuations of a squeezing-cat state. However, we can use the approach summarized in Sec. II to compute the quantum-optical QW absorption, resulting from a quantum source that has quantum statistics of a squeezing-cat state.

To project quantum-optical responses from pump-probe measurements, we start from the measured QW absorption spectra $\alpha_{\rm QW}(E,\Delta t,|\beta_0\rangle)$. We then apply the CET to convert the measurements into an analytical phase-space distribution, as explained in connection with Fig. 1(c). To convert the measured $\alpha_{\rm QW}(E,\Delta t,|\beta_0\rangle)$ into the CET form $\alpha_{\rm CET}(E,\Delta t,|\beta_0\rangle)$, we have performed an independent CET cycle for each probe photon energy E and pump-probe delay Δt separately. Technically, this means that each E and Δt produces its own set of CET coefficients $\Delta x_R(E,\Delta t)$ and $a_R(J,E,\Delta t)$, computed with the algorithm presented in Appendix B. To simplify the notation, we suppress denoting the explicit E and Δt dependence in these coefficients.

Once Δx_R and $a_R(J)$ of the measured $\alpha_{\rm QW}(E,\Delta t,|\beta_0\rangle)$ are known, the Gaussian decay in $\alpha_{\rm CET}(E,\Delta t,|\beta_0\rangle)$ guarantees the full integrability of the convolution integral (2) for any quantum-optical pump source.

As elaborated in Appendix C, the squeezing-cat state's quantum-optical response can be efficiently computed using Eq. (C3), which is an integral of well-behaved functions. By inserting Eqs. (C4) and (B5) into Eq. (C3), we obtain [10]

$$\alpha_{|\beta_0,\gamma\rangle}(E,\Delta t)=\frac{\mathcal{N}_R}{4\Delta x_R^2}\sum_{J=0}^{\frac{C}{2}}(-1)^J a_R(J)\times\mathcal{N}^2\left(G_J\left(\frac{|\Gamma_+|^2}{4\Delta x_R^2}\right)+G_J\left(\frac{|\Gamma_-|^2}{4\Delta x_R^2}\right)+2\,e^{-2|\gamma|^2}{\rm Re}\left[G_J\left(\frac{\Gamma_-^\star\Gamma_+}{4\Delta x_R^2}\right)\right]\right), \tag{4}$$

which is the *projected response* to the Schrödinger cat state (3). In more detail, the $G_J(\frac{|\Gamma_\pm|^2}{4\Delta x_R^2})$ are defined in Appendix B and they describe semiclassical properties because they produce a displaced classical response for a real-valued argument. In contrast to that, the ${\rm Re}[G_J(\frac{\Gamma_-^\star\Gamma_+}{4\Delta x_R^2})]$ has a complex-valued argument such that it corresponds to an analytic continuation of the classical response into the complex plane. Therefore, it cannot be understood semiclassically, and thus squeezing-cat states must induce effects beyond classical spectroscopy.

In this connection, we compute how the QW absorption changes when the laser β_0 is changed classically, yielding the differential absorption

$$\Delta\alpha_{\rm cl}(E,\Delta t,|\beta_0\rangle)\equiv\alpha_{\rm CET}(E,\Delta t,|\beta_0+\Delta\beta\rangle)-\alpha_{\rm CET}(E,\Delta t,|\beta_0\rangle). \tag{5}$$

We choose $\Delta\beta$ so that the pump intensity $|\beta_0 + \Delta\beta|^2 = N_0 + 1$ is increased by one photon compared with the original $|\beta_0|^2 = N_0$. This result is compared with the *quantum-optical differential absorption*

$$\Delta\alpha_{\mathrm{cat}}(E,\Delta t,|\beta_0\rangle) \equiv \alpha_{|\beta_0',\gamma\rangle}(E,\Delta t) - \alpha_{\mathrm{CET}}(E,\Delta t,|\beta_0\rangle) \quad (6)$$

between a classical laser $|\beta_0\rangle$ and its perturbation with a squeezing-cat state $|\beta_0', \gamma\rangle$. We choose γ so that the cat state contains one more photon *in quantum fluctuations* than the coherent state. At the same time, we compensate the increase of the photon number by lowering the β_0' displacement so that $|\beta_0',\gamma\rangle$ contains exactly the same number of photons as the classical state $|\beta_0\rangle$ does. Therefore, $\Delta\alpha_{\mathrm{cat}}(E,\Delta t,|\beta_0\rangle)$ projects the pure quantum-statistics-induced changes to the QW absorption.

To directly compare the relative magnitude of both excitations, we normalize the differential absorption spectrum of each excitation type with respect to the peak differential absorption α_{peak} among all E, Δt, $|\beta_0\rangle$ values studied:

$$\Delta\bar{\alpha}_{\mathrm{type}}(E,\Delta t,|\beta_0\rangle) \equiv \frac{\Delta\alpha_{\mathrm{type}}(E,\Delta t,|\beta_0\rangle)}{\alpha_{\mathrm{peak}}}, \quad (7)$$

where type is either cl (classical) or cat (cat-state quantum response). The ranges of all E include the biexciton and exciton resonances [see Fig. 1(a)], and the range of all $|\beta_0\rangle$ is shown in Fig. 1(c). The studied pump-probe delay range is $\Delta t =$ [1,40] ps.

We compare classical $\Delta\bar{\alpha}_{\mathrm{cl}}(E,\Delta t = 12\ \mathrm{ps},|\beta_0\rangle)$ with the projected response for a squeezing cat $\Delta\bar{\alpha}_{\mathrm{cat}}(E,\Delta t = 12\ \mathrm{ps},|\beta_0\rangle)$ in Fig. 2 for four representative pump intensities: 1 M (shaded area), 2 M (red line), 3 M (cyan line), and 4 M (black line). We focus the analysis around the biexciton resonance (vertical line); the classical results are shown in Fig. 2(a), while Fig. 2(b) presents the squeezing-cat differential.

We see that the classical differential shows a peak around the biexciton resonance for a pump intensity of $N_0 = 1$ M. This very much corresponds to the intensity where the biexciton resonance starts to emerge into the actual absorption spectrum shown in Fig. 1(b). As the main difference between the actual and the differential spectrum, $\Delta\bar{\alpha}_{\mathrm{cl}}(E,\Delta t,|\beta_0\rangle)$ resolves the biexciton resonance much more clearly, as it is to be expected. However, the biexciton resonance starts to significantly broaden for elevated pump intensities, which is a typical behavior for excitation-induced broadening [21]. Additionally, the resonance is slightly red shifted with increasing pump intensity N_0. We also see that the high-energy part of the peak is strongly influenced by the tail of the 1*s* feature, 2.2 meV above the biexciton resonance, such that an accurate characterization of the biexciton properties has complications when classical spectroscopy is used.

The biexciton resonance emerges in the same way in the squeezing-cat differential, shown in Fig. 2(b). However, the squeezing-cat excitation generates a very *narrow* peak for a pump photon number of $N_0 = 1$ M that stays narrow across a wide range of pump intensities, indicating that the excitation-induced dephasing is reduced compared to the classical result. Furthermore, the energetic position of the resonance remains essentially constant, in contrast to the result of classical spectroscopy. At the same time, the relative strength grows as the number of photons is increased, and the 1*s* resonance distorts the biexciton resonance much less than for the classical excitation. This shows that the quantum-optical differential reveals the properties of biexciton coherences much more sensitively than classical spectroscopy does.

These observations are consistent with the state-injection aspects of quantum-optical spectroscopy, predicted theoretically in Ref. [8]. This work identified that the quantum statistics of the pump are directly mapped onto the electronic many-body state in the semiconductor by the absorption of quantum light before the onset of Coulomb and phonon scattering. Therefore, quantum-optical correlations of the light source inject corresponding many-body correlations in the excited electron-hole pairs. As shown in Ref. [10], squeezing-cat differential spectroscopy directly excites unbound biexciton coherences. Since the probe has an opposite circular polarization, it detects a bound biexciton resonance stemming directly from this biexciton coherence. Thus the direct injection of the biexciton coherences explains the narrow biexciton feature and the high sensitivity of quantum-optical spectroscopy. Under otherwise equivalent conditions, the classical differential spectroscopy excites only excitonic polarization. Therefore, the classical excitation detects the biexciton resonance indirectly [22,35], only after Coulombic scattering processes create biexciton coherences, which degrades the classical characterization of the biexciton line.

Figure 2 shows also the differential absorption spectra (dashed line) projected from the unfiltered measured QW absorption [Fig. 1(a)] for $N_0 = 3$ M. We see that the low-pass filtering effectively produces the same result as the original data, except some experimental noise is removed, yielding smooth quantum-optical differential spectra. We use the low-pass filtered input from now on because it allows us to determine the biexciton line shape slightly more accurately than the unprocessed data does.

C. Excitation-induced dephasing of the biexciton resonance

To study the effect of excitation-induced dephasing on the biexciton resonance quantitatively, we determine the strength and width of the biexciton resonance as a function of the pump intensity. For the classical differential, the biexciton resonance decays to a floor value $\Delta\bar{\alpha}_{\mathrm{floor}}$ of zero. At the same time, the squeezing-cat's biexciton resonance grows from a floor value that is slightly negative and density dependent, as seen from Fig. 2(b). With this information, we determine the peak value of the differential $\Delta\bar{\alpha}_{\mathrm{peak}}$ and define the strength of the biexciton resonance by

$$\Delta\bar{\alpha}_{\mathrm{strength}} \equiv \Delta\bar{\alpha}_{\mathrm{peak}} - \Delta\bar{\alpha}_{\mathrm{floor}}\,. \quad (8)$$

Once this value is known, we can directly determine the half-width of the biexciton resonance. Since the classical $\Delta\bar{\alpha}_{\mathrm{cl}}$ resonance is strongly asymmetric due to the 1*s* distortions, we determine the width from the low-energy side that is less influenced by the 1*s* resonance.

To confirm the accuracy of the projection, we construct the classical and squeezing-cat differential absorption for $C = 56$, $C = 77$, and $C = 103$ clusters. We then determine the strength

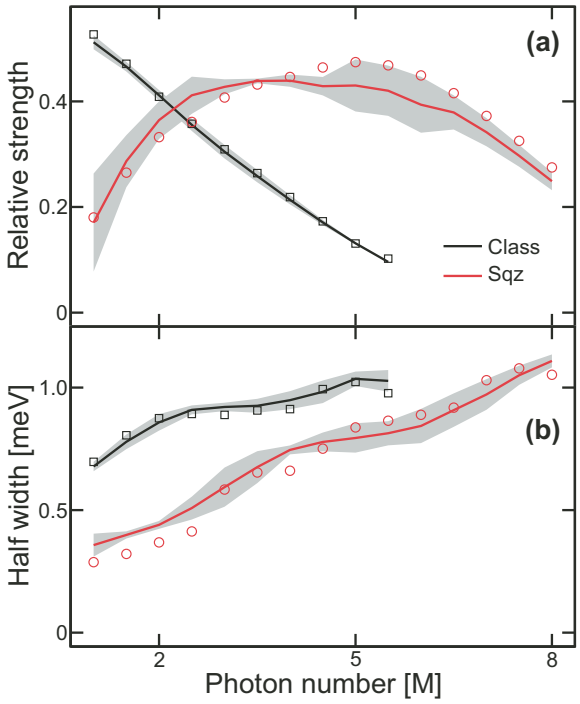

FIG. 3. (Color online) Excitation-induced dephasing of the biexciton resonance. (a) The strength of the biexciton resonance $\Delta\bar{\alpha}_{\text{strength}}$ is presented as a function of pump photon number for classical (black line) and squeezing-cat differential spectroscopy (red line). The pump-probe delay is 12 ps. The confidence interval is indicated as a shaded area. The corresponding $\Delta\bar{\alpha}_{\text{strength}}$, resulting from the projection from the raw data, is shown as squares (classical spectroscopy) and circles (squeezing-cat spectroscopy). (b) The corresponding results for the half-width γ_{half} of the biexciton resonance.

and width of the biexciton resonance for each of these cluster numbers and compute the mean and variance of these three analyses. We take the mean as the projected response, while the mean $\pm$ variance defines the confidence interval of the projection.

The strength of the biexciton resonance, $\Delta\bar{\alpha}_{\text{strength}}$ (solid line), is shown together with its confidence interval (shaded area) in Fig. 3(a) as a function of N_0 for classical (black line) and squeezing-cat differential spectroscopy (red line). The pump-probe delay is $\Delta t = 12$ ps. We observe that classical spectroscopy produces a monotonically decaying strength for the biexciton resonance, while the squeezing cat leads to a nearly monotonic increase in biexciton-resonance strength up to a photon number of 5 M. The peak $\Delta\bar{\alpha}_{\text{strength}}$ in quantum spectroscopy emerges at the same pump intensity, roughly 5 M, above which classical spectroscopy cannot resolve a clear biexciton resonance anymore due to the excessive broadening (compare Fig. 2). Above 5 M photons, the squeezing-cat excitation produces only a slow decrease of the strength until the 8-M photon excitation. This means that quantum spectroscopy resolves the biexciton coherence for a much broader excitation range than classical spectroscopy does.

To quantify the excitation-induced broadening, the half-width γ_{half} of the biexciton resonance is analyzed in Fig. 3(b), using the same line styles as in Fig. 3(a). The squeezing cat produces $\gamma_{\text{half}} = 0.36$ meV at the lowest pump $N_0 = 1$ M. For the same pump N_0, classical spectroscopy produces $\gamma_{\text{half}} = 0.68$ meV, which is 1.9 times broader than the used quantum spectroscopy resolves. This confirms that the squeezing cat indeed yields an anomalous reduction of the biexcitonic scattering.

As the pump intensity is elevated further, the classical γ_{half} increases slightly while the cat state induces a significant increase in the biexciton linewidth. In particular, classical spectroscopy is not capable of resolving the actual excitation-induced broadening because it already broadens the biexciton line via the scattering related to the state creation, not the actual biexcitonic dephasing. Quantum spectroscopy avoids this because it directly injects biexciton coherences such that we can use the quantum spectroscopy to monitor exclusively the excitation-induced dephasing acting upon the biexciton resonance. As for sheer numbers, our quantum spectroscopy resolves a 3.1-fold broadening from $\gamma_{\text{half}} = 0.36$ meV to $\gamma_{\text{half}} = 1.11$ meV as the pump N_0 is increased from 1to 8 M. We also see that the squeezing-cat excitation resolves roughly the same biexciton broadening as the classical case ($\gamma_{\text{half}} \cong 1$ meV) above the pump $N_0 = 5$ M, defining the upper limit for classically resolvable biexciton resonance.

As the last point of this study, we confirm that both the raw and the low-pass filtered input data yield the same results. The projection from the raw data produces $\Delta\bar{\alpha}_{\text{strength}}$ and γ_{half}, shown as squares (classical spectroscopy) and circles (quantum spectroscopy). These values are well within the confidence intervals, which confirms that low-pass filtering can be applied to remove the spectral noise.

D. Dynamics of the biexciton resonance

We also study how the features of the biexciton resonance evolve after excitation with a pump source having different quantum fluctuations. Therefore, we project $\Delta\bar{\alpha}_{\text{type}}$ for ten different pump-probe delays ranging from $\Delta t = 1$ ps to $\Delta t = 40$ ps. Figure 4(a) shows how the strength of the biexciton resonance evolves for classical (black line) vs squeezing-cat (red line) differential. The initial pump has $N_0 = 3$ M photons. The classical $\Delta\bar{\alpha}_{\text{strength}}$ decreases from its initial value, 0.52–0.22 at 40 ps. The corresponding squeezing cat $\Delta\bar{\alpha}_{\text{strength}}$ starts at a much higher value of 0.86 due to the direct injection of biexciton coherences identified in Figs. 2 and 3. Also, it decays roughly to the same level as the classical $\Delta\bar{\alpha}_{\text{strength}}$ for delays beyond 20 ps. Making an exponential fit to this dynamics, we find the decay constant $\tau_{\text{cat}} = 12.9$ ps for the cat-state injection, confirming that quantum-state injection can be detected for substantially long times. For otherwise the same conditions, the classical $\Delta\bar{\alpha}_{\text{class}}$ does not decay exponentially, which is consistent with the observation that the classical pump excites a distribution of states having multiple decay constants.

The corresponding time evolution of the half-width γ_{half} is shown in Fig. 4(b). The classical excitation produces a broadening $\gamma_{\text{half}}(\Delta t)$ that grows from 0.79 to 1.02 meV while the cat-state excitation yields essentially a constant $\gamma_{\text{half}} = 0.5$ meV. Also, this comparison is consistent with the direct excitation of a single biexcitonic state in quantum spectroscopy, while the classical excitation creates a distribution of biexcitonic states.

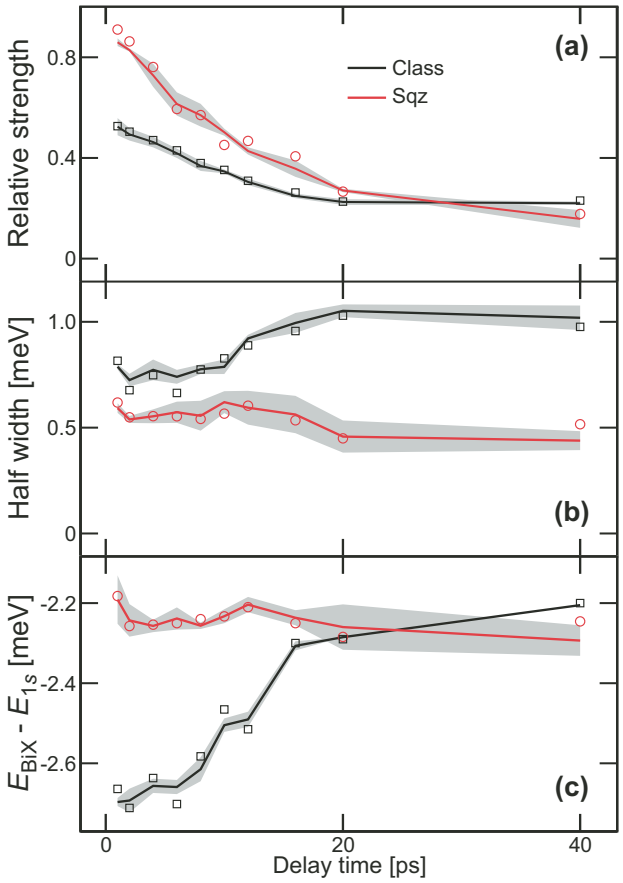

FIG. 4. (Color online) Dynamics of the biexciton resonance. (a) The strength $\Delta\bar{\alpha}_{\text{strength}}$ of the biexciton resonance as a function of pump-probe delay for classical (black line) vs squeezing-cat differential spectroscopy (red line) projected from the low-pass filtered data. The pump has 3 M photons. The corresponding (b) half-width and (c) position of the biexciton resonance. In all frames, the shaded area defines the confidence interval of the projection and the raw-data projection results are shown for classical (squares) and quantum (circles) spectroscopy.

The difference between classical and quantum spectroscopy becomes particularly visible as we analyze the energetic position of the biexciton resonance E_{BiX}. The dynamics of E_{BiX} is shown in Fig. 4(c) for the classical (black line) vs the quantum excitation (red line). The classical E_{BiX} changes strongly after the state generation at $t = 0$ ps. In more detail, the resonance shifts from its initial value of -2.7 to -2.2 meV. At the same time, the squeezing cat E_{BiX} remains essentially stationary for the delay-time range studied. In particular, the energetic position is close to the spectral position where the biexciton resonance emerges in Fig. 1(b), verifying again the state-injection aspects of quantum-optical spectroscopy. We have also confirmed that the unfiltered input data produces essentially the same results for both classical (squares) and quantum (circles) spectroscopy.

IV. DISCUSSION

We have analyzed the biexciton feature in the absorption of GaAs quantum wells using quantum-optical spectroscopy. More specifically, we have projected classical absorption measurements into quantum responses with the cluster-expansion transformation. The analysis with the raw and low-pass filtered input data produces essentially the same results, which confirms the robustness of our approach against small experimental noise.

This analysis demonstrates that classical and quantum sources produce a significantly different QW absorption. While classical spectroscopy produces a biexciton resonance which broadens and decays fast as a function of pump intensity, the quantum-optical spectroscopy with squeezing-cat states generates a sharp resonance that remains in the system across a wide range of intensities. We also have shown that only the quantum spectroscopy accesses the correct biexciton energy and the excitation-induced broadening, because the classical excitations induce a distribution of states around the biexciton coherence. Our results also imply that the quantum spectroscopy directly injects biexciton coherences, yielding an anomalous reduction in scattering. Consequently, quantum-optical spectroscopy can characterize the features of the biexciton resonance with a much higher sensitivity than classical spectroscopy.

We find that the biexciton resonance has a linewidth of 0.36 meV at low pump intensities and it grows above 1.11 meV due to the excitation-induced dephasing. We also have analyzed the dynamics of the biexciton resonance after its creation. The biexciton resonance of the classical excitation shifts in energy and broadens after the excitation. As the pump fluctuations are changed into a squeezing-cat state, the biexciton position and linewidth remain essentially constant. Both the dynamic and excitation-induced dephasing aspects confirm that quantum spectroscopy can be applied to directly access the many-body physics that remains hidden in classical spectroscopy.

ACKNOWLEDGMENTS

The work in Marburg is supported by the Deutsche Forschungsgemeinschaft (DFG) under Grant No. KI 917/2-1. The work at JILA is supported by NIST and the NSF under Grant No. 1125844. S.T.C. acknowledges support from the Alexander von Humboldt Foundation. M.K., A.E.H., and S.T.C. thank R. P. Smith for fruitful discussions in developing quantum spectroscopy.

APPENDIX A: FORMAL CLUSTER-EXPANSION TRANSFORMATION

Cluster-expansion transformation (CET) was initially introduced in Ref. [31] to provide a numerically stable transformation between particlelike correlations and phase-space distributions of any quantum-optical field. The CET approach was generalized to a new realm in Ref. [10] by showing that it can be applied to robustly project a set of classically measured optical responses into a quantum-optical response depending exclusively on the quantum-optical fluctuations of the light. This important step makes pragmatic quantum spectroscopy studies possible as an extension to traditional laser spectroscopy, which is already widely used to characterize and control the quantum properties of matter.

As demonstrated in Ref. [10], the measured classical optical response can be perceived as an un-normalized Wigner-like phase-space distribution $W(\beta)$, where $\beta = \beta_1 + \mathrm{i}\beta_2$ is a two-dimensional phase-space coordinate. We present next the formal aspects of the CET for a distribution

$$W(\beta) = W(|\beta|), \tag{A1}$$

because the analyzed experiment does not depend on the phase of β; the explicit CET algorithm is presented in Appendix B.

As a starting point, we express $W(\beta)$ via a Fourier transformation

$$\begin{aligned} W(\beta) &= \frac{1}{\pi^2}\int d^2\eta\, \chi(\eta)\, e^{\eta^\star\beta-\eta\beta^\star} \\ \Leftrightarrow\ \chi(\eta) &= \int d^2\beta\, W(\beta)\, \mathrm{e}^{-\eta^\star\beta+\eta\beta^\star}\,, \end{aligned} \tag{A2}$$

where $\chi(\eta)$ is a formal analog to a symmetric characteristic function of quantum-optical fields. By Taylor expanding the function $e^{-\eta^\star\beta+\eta\beta^\star}$ in Eq. (A2), we obtain

$$\chi(\eta) = \sum_{J,K=0}^{\infty} \frac{\eta^J(-\eta^\star)^K}{J!K!}\int d^2\beta\, W(\beta)[\beta^\star]^J\beta^K\,. \tag{A3}$$

Due to the phase insensitivity (A1), only diagonal ($J = K$) phase-space integrals

$$I(J) \equiv \int d^2\beta\, W(\beta)|\beta|^{2J} \tag{A4}$$

are needed to express

$$\chi(\eta) = \sum_{J=0}^{\infty}\frac{(-|\eta|^2)^J}{J!J!}I(J)\,. \tag{A5}$$

As shown in Ref. [31], the conversion from $W(\beta)$ to $I(J)$ or $\chi(\eta)$ representation is numerically stable, while the conversion from $I(J)$ to $W(\beta)$ can become numerically problematic.

One can overcome this problem by identifying clusters of $W(\beta)$ that correspond to mean, variance, and higher-order cumulants of the distribution. For rotationally symmetric $W(|\beta|)$, the mean $\int d^2\beta\,\beta\, W(|\beta|) = 0$ vanishes based on property (A1), while the variance is given by

$$\Delta x^2 \equiv \int d^2\beta\,\beta_1^2\, W(|\beta|) = \int d^2\beta\,\beta_2^2\, W(|\beta|)\,. \tag{A6}$$

Formally, the mean and variance correspond to singlet and doublet clusters of a quantum-optical field.

Following the central idea of Ref. [31], we split $\chi(\eta)$ into singlet-doublet clusters and higher-order correlation contributions by introducing the cluster-expansion separation

$$\chi(\eta) = e^{-2\Delta x^2|\eta|^2}\, A(2\Delta x\,\eta)\,, \quad A(\eta) = \sum_{J=0}^{\infty}\frac{(-|\eta|^2)^J}{J!J!}a(J)\,, \tag{A7}$$

where $A(\eta)$ is formally expressed using an equivalent Taylor expansion as in Eq. (A5); the CET coefficients $a(J)$ are defined by correlations [31]. They can be obtained by Taylor expanding $A(\eta) = e^{\frac{|\eta|^2}{2}}\chi(\eta)$, yielding

$$A(\eta) = \sum_{J=0}^{\infty}\frac{(-|\eta|^2)^J}{[4\Delta x^2]^J}\sum_{L=0}^{J}\frac{[-2\Delta x^2]^L I(J-L)}{L!(J-L)!(J-L)!}\,, \tag{A8}$$

after we reorganize the sums. By comparing Eq. (A7) with Eq. (A8), we may identify

$$a(J) = \frac{J!J!}{[4\Delta x^2]^J}\sum_{L=0}^{J}\frac{[-2\Delta x^2]^L I(J-L)}{L!(J-L)!(J-L)!}\,, \tag{A9}$$

which provides a convergent mapping from $I(J)$ to $a(J)$.

Due to the additional convergence factor $e^{-2\Delta x^2|\eta|^2}$ in Eq. (A7), the mapping from $a(J)$ [that defines $A(\eta)$] to $W(\beta)$ becomes numerically robust. To explicitly map $a(J)$ to $W(\beta)$, we insert Eq. (A7) into Eq. (A2), yielding

$$W(\beta) = \frac{1}{\pi^2}\int d^2\eta\, A(\eta)\, e^{\eta^\star\beta-\eta\beta^\star}e^{-2\Delta x^2|\eta|^2}\,. \tag{A10}$$

A straightforward calculation of the Gaussian integral (A10) produces the CET form

$$\begin{aligned} W_{\mathrm{CET}}(\beta) &= \frac{1}{4\Delta x^2}\sum_{J=0}^{\frac{C}{2}}(-1)^J a(J)\, G_J\!\left(\frac{\beta}{2\Delta x}\right), \\ G_J(\beta) &= \frac{2}{\pi}\, e^{-2|\beta|^2}\sum_{j=0}^{J}\frac{2^{2J-j}(-|\beta|^2)^{J-j}}{j!(J-j)!(J-j)!}\,, \end{aligned} \tag{A11}$$

which essentially is a numerically stable conversion of $W(\beta)$ to clusters and back, even when $W(\beta)$ contains experimental noise. As the virtue of the CET, physically relevant contributions reside in the low-rank C, while experimental noise induces high-rank C, as explained in Refs. [10] and [31]. Therefore, only clusters up to C-particle correlations need to be included in the CET reconstruction (A11).

As a result, the CET converts classical measured $W(\beta)$ into an analytical phase-space distribution. In particular, the CET-constructed form (A11) contains a Gaussian times polynomials. The Gaussian that appears guarantees the integrability of the convolution integral (2) for any physical $P(\beta)$ when $R_{|\beta\rangle}$ is replaced by $W_{\mathrm{CET}}(\beta)$; Appendix C shows how the projection integral (2) can be efficiently computed with the help of the CET.

APPENDIX B: CET ALGORITHM

To determine the explicit procedure from the measured response $R_{|\beta\rangle}$ to CET form $R_{\mathrm{CET}}(\beta)$, we start from $R_{|\beta\rangle}$ that is measured over a phase-space region Ω. The corresponding *normalized* phase-space distribution is given by

$$W_R(\beta) \equiv \frac{R_{|\beta\rangle}}{\mathcal{N}_R}\,, \quad \mathcal{N}_R = \int_\Omega d^2\beta\, R_{|\beta\rangle}\,, \tag{B1}$$

where $\mathcal{N}_R$ defines the norm. Since also $W_R(\beta)$ depends on a phase-space coordinate, defined by the laser's displacement $\beta = \beta_1 + \mathrm{i}\beta_2$, we formally connect $W_R(\beta)$ with $W(\beta)$ such that we can directly apply the CET outlined in Appendix A. In the following, we present the CET algorithm for a situation where the measured response depends only on the photon

number. In this situation, $W_R(\beta) = W_R(|\beta|)$ depends only on the magnitude $|\beta|$ such that we can apply the steps presented in Appendix A.

The variance is then given by

$$\Delta x_R^2 = \int_\Omega d^2\beta\, \beta_1^2\, W_R(|\beta|) = \int_\Omega d^2\beta\, \beta_2^2\, W_R(|\beta|)\,, \quad \text{(B2)}$$

based on Eq. (A6). All higher-order moments follow from

$$I_R(J) = \int_\Omega d^2\beta\, |\beta|^{2J}\, W_R(|\beta|)\,, \quad \text{(B3)}$$

which has a formal analog to Eq. (A4). According to Eq. (A9), $I_R(J)$ produces the CET coefficients via the transformation

$$a_R(J) = \frac{J!J!}{\left[4\Delta x_R^2\right]^J} \sum_{L=0}^{J} \frac{\left[-2\Delta x_R^2\right]^L I_R(J-L)}{L!(J-L)!(J-L)!}\,, \quad \text{(B4)}$$

and the CET characteristic function (A7) becomes

$$\chi_{\mathrm{CET}}(\eta) = e^{-2\Delta x_R^2|\eta|^2} \sum_{J=0}^{\frac{C}{2}} \frac{\left(-4\Delta x_R^2\right)^J |\eta|^{2J}}{J!J!} a_R(J)\,, \quad \text{(B5)}$$

where we have included terms up to C-particle clusters. The CET cycle is completed by computing the CET response $R_{\mathrm{CET}} = \mathcal{N}_R W_{\mathrm{CET}}(\beta)$, yielding

$$\begin{aligned} R_{\mathrm{CET}}(\beta) &= \frac{\mathcal{N}_R}{4\Delta x_R^2} \sum_{J=0}^{\frac{C}{2}} (-1)^J a_R(J)\, G_J\!\left(\frac{|\beta|^2}{4\Delta x_R^2}\right), \\ G_J(x) &= \frac{2}{\pi} e^{-2x} \sum_{k=0}^{J} \frac{2^{2J-k}(-x)^{J-k}}{k!(J-k)!(J-k)!}, \end{aligned} \quad \text{(B6)}$$

based on Eq. (A11).

APPENDIX C: EFFICIENT COMPUTATION OF THE PROJECTION INTEGRAL

In general, the projection integral (2) can be computed even for nonanalytic $P(\beta)$ when $R_{|\beta\rangle}$ is replaced by $R_{\mathrm{CET}}(\beta)$. However, it is more convenient to express $P(\beta)$ of the intended quantum source via the Fourier transformation of its normally ordered characteristic function $\chi_N(\eta)$ [23] is

$$\begin{aligned} P(\beta) &= \frac{1}{\pi^2} \int d^2\eta\, \chi_N(\eta)\, e^{\eta^\star\beta - \eta\beta^\star} \\ &\Leftrightarrow\ \chi_N(\eta) = \int d^2\beta\, P(\beta)\, e^{-\eta^\star\beta + \eta\beta^\star}\,. \end{aligned} \quad \text{(C1)}$$

As the major benefit, $\chi_N(\eta)$ is a well-behaved function even for quantum sources.

As explained in Appendix B, $R_{\mathrm{CET}}(\beta)$ can be viewed as an un-normalized Wigner-like phase-space distribution such that we can Fourier transform it [23] as follows:

$$\begin{aligned} R_{\mathrm{CET}}(\beta) &= \frac{\mathcal{N}_R}{\pi^2} \int d^2\eta\, \chi_{\mathrm{CET}}(\eta)\, e^{\eta^\star\beta - \eta\beta^\star} \\ &\Leftrightarrow\ \chi_{\mathrm{CET}}(\eta) = \frac{1}{\mathcal{N}_R} \int d^2\beta\, R_{\mathrm{CET}}(\beta)\, e^{-\eta^\star\beta + \eta\beta^\star}. \end{aligned} \quad \text{(C2)}$$

By Fourier transforming both $P(\beta)$ and $R_{\mathrm{CET}}(\beta)$, integral (2) produces straightforwardly

$$R_P = \frac{\mathcal{N}_R}{\pi^2} \int d^2\eta\, \chi_N(\eta)\, \chi_{\mathrm{CET}}(-\eta)\,, \quad \text{(C3)}$$

according to the convolution theorem. As a major benefit, both $\chi_N(\eta)$ and $\chi_{\mathrm{CET}}(\eta)$ are well-behaved functions such that the projection integral can be performed with relative ease.

The squeezing-cat state's normally ordered characteristic function is defined by [10]

$$\begin{aligned} \chi_N^{|\beta_0,\gamma\rangle}(\eta) = \mathcal{N}^2 (&e^{\Gamma_-^\star\eta - \Gamma_-\eta^\star} + e^{\Gamma_+^\star\eta - \Gamma_+\eta^\star} \\ &+ e^{-2|\gamma|^2} [e^{\Gamma_-^\star\eta - \Gamma_+\eta^\star} + e^{\Gamma_+^\star\eta - \Gamma_-\eta^\star}])\,, \end{aligned} \quad \text{(C4)}$$

which is an analytical function. When inserting Eqs. (C4) and (B5) into Eq. (C3), we find the CET projected quantum response (4) to Schrödinger's cat state.

[1] K. Vogel and H. Risken, Phys. Rev. A **40**, 2847 (1989).
[2] D. T. Smithey, M. Beck, M. G. Raymer, and A. Faridani, Phys. Rev. Lett. **70**, 1244 (1993).
[3] G. Breitenbach, S. Schiller, and J. Mlynek, Nature (London) **387**, 471 (1997).
[4] A. I. Lvovsky, H. Hansen, T. Aichele, O. Benson, J. Mlynek, and S. Schiller, Phys. Rev. Lett. **87**, 050402 (2001).
[5] J. S. Lundeen, B. Sutherland, A. Patel, C. Stewart, and C. Bamber, Nature (London) **474**, 188 (2011).
[6] D. Leibfried, D. M. Meekhof, B. E. King, C. Monroe, W. M. Itano, and D. J. Wineland, Phys. Rev. Lett. **77**, 4281 (1996).
[7] C. Kurtsiefer, T. Pfau, and J. Mlynek, Nature (London) **386**, 150 (1997).
[8] M. Kira and S. W. Koch, Phys. Rev. A **73**, 013813 (2006).
[9] S. W. Koch, M. Kira, G. Khitrova, and H. M. Gibbs, Nature Mater. **5**, 523 (2006).
[10] M. Kira, S. W. Koch, R. P. Smith, A. E. Hunter, and S. T. Cundiff, Nat. Phys. **7**, 799 (2011).
[11] M. Aßmann and M. Bayer, Phys. Rev. A **84**, 053806 (2011).
[12] L. Schneebeli, M. Kira, and S. W. Koch, Phys. Rev. Lett. **101**, 097401 (2008).
[13] T. Yoshie, A. Scherer, J. Hendrickson, G. Khitrova, H. M. Gibbs, G. Rupper, C. Ell, O. B. Shchekin, and D. G. Deppe, Nature (London) **432**, 200 (2004).
[14] J. P. Reithmaier, G. Sek, A. Loffler, C. Hofmann, S. Kuhn, S. Reitzenstein, L. V. Keldysh, V. D. Kulakovskii, T. L. Reinecke, and A. Forchel, Nature (London) **432**, 197 (2004).
[15] I. Schuster, A. Kubanek, A. Fuhrmanek, T. Puppe, P. W. H. Pinkse, K. Murr, and G. Rempe, Nature Mater. **4**, 382 (2008).

[16] J. Wiersig, C. Gies, F. Jahnke, M. Aszmann, T. Berstermann, M. Bayer, C. Kistner, S. Reitzenstein, C. Schneider, S. Hofling, A. Forchel, C. Kruse, J. Kalden, and D. Hommel, Nature (London) **460**, 245 (2009).
[17] M. Richter, A. Carmele, A. Sitek, and A. Knorr, Phys. Rev. Lett. **103**, 087407 (2009).
[18] S. Ritter, P. Gartner, C. Gies, and F. Jahnke, Opt. Express **18**, 9909 (2010).
[19] A. Carmele, M. Richter, W. W. Chow, and A. Knorr, Phys. Rev. Lett. **104**, 156801 (2010).
[20] A. Reinhard, T. Volz, M. Winger, A. Badolato, K. J. Hennessy, E. L. Hu, and A. Imamoğlu, Nature Photon. **6**, 93 (2012).
[21] R. P. Smith, J. K. Wahlstrand, A. C. Funk, R. P. Mirin, S. T. Cundiff, J. T. Steiner, M. Schafer, M. Kira, and S. W. Koch, Phys. Rev. Lett. **104**, 247401 (2010).
[22] M. Kira and S. W. Koch, *Semiconductor Quantum Optics*, 1st ed. (Cambridge University Press, Cambridge, UK, 2011).
[23] D. F. Walls and G. J. Milburn, *Quantum Optics*, 2nd ed. (Springer-Verlag, New York, 2008).
[24] R. J. Glauber, Phys. Rev. **131**, 2766 (1963).
[25] E. C. G. Sudarshan, Phys. Rev. Lett. **10**, 277 (1963).
[26] H. J. Kimble, M. Dagenais, and L. Mandel, Phys. Rev. Lett. **39**, 691 (1977).
[27] P. Michler, A. Kiraz, C. Becher, W. V. Schoenfeld, P. M. Petroff, L. Zhang, E. Hu, and A. Imamoglu, Science **290**, 2282 (2000).
[28] R. E. Slusher, L. W. Hollberg, B. Yurke, J. C. Mertz, and J. F. Valley, Phys. Rev. Lett. **55**, 2409 (1985).
[29] W. Schleich and J. A. Wheeler, Nature (London) **326**, 574 (1987).
[30] M. Lobino, D. Korystov, C. Kupchak, E. Figueroa, B. C. Sanders, and A. I. Lvovsky, Science **322**, 563 (2008).
[31] M. Kira and S. W. Koch, Phys. Rev. A **78**, 022102 (2008).
[32] E. Jaynes and F. Cummings, Proc. IEEE **51**, 89 (1963).
[33] M. Kira and S. W. Koch, Prog. Quantum Electron. **30**, 155 (2006).
[34] C. Gerry and P. Knight, *Introductory Quantum Optics*, 3rd ed. (Cambridge University Press, Cambridge, UK, 2005).
[35] M. Mootz, M. Kira, and S. W. Koch, J. Opt. Soc. Am. B **29**, A17 (2012).

Paper V

C. Berger, U. Huttner, **M. Mootz**, M. Kira, S. W. Koch, J.-S. Tempel, M. Aßmann, M. Bayer, A. M. Mintairov, and J. L. Merz
Quantum-memory effects in the emission of quantum-dot microcavities
Phys. Rev. Lett. **113**, 093902 (2014)

Quantum-Memory Effects in the Emission of Quantum-Dot Microcavities

C. Berger,[1,*] U. Huttner,[1] M. Mootz,[1] M. Kira,[1] S. W. Koch,[1] J.-S. Tempel,[2] M. Aßmann,[2] M. Bayer,[2,3] A. M. Mintairov,[3,4] and J. L. Merz[4]

[1]*Department of Physics, Philipps-Universität Marburg, Renthof 5, D-35032 Marburg, Germany*
[2]*Experimentelle Physik 2, Technische Universität Dortmund, D-44221 Dortmund, Germany*
[3]*Ioffe Physical-Technical Institute of the Russian Academy of Sciences, Saint Petersburg, 194021, Russia*
[4]*Department of Electrical Engineering, University of Notre Dame, Notre Dame, Indiana 46556, USA*

(Received 20 December 2013; published 29 August 2014)

The experimentally measured input-output characteristics of optically pumped semiconductor microcavities exhibits unexpected oscillations modifying the fundamentally linear slope in the excitation power regime below lasing. A systematic microscopic analysis reproduces these oscillations, identifying them as a genuine quantum-memory effect, i.e., a photon-density correlation accumulated during the excitation. With the use of projected quantum measurements, it is shown that the input-output oscillations can be controlled and enhanced by an order of magnitude when the quantum fluctuations of the pump are adjusted.

DOI: 10.1103/PhysRevLett.113.093902 PACS numbers: 42.55.Px, 42.50.Pq, 78.55.-m

Quantum-dot microcavities have been used to demonstrate a number of intriguing quantum phenomena such as the Purcell effect [1], vacuum Rabi splitting [2,3], strong light-matter coupling [3–5], and single-photon [6–8] as well as entangled photon-pair [9] emission. These systems are, thus, prototypical for semiconductor-based cavity quantum electrodynamic (QED) studies [10–12] exploring the foundations of quantum mechanics. Moreover, microcavity structures can be utilized to produce new components and algorithms for quantum-information processing [13] and they can be used as high-quality lasers [14–16] that show a nearly thresholdless input-output (I/O) characteristics.

In the lasing regime, the system's output approaches a coherent state [17], which as the most classical form of light, is not interesting for QED studies. However, true QED effects can still be observed in the regime of low output power [18] where they may even become strong enough to produce visible deviations from the expected linear I/O behavior. According to the quantum-optical response theory developed in Ref. [19], any form of optical nonlinearity in the matter's response to classical light implies that the response must necessarily be sensitive to the light's quantum fluctuations. This completely general result implies that one should be able to find quantum-fluctuation signatures in the light-matter correlations even when the nonlinearity was originally identified completely classically.

In this Letter, we analyze the quantum-optical sensitivity of quantum-dot microcavities with a three-step approach: (i) We present the experimental observation of well-defined I/O oscillations as the nonlinear response; (ii) we use a quantum analysis to show that these oscillations originate from quantum-memory effects related to photon-density correlations; (iii) we demonstrate that the quantum-optical sensitivity of the I/O curve exhibits the predicted signatures for the identified quantum-memory correlation.

Our sample contains microring cavities [20,21] fabricated from a 150 nm thick $Ga_{0.52}In_{0.48}P$ waveguide including self-assembled InP quantum dots with a dot density of $(1–2) \times 10^9/cm^2$ and a mean dot size of 75 nm. Because of the large diameter, the dots host multiple confined levels with level spacings on the order of 3–5 meV, as demonstrated in single-dot luminescence spectra [21]. The central emission wavelength of the dot ensemble is close to 720 nm, and the inhomogeneous linewidth is 25 nm at cryogenic temperatures. The inset to Fig. 1 shows a scanning electron micrograph of the used ring cavity with a 2.2 μm outer and 1.5 μm inner diameter. The sample is kept in a helium-flow cryostat at 10 K temperature and excited using a Ti-sapphire laser emitting pulses with 2 ps duration at 75.39 MHz repetition rate. The linearly polarized pump beam is focused onto the cavity using a $100\times$ microscope objective with a numerical aperture of 0.55, resulting in a spot size of 2–3 μm covering the ring. We excite the dots quasiresonantly by detuning the photon energy 30.7 meV above the $M1$ main cavity mode

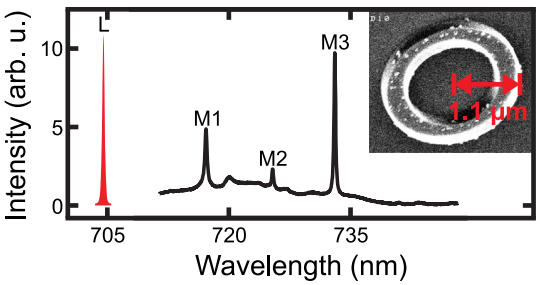

FIG. 1 (color online). μPL spectrum of the investigated microring cavity. The excitation laser was tuned to the wavelength of 705 nm. Inset: Scanning electron micrograph (side view) of the microring cavity used.

energy (see Fig. 1) but below the GaInP band gap. For this detuning, the highest excitation power generates less than 0.26 electrons per electronic level, as shown in the Supplemental Material [22]. This is well below inversion and lasing even though these structures have extremely low lasing thresholds for strongly nonresonant excitations [21]. From the dot density and the ring area in combination with the quasiresonant excitation, we estimate that the $M1$ mode emission can basically be attributed to a single dot [21], while off-resonant dots only contribute to the broad background.

The emission is collected using the same $100\times$ microscope objective that is used for the pump focusing. To minimize stray light from the excitation laser, a cross-polarized Glan prism is inserted in the detection path. Microphotoluminescence (μPL) spectra are measured using a 500 mm focal length spectrometer equipped with a liquid-nitrogen-cooled CCD camera. A μPL spectrum of the investigated microring cavity is shown in Fig. 1. Three main whispering-gallery modes labeled $M1$-$M3$ are observed.

Our three-step approach starts with Fig. 2(a) that presents the measured output power at the $M1$ cavity mode as a function of the input power. While the I/O curve at first sight appears to show a linear behavior, a closer look at the data reveals small but systematic deviations from a perfect linear I/O dependence (solid line). To clearly visualize the nonlinearities, we subtract the linear straight line from the I/O data and plot in Fig. 2(b) the difference $I_{\rm osc}$; this procedure nicely highlights the oscillatory deviations. We see that the first minimum dips down to -0.1, i.e., 10%, below the expected linear output, which significantly exceeds the 6% noise level. As discussed in the Supplemental Material [22], we have verified that the $I_{\rm osc}$ oscillations are reproduced for a large variety of experimental conditions.

In the second step of our analysis, we want to identify a particular quantum correlation that is responsible for the experimentally observed oscillatory nonlinearity. For this purpose, we extend the standard Jaynes-Cummings model [28] to include the four relevant electronic states in our large dot. Denoting the polarization operator for the state n by $\hat{P}_n$, the cavity-dot interaction follows from $\hat{H}_{\rm int} = -\hbar g\sum_n(\hat{B}\hat{P}_n^\dagger + \hat{B}^\dagger\hat{P}_n)$, containing an effective coupling strength g and the Boson operator $\hat{B}$ for the cavity mode. We use $\hbar g = 0.405$ meV that agrees with the typical Rabi splitting in similar quantum-dot experiments [11]. The experimental emission is best reproduced when the four states have a detuning δ_n between 2 and 8 meV above the cavity mode, comparable with the dot energetics identified in Ref. [21]. These states contribute to the Hamiltonian via $\sum_n\hbar\delta_n\hat{P}_{z,n}$ where $\hat{P}_{z,n}$ is the inversion operator for the state n.

The dot is optically driven by a classical pump pulse $\alpha(t) = \alpha_0 e^{-(t^2/\tau^2)}e^{-i\Delta_L t}$ where α_0 is the amplitude, τ gives the duration, and $\hbar\Delta_L$ defines the laser detuning with respect to the cavity. The pump-dot interaction follows from $\hat{H}_{\rm pump} = -\sum_n[\alpha^\star(t)\hat{P}_n + \alpha(t)\hat{P}_n^\dagger]$. We set $\hbar\Delta_L = 30.7$ meV as in the experiment and use the Lindbladian [29] to systematically introduce dephasing for the dot

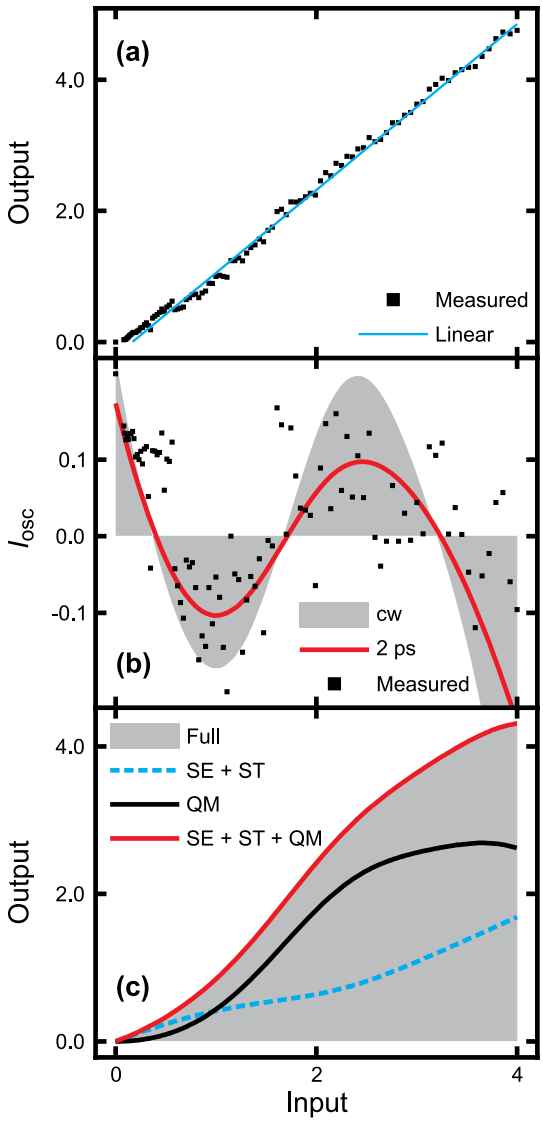

FIG. 2 (color online). Characterizing the I/O oscillations. (a) Measured I/O curve (squares) is compared with a linear output (solid line). The powers are scaled to 1 at the first sublinear dip, which corresponds to an input power of 7.6 μW resulting in 500 photons per dot in the experiment. (b) Difference of measured and linear output $I_{\rm osc}$ (squares) is shown as function of the input together with computed $I_{\rm osc}$ using a cw (shaded area) and a pulsed 2-ps-long (solid line) excitation. (c) Computed I/O responses for a cw excitation. Full computation (shaded area) is compared with the emission stemming from the sum of the spontaneous-emission (SE) and stimulated-emission (ST) sources (dashed line), the quantum-memory (QM) source only (black solid line), and the sum of SE, ST, and QM sources (red solid line).

excitation and the cavity photons. The dephasing parameters are chosen to reproduce the 0.8 ps cavity-photon lifetime as well as the $T_1 = 2.1$ ps polarization and $T_2 = 2.1$ ps occupation decay times. These values not only reproduce the correct emission linewidth in our system but are also very close to the parameters deduced from other experiments [4,20,21].

We solve the full quantum dynamics exactly by evolving the dot-cavity mode density matrix $\hat{\rho}$ in time. The input intensity is defined by the pump amplitude, i.e., $I_{\text{in}} \propto \int |\alpha(t)|^2 dt$, while the dot emits the output intensity $I_{\text{out}} \propto \langle \hat{B}^\dagger \hat{B} \rangle = \text{Tr}[\hat{B}^\dagger \hat{B} \hat{\rho}]$. We scale the computed input power to match the experiment at the first sublinear dip. We then find the linear fit $I_{\text{lin}} = aI_{\text{in}} + b$ for both experiment and theory and fix the scale of I_{out} so that it has the same linear coefficient a as the experiment. This procedure only matches the I/O scales while the relative magnitude of the I_{osc} oscillations is not *a priori* fixed.

The resulting computed I_{osc} is shown in Fig. 2(b) for a 2-ps-long (solid line) and a continuous-wave (cw) pump (shaded area) as function of pump power. We see that the computed I_{osc} reproduces the experimentally observed nonlinearities. We also conclude that the 2-ps-long pump pulse is sufficiently long such that the I_{osc} oscillations approach the cw result.

In our experiment, the pump generates detuned Rabi oscillations that favor (inhibit) emission at the peak (dip) of the dot excitation. For the chosen detuning, the dot excitation both remains very small and oscillates more than five times during a photon emission. Such oscillations not only regulate the instantaneous emission but also induce quantum-memory contributions that remember excitations prior to the emission. Intuitively, the quantum memory must then involve both photons and the oscillating excitation density, yielding an accumulation of photon-density correlations. Since any photon-density correlation must be nonlinear in the pump, the quantum-memory effects must contribute nonlinearly to the I/O curve.

To verify this intuitive interpretation, we express the emitted photon flux exactly via [10]

$$\frac{\partial}{\partial t} \Delta \langle \hat{B}^\dagger \hat{B} \rangle = 2g \int_{-\infty}^{t} dt' \text{Re}[S(t,t')] - 2\kappa \Delta \langle \hat{B}^\dagger \hat{B} \rangle, \quad (1)$$

that is driven by a kernel $S = S^{\text{SE}} + S^{\text{QM}} + S^{\text{ST}} + S^{\text{tri}}$, as discussed in the Supplemental Material [22]. The emission is initiated by the spontaneous source $S^{\text{SE}} = g \sum_{n,n'} [\langle \hat{P}^\dagger_{n'} \hat{P}_n \rangle - \langle \hat{P}^\dagger_{n'} \rangle \langle \hat{P}_n \rangle]$ that is nonvanishing whenever one or more states are excited. The stimulated contribution $S^{\text{ST}} = 2g \sum_n \langle \hat{P}_{z,n} \rangle \Delta \langle \hat{B}^\dagger \hat{B} \rangle$ modifies the emission via the photon correlations inside the cavity. The quantum-memory contribution $S^{\text{QM}} = \Omega \Delta \langle \hat{B}^\dagger \hat{P}_{z,n} \rangle$ contains a product of the classical Rabi frequency Ω and $\Delta \langle \hat{B}^\dagger \hat{P}_{z,n} \rangle$ that describes a photon-density correlation. In addition, S^{tri} defines a three-particle correlation.

The relative influences of the different source terms on the emission are identified via a straightforward switch-off analysis. Figure 2(c) compares I_{out} of the full computation (shaded area) with the emission stemming from $S^{\text{SE}} + S^{\text{ST}}$ (dashed line) and from the sum of spontaneous, stimulated, and quantum-memory sources (red solid line). We observe that $S^{\text{SE}} + S^{\text{ST}}$ produces a monotonically increasing output. For larger I_{in}, I_{out} becomes essentially a linear function of I_{in}, while it still deviates significantly from the full computation result. However, combining $S^{\text{SE}} + S^{\text{ST}}$ with S^{QM} results in an almost perfect reproduction of the full I_{out}. Especially, S^{QM} (black solid line) alone contains large oscillations that remain visible also in the full I_{out}, verifying our intuitive explanation above. Since the calculated results for $S^{\text{SE}} + S^{\text{ST}} + S^{\text{QM}}$ are very close to the experimentally observed emission, we can conclude that S^{tri} has a minor effect on I_{out} in our experiment. In the Supplemental Material [22], we discuss that different coupling strengths for each emitting state and modified dot energetics do not produce quantitative changes of the scaled I/O characteristics. The further analysis also indicates that the quantum-memory effect can be enhanced by changing the detuning and engineering the coupling strength.

The third step of our analysis verifies that I_{osc} and S^{QM} have the same quantum-optical sensitivity. The detailed analysis in the Supplemental Material [22] shows that S^{QM} is driven by coherences involving a product of Ω and the squeezing of the light emission. Consequently, according to the principles of quantum-optical spectroscopy [10,30–34], I_{osc} should also depend on the pump field's quantum fluctuations following the same control rules as the quantum memory does. To fully demonstrate this experimentally, one would need to adjust the quantum fluctuations of the source. Unfortunately, this level of control is not yet possible in present-day experiments. However, a set of classical measurements can be projected to any quantum-optical response to access the quantum-optical dependence of I_{osc}, as demonstrated in Ref. [19] and utilized in Refs. [35,36] to realize a superior characterization of different quasiparticles. The projection algorithm is discussed in the Supplemental Material [22] together with all quantum-light sources studied.

Since S^{QM} is generated via the simultaneous presence of coherences and squeezing of the emission, we test if we can quench the I/O oscillations by a pump field that has either no coherences or does not produce squeezed emission. Figure 3(a) compares the classical measurement (squares) with the quantum (solid line) I/O curve when we use a squeezed vacuum state as quantum source in the projection. Since the squeezed vacuum lacks first-order coherences, it cannot induce a coherent Ω. As a result, it produces an output response *without* the oscillations, simply, because it does not generate the required quantum-memory correlations. In contrast to this, a coherent state has a nonvanishing Ω while it generates squeezing as a natural part of

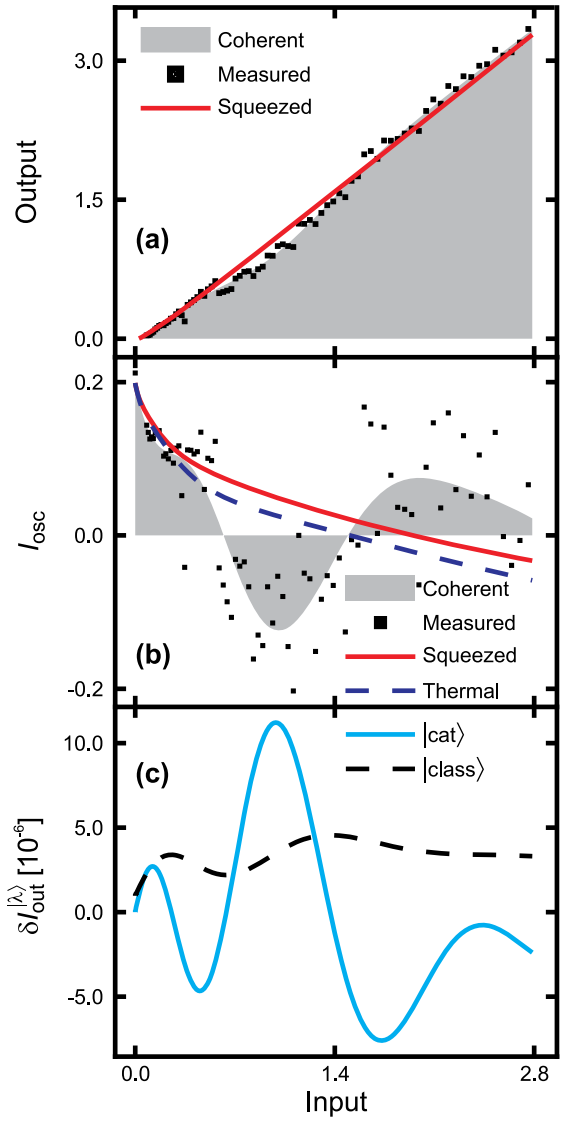

FIG. 3 (color online). Quantum-optical control of I/O oscillations. (a) Measured I/O curve (squares) is compared with the projected coherent-state (shaded area) and squeezed-vacuum output (solid line). (b) Corresponding I_{osc} and thermal-state I_{osc} (dashed line) values are shown. (c) Differential response as function of input power. The classical differential (dashed line) is compared with the stretching-cat state's differential (solid line).

resonance fluorescence emission [37]. For a consistency check, we have also projected the coherent-state response (shaded area) and, as expected, it reproduces the measured I/O oscillations.

The quantum-optical control of the I/O oscillations becomes particularly clear when we construct I_{osc} as in Fig. 2(b) by removing the line from the I/O curve. Figure 3(b) compares the measured I_{osc} (squares) with the projected coherent-state (shaded area), squeezing (solid line), and thermal-state (dashed line) source outputs. The thermal source has neither coherences nor does it generate squeezed emission such that it produces essentially the same output as the squeezed-state source. In other words, we have verified that I_{osc} indeed stems from the quantum-memory correlations because they obey the same, nontrivial, control rules.

The dependence of the output super- or sublinearity on the quantum fluctuations of the source can be directly characterized by defining an output differential,

$$\delta I_{out}^{|\lambda\rangle} \equiv I_{out}^{|\lambda\rangle} - I_{out}, \tag{2}$$

when one changes the laser's fluctuations from a classical source (giving I_{out}) to a quantum state $|\lambda\rangle$; we project $I_{out}^{|\lambda\rangle}$ from the measured I/O curve. For the classical differentials, we use $|\lambda\rangle = |\text{class}\rangle$ that is a coherent state having one more photon than when measuring I_{out}. For the quantum differentials, we use the so-called stretching-cat state [19] $|\lambda\rangle = |\text{cat}\rangle$ that consists of a superposition of two *different* coherent states displaced along the direction of the classical field's original displacement. We adjust $|\text{cat}\rangle$ such that its quantum fluctuations add one photon to the source while its coherences are reduced so that its average photon number is equal to that of the classical reference I_{out}. As a result, $\delta I_{out}^{|\lambda\rangle}$ measures the effects generated by pure quantum fluctuations. The cat state is expected to enhance the oscillatory nonlinearities because it contains both coherences and squeezing.

Figure 3(c) compares the projected $\delta I_{out}^{|\text{class}\rangle}$ (dashed line) with the differential $\delta I_{out}^{|\text{cat}\rangle}$ (solid line). We see that the classical differential response is always positive valued and oscillatory. The maxima and minima of $\delta I_{out}^{|\text{class}\rangle}$ match with the nodes of the measured I_{osc} oscillations in Fig. 3(b). At the same time, $|\text{cat}\rangle$ produces a differential $\delta I_{out}^{|\text{cat}\rangle}$ whose oscillation amplitude is an order of magnitude greater than the result of classical spectroscopy, verifying that a suitable quantum source can indeed amplify the quantum-memory effects. By comparing this result with I_{osc} in Fig. 3(b), we also see that the used $|\text{cat}\rangle$ produces a *superlinear* increase (sublinear decrease) when the classical pump yields *sublinear* (superlinear) output. Since the super-or sublinear oscillations have an opposite phase, one can control the super- or sublinear nature of quantum-memory effects completely via the quantum fluctuations of the pump.

In conclusion, our measurements identify nontrivial I/O oscillations for a quantum dot in a microcavity. Using the methodology of quantum-optical spectroscopy, we show that the I/O oscillations are initiated by the simultaneous presence of coherences and squeezed-light emission. Physically, the excitation drives photon-density correlations that act as a quantum memory for the Rabi oscillations and, thus, induce the oscillatory nonlinearities in the I/O curve. Our projected measurements demonstrate that the super- and sublinear variations can be controlled by modifying the quantum statistics of the pump.

The Marburg group is partially funded by the Deutsche Forschungsgemeinschaft (DFG) via Grants No. KI 917/2-1 and No. SFB 1083. The Dortmund group acknowledges support by the DFG through research Grant No. DFG 1549/19-1. M. B. and A. M. M. acknowledge support from the Russian Ministry of Science and Education (Contract No. 14.Z50.31.0021).

*Corresponding author.
christian.berger@physik.uni-marburg.de

[1] A. Badolato, K. Hennessy, M. Atatüre, J. Dreiser, E. Hu, P. M. Petroff, and A. Imamoğlu, Science **308**, 1158 (2005).
[2] T. Yoshie, A. Scherer, J. Hendrickson, G. Khitrova, H. M. Gibbs, G. Rupper, C. Ell, O. B. Shchekin, and D. G. Deppe, Nature (London) **432**, 200 (2004).
[3] J. P. Reithmaier, G. Sęk, A. Löffler, C. Hofmann, S. Kuhn, S. Reitzenstein, L. V. Keldysh, V. D. Kulakovskii, T. L. Reinecke, and A. Forchel, Nature (London) **432**, 197 (2004).
[4] E. Peter, P. Senellart, D. Martrou, A. Lemaître, J. Hours, J. M. Gérard, and J. Bloch, Phys. Rev. Lett. **95**, 067401 (2005).
[5] J. Kasprzak, S. Reitzenstein, E. A. Muljarov, C. Kistner, C. Schneider, M. Strauss, S. Höfling, A. Forchel, and W. Langbein, Nat. Mater. **9**, 304 (2010).
[6] P. Michler, A. Kiraz, C. Becher, W. V. Schoenfeld, P. M. Petroff, L. Zhang, E. Hu, and A. Imamoğlu, Science **290**, 2282 (2000).
[7] Z. Yuan, B. E. Kardynal, R. M. Stevenson, A. J. Shields, C. J. Lobo, K. Cooper, N. S. Beattie, D. A. Ritchie, and M. Pepper, Science **295**, 102 (2002).
[8] D. Press, S. Götzinger, S. Reitzenstein, C. Hofmann, A. Löffler, M. Kamp, A. Forchel, and Y. Yamamoto, Phys. Rev. Lett. **98**, 117402 (2007).
[9] R. Johne, N. A. Gippius, G. Pavlovic, D. D. Solnyshkov, I. A. Shelykh, and G. Malpuech, Phys. Rev. Lett. **100**, 240404 (2008).
[10] M. Kira and S. W. Koch, *Semiconductor Quantum Optics* (Cambridge University Press, Cambridge, England, 2012).
[11] G. Khitrova, H. M. Gibbs, M. Kira, S. W. Koch, and A. Scherer, Nat. Phys. **2**, 81 (2006).
[12] K. Hennessy, A. Badolato, M. Winger, D. Gerace, M. Atatüre, S. Gulde, S. Fält, E. L. Hu, and A. Imamoğlu, Nature (London) **445**, 896 (2007).
[13] D. D. Awschalom, L. C. Bassett, A. S. Dzurak, E. L. Hu, and J. R. Petta, Science **339**, 1174 (2013).
[14] Z. G. Xie, S. Götzinger, W. Fang, H. Cao, and G. S. Solomon, Phys. Rev. Lett. **98**, 117401 (2007).
[15] J. Wiersig, C. Gies, F. Jahnke, M. Aßmann, T. Berstermann, M. Bayer, C. Kistner, S. Reitzenstein, C. Schneider, S. Höfling, A. Forchel, C. Kruse, J. Kalden, and D. Hommel, Nature (London) **460**, 245 (2009).
[16] F. Albert, C. Hopfmann, A. Eberspächer, F. Arnold, M. Emmerling, C. Schneider, S. Höfling, A. Forchel, M. Kamp, J. Wiersig, and S. Reitzenstein, Appl. Phys. Lett. **101**, 021116 (2012).
[17] S. M. Ulrich, C. Gies, S. Ates, J. Wiersig, S. Reitzenstein, C. Hofmann, A. Löffler, A. Forchel, F. Jahnke, and P. Michler, Phys. Rev. Lett. **98**, 043906 (2007).
[18] M. Nomura, N. Kumagai, S. Iwamoto, Y. Ota, and Y. Arakawa, Nat. Phys. **6**, 279 (2010).
[19] M. Kira, S. W. Koch, R. P. Smith, A. E. Hunter, and S. T. Cundiff, Nat. Phys. **7**, 799 (2011).
[20] Y. Chu, A. M. Mintairov, Y. He, J. L. Merz, N. A. Kalyuzhnyy, V. M. Lantratov, and S. A. Mintairov, Phys. Lett. A **373**, 1185 (2009).
[21] Y. Chu, A. M. Mintairov, Y. He, J. L. Merz, N. A. Kalugnyy, V. M. Lantratov, and S. A. Mintairov, Phys. Status Solidi C **8**, 325 (2011).
[22] See the Supplemental Material at http://link.aps.org/supplemental/10.1103/PhysRevLett.113.093902, which includes Refs. [23–27].
[23] D. F. Walls and G. J. Milburn, *Quantum Optics*, 2nd ed. (Springer, Berlin, 2008).
[24] R. J. Glauber, Phys. Rev. **131**, 2766 (1963).
[25] E. C. G. Sudarshan, Phys. Rev. Lett. **10**, 277 (1963).
[26] M. Kira and S. W. Koch, Prog. Quantum Electron. **30**, 155 (2006).
[27] M. Kira, F. Jahnke, W. Hoyer, and S. W. Koch, Prog. Quantum Electron. **23**, 189 (1999).
[28] E. T. Jaynes and F. W. Cummings, Proc. IEEE **51**, 89 (1963).
[29] G. Lindblad, Commun. Math. Phys. **48**, 119 (1976).
[30] M. Kira and S. W. Koch, Phys. Rev. A **73**, 013813 (2006).
[31] S. W. Koch, M. Kira, G. Khitrova, and H. M. Gibbs, Nat. Mater. **5**, 523 (2006).
[32] M. Kira and S. W. Koch, Phys. Rev. A **78**, 022102 (2008).
[33] M. Aßmann and M. Bayer, Phys. Rev. A **84**, 053806 (2011).
[34] A. Carmele, A. Knorr, and M. Richter, Phys. Rev. B **79**, 035316 (2009).
[35] M. Mootz, M. Kira, S. W. Koch, A. E. Almand-Hunter, and S. T. Cundiff, Phys. Rev. B **89**, 155301 (2014).
[36] A. E. Almand-Hunter, H. Li, S. T. Cundiff, M. Mootz, M. Kira, and S. W. Koch, Nature (London) **506**, 471 (2014).
[37] M. Kira, F. Jahnke, and S. W. Koch, Phys. Rev. Lett. **82**, 3544 (1999).

Supplemental Material to Paper V

Supplemental Material: Quantum-memory effects in the emission of quantum-dot microcavities

C. Berger,[1,*] U. Huttner,[1] M. Mootz,[1] M. Kira,[1] S. W. Koch,[1] J.-S. Tempel,[2]
M. Aßmann,[2] M. Bayer,[2,3] A. M. Mintairov,[3,4] and J. L. Merz[4]

[1] *Department of Physics, Philipps-Universität Marburg, Renthof 5, D-35032 Marburg, Germany*
[2] *Experimentelle Physik 2, Technische Universität Dortmund, D-44221 Dortmund, Germany*
[3] *Ioffe Physical-Technical Institute of the Russian Academy of Sciences, St. Petersburg, 194021, Russia*
[4] *Department of Electrical Engineering, University of Notre Dame, Notre Dame, IN, 46556, USA*

I. GENERAL IMPLICATIONS OF QUANTUM-OPTICAL RESPONSE THEORY

Classical spectroscopy measures matter's response as a function of pump field's amplitude, frequency, duration, or carrier envelope phase, i. e. the classical aspects of light. Quantum mechanically, the light field fluctuates around its classical value defined by the expectation value of the electric field. We call a distribution that uniquely defines these intrinsic fluctuations *quantum statistics*. For any fixed classical aspect of light, there exist infinitely many quantum-statistical forms that all correspond to different quantum fluctuations, cf. Refs. [10, 23]. Our analysis is guided by the rigorous steps one must undertake in order to find which aspects of matter's (optical) response are sensitive to quantum fluctuations of the light source. More specifically, Ref. [19] formulates a quantum-optical response theory that is based on a completely general argumentation; we next summarize its main points.

As defined by Glauber [24], quantum statistics of a high-quality pump laser is described by a coherent state $|\beta\rangle$ where β labels the complex-valued amplitude of the field. The optical response of any matter to $|\beta\rangle$ can be uniquely identified by a function $R_{|\beta\rangle}$; in other words, $R_{|\beta\rangle}$ labels all responses measured with classical spectroscopy by adjusting the pump laser's amplitude. We denote the matter's response to a real quantum-light source by $R_{|\mathrm{QM}\rangle}$. As formulated by Sudershan [25], the $R_{|\beta\rangle}$ and $R_{|\mathrm{QM}\rangle}$ are uniquely connected via a general relation

$$R_{|\mathrm{QM}\rangle} = \int \mathrm{d}^2\beta \, P^{|\mathrm{QM}\rangle}(\beta) \, R_{|\beta\rangle} \,, \tag{S1}$$

where $P^{|\mathrm{QM}\rangle}(\beta)$ is the Glauber–Sudarshan function [24, 25] of the quantum source.

A classical field $|\beta\rangle$ has intensity $I_{\mathrm{in}} \propto |\beta|^2$ defined by the average photon number $N = |\beta|^2$. In case the classical measured $R_{|\beta\rangle}$ depends linearly on N, i. e. $R_{|\beta\rangle} = a\,|\beta|^2 + b$, we find $R_{|\mathrm{QM}\rangle} = \int \mathrm{d}^2\beta \left(a\,|\beta|^2 + b\right) P^{|\mathrm{QM}\rangle}(\beta) = a\,N + b$ for all sources because $P^{|\mathrm{QM}\rangle}(\beta)$ is normalized and $\int \mathrm{d}^2\beta \, P^{|\mathrm{QM}\rangle}(\beta)\,|\beta|^2 = N$ produces the average photon number for all quantum sources. Therefore, the linear classical response is completely insensitive to the quantum fluctuations of the pump. Consequently, *the quantum-optical sensitivity must reside within the nonlinear contributions of* $R_{|\beta\rangle}$. In complex systems, such nonlinearities are related to many-body and/or quantum-optical correlations. As a key element of quantum-optical spectroscopy [26, 30, 31], specific forms of $R_{|\mathrm{QM}\rangle}$ nonlinearities can be directly excited via suitably tailored quantum sources. As a result, quantum sources can characterize and control complicated processes much more accurately than the conventional classical spectroscopy does. Especially, this quantum-optical sensitivity is a gateway to identify individual quantum correlations in matter [19, 35, 36].

We seek for unexpected nonlinear responses to discover new quantum-optical effects in quantum-dot (QD) microcavities in the Letter. Since a linear response is uninteresting from a quantum-optical point of view, we remove it from the input/output (I/O) curves to isolate the true nonlinearity. When the I/O curve exhibits the oscillatory nonlinearities a linear fit contains also a constant contribution depending on the oscillation period which is unknown due to the unknown nature of the nonlinearities. In general, the line-removal does not affect the identification of the nonlinearities because they cannot be removed by a line. In this sense, removing a line from the I/O curve is just a visual aid that allows us to exclusively see the most interesting part of the data, i. e. the oscillatory nonlinearities. Since the quantum-optical sensitivity of the response is caused exclusively by the nonlinear response, the line-removal does also not affect the projection results presented in Fig. 3.

* Corresponding author.
christian.berger@physik.uni-marburg.de

II. QUANTUM-MEMORY OSCILLATIONS IN DIFFERENT EXPERIMENTS

To compare different measurements systematically, we introduce the following iterative procedure for the measured I/O intensities $I_{\rm in}^{\rm org}$ and $I_{\rm out}^{\rm org}$, respectively; superscript "org" denotes that the original intensities without any normalization procedure are used. We first define the region of interest (ROI) for $I_{\rm in}^{\rm org}$ where a linear fit $I_{\rm lin}^{\rm org} = a\, I_{\rm in}^{\rm org} + b$ is performed to extract the linear part of $I_{\rm out}^{\rm org}$. As the second step, we determine $I_{\rm osc}^{\rm org} = I_{\rm out}^{\rm org} - I_{\rm lin}^{\rm org}$ as the difference of the measured data and its linear fit. As the third step, we determine which input intensity $I_{\rm in}^{\rm dip}$ produces the first oscillation dip in $I_{\rm osc}^{\rm org}$. In other words, we find a unique I/O value ($I_{\rm in}^{\rm dip}$, $I_{\rm out}^{\rm dip}$) of the first oscillation dip. Since the I/O data has experimental noise, we low-pass filter the $I_{\rm osc}^{\rm org}$ data to determine the ($I_{\rm in}^{\rm dip}$, $I_{\rm out}^{\rm dip}$) point more accurately, which constitutes the fourth step of our algorithm. Since the ($I_{\rm in}^{\rm dip}$, $I_{\rm out}^{\rm dip}$) outcome depends slightly on the ROI choice we iterate steps 1-4 by setting the ROI to extend from $0.33 \times I_{\rm in}^{\rm dip}$ to $6 \times I_{\rm in}^{\rm dip}$ in step 1.

We iterate steps 1-4 until the dip position becomes stable to find a unique linear fit $I_{\rm lin}^{\rm org}$ and dip positions for each measured data. These positions are used to scale input and output with $I_{\rm in} = I_{\rm in}^{\rm org}/I_{\rm in}^{\rm dip}$ and $I_{\rm out} = I_{\rm out}^{\rm org}/I_{\rm out}^{\rm dip}$. For later reference, we denote the linear fit of the scaled output as

$$I_{\rm lin} = a_{\rm exp}\, I_{\rm in} + b_{\rm exp}\,, \tag{S2}$$

where the scaling coefficients follow from the linear fit of step 2, i. e. $a_{\rm exp} = a\, I_{\rm in}^{\rm dip}/I_{\rm out}^{\rm dip}$ and $b_{\rm exp} = b/I_{\rm out}^{\rm dip}$.

Computed I/O results are processed analogously as experiments. Since the computations do not contain random noise, iterations are not needed to locate the position of the first oscillation dip ($I_{\rm in}^{\rm dip}$, $I_{\rm out}^{\rm dip}$). However, the computed $I_{\rm out}^{\rm org}$ saturates faster than in the experiment such that the computational ROI includes some saturation aspects. To eliminate such saturation effects from the $I_{\rm osc}^{\rm org}$ identification, we use the same linear $a_{\rm exp}$ coefficient as in the experiment to describe the normalized linear computation $I_{\rm lin} = a_{\rm exp} I_{\rm in} + b_{\rm num}$. Technically, this is obtained by scaling the output with a slightly modified value $\widetilde{I}_{\rm out}^{\rm dip}$, compared with $I_{\rm out}^{\rm dip}$, yielding $I_{\rm out} = I_{\rm out}^{\rm org}/\widetilde{I}_{\rm out}^{\rm dip}$. Typically, $\widetilde{I}_{\rm out}^{\rm dip}$ is very close to $I_{\rm out}^{\rm dip}$ with only 1 % difference.

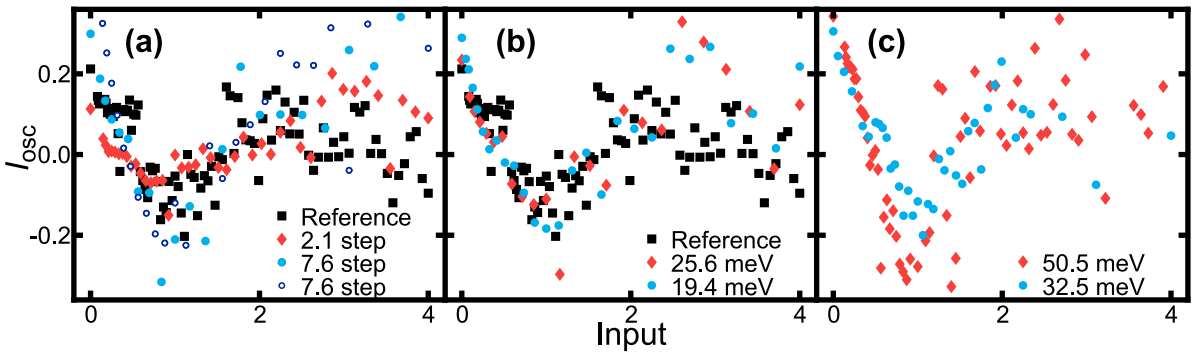

FIG. S1. Scaled experimental output after the subtraction of the linear part. (a) Dependence of output on intensity steps in input. Reference (squares) is compared with measurements having 2.1 (diamonds), 7.6 (filled circles), and 7.6 (open circles) times larger intensity steps than the reference. (b) Dependence on cavity detuning. Reference (squares) has 30.7 meV detuning while two other measurements have 25.6 meV (diamonds) and 19.4 meV (circles) detuning. (c) Effect of cavity mode. Output to cavity mode M2 (see Fig. 1) is measured for 50.5 meV (diamonds) and 32.5 meV (circles) detuning. Frames (a) and (b) were measured for cavity mode M1.

We check the repeatability of the $I_{\rm osc}$ oscillations by performing experiments under nominally the same conditions as the data shown in Fig. 2. Figure S1(a) presents the input dependence of $I_{\rm osc}$ that is constructed with the algorithm above; the squares are exactly the same data as presented in the Letter. We also have performed the I/O measurements with two different intensity steppings in the pump. The filled diamonds correspond to data measured with roughly 2.1 times larger intensity steps than for the reference while the intensity steps are 7.6 times the reference value for both open and filled circles. Since the different measurements have different noise levels the individual measurement points scatter quite differently and cannot be directly compared. However, the mean I/O curves coincide within the experimental scatter, verifying the repeatability of quantum-memory oscillations. In other words, all step sizes indeed reproduce essentially the same oscillatory nonlinearity, dipping roughly to 10 % at the dip.

We also can change the detuning of the pump laser with respect to the emission energy. Figure S1(b) shows the measured $I_{\rm osc}$ when the detuning is 30.7 meV (squares), 25.6 meV (diamonds), and 19.4 meV (circles). As before, the squares correspond to the same data presented in Fig. 2. The mean curves still produce qualitatively similar

oscillatory nonlinearities, which verifies that quantum-memory effects emerge for a broad range of experimentally relevant situations. Since our photoluminescence spectrum shows three main emission resonances (M1-M3 see Fig. 1), we may directly analyze the cavity-mode dependence of the $I_{\rm osc}$ oscillations. Figure S1(c) shows the measured $I_{\rm osc}$ for the M2 mode. Diamonds correspond to 50.5 meV detuning while circles are measured with 32.5 meV. In both cases, the quantum-memory oscillations appear in the same way as for the M1 mode (compare Fig. S1(a)-(b)), but only the mean of 32.5 meV has a similar amplitude than the M1 data because 50.5 meV detuning produces roughly 40 % increase in the nonlinear dip depth. We attribute this to a rather large change in the detuning, as discussed in more detail in connection with Fig. S2(a).

Our QD is so large that it hosts several close-by single-electron levels that can be independently excited. Therefore, it is straight forward to estimate the QD excitation for each level separately. In more detail, we estimate the inversion level by computing how much a single dot level is excited by our detuned pump laser. The maximum occupation of the excited state becomes then

$$f_{\rm max} = \frac{1}{1+\left|\frac{\Delta}{\Omega}\right|^2}\,, \tag{S3}$$

based on Eq. (18.70) in Ref. [10], which presents $f_{\rm max}$ of an ideal two-level system without further coupling to a reservoir or other states. In other words, $f_{\rm max}$ estimates the upper limit of excitation for the most resonant dot level. In general, $f_{\rm max}$ depends on the detuning Δ between the two-level system and the exciting laser and the Rabi frequency Ω. In the study of our Letter, the pump laser is $\hbar\,\Delta = 28.7\,$meV above this dot level. To estimate Ω, we measured the excitation power P of the pump at 75.4 MHz repetition rate and central photon energy $\hbar\,\omega = 1.76\,$eV; it was $P = 30.4\,\mu$W for the maximum excitation used in Fig. 2 and four times lower at the first nonlinear dip. For a $2\,\mu$m excitation spot, this gives 33.7 kV/cm as peak electric field for the 2 ps-long pump pulse. In principle, only a fraction of this pulse reaches the QD due to reflection at the cavity and features in the optical path such as microscope objective and cryostat windows. We ignore this "loss" and use $E = 33.7\,$kV/cm as the upper limit. The Rabi frequency is determined by $\hbar\,\Omega = 2d\,E$ where d is the dipole of the transition. For the InP QDs, the upper limit of d is roughly $25e$ Å, which yields $\hbar\,\Omega = 16.8\,$meV as peak Rabi energy. By inserting Ω and Δ into Eq. (S3), we find $f_{\rm max} = 0.26$ as the upper limit of excitation. At the nonlinear dip, the same estimate yields $f_{\rm max} = 0.08$. Since this number is so small, it is impossible that other higher excited states could invert the system. In other words, this estimate shows convincingly that the system is certainly not inverted.

We also have computed the maximum occupation based on our microscopic model discussed in Sec. III. Including all dot levels, the actual computations yield $f_{\rm max} = 0.07$ and 0.24 at the nonlinear dip and maximum power, respectively. These numbers agree well with the experimental estimate, showing that the oscillatory nonlinearities indeed appear in the excitation power regime well below inversion, (i. e. $f_{\rm max}$ remains smaller than 0.5). The detuned Rabi frequency $\Upsilon = \sqrt{|\Delta|^2 + |\Omega|^2}$ produces Rabi flopping faster than 144 fs for all pump intensities. Therefore the dot level oscillates at least 5 times during each radiative process, defined by the 0.8 ps radiative decay. In other words, quantum memory accumulated during many detuned Rabi flops contributes to emission even though the maximum excitation remains low. That the QD occupation at the used excitation powers stays well below unity is also suggested by the background emission, that is contributed by QDs off-resonant with the cavity modes, which scales linearly with excitation power, so that any effects from biexcitons can be excluded.

In addition, despite of the low lasing threshold, the output intensity still undergoes a jump by an order of magnitude when crossing the threshold. In our experiment we use excitation power densities which are well below those at which this jump occurs, so that it does not occur in the scanned power range.

III. THEORY OF QUANTUM-MEMORY EFFECTS

We explain the quantum-memory effects using the standard Jaynes–Cummings Hamiltonian [28] for a detuned QD with N electronic states inside a cavity. Each of the states can either be excited or unexcited defining 2^N different basis states $|S\rangle$. Additionally, the Hamiltonian contains classical pumping of the two-level system, yielding

$$\hat{H} = \hbar\,\omega(\hat{B}^\dagger\hat{B} + \frac{1}{2}) + \sum_{n=1}^{N}\hbar\,\omega_{21,n}\hat{P}_{z,n} - \hbar\,g\sum_{n=1}^{N}(\hat{B}^\dagger\hat{P}_n + \hat{B}\hat{P}_n^\dagger) - \sum_{n=1}^{N}(\alpha_{\rm L}^\star(t)\hat{P}_n + \alpha_{\rm L}(t)\hat{P}_n^\dagger)\,, \tag{S4}$$

where $\hat{B}$ and $\hat{B}^\dagger$ are photon operators for a single-mode light field with energy $\hbar\,\omega$. The QD population is described by the population-inversion operator $\hat{P}_{z,n}$ while $\hat{P}_n$ and $\hat{P}_n^\dagger$ are the corresponding polarization operators for the dot state n. Mathematically, $\hat{P}_n$ and $\hat{P}_n^\dagger$ are the usual lowering and rising Pauli operators. The energy differences of the states $\hbar\,\omega_{21,n}$ are detuned against the cavity mode. The effective coupling strength between light and matter is chosen

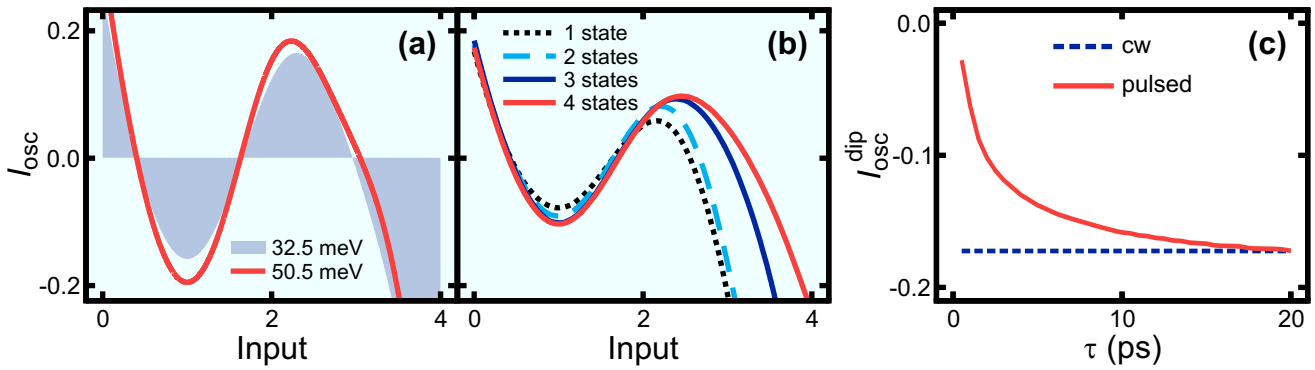

FIG. S2. Effect of detuning and state-number on oscillatory nonlinearities and normalized oscillation amplitude as function of pulse duration τ. (a) Normalized $I_{\rm osc}$ is plotted for $\hbar\Delta_{\rm L} = 32.5\,\text{meV}$ (shaded area) and $\hbar\Delta_{\rm L} = 50.5\,\text{meV}$ (solid line). (b) Normalized $I_{\rm osc}$ is presented for $N = 1$ (dotted line), $N = 2$ (dashed line), $N = 3$ (blue-solid line), and $N = 4$ (red-solid line) states. (c) Pulsed result (solid line) is compared with the cw computation (dashed line).

g for all states. In the Letter, we use the interaction picture that replaces $\hbar\omega_{21,n}$ in Eq. (S4) by the detuned energy $\hbar\delta_n = \hbar(\omega_{21,n} - \omega)$ and eliminates the pure photon part from the Hamiltonian.

The classical pump field is described by a complex-valued amplitude $\alpha_{\rm L}(t)$. We use either a continuous wave (cw) or pulsed, $\alpha_{\rm L}(t) = \alpha_0 \mathrm{e}^{-\frac{t^2}{\tau^2}} \mathrm{e}^{-\mathrm{i}\omega_{\rm L} t}$, where $\hbar\omega_{\rm L}$ is the pump-photon energy and τ determines the pulse width. We then solve the time dynamics via the density matrix $\hat{\rho} = \sum_{n_1,n_2}^{\infty} \sum_{S_1,S_2} |S_1\rangle|n_1\rangle C_{n_2,S_2}^{n_1,S_1} \langle n_2|\langle S_2|$, where $|n_j\rangle$ is a Fock state of the quantized light and $|S_j\rangle$ denotes the basis states of the dot. The quantum dynamics of $\hat{\rho}$ is solved from the Liouville–von Neumann equation

$$\mathrm{i}\hbar \frac{\partial}{\partial t}\hat{\rho}(t) = [\hat{H}, \hat{\rho}]_- + \mathrm{i}\hbar \left(\gamma_z \sum_{n=1}^{N} \mathrm{L}[\hat{P}_{z,n}] + \gamma_{\rm a} \sum_{n=1}^{N} \mathrm{L}[\hat{P}_n] + \kappa \mathrm{L}[\hat{B}] \right), \tag{S5}$$

where we have added the Lindbladian, $\mathrm{L}[\hat{O}] = 2\hat{O}\hat{\rho}\hat{O}^\dagger - \hat{O}^\dagger\hat{O}\hat{\rho} - \hat{\rho}\hat{O}^\dagger\hat{O}$ [29], to account for the dephasing of polarization, population, and cavity photons with dephasing constants $\gamma = \gamma_z + \gamma_{\rm a}$, $2\gamma_{\rm a}$, and κ, respectively. The usual T_1- and T_2-decay times become equal when we set $\gamma_z = \gamma_{\rm a}$, as it is done in our Letter.

We solve Eq. (S5) numerically, to compute the output intensity $I_{\rm out}^{\rm org} = \langle \hat{B}^\dagger \hat{B} \rangle$ defined at the steady state. In the same way, we compute numerically the correlations

$$\begin{gathered} \Pi_{-,n} \equiv \Delta\langle \hat{B}^\dagger \hat{P}_n \rangle = \langle \hat{B}^\dagger \hat{P}_n \rangle - \langle \hat{B}^\dagger \rangle \langle \hat{P}_n \rangle, \qquad \Pi_{z,n} \equiv \Delta\langle \hat{B}^\dagger \hat{P}_{z,n} \rangle = \langle \hat{B}^\dagger \hat{P}_{z,n} \rangle - \langle \hat{B}^\dagger \rangle \langle \hat{P}_{z,n} \rangle, \\ \Delta\langle \hat{B}^\dagger \hat{B} \rangle = \langle \hat{B}^\dagger \hat{B} \rangle - \langle \hat{B}^\dagger \rangle \langle \hat{B} \rangle, \\ \Delta\langle \hat{B}^\dagger \hat{B} \hat{P}_{z,n} \rangle = \langle \hat{B}^\dagger \hat{B} \hat{P}_{z,n} \rangle - \langle \hat{B}^\dagger \rangle \Delta\langle \hat{B} \hat{P}_{z,n} \rangle - \langle \hat{B} \rangle \Delta\langle \hat{B}^\dagger \hat{P}_{z,n} \rangle - \langle \hat{P}_{z,n} \rangle \Delta\langle \hat{B}^\dagger \hat{B} \rangle - \langle \hat{B}^\dagger \rangle \langle \hat{B} \rangle \langle \hat{P}_{z,n} \rangle, \end{gathered} \tag{S6}$$

that are used this Section and Fig. 2 to reveal the source of $I_{\rm osc}$ oscillations.

The density-matrix computation produces fully converging results when it contains 12 Fock states for the conditions studied. As system parameters, we use $\hbar g = 0.405\,\text{meV}$, $\hbar\gamma = 0.32\,\text{meV}$, and $\hbar\kappa = 0.8\,\text{meV}$ that are very typical values [11, 20, 21] for similar samples like ours. To explain the experimental observations in our Letter, we use the experimental parameters $\hbar\Delta_{\rm L} = 30.7\,\text{meV}$ and $\tau = 2\,\text{ps}$ (pulsed) or $\tau = \infty$ (cw) for the pump. The individual $\delta_n = \omega_{21,n} - \omega$ define the state-cavity detuning. The experimental emission is best reproduced when we use $N = 4$ states that are detuned $\hbar\delta_1 = 2\,\text{meV}$, $\hbar\delta_2 = 2.6\,\text{meV}$, $\hbar\delta_3 = 4.58\,\text{meV}$, and $\hbar\delta_4 = 8\,\text{meV}$ above the cavity mode, which yields a similar dot energetics as observed in a comparable system in Ref. [21]. The four dot states are either excited or unexcited, producing $2^4 = 16$ basis states. Altogether, $\hat{\rho}$ contains $(12 \times 16)^2 = 36864$ elements. The energy splitting $\hbar\omega \approx 2.5\,\text{meV}$ and exciton mass $m = 0.135$ predict a QD diameter very close to the estimated dot size of 75 nm when the dot is assumed spherical. Therefore, the chosen energy levels are consistent with the dot size.

Motivated by the measured $\Delta_{\rm L}$ dependence of amplitude in oscillatory nonlinearities (Fig. S1(c)), it is interesting to check whether the computations explain this tendency. Figure S2(a) presents the computed $I_{\rm osc}$ for $\hbar\Delta_{\rm L} = 32.5\,\text{meV}$ (shaded area) and $\hbar\Delta_{\rm L} = 50.5\,\text{meV}$ (solid line). Increasing $\Delta_{\rm L}$ yields 25 % increase in the $I_{\rm osc}$ dip amplitude, which confirms the experimental change in Fig. S1(c). As explained in our Letter, $I_{\rm osc}$ results from the quantum memory accumulated during each pump-induced Rabi flop. Since the effective Rabi frequency Υ increases with growing detuning, higher $\Delta_{\rm L}$ induces more flops and, thus, a larger quantum-memory accumulation, which provides an intuitive explanation for the detected $\Delta_{\rm L}$ dependence. Naturally, a too large $\Delta_{\rm L}$ will eventually decrease the

excitation emission when it becomes too nonresonant, which sets physical limits how much $I_{\rm osc}$ can be enhanced by $\Delta_{\rm L}$.

We also have investigated the effect of the coupling strength g on the oscillatory nonlinearities. We find that the scaled oscillation amplitude increases with decreasing coupling strength and scales as $\frac{1}{g}$, which again has a simple connection to the intuitive quantum-memory source. More specifically, lowering g means that the relative effect of pumping induced Rabi flopping, scaling with the pump (not g), becomes more prominent in the QD emission that scales with g. Therefore, the relative strength of quantum-memory effects increases with decreasing g. However, this argument holds only until g is large enough to favor single-mode emission. We also have verified that changing each g separately does not alter the overall $I_{\rm osc}$ behavior. In summary, the pump-dot detuning and g provide most control for the magnitude of $I_{\rm osc}$.

It is also interesting to study how the quantum-memory oscillations are modified by the state number N included to the model. Therefore, we perform a computation where one, two, or three highest-energy states are eliminated from the computation. The full computation is solved with $N = 4$ states. Figure S2(b) shows the normalized $I_{\rm osc}$ for $N = 1$ (dotted line), $N = 2$ (dashed line), $N = 3$ (blue-solid line), and $N = 4$ (red-solid line) states. We see that the oscillation amplitude increases with elevated N. In addition, higher N yields an extended range for the second oscillation. Therefore, we conclude that the quantum-memory effects are slightly enhanced when the number of emitting states increases, but are not critically dependent on N. Additional numerical studies show that $I_{\rm osc}$ has only a weak dependence on the specific energy values of the dot states.

Even though the experiment is performed with a pulsed excitation, the switch-off analysis shown in Fig. 2(c) becomes significantly simpler when the steady-state emission of the cw pumping is analyzed. Therefore, we studied how $I_{\rm osc}$ of the pulsed excitation approaches the cw result by increasing the pulse duration τ. Figure S2(c) presents the magnitude of the normalized $I_{\rm osc}$ dip (solid line) as function of τ. As a clear trend, the pulsed excitation approaches the cw result. In particular, the $\tau = 2\,$ps pulsed result is sufficiently close to the cw-case such that the basic features of quantum-memory oscillations can be studied with a cw computation.

A. Sources to quantum-dot emission

The quantum-emission dynamics of the Jaynes–Cummings model is already worked out, e. g., in a textbook [10] such that we only need to collect here the central equations. The light emission to the cavity mode is defined by the correlated intensity $\Delta\langle\hat{B}^\dagger\hat{B}\rangle$. As we generalize Eq. (23.42) of Ref. [10], we find that the output intensity follows from

$$\frac{\partial}{\partial t}\Delta\langle\hat{B}^\dagger\hat{B}\rangle = -2\kappa\Delta\langle\hat{B}^\dagger\hat{B}\rangle - 2\,g\sum_{n=1}^{N}{\rm Im}[\Pi_{-,n}]\,, \tag{S7}$$

that contains the decay constant κ and couples to photon-assisted polarizations $\Pi_{-,n}$. The emission is driven by $\Pi_{-,n}$ whose dynamics becomes [10]

$$\mathrm{i}\frac{\partial}{\partial t}\Pi_{-,n} = [\delta_n - \mathrm{i}(\gamma+\kappa)]\,\Pi_{-,n} + s_n^{\rm SE} + s_n^{\rm ST} + s_n^{\rm QM} + s_n^{\rm tri}\,, \tag{S8}$$

that contains four different sources. The $\Pi_{-,n}$ correlation is initiated by the *spontaneous-emission* source $s_n^{\rm SE} = g\sum_{n'=1}^{N}\Big[\langle\hat{P}_{n'}^\dagger\hat{P}_n\rangle - \langle\hat{P}_{n'}^\dagger\rangle\langle\hat{P}_n\rangle\Big]$, whose diagonal part, i. e. $g[\langle\hat{P}_n^\dagger\hat{P}_n\rangle - \langle\hat{P}_n^\dagger\rangle\langle\hat{P}_n\rangle]$, is proportional to the incoherent occupation at the excited state of level n. The nondiagonal ($n' \neq n$) contributions result from the collective recombination processes where state n' is excited by recombining state n. These processes describe either sub- or super-radiant effects when N states collectively emit light to a single mode [27].

The spontaneous emission also enables the *stimulated contribution* $s_n^{\rm ST} = 2\,g\langle\hat{P}_{z,n}\rangle\Delta\langle\hat{B}^\dagger\hat{B}\rangle$, that is a product of the population inversion of state n and correlated photon intensity. In other words, the more photons remain inside the cavity, the more stimulation of $\Pi_{-,n}$ processes emerges in the system. Besides stimulation, each emission also generates a *quantum-memory contribution* $s_n^{\rm QM} = \Omega\,\Pi_{z,n}$, that is a product of a Rabi frequency $\Omega = 2(g\langle\hat{B}\rangle + \frac{\alpha_{\rm L}(t)}{\hbar})$ and the photon-density correlation $\Pi_{z,n} = \Delta\langle\hat{B}^\dagger\hat{P}_{z,n}\rangle$. Intuitively, $\Pi_{z,n}$ records dot's previous emission events giving rise to quantum memory because it defines how excitation depends on the emitted photons; the exact form of quantum-memory accumulations is studied below. Also correlations involving three operators, $s_n^{\rm tri} = 2\,g\Delta\langle\hat{B}^\dagger\hat{B}\hat{P}_{z,n}\rangle$, act as a source.

Equation (S8) can be solved exactly, $\Pi_{-,n}(t) = -\mathrm{i}\int_{-\infty}^{t}\mathrm{d}t'\,\big[s_n^{\rm ST}(t') + s_n^{\rm QM}(t') + s_n^{\rm SE}(t') + s_n^{\rm tri}(t')\big]\,\mathrm{e}^{-\mathrm{i}[\delta_n - \mathrm{i}(\gamma+\kappa)](t-t')}$, in terms of its source terms. When this is inserted into Eq. (S7), we find

$$\frac{\partial}{\partial t}\Delta\langle\hat{B}^\dagger\hat{B}\rangle = 2\,g\int_{-\infty}^{t}\mathrm{d}t'{\rm Re}[S(t,t')] - 2\kappa\Delta\langle\hat{B}^\dagger\hat{B}\rangle\,, \tag{S9}$$

where we have identified $S(t,t') = S^{\rm SE}(t,t') + S^{\rm ST}(t,t') + S^{\rm QM}(t,t') + S^{\rm tri}(t,t')$. Each of the macroscopic sources that appear are obtained from $S^{\rm type}(t,t') = \sum_n s_n^{\rm type}(t') {\rm e}^{-{\rm i}[\delta_n - {\rm i}(\gamma+\kappa)](t-t')}$, where type refers to SE, ST, QM, or tri.

By solving Eq. (S9) in steady state, the emission becomes

$$\Delta\langle \hat{B}^\dagger \hat{B}\rangle = \frac{g}{\kappa} \sum_{n=1}^{N} {\rm Im}\left[\frac{s_n^{\rm SE} + s_n^{\rm ST} + s_n^{\rm QM} + s_n^{\rm tri}}{\delta_n - {\rm i}(\gamma+\kappa)}\right]. \tag{S10}$$

This relation can be applied to determine the effect of spontaneous emission, stimulated emission, quantum memory, and three-particle correlations output, as done in Fig. 2(c) in our Letter. This cw analysis is simpler than the corresponding switch-off study with the pulsed excitation, because one does not need to integrate Eqs. (S8) and (S9). Also the $\Pi_{z,n}$ dynamics is worked out in Ref. [10] for $N = 1$ state so that we can directly study how the quantum memory is generated. By generalizing Eq. (23.42) of Ref. [10] for N states, we find an exact dynamics,

$$\begin{aligned} {\rm i}\frac{\partial}{\partial t}\Pi_{z,n} =& -{\rm i}(\kappa + 2\gamma_{\rm a})\Pi_{z,n} + g(\Delta\langle \hat{B}^\dagger \hat{B}^\dagger\rangle\langle \hat{P}_n\rangle - \Delta\langle \hat{B}^\dagger \hat{B}\rangle\langle \hat{P}_n^\dagger\rangle) \\ &+ g\sum_{n'}(\langle \hat{P}_{n'}^\dagger \hat{P}_{z,n}\rangle - \langle \hat{P}_{n'}^\dagger\rangle\langle \hat{P}_{z,n}\rangle) + \frac{\Omega^\star \Pi_{-,n} - \Omega\Pi_{+,n}}{2} + g[\Delta\langle \hat{B}^\dagger \hat{B}^\dagger \hat{P}_n\rangle - \Delta\langle \hat{B}^\dagger \hat{B}\hat{P}_{n'}^\dagger\rangle]. \end{aligned} \tag{S11}$$

The second term induces $\Pi_{z,n}$ when the system simultaneously contains squeezing correlation $\Delta\langle \hat{B}^\dagger \hat{B}^\dagger\rangle$ and polarization. The third term generates $\Pi_{z,n}$ spontaneously whenever the system has polarization or coherent $\langle \hat{P}_{n'}^\dagger \hat{P}_{z,n}\rangle$ contributions. Also the remaining sources exist only when coherences are present. In particular, Eq. (S11) identifies two main mechanisms for generating quantum-memory correlations; either pure coherence or a combination of polarization and squeezing induces $\Pi_{z,n}$.

IV. QUANTUM-OPTICAL SPECTROSCOPY

In our Letter, we measure the output intensity $I_{\rm out}(\beta)$ as function of the input-laser's amplitude β or equivalent as function of photon number $N = |\beta|^2$ because our measurement is not phase sensitive. Unfortunately, lasers with arbitrary quantum statistics are not yet available in order to measure the output intensity $I_{\rm out}^{|\lambda\rangle}$ as function of an arbitrary quantum state $|\lambda\rangle$. However,

$$I_{\rm out}^{|\lambda\rangle} = \int {\rm d}^2\beta \; P^{|\lambda\rangle}(\beta)\, I_{\rm out}(\beta) \tag{S12}$$

establishes a fundamental connection [25] between $I_{\rm out}^{|\lambda\rangle}$ and a set of classical responses $I_{\rm out}(\beta)$, where the Glauber–Sudarshan $P^{|\lambda\rangle}(\beta)$ function represents the quantum statistics of the desired light source. As demonstrated in Ref. [19], the projection (S12) can be efficiently implemented with the help of the so-called cluster-expansion transformation (CET), even when the measurement contains noise and is performed in a limited phase space $\beta \in \Gamma$. In particular, this work introduces an experimentally robust algorithm to project a set of measured $I_{\rm out}$ to any desired quantum response $I_{\rm out}^{|\lambda\rangle}$. The extreme accuracy of this method is demonstrated by the high-precision characterization of biexcitons [35] and the discovery of a new quasiparticle, the dropleton [36].

Technically, the CET finds correlation coefficients $a_R(J)$ based on the set of measured $I_{\rm out}(\beta)$. They are connected to physical correlations like mean, variance, and higher order cumulants. The explicit algorithm from measurement-to-$a_R(J)$ is provided in Appendix B of Ref. [35] for the phase insensitive measurements studied here. Once the $a_R(J)$ coefficients are known, they uniquely define any quantum response. As a consistency check, we first analyze the CET projection to a classical source $|\beta_0\rangle$, yielding [19]

$$I_{\rm CET}(\beta) = \frac{\mathcal{N}_R}{4\Delta x_R^2} \sum_{J=0}^{C/2} (-1)^J a_R(J) W_J\left(\tfrac{|\beta|^2}{4\Delta x_R^2}\right), \quad W_J(x) = \frac{2}{\pi}{\rm e}^{-2x} \sum_{k=0}^{J} \frac{2^{2J-k}\,(-x)^{J-k}}{k!(J-k)!(J-k)!}, \tag{S13}$$

where $\mathcal{N}_R = \int_\Gamma {\rm d}^2\beta\, I_{\rm out}(|\beta|)$ is the norm and $\Delta x_R^2 \equiv \frac{1}{2\mathcal{N}_R}\int_\Gamma {\rm d}^2\beta\, |\beta|^2 I_{\rm out}(|\beta|)$ is the normalized variance. Both Δx_R^2 and $a_R(j)$ can be accurately determined from the high-precision measurements shown in our Letter. In practice, one adjusts the maximum number of clusters C such that $I_{\rm CET}(\beta)$ reproduces the experimental input accurately. We use $C = 192$ clusters to project the data in the Letter and produce I/O curves resulting from pumping a QD with different quantum-light sources.

A. Projection to quantum sources

A thermal state is completely defined by its photon-number fluctuations $\Delta\langle B^\dagger B\rangle_{\rm th} = \langle B^\dagger B\rangle_{\rm th} \equiv \overline{n}$ which are equal to the average photon number since the first-order coherences $\langle B\rangle_{\rm th}$ vanish [23]. The CET projection algorithm (S12) with a thermal state yields [19]

$$I_{\rm out}^{|{\rm th}\rangle} = \frac{\mathcal{N}_R}{\pi(2\Delta x_R^2+\overline{n})}\sum_{J=0}^{C/2}\frac{a_R(J)}{J!}\left(\frac{-4\Delta x_R^2}{2\Delta x_R^2+\overline{n}}\right)^J . \tag{S14}$$

A squeezed vacuum state is characterized by the two-photon correlation $|\Delta\langle BB\rangle_{\rm sqz}| = s$ that defines the average photon number $N_{\rm sqz}$ via $s \equiv \sqrt{N_{\rm sqz}^2+N_{\rm sqz}}$. The CET projection of Eq. (S12) with squeezed vacuum produces [19]

$$I_{\rm out}^{|{\rm sqz}\rangle} = \frac{\mathcal{N}_R}{\pi\sqrt{S^2-s^2}}\sum_{J=0}^{C/2}a_R(J)\left(\frac{-2\Delta x_R^2}{S^2-s^2}\right)^J\sum_{k=0}^{J/2}\frac{[2S]^{J-2k}s^{2k}}{k!k!(J-2k)!}, \tag{S15}$$

where we have identified $S \equiv 2\Delta x_R^2 + N_{\rm sqz}$.

A Schrödinger-cat state is a superposition of two coherent states with common displacement β_0 along the x-quadrature and separation determined by γ. By choosing γ to be aligned parallel to β_0, we obtain the so-called *stretching-cat* state [19]. The wave function is then $|{\rm cat}\rangle \equiv \mathcal{N}_{\rm cat}\left(|\beta_0-\gamma\rangle + |\beta_0+\gamma\rangle\right)$ with coherent states $|\beta_0\pm\gamma\rangle$ and the normalization constant $\mathcal{N}_{\rm cat} = (2+2\,{\rm e}^{-2|\gamma|^2})^{-\frac{1}{2}}$. The average coherent displacement of the cat state becomes then $\langle B\rangle_{\rm cat} = \beta_0$, while its squeezing correlation is $\Delta\langle BB\rangle_{\rm cat} = \gamma^2$. As a result, this stretching-cat state is squeezed while having also coherence. The CET projection of Eq. (S12) with $|{\rm cat}\rangle$ yields [19]

$$I_{\rm out}^{|{\rm cat}\rangle} = \frac{\mathcal{N}_R}{4\Delta x_R^2}\sum_{J=0}^{C/2}(-1)^J a_R(J)\mathcal{N}_{\rm cat}^2\left[W_J\left(\tfrac{|\beta_0+\gamma|^2}{4\Delta x_R^2}\right)+W_J\left(\tfrac{|\beta_0-\gamma|^2}{4\Delta x_R^2}\right)+2\,{\rm e}^{-2|\gamma|^2}{\rm Re}\left[W_J\left(\tfrac{(\beta_0+\gamma)^\star(\beta_0-\gamma)}{4\Delta x_R^2}\right)\right]\right] . \tag{S16}$$

In the Letter, we choose β_0 and γ so that $|{\rm cat}\rangle$ has the *same* average photon number as the coherent state $|\beta = \sqrt{|\beta_0|^2+1}\rangle$ while the $|{\rm cat}\rangle$ state's fluctuations correspond to the addition of a single photon.